Hydrodynamics of Francis turbine operation at deep part load condition

THÈSE N^{O} 7730 (2017)

PRÉSENTÉE LE 16 JUIN 2017
À LA FACULTÉ DES SCIENCES ET TECHNIQUES DE L'INGÉNIEUR
LABORATOIRE DE MACHINES HYDRAULIQUES
PROGRAMME DOCTORAL EN ENERGIE

ÉCOLE POLYTECHNIQUE FÉDÉRALE DE LAUSANNE

POUR L'OBTENTION DU GRADE DE DOCTEUR ÈS SCIENCES

PAR

Keita YAMAMOTO

acceptée sur proposition du jury:

Prof. J. A. Schiffmann, président du jury
Prof. F. Avellan, directeur de thèse
Dr A. Jung, rapporteur
Prof. K. Miyagawa, rapporteur
Prof. K. Mulleners, rapporteuse

EPFL
ÉCOLE POLYTECHNIQUE
FÉDÉRALE DE LAUSANNE
Suisse
2017

I have no special talent.
I am only passionately curious.
— Albert Einstein

Acknowledgements

To begin with, I would like to express my deep appreciation to the members of the jury for my doctoral thesis, Prof. Jürg Alexander Schiffmann, Prof. François Avellan, Prof. Karen Mulleners, Dr Alexander Jung, and Prof. Kazuyoshi Miyagawa for their valuable time and helpful comments to brush up and accomplish the thesis. The research presented in this thesis was realized thanks to the financial support of the European Commission (HYPERBOLE Research project, ERC/FP7-ENERGY-2013-Grant 608532) as well as the great support by all the research partners of HYPERBOLE project.

I wish to express my most sincere gratitude to my thesis director, Prof. François Avellan, for offering me such a great opportunity to be a member of the Laboratory for Hydraulic Machines and participate in a fascinating research project for hydraulic turbines. His precise advices for the research and constant encouragement were essential to succeed in my thesis. I would also like to thank him for giving me a lot of chances to present my research work in various international conferences and meetings.

It goes without saying that my doctoral thesis was achieved by great assistance by the HYPERBOLE research team in Laboratory for Hydraulic Machines. First of all, I would like to show my heartfelt appreciation to Dr Andres Muller for his great support to come to Switzerland and start working in LMH, as well as many inspiring comments he gave me throughout all my doctoral works. I would also like to give my special thanks to Dr Arthur Favrel for supporting me a lot during the Experimental campaign and many helpful comments and feedbacks to brush up the thesis. I wish to extend my thanks as well to Dr Christian Landry for a lot of interesting discussions and his great support for my experimental works in the test rig.

It should be mentioned that the great success in conducted work would not be achieved without the skillful support from the technical staff and other members in LMH. First, I would like to show my deep appreciation to Dr Philippe Cerrutti for the development of the workspace for HYPERBOLE research project and his technical support for software, as well as Dr Mohamed Farhat for his interesting and inspirational comments for research. Also, I wish to thank Henri-Pascal Mombelli and Georges Crittin for their great support about the experimental facilities and instrumentation. My special thanks also go to Lillie Aurelia Rumpf for her special support for the test facilities as well as the emendation of my thesis. I would also like to extend my thanks to the other members in the design office, Vincent Berruex, Philippe

Faucherre, and Alain Renaud, for providing accurate designs of experimental equipment, the group of test engineers, Alberto Bullani, Ambrosio Acal Ganaza, and Monica Suarez, for their technical support in the test facilities, and the members of Mechanic group, Maxime Raton, Victor Rivas, David Buzzi, Raymond Fazan, Christian Sierro, and Louis Vina, for their mechanical support in the experimental facilities.

My deep thanks go as well to all the Post-doctoral members and PhD students in LMH, especially; Dr Martino Reclari: Thank you very much for your warm hospitality when visiting Takasago.; Dr Ebrahim Jahanbakhsh: I still remember that you spoke to me so many times to encourage me just after I came here from Japan, and gave me a lot of advices to live in Switzerland.; Dr Christian Vessaz: I was always surprised at how delicious your cook is!!; Dr Matthieu Dreyer: I will never forget the nickname you gave me "Pillow Slayer", and wonderful moment we shared in Japan!!; Simon Pasche: Thank you very much for a lot of advices regarding CFD. Your advices were always helpful to improve my simulations!!; Outi Supponen: I always enjoyed having a chat with you over a cup of coffee in cafeteria.; Elena Vagnoni: I will never forget the time we spent together with Alex, David, and Uroš in Ljubljana.; Joao Gomes: Thank you very much for helping me organize a Christmas dinner, in fact you almost did everything.; and off course, many thanks to other members, Dr Loïc Andolfatto, Dr Audrey Maertens, Dr Pascal Clausen, João Delgado, Sebastián Leguizamón, Siamak Alimirzazadeh, Ali Amini, and Alexis Papagiannopoulos for the precious time and wonderful experiences in the lab. I would also like to show my special thanks to Isabelle Stoudmann Schmutz for her continuous support and kind consideration throughout my stay in LMH.

I would also like to express my deep appreciation to Prof. Yoshinobu Tsujimoto for giving me a first opportunity to study in Switzerland for my doctoral degree. My special thanks also go to Prof. Kazuyasu Sugiyama in Osaka university for kindly accepting Andres and me for the additional experimental measurements, as well as the members in Sugiyama lab for their tremendous support while we stayed in Osaka university. It goes without saying that I decided to start my doctoral research thanks to the advices from Dr Koichi Yonezawa, and I leaned a lot from his inspiring comments for research and attitude towards scientific studies. I would therefore like to express my sincere appreciation to him. I would also like to show my special thanks to Takashi Kumashiro for giving me lots of advices and encouragement, which were great aid to accomplish my doctoral work.

Finally, it should be emphasized that my doctoral work as well as academic studies would not be accomplished without my family's support. Especially, I would like to express my deep appreciation to Noriko Yamamoto for her continuous support and encouragement to go further.

Lausanne, 1 Mai 2017 K. Y.

Abstract

The electrical energy production from New and Renewable Energy (NRE) sources have become increasingly important in the past decades. However, intermittent electrical generation from NRE sources due to their stochastic nature often prevents stable power output from existing power grids. To enable a smooth integration of NRE sources, flexible operations at hydraulic power plants are key to providing the capability of primary and secondary grid control to balance the energy production. The rapid growth of the NRE sources nonetheless requires hydraulic machines to function in an extended operating range, especially down to extremely low discharge conditions called deep part load operation. Such off-design conditions provoke various types of cavitation flows, posing a threat to stable operations at hydraulic units. Inter-blade cavitation vortices are a typical example of cavitation phenomena observed at deep part load operation. However, its dynamic characteristics are insufficiently understood today. The main objective of the present research is to unveil the flow characteristics at deep part load conditions and the physical mechanisms responsible for the inter-blade vortex development by means of the experimental and simulation approaches.

The experimental approach is carried out with a physical reduced scale model of a Francis turbine, precisely reproducing actual behaviors in prototype hydraulic power units. The characteristics of the flow in the draft tube is first investigated by wall pressure fluctuation and velocity surveys by Particle Image Velocimetry (PIV). For investigations of inter-blade cavitation vortices, the present study introduces a novel visualization technique with instrumented guide vanes, providing unprecedented images of cavitation development inside the runner blade channel. The binary image processing technique enables the successful evaluation of inter-blade cavitation vortices in the images. The analyses demonstrate that the probability of the inter-blade cavitation development is significantly high close to the runner hub. Furthermore, the mean vortex line is calculated and the vortex region is estimated in the three-dimensional domain for the comparison with numerical simulation results. Additionally, the impact of the inter-blade vortex on the pressure field is investigated by on-board instrumentation on the runner blade. It reveals that the presence of an inter-blade vortex induces stochastic pressure oscillations on the blade, and the pressure amplitude is locally intensified especially on the blade suction side. Moreover, the survey of the wall pressure difference between pressure and suction sides of the blade suggests the development of a backflow region near the hub, which it is assumed is closely related to the development of the inter-blade vortex.

In an effort to better understand the flow structure in the draft tube, as well as the development of inter-blade vortices, numerical simulations by an unsteady RANS approach are performed. Flow analysis in the draft tube and the simulated inter-blade vortices are in good agreement with the experimental results. Furthermore, the simulated flow inside the blade channel confirms the development of a backflow region on the runner hub near the runner outlet. The skin-friction analyses evidence that the backflow region as well as inter-blade vortex development are provoked by flow separation on the runner hub, which is caused by the misaligned flow condition inside the blade channel. The investigations are furthermore extended to identify the influence of inter-blade vortices on the specific energy dissipation in the runner. The quantitative evolution of the specific energy loss, based on the principle of the specific rothalpy conservation, reveals that the presence of inter-blade vortices creates the energy loss through the blade channel.

Key words: Francis turbine, deep part load, cavitation, inter-blade vortex, visualization, on-board measurement, numerical simulation, unsteady RANS

Résumé

La production d'énergie électrique à partir de sources d'énergies nouvelles et renouvelables (NRE) est devenue de plus en plus importante au cours de la décennie passée. Cependant, la production électrique à partir de ce type de source d'énergie est intermittente du fait de leur nature stochastique et impacte directement la stabilité des réseaux électriques existants. Pour garantir l'intégration des sources d'énergie renouvelables, la flexibilité des centrales hydrauliques est cruciale afin de fournir des capacités de contrôle primaire et secondaire au réseau électrique et pour équilibrer la production d'énergie. La croissance rapide des sources NRE nécessite cependant que les machines hydrauliques fonctionnent dans une plage d'exploitation étendue, en particulier jusqu'à des conditions de débit extrêmement faible appelées fonctionnement à très faible charge partielle. De telles conditions de fonctionnement provoquent divers types d'écoulement cavitant, ce qui constitue une menace pour la stabilité des unités hydrauliques. Les vortex inter-aube de cavitation sont un exemple typique de phénomènes de cavitation observés lors de fonctionnement à très faible charge partielle. Cependant, leurs caractéristiques dynamiques sont insuffisamment comprises aujourd'hui. L'objectif principal de la présente recherche est de dévoiler les caractéristiques de l'écoulement en conditions de très faible charge partielle et les mécanismes physiques responsables du développement des vortex inter-aube au moyen d'approches expérimentales et numériques.

L'approche expérimentale est réalisée sur un modèle physique réduit d'une turbine Francis, reproduisant parfaitement le comportement hydraulique de la machine réelle. Les caractéristiques de l'écoulement dans le diffuseur sont d'abord étudiées par des mesures de pression aux parois et des mesures PIV de champs de vitesse. Pour l'étude sur les vortex inter-aube de cavitation, la présente étude introduit une nouvelle technique de visualisation avec des directrices instrumentées, fournissant des images sans précédent du développement de la cavitation à l'intérieur du canal inter-aube de la roue. Une technique de traitement d'image par binarisation permet d'évaluer avec succès le vortex inter-aube de cavitation dans les images. Les analyses démontrent que la probabilité de développement de la cavitation entre les aubes est significativement élevée à proximité du moyeu de la roue. De plus, la ligne moyenne du vortex est calculée et le vortex est reconstruit dans l'espace pour comparaison et validation des résultats de simulation numérique. De plus, l'impact du vortex sur le champ de pression est étudié en utilisant une instrumentation embarquée sur les aubes de la roue. Les résultats révèlent que la présence du vortex inter-aube induit des oscillations de pression stochastiques sur l'aube alors que l'amplitude des fluctuations de pression est localement amplifiée, en particulier sur la face extrados de l'aube. De plus, la différence de pression entre les deux

faces de l'aube suggère le développement d'une zone de recirculation près du moyeu, qui est supposée être étroitement liée au développement du vortex inter-aube.
Dans le but de mieux comprendre la structure de l'écoulement dans l'aspirateur, ainsi que le développement des vortex inter-aube, des simulations numériques par une approche RANS instationnaire sont effectuées. Les résultats pour l'écoulement dans l'aspirateur et les vortex inter-aube sont en accord avec les résultats expérimentaux. De plus, l'écoulement simulé dans le canal inter-aube confirme le développement d'une zone de recirculation sur le moyeu près de la sortie du canal. Les analyses des coefficients de frottement prouvent que la région de recirculation ainsi que le développement des tourbillons inter-aube sont provoqués par un décollement d'écoulement sur le moyeu de la roue, qui est provoqué par un défaut d'alignement de l'écoulement à l'intérieur du canal inter-aube. Les recherches sont en outre étendues pour identifier l'influence des vortex inter-aube sur la dissipation d'énergie spécifique dans le canal inter-aube de la roue. L'évolution quantitative de la perte d'énergie spécifique, basée sur le principe de la conservation spécifique de la rothalpie, révèle que la présence de vortex inter-aube crée une perte d'énergie additionnelle dans le canal inter-aube.

Mots clefs : turbine Francis, très faible charge partielle, cavitation, vortex inter-aube, visualisation, instrumentation embarquée, simulation numérique, RANS instationnaire

Contents

Acknowledgements **i**

Abstract (English/Français) **iii**

List of figures **xi**

List of tables **xxi**

Nomenclature **xxiii**

Introduction **1**
- 0.1 Energy context 1
- 0.2 Francis turbines 2
- 0.3 Off-design operating conditions 3
- 0.4 State of the art 4
- 0.5 Research objective 6
- 0.6 Document structure 6

1 General experimental setup **9**
- 1.1 Physical reduced scale model 9
- 1.2 Pressure sensors on the model and test rig 10
- 1.3 Targeted operating conditions at deep part load operation 11
  - 1.3.1 Operating parameters for targeted operating points 11
  - 1.3.2 Velocity triangles at the selected points 12

2 Flow investigation in draft tube **13**
- 2.1 Introduction 13
- 2.2 Experimental setup 14
  - 2.2.1 Visualization of the cavitation vortex rope 14
  - 2.2.2 Particle Image Velocimetry (PIV) 14
- 2.3 Characteristics of the vortex rope at deep part load 15
  - 2.3.1 Frequency analysis of the vortex rope 15
  - 2.3.2 High-speed visualizations of the vortex rope 17
- 2.4 Flow analysis by PIV measurements 19
  - 2.4.1 Axial velocity distribution 19

2.4.2 Circumferential velocity distribution . . . 21
2.4.3 Swirl number calculation . . . 21
2.5 Summary . . . 24

3 Investigation of inter-blade vortices by visualization 25
3.1 Introduction . . . 25
3.2 Experimental setup for visualization . . . 26
3.2.1 Setup for visualization from downstream . . . 26
3.2.2 Setup for visualization from upstream . . . 27
3.2.3 Operating conditions for visualizations . . . 30
3.3 Visualization results . . . 31
3.3.1 Visualizations from downstream of the runner . . . 31
3.3.2 Visualization from upstream of the runner . . . 33
3.4 Characterization of the inter-blade cavitation vortex by image processing . . . 33
3.4.1 Evaluation of the inter-blade cavitation vortex region . . . 33
3.4.2 Estimation of the vortex region in a three-dimensional domain . . . 36
3.5 Summary . . . 39

4 Investigation of inter-blade vortex by on-board pressure measurement 41
4.1 Introduction . . . 41
4.2 Experimental setup for on-board measurement . . . 42
4.2.1 Instrumented runner . . . 42
4.2.2 Telemetry acquisition system . . . 43
4.2.3 Operating conditions for on-board pressure measurement . . . 43
4.3 Pressure measurement results . . . 44
4.3.1 Comparison of the raw pressure signals measured on the blade . . . 44
4.3.2 Frequency analysis . . . 44
4.3.3 Evaluation of the pressure amplitude . . . 51
4.3.4 Pressure difference on the blade . . . 55
4.4 Flow structure inside the blade channel . . . 58
4.5 Summary . . . 59

5 Numerical setup 61
5.1 Introduction . . . 61
5.2 Governing equation . . . 62
5.2.1 Conservation equations . . . 62
5.2.2 Reynolds Averaged Navier-Stokes Equations . . . 64
5.2.3 Eddy viscosity turbulence model . . . 64
5.2.4 Cavitation model . . . 66
5.2.5 Discretization . . . 66
5.3 Calculation domain . . . 67
5.3.1 Calculation setup . . . 67
5.3.2 Computational grid . . . 68

5.3.3 Computational convergence 70
5.3.4 Preliminary computation result 70

6 Flow simulations in draft tube **73**
6.1 Introduction 73
6.2 Flow analysis in the draft tube 74
6.2.1 Mean flow characteristics 74
6.2.2 Transient characteristics of the simulated flow in the draft tube 77
6.2.3 Pressure recovery and loss coefficient in the draft tube 81
6.3 Summary 84

7 Simulated flow investigations in blade channels **85**
7.1 Introduction 85
7.2 Inter-blade cavitation vortex structure 86
7.2.1 Comparison of simulated and visualized inter-blade cavitation vortices 86
7.2.2 Comparison of vortex structures for different operating points 88
7.3 Velocity investigation inside the blade channel 89
7.3.1 Velocity distribution 89
7.3.2 Meridional velocity distribution 94
7.3.3 Flow incident angle 96
7.4 Inter-blade vortex intensity 99
7.4.1 Vorticity distribution inside blade channel 99
7.4.2 Vortex circulation 99
7.5 Pressure distribution 102
7.5.1 Pressure distribution in the blade channel 102
7.5.2 Blade loading 102
7.5.3 Pressure fluctuation on the blade 105
7.6 Flow topology 107
7.6.1 Skin-friction pattern on the hub 107
7.6.2 Pressure gradient along the flow streamline 109
7.6.3 Three dimensional flow pattern near the hub 110
7.7 Influence of inter-blade vortices on the specific energy loss 112
7.7.1 Specific energy distribution 112
7.7.2 Specific energy dissipation evaluated from rothalpy 114
7.8 Summary 118

8 Conclusions and perspectives **121**
8.1 Conclusions 121
8.2 Perspectives 123

A Hill-chart of the reduced scale model **125**

B High-speed visualizations **127**

C Calculation of the velocity component 129

D Inter-blade vortex identification 131

Bibliography 141

Curriculum Vitae 143

List of Figures

1 Electricity generation from Hydraulic power plants from 1971 to 2014 [4] 1

2 Main components of a Francis turbine 2

3 Velocity triangles at the runner inlet and the runner outlet 3

4 Velocity triangle at the runner outlet for full load operation (a), part load operation (b) and deep part load operation (c) 3

5 Axisymmetric cavitation vortex rope at full load operating conditions (a) [57], helical cavitation vortex rope at part load operating conditions (b) [23], and inter-blade cavitation vortices at deep part load operating conditions (c) [91] . 5

1.1 Schematics of the physical reduced scale model of the studied Francis turbine installed on EPFL test rig PF3 [23, 57] 9

1.2 View of the spiral case, runner, and draft tube cone with the sections for the pressure measurement in the draft tube (a) and the locations of the pressure transducers at section #1 (b) [23] 10

1.3 Top view of the physical reduced scale model with the locations of pressure transducers installed in the straight draft tube and upstream feeding pipe together with upstream and downstream evaluate sections [57] 10

1.4 Theoretical velocity triangles at the runner inlet for the BEP (a), OP#1 (b), OP#2 (c), and OP#3 (d). The dashed blue line indicates the geometrical blade angle at the inlet. 12

2.1 Flat rectangular window for visualizations of the cavitation vortex rope and PIV measurements in the draft tube cone (a) and the experimental setup of high-speed visualizations with the LED screen (b) 14

2.2 Experimental setups of PIV measurements respectively for the circumferential velocity component C_u (a) and the axial velocity component C_m (b) 15

2.3 Influence of Q_{ED} on the spectral peaks of the pressure fluctuations measured at C1N for broad discharge range (a) and focused range at deep part load (b) at rated n_{ED} and $\sigma = \sigma_{plant} = 0.11$, together with the linear estimation of the vortex precession frequency f_{rope} and the estimated frequencies of the multiple vortex ropes f_{ke} (dashed blue lines) 16

2.4 Influence of Q_{ED} on the vortex rope precession frequency for broad discharge range (a) and the evolution of the multiple frequencies detected at deep part load operation (b) at rated n_{ED} and $\sigma = 0.11$ 17

2.5 High speed visualizations of the cavitation vortex rope under deep part load operations together with fluctuating pressure signals at C1N and spectral analysis results at Q_{ED} = 0.090 (a), 0.070 (b) and 0.054 (OP#2) (c) at rated n_{ED} and $\sigma = 0.11$ 18

2.6 Distribution of the non-dimensional axial velocity C_m^* for Q_{ED} = 0.100 (a), 0.070 (b), 0.053 (OP#2) (c), and 0.040 (d) at atmospheric pressure condition and rated n_{ED}. The locations of backflow inception ($C_m^* = 0$) are highlighted by solid black lines. 19

2.7 Velocity profiles of the non-dimensional axial velocity C_m^* along the x-axis at section #1 (a) and section #2 (b) 20

2.8 Influence of Q_{ED} on backflow inception point in the draft tube at section #1 and section #2 20

2.9 Distribution of the non-dimensional circumferential velocity C_u^* for Q_{ED} = 0.100 (a), 0.070 (b), 0.054 (OP#2) (c), and 0.040 (d) at atmospheric pressure condition and rated n_{ED} at section #1 22

2.10 Distribution of the non-dimensional circumferential velocity C_u^* for Q_{ED} = 0.100 (a), 0.070 (b), 0.054 (OP#2) (c), and 0.040 (d) at atmospheric pressure condition and rated n_{ED} at section #2 22

2.11 Velocity profiles of the non-dimensional circumferential velocity C_u^* along the x-axis at section #1 (a) and section #2 (b) 23

2.12 Influence of Q_{ED} on the swirl number S calculated by the velocity profiles acquired from PIV measurements at section #1 and section #2 24

3.1 The inclined window installed on the transparent draft tube cone (a) and the setup of visualizations of inter-blade cavitation vortices from the runner downstream (b) 26

3.2 Xenon flash light (a) and its characteristics of light emission intensity (b) 26

3.3 Sketch of the instrumented guide vane with a transparent acrylic window and the hollow space manufactured inside the guide vane 27

3.4 Schematics of the general structure of the borescope and the adopted borescope with a swivel deflecting prism 28

3.5 Compact LED (a) and light probe with aluminium heat sink (b) 28

3.6 Installation of the instrumented guide vanes and visualization devices 29

3.7 Acquisition system for guide vane visualization 30

3.8 Visualizations from the runner downstream for different Q_{ED} conditions at rated n_{ED} and $\sigma = 0.11$. The discharge values correspond to Q_{ED} = 0.010 (a), 0.018 (speed-no-load condition) (b), 0.054 (OP#2) (c), 0.070 (d), 0.080 (e), and 0.090 (f). 31

3.9 Visualization from the runner downstream for different n_{ED} conditions at constant guide vane opening $GVO = 5$ ° and $\sigma = 0.11$. The n_{ED} values correspond to n_{ED} = 0.317 (OP#1) (a), 0.288 (OP#2) (b), and 0.268 (OP#3) (c). 32

3.10 Instantaneous views of the inter-blade cavitation vortex using the instrumented guide vane at OP#1 (a), OP#2 (b), and OP#3 (c) at $\sigma = 0.11$ with different swivel prism angles looking at the hub (upper side) and the shroud (lower side), respectively 32

3.11 An example of a binarized image of the inter-blade cavitation vortex (a) and the threshold of cavitation based on the edge detection (b) 34

3.12 Contour of the calculated probability P overlaid on the each reference image for the targeted operating conditions OP#1 (a), OP#2 (b), and OP#3 (c) 35

3.13 Histogram of the probability P along the horizontal line on the hub 35

3.14 An example of the detected cavitation edge with the vortex center line (a) and the instantaneous vortex inception points together with the averaged location of the vortex inception point on the reference image (b) 36

3.15 Averaged vortex center lines with the corresponding standard deviation as well as the location of the vortex inception at OP#1 illustrated on the reference image 36

3.16 Lines of constant streamwise (st.) location, θ, and span-wise (sp.) location on the same view of the visualization from the CFD domain (a) and the overlaid mesh lines on the visualized blade channel (b) 37

3.17 The estimated inter-blade vortex center locations given by intersections with constant span-wise lines at a constant streamwise location (a) and comparison of the calculated vortex line with the estimated location of the vortex center with the standard deviation in the 3-D domain (b) 38

3.18 View of the mapped vortex line from downstream of the runner (a) and the projected vortex line on the meridional plane (b) 38

4.1 Schematics of the instrumented runner (a) and the locations of the installed pressure transducers on the runner blade (b) 42

4.2 Instrumented shaft used for on-board pressure measurements (a) and the wireless transmission system installed inside the shaft (b) 43

4.3 Comparison of the measured pressure signals over 16 runner revolutions at #1 Prs (a), #1 Suc (b), #2 Prs (c), and #2 Suc (d) for OP#1, #2 and #3 at $\sigma = \sigma_{plant}$ 45

4.4 Comparison of the frequency spectrum of the pressure signals measured at #2 Suc over a wide range of frequencies (a) and in the low frequency range (b) for OP#1, #2 and #3 at $\sigma = \sigma_{plant}$ 46

4.5 Influence of Q_{ED} at deep part load condition on the spectral peaks of the pressure fluctuations measured at location #2 Suc for the different n_{ED} conditions $n_{ED} =$ 0.317 (i), 0.288 (ii), and 0.268 (iii) over a wide range of the frequencies (a) and in the low frequency range (b) at $\sigma = \sigma_{plant}$. The blue arrow in (i) indicates the discharge range of the inter-blade cavitation vortex development. 47

4.6 Appearance of inter-blade cavitation vortices for different n_{ED} conditions at constant guide vane opening $GVO = 5\,°$ and $\sigma = 0.11$ 48

4.7 Influence of n_{ED} on the spectral peaks of the pressure fluctuations measured at all sensors on the runner blade #1 Prs (a), #1 Suc (b), #2 Prs (c), and #2 Suc (d) at constant guide vane opening $GVO = 5$ ° and $\sigma = 0.11$. The blue arrow indicates the range of inter-blade cavitation vortex development. 49
4.8 Comparison of fluctuating pressure signals measured at #2 Suc for the different n_{ED} conditions, $n_{ED} = 0.360$ (a), 0.317 (OP#1) (b), 0.288 (OP#2) (c), and 0.245 (d) at $\sigma = 0.11$ 49
4.9 Influence of the cavitation number σ on the spectral peaks of the pressure fluctuations measured at #2 Suc at OP#1 (a) and OP#2 (b). The value of σ is changed from the lowest value $\sigma = 0.07$ to the value corresponding to atmospheric pressure condition σ_{atm} 51
4.10 Influence of Q_{ED} on the pressure amplitude measured at the pressure sensors on the blade, #1 Prs (a), #1 Suc (b), #2 Prs (c), #2 Suc (d) for three different n_{ED} conditions at $\sigma = \sigma_{plant}$ 52
4.11 Influence of Q_{ED} on the pressure amplitude measured at the pressure sensors on the blade, #1 Prs (a), #1 Suc (b), #2 Prs (c), #2 Suc (d) for three different n_{ED} conditions at atmospheric pressure condition σ_{atm} 53
4.12 Influence of n_{ED} on the amplitude of the pressure measured on the pressure side of the blade (a) and the suction side of the blade (b) at both the locations #1 and #2 at $GVO = 5$ ° and $\sigma = 0.11$ 54
4.13 Influence of σ on the pressure amplitude measured at location #1 (a) and location #2 (b) on the suction side of the blade at a constant guide vane opening $GVO = 5$ ° 55
4.14 Influence of Q_{ED} on the mean pressure factor C_p on the blade wall at location #1 (a) and location #2 (b) at atmospheric pressure condition σ_{atm} 56
4.15 Influence of Q_{ED} on the non-dimensional pressure difference ΔC_p between pressure and suction sides of the blade at atmospheric pressure condition σ_{atm} (a) and $\sigma = \sigma_{plant}$ (b) 56
4.16 Influence of n_{ED} on the mean pressure factor C_p on the blade wall at location #1 (a) and location #2 (b) at constant guide vane opening $GVO = 5$ ° and $\sigma = 0.11$. 57
4.17 Influence of n_{ED} on the non-dimensional pressure difference ΔC_p between pressure and suction sides of the blade at constant guide vane opening $GVO = 5$ ° and $\sigma = 0.11$ 57
4.18 Meridional view of the estimated flow structure in the blade channel and inter-blade vortex development at deep part load condition 59

5.1 Calculation domain for numerical simulations 67
5.2 Two runner calculation grids: coarse grid (a) and refined grid (b) 68
5.3 Computational convergence of the unsteady RANS simulation at OP#1 during four runner revolutions 69
5.4 Comparison of the simulated specific energy E (a) and torque T (b) with the experimental results 71

5.5 The flow structure highlighted by the streamline (skin-friction line) and the distribution of the pressure coefficient C_p on the hub with the coarse runner grid (a) and the refined runner grid (b) by steady state calculation 72

6.1 Velocity vector plot at $y = 0$ cross-section in the draft tube (a) and flow streamlines colored by specific kinetic energy of the flow (b) at OP#1. Both the velocity vector and the flow streamlines are drawn by the averaged velocity over four runner revolutions. 74

6.2 Instantaneous (a) and averaged (b) distributions of the non-dimensional axial velocity C_m^* at $y = 0$ and the PIV measurement result (c) at OP#1. The averaged velocity of the simulation is calculated over four runner revolutions. Threshold of the backflow region is highlighted by a solid black line. Both sections #1 and #2 are indicated as dashed black lines. 75

6.3 Velocity profile of C_m at $y = 0$ together with the standard deviation at section #1 (a) and section #2 (b) 75

6.4 Instantaneous (a) and averaged (b) distributions of the non-dimensional circumferential velocity C_u^* at section #1 and the PIV measurement results (c) at OP#1. The averaged velocity of the simulation is calculated over four runner revolutions. 76

6.5 Instantaneous (a) and averaged (b) distributions of the non-dimensional circumferential velocity C_u^* at section #2 and the PIV measurement result (c) at OP#1. The averaged velocity of the simulation is calculated over four runner revolutions. 76

6.6 Velocity profile of C_y^* at $y = 0$ together with the standard deviation at section #1 (a) and section #2 (b) 77

6.7 Comparison of the low pressure structure at OP#1 in the simulation with the visualized cavitation vortex rope at the lowest cavitation number $\sigma = 0.07$. The simulated low pressure core is highlighted by the iso-surface of $C_p = 0.08$ 78

6.8 Contour of the instantaneous pressure factor distribution (a) and the tangential streamlines drawn by the instantaneous velocity (b) and fluctuating velocity together with the vorticity ω_z (c) 78

6.9 Time history of the rotating low pressure cores caused by the multiple vortex ropes in the draft tube cone (a) and the pressure signals at section #1 over 5 runner revolutions (b). The roman numbers shown in (b) correspond to the points in (a). 79

6.10 Time history of instantaneous distributions of the pressure factor C_p together with the tangential flow streamline drawn by the fluctuating velocity components 80

6.11 Comparison of the centered pressure signals at C1N of the simulation (a) and the experiment (b) for five runner revolutions. 80

6.12 Time history of the non-dimensional axial velocity C_m^* (a) and the non-dimensional circumferential velocity C_u^* (b) at both sections #1 and #2. The roman numbers correspond to the points shown in Figure 6.9a 81

6.13 Evaluation planes of the pressure recovery factor χ and the loss coefficient ζ in the draft tube 82

6.14 Calculated mean recovery factor χ (a) and loss coefficient ζ (b) together with the standard deviations in the draft tube . . . 83

6.15 Time history of the specific kinetic energy K at the draft tube inlet (a) and the pressure recovery factor χ as well as the loss coefficient ζ through the draft tube (b) over two runner revolutions. The roman numbers correspond to the points shown in Figure 6.9a . . . 83

7.1 Instantaneous view of the cavitation structure of inter-blade cavitation vortices (a) and the visualized inter-blade cavitation vortices in the experiment (b) for OP#1 at $\sigma = 0.11$. The cavitation surface is determined by the iso-surface of the vapor volume fraction $\gamma_v = 0.1$ . . . 86

7.2 Instantaneous view of the inter-blade vortex structure highlighted by non-dimensional Q-criterion $Q^* = 3.0 \times 10^4$. The vortex structure is colored by the level of the vapor volume fraction γ_v. . . . 86

7.3 Comparison of the averaged inter-blade vortex structure and vortex center locations of the simulation with the vortex line evaluated based on the visualization (a) and the projected vortex line on the meridional plane (b). The mean vortex structure is highlighted by $Q^* = 3.0 \times 10^4$, which is averaged over four runner revolutions. . . . 87

7.4 Comparison of the averaged inter-blade vortex structure (white surface, $Q^* = 3.0 \times 10^4$) and cavitation structure (blue surface, $\gamma_v = 0.1$) at the targeted operating conditions OP#1, #2, and #3 (a) and the averaged cavitation volume in the runner domain together with the standard deviation (b). The quantities are averaged over four runner revolutions. . . . 88

7.5 Investigated non-dimensional span-wise location $s^* = 0.99$ (blue), 0.50 (black), 0.10 (green) in the runner domain (a) and on the meridional plane (b) . . . 89

7.6 Velocity vectors together with the tangential flow streamlines and the distributions of the non-dimensional meridional velocity C_m^* and the non-dimensional relative circumferential velocity W_u^* at constant span-wise location of $s^* = 0.99$ for OP#1 (a), #2 (b), and #3 (c). All velocities are averaged over four runner revolutions . . . 90

7.7 Velocity vectors together with the tangential flow streamlines and the distributions of the non-dimensional meridional velocity C_m^* and the non-dimensional relative circumferential velocity W_u^* at constant span-wise location of $s^* = 0.50$ for OP#1 (a), #2 (b), and #3 (c). All velocities are averaged over four runner revolutions . . . 91

7.8 Velocity vectors together with the tangential flow streamlines and the distributions of the non-dimensional meridional velocity C_m^* and the non-dimensional relative circumferential velocity W_u^* at constant span-wise location of $s^* = 0.10$ for OP#1 (a), #2 (b), and #3 (c). All velocities are averaged over four runner revolutions . . . 92

7.9 Distribution of the velocity along the blade together with the tangential flow streamlines at the span-wise location $s^* = 0.99$ (a), 0.50 (b). and 0.10 (c) for OP#1. The flow streamlines starting from the blade channel inlet are highlighted in blue. All velocities are averaged over four runner revolutions. 94

7.10 Meridional distribution of the meridional velocity C_m^* averaged in one blade channel at OP#1, #2, and #3. At OP#1, the simulated vortex locations as well as the vortex center locations estimated by the visualization are shown together. The threshold of a backflow region is highlighted by a solid black line. 95

7.11 Definition of the incident angle at the inlet of the blade channel and relative flow angle at the outlet of the blade channel 96

7.12 Variations of the flow incident angle at the blade channel inlet β_1' (a) and the relative flow angle at the blade channel outlet $\beta_{\bar{1}}'$ (b) from the blade suction side to the pressure side for OP#1, #2, and #3. The angles are calculated from the averaged velocity over four runner revolutions 97

7.13 Variations of the flow incident angle at the blade channel inlet β_1' (a) and the relative flow angle at the blade channel outlet $\beta_{\bar{1}}'$ (b) over the non-dimensional span-wise location s^*. The angles are averaged in one blade channel and calculated from the averaged velocity over four runner revolutions 98

7.14 Distribution of the vorticity ω_z at constant span-wise locations $s^* = 0.99$, 0.50, and 0.10 for OP#1 (a), #2 (b), and #3 (c) 100

7.15 Comparison of the calculated circulation Γ (a) and corresponding standard deviation (b) at OP#1, #2, and #3. The circulation Γ is evaluated at each constant span-wise location using the inter-blade vortex threshold identified by $Q^* = 0$. 101

7.16 Distribution of the pressure factor C_p at the middle span-wise location $s^* = 0.50$ for OP#1, #2, and #3. The pressure is averaged over four runner revolutions. . . 102

7.17 Comparison of the static pressure coefficient Ψ_b along the non-dimensional streamwise location m^* on both the suction and pressure side of the blade (left side) and the difference of the static pressure coefficient $\Delta\Psi_b$ (right side) at three span-wise locations $s^* = 0.99$ (a), 0.50 (b), and 0.10 (c) for OP#1, #2, and #3 . . . 104

7.18 Comparison of the simulated pressure fluctuations at the same locations as on-board pressure measurements on the runner blade (#1 Prs, #1 Suc, #2 Prs and #2 Suc) for OP#1, #2, and #3 over four runner revolutions 105

7.19 Comparison of the standard deviation of pressure oscillations on the blade pressure side (a) and the blade suction side (b) for OP#1, #2, and #3 106

7.20 Examples of the singular points identified by the combination of the eigenvalues, saddle (a), node (b), and focus (c) [41] 108

7.21 Skin-friction pattern on the hub together with the region of focus identified by Equation 7.6 at OP#1 (a), #2 (b) and #3 (c) ($\mathscr{F}$: Focus, $\mathscr{N}$: Node, $\mathscr{S}$: Saddle). The skin-friction lines are written by the averaged wall shear stress over four runner revolutions. 109

7.22 Variation of the pressure factor C_p and the pressure gradient $\partial C_p/\partial l_{str}$ along one flow streamline starting from the blade channel inlet (a) and the region of the adverse pressure gradient along streamline (light blue zone) created near the separation line (b). The selected flow streamline in (a) is highlighted by solid black line in (b) 110
7.23 3-D flow streamlines starting from the inlet of blade channel inlet from $s^* = 0.95$ to 1.00 at OP#1 (a), #2 (b), and #3 (c). The streamlines are written by the averaged velocity over four runner revolutions. 111
7.24 Comparison of the inter-blade vortex structure highlighted by the flow streamlines starting from the hub with the locations of the inter-blade vortex estimated by the visualization results (red line) together with the skin-friction lines on the hub 111
7.25 Meridional distribution of the specific energy gH/E_b averaged in one blade channel at each streamwise and span-wise location for OP#1 (a), #2 (b), #3 (c). The quantity is averaged over four runner revolutions. 113
7.26 Evolution of the non-dimensional specific energy E^* over the non-dimensional streamwise location m^* 114
7.27 Meridional distribution of the non-dimensional specific rothalpy I^* averaged in one blade channel at each streamwise and span-wise location for OP#1 (a), #2 (b), #3 (c). The quantity is averaged over four runner revolutions. 114
7.28 Evolution of the non-dimensional energy loss e (a) and the derivative $\partial e/\partial m^*$ (b) over the non-dimensional streamwise location for OP#1, #2, and #3 116
7.29 Distribution of the specific turbulence kinetic energy k at the middle span-wise loction $s^* = 0.50$ for OP#1 (a), #2 (b), and #3 (c). The values are averaged over four runner revolutions. 117
7.30 Standard deviation of the specific turbulence kinetic energy k_{STD} calculated over four runner revolutions at the middle span-wise loction $s^* = 0.50$ for OP#1 (a), #2 (b), and #3 (c) 117

A.1 Hill-chart of the reduced scale physical model of the tested Francis turbine. (1: Region of no cavitation vortex rope, 2: Visual limit of the cavitation vortex rope, 3: Visual limit of the inter-blade cavitation vortices) 125

B.1 High speed visualization of the inter-blade cavitation vortex from the runner downstream using a xenon flash light at OP #1 and $\sigma = 0.11$ 127
B.2 High speed visualization of the inter-blade cavitation vortex on the hub side from the runner upstream using the instrumented guide vane at OP #1 and $\sigma = 0.11$ 127
B.3 High speed visualization of the inter-blade cavitation vortex on the shroud side from the runner upstream using the instrumented guide vane at OP #1 and $\sigma = 0.11$ 128
B.4 Comparison of the high-speed visualization of inter-blade cavitation vortices between the experiment and the simulation at OP #1 and $\sigma = 0.11$ 128

C.1 Definition of the meridional coordinate (a) and the calculation of the velocity along the blade chamber line (b) 129

D.1 Contour of the non-dimensional Q-criterion Q^* (a) and the non-dimensional lambda-2 criterion λ_2^* (b) and the vector and streamline plots (c) at the middle span plane ($s^* = 0.50$) at OP#1, together with the detected center and threshold of the inter-blade vortex region 132

List of Tables

1.1 Operating parameters for the targeted operating points at the deep part load condition 11

3.1 Specifications of the compact LED light used for the visualization from the runner upstream 29
3.2 Operating conditions for the presented visualizations from downstream and upstream of the runner 30

4.1 Summary of the normalized span-wise and streamwise locations of the pressure sensors installed on the runner blade 42
4.2 Operating conditions of the on-board pressure measurements on the runner blade 44
4.3 Detected frequencies f_k of the pressure oscillations caused by the multiple vortex ropes measured at C1N, estimated frequencies f'_{ke} from Equation 4.1 and the measured frequency f'_k on the blade at location #2 Suc from $k = 1$ (f_{rope}) to 5 . 47

5.1 Number of nods for each calculation domain and the evaluation criteria of equiangular skew (Eq. skew), volume change (Vol. change), and aspect ratio (Asp. ratio) 69
5.2 Averaged and maximum y^+ values for each computational domain for the steady state calculation at OP#1 70

7.1 Blade geometric angle at given span-wise locations 96
7.2 Comparison of the simulated non-dimensional pressure difference $\Delta\Psi_b$ with the experimental results at both locations #1 and #2 for on-board pressure measurements 104

Nomenclature

Acronyms

BEP	**B**est **E**fficiency **P**oint
CFD	**C**omputational **F**luid **D**ynamics
DES	**D**etached **E**ddy **S**imulation
DNS	**D**irect **N**umerical **S**imulation
EPFL	**É**cole **P**olytechnique **F**édérale de **L**ausanne
EXP	**EXP**eriment
fps	**f**rames **p**er **s**econd
GVO	**G**uide **V**ane **O**pening
LED	**L**ight-**E**mitting **D**iode
LES	**L**arge **E**ddy **S**imulation
LDV	**L**aser **D**oppler **V**elocimetry
NRE	**N**ew **R**enewable **E**nergy
OECD	**O**rganization for **E**conomic **C**o-operation and **D**evelopment
OP	**O**perating **P**oint
PIV	**P**article **I**mage **V**elocimetry
Prs	**Pr**e**s**sure side
PXI	**P**CI e**X**tensions for **I**nstrumentation
RANS	**R**eynolds **A**veraged **N**avie **S**tokes equation
RMS	**R**oot **M**ean **S**quare
rpm	**r**evolutions **p**er **m**inute
SAS	**S**cale **A**daptive **S**imulation
SNL	**S**peed **N**o **L**oad
SRS	**S**cale **R**esolving **S**imulation
Suc	**Suc**tion side
URANS	**U**nsteady **RANS**

Subscripts

1	runner high pressure reference section
$\bar{1}$	runner low pressure reference section

I	power unit high pressure reference section
$\bar{I}$	power unit low pressure reference section
$\bar{B}$	tailwater reservoir reference section
B	headwater reservoir reference section
b	blade
atm	atmospheric condition
cn	condensation
$diff$	diffuser
$elbw$	elbow
hb	hub
p	pressure side
$plant$	power plant
$P-P$	peak-to-peak
ref	reference
$rope$	precessing vortex rope
s	suction side
sh	shroud
STD	standard deviation
str	streamline
t	turbulence
vp	vaporization

Latin letters

x, y, z	Cartesian coordinates	(m)
C	absolute flow velocity	($\mathrm{m\,s^{-1}}$)
C_m	axial (meridional) velocity component	($\mathrm{m\,s^{-1}}$)
C_u	circumferential velocity component	($\mathrm{m\,s^{-1}}$)
C_r	radial velocity component	($\mathrm{m\,s^{-1}}$)
C_x	velocity component along the x-axis	($\mathrm{m\,s^{-1}}$)
C_y	velocity component along the y-axis	($\mathrm{m\,s^{-1}}$)
C_Q	discharge velocity; $C_Q = Q/A$	($\mathrm{m\,s^{-1}}$)
W	relative flow velocity	($\mathrm{m\,s^{-1}}$)
W_u	relative circumferential velocity component	($\mathrm{m\,s^{-1}}$)
U	peripheral runner velocity	($\mathrm{m\,s^{-1}}$)
A	Area	($\mathrm{m^2}$)
C_μ	model constant	(-)
D	diameter	(m)
H	head; $H = p/(\rho \cdot g) + Z + C^2/(2 \cdot g)$	(m)
E	specific energy; $E = g \cdot (H_I - H_{\bar{I}})$	($\mathrm{J\,kg^{-1}}$)
E^*	non-dimensional specific energy	(-)
e	non-dimensional energy loss	(-)

f	frequency	(Hz)
g	gravitational acceleration	(m s^{-2})
H	head; $H = p/(\rho \cdot g) + Z + C^2/(2 \cdot g)$	(m)
H_s	$Z_{\text{ref}} - Z_{\overline{B}}$	(m)
I	specific rothalpy; $I = \frac{p}{\rho} + \frac{1}{2}\vec{W}^2 - \frac{1}{2}\vec{U}^2 + gz$	(J kg^{-1})
I^*	non-dimensional specific rothalpy	(-)
J	Jacobian matrix	(-)
K	specific kinetic energy	(m^2 s^{-2})
k	specific turbulence kinetic energy	(m^2 s^{-2})
k	number of vortex ropes	(-)
$\mathbf{L}$	velocity gradient tensor	(s^{-1})
l	length	(m)
m	dimensional streamwise location	(m)
m^*	non-dimensional streamwise location	(-)
$\mathbf{N}$	natural number	(-)
n	runner rotational frequency	(Hz)
NPSE	net Positive Suction Energy; NPSE $= gH_{\bar{I}} - gZ_{ref} - \frac{p_v}{\rho}$	(J kg^{-1})
p_{atm}	atmospheric pressure	(Pa)
p_v	vapor pressure	(Pa)
Q	discharge	(m^3 s^{-1})
Q	Q-criterion	(s^{-2})
Q^*	non-dimensional Q-criterion	(-)
R	radius	(m)
R_b	bubble radius	(m)
S	swirl number	(-)
S	source term	(-)
$\mathbf{S}$, S_{ij}	rate-of-strain tensor	(s^{-1})
s	dimensional span-wise location	(m)
s^*	non-dimensional span-wise location	(-)
T	torque	(Nm)
t	time	(s)
V	volume	(m^3)
V_c	cavitation volume	(m^3)
y^+	dimensionless wall distance	(-)
Z	elevation	(m)
Z_{ref}	power unit reference level (horizontal spiral case symmetry plane)	

Greek letters

α	absolute flow angle	(°)
β	relative flow angle	(°)
β_1'	flow incident angle at the blade channel inlet; $90 - \beta_1$	(°)

$\beta'_{\bar{1}}$	relative flow angle at the blade channel outlet; $90-\beta_{\bar{1}}$	(°)
Γ	circulation	($\mathrm{m}^2\,\mathrm{s}^{-1}$)
γ	deflection angle	(-)
γ_l	water volume fraction	(-)
γ_v	vapor volume fraction	(-)
ζ	loss coefficient	(-)
η	efficiency	(-)
θ	angular position	(rad)
λ	eigenvalue	(-)
λ_2	lambda-2 criterion	(s^{-2})
λ_2^*	non-dimensional lambda-2 criterion	(-)
μ	viscosity	(Pa s)
ν	kinematic viscosity	($\mathrm{m}^2\,\mathrm{s}^{-1}$)
ρ	density	($\mathrm{kg}\,\mathrm{m}^{-3}$)
τ	shear stress	(s^{-1})
τ_t	Reynolds stress	(s^{-1})
τ_w	wall shear stress	(s^{-1})
χ	pressure recovery factor	(-)
Ψ_b	static pressure coefficient on blade walls	(-)
$\mathbf{\Omega}$, Ω_{ij}	vorticity tensor	(s^{-1})
ω	angular velocity	($\mathrm{rad}\,\mathrm{s}^{-1}$)
ω	vorticity	(s^{-1})

Non-dimensional variables

C'_p	fluctuating pressure factor; $C_p=(p-\overline{p})/(\rho E)$	(-)
C_p	pressure factor; $C_p=(\overline{p}-p_{\mathrm{ref}})/(\rho E)$	(-)
Fr	Froude number; $Fr=\sqrt{H/D_{\bar{1}}}$	(-)
n_{ED}	speed factor; $n_{ED}=(n\cdot D)/\sqrt{E}$	(-)
Q_{ED}	discharge factor; $Q_{ED}=Q/(D^2\cdot\sqrt{E})$	(-)
Re	Reynolds number; $Re=(D\cdot U)/\nu$	(-)
ν	specific speed; $\nu=\omega\cdot\sqrt{Q}/(\sqrt{\pi}\cdot(2\cdot E)^{3/4})$	(-)
σ	Thoma number or cavitation number; $\sigma=\mathrm{NPSE}/E$	(-)

Introduction

0.1 Energy context

Hydraulic power plants play an important role in the world's energy supply. The electrical energy production from hydraulic power plants has been constantly increasing over the past few decades as illustrated in Figure 1. As of 2016, they contributed to about 4'200 TWh of the annual electric power generation, which is more than 16 % of the global electricity generation [4]. In addition, there is still a great amount of hydropower potential. Recently, in an objective to generate power with low environmental impact and induced greenhouse gas emissions, electricity production from New and Renewable Energy (NRE) sources such as solar and wind powers are promoted increasingly. Particularly in Europe, the European Union has defined a policy named the *2020 climate and energy package*, with the objective of 20 % reduction of green house gas emissions referenced to 1990 levels and to increase the NRE energy consumption rate in the EU up to 20 %.

To support renewable energy policies, it is a crucial issue to guarantee the smooth integration of NRE sources into existing power grids. However, NRE sources cause perturbations in the electrical power grid due to their stochastic nature of power output. Thus, it is required to secure a sufficient storage capacity in the electric grid and to ensure that primary and secondary grid controls are capable of balancing the produced energy. For this purpose,

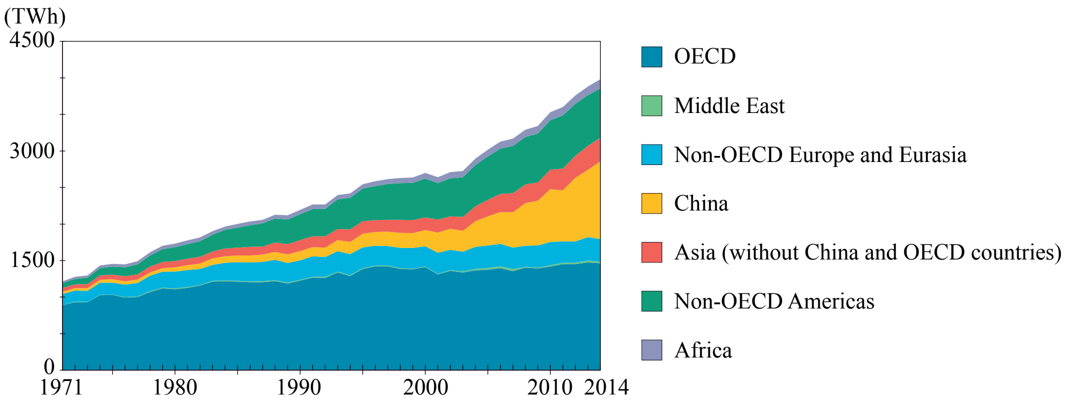

Figure 1 – Electricity generation from Hydraulic power plants from 1971 to 2014 [4]

pumped storage and hydraulic power plants are one of the key components to providing the necessary energy storage to stabilize the electric grid. Hydraulic turbines are characterized by their flexible electric power generation and wide operating ranges. However, when functioning under off-design conditions, hydraulic turbines are subject to unstable flow conditions which provoke various undesirable system instabilities. As a result of the rapid increase of NRE sources, hydraulic machines are required to function more and more often into the extended operating range, especially down to the extremely low discharge condition called deep part load condition. Here, the characteristics of flow are still veiled.

The present research work aims to investigate hydrodynamics and flow structures at deep part load operating conditions of a Francis turbine. The corresponding operating range is defined by a discharge value which is considerably lower than the discharge at the Best Efficiency Point (BEP), such as $Q < 0.5 \times Q_{BEP}$.

0.2 Francis turbines

Francis turbines are one of the turbines classified as a reaction turbine. They are adopted for use through a relatively wide range of the head H, specifically from 40 to 600 m. The Francis turbine is the most common hydraulic unit in power plants, representing more than 60 % of the installed hydropower capacity around the world. The main parts of the Francis turbine are a spiral case, stay vanes, guide vanes, runner, and draft tube as shown in Figure 2. The water from an upstream reservoir is first fed through the penstock to the spiral case. The water velocity is then optimized by the stay vanes as well as the guide vanes before flowing into the runner. The guide vanes also play a role in adjusting discharge by changing their opening angle. The flow leaving the runner is then led to a downstream reservoir through a draft tube, which is installed to recover the kinetic energy of the flow into static pressure to maximize efficiency.

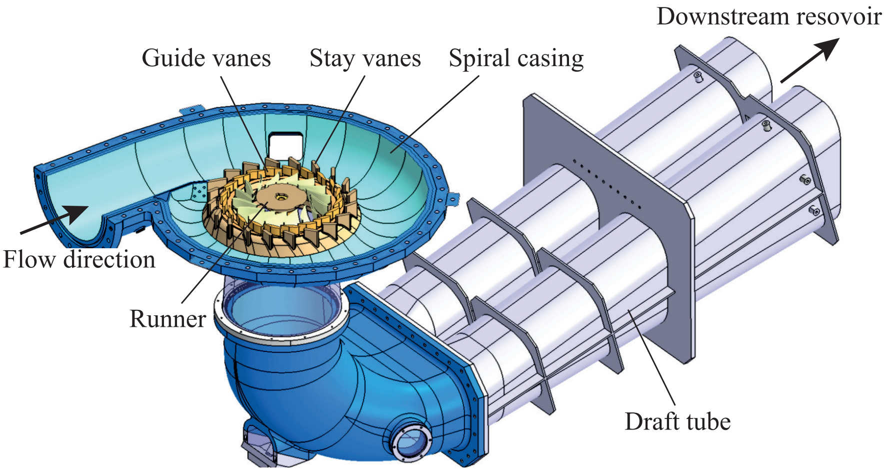

Figure 2 – Main components of a Francis turbine

0.3 Off-design operating conditions

The operating conditions of Francis turbines are determined by non-dimensional discharge and speed factors, which are defined according to IEC Standard [1] as follows.

$$Q_{ED} = \frac{Q}{D_{ref}^2\sqrt{E}} \qquad\qquad n_{ED} = \frac{nD_{ref}}{\sqrt{E}} \tag{1}$$

where Q represents the discharge, D_{ref} the reference diameter of the runner, n the runner rotational frequency, and E the specific energy. The variation of these non-dimensional parameters causes a change of velocity triangles which characterize the flow through the runner as shown in Figure 3. At the BEP, Francis turbines are generally designed to have a purely axial flow at the outlet of the runner. Under off-design operating conditions, however, a circumferential velocity component appears in addition to the axial component. This leads to the development of a vortex structure in the draft tube. At the vortex core, the static pressure may reach the vapor pressure which provokes the development of the cavitation [11, 26].

When discharge is varied for a given value of specific energy, the velocity triangle at the runner outlet is principally affected. At full load operating conditions, the flow at the outlet of the runner has a circumferential velocity component rotating in the opposite direction of the runner rotation (see Figure 4a), which may give rise to the development of axisymmetric cavitation

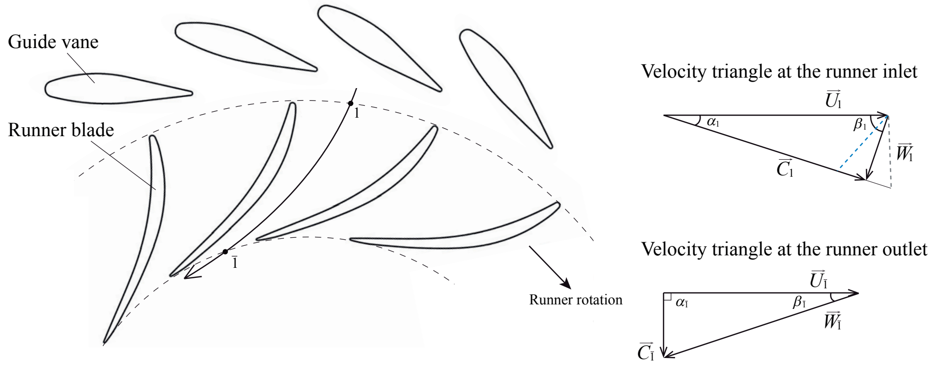
Guide vane
Runner blade
1̄
1̄
Runner rotation
Velocity triangle at the runner inlet
$\vec{U}_1$
α_1
β_1
$\vec{W}_1$
$\vec{C}_1$
Velocity triangle at the runner outlet
$\vec{U}_1$
α_1
β_1
$\vec{W}_1$
$\vec{C}_1$

Figure 3 – Velocity triangles at the runner inlet and the runner outlet

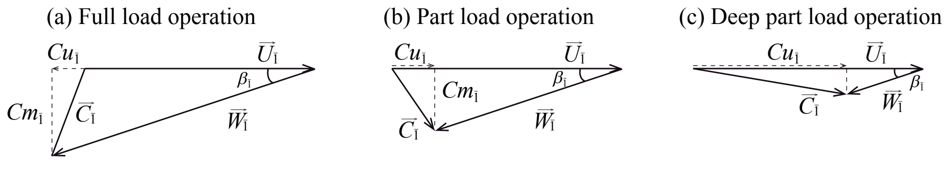
(a) Full load operation

(b) Part load operation

(c) Deep part load operation
Cu_1
$\vec{U}_1$
β_1
Cm_1
$\vec{C}_1$
$\vec{W}_1$
Cu_1
$\vec{U}_1$
β_1
Cm_1
$\vec{C}_1$
$\vec{W}_1$
Cu_1
$\vec{U}_1$
β_1
$\vec{C}_1$
$\vec{W}_1$

Figure 4 – Velocity triangle at the runner outlet for full load operation (a), part load operation (b) and deep part load operation (c)

at the center of the draft tube [57]. On the contrary, the circumferential velocity component in the flow at the outlet of the runner is in the same rotating direction as the runner rotation at part load operating conditions (see Figure 4b). This swirling flow creates a recirculating flow region at the center of the draft tube, leading to the development of a helical shape cavitation vortex rope wrapping around the recirculating region [23, 63]. When the discharge value is further decreased into to deep part load conditions, the swirling flow is expected to intensify due to the decrease of the axial velocity component while the circumferential velocity component increases as shown in Figure 4c.

Francis turbines may also experience variations of the specific energy, which change the value of n_{ED}, depending on the water level in the upstream reservoir. When the specific energy is changed for a given guide vane opening, the velocity triangle at the runner inlet is modified. At the BEP, the flow at the runner inlet generally has an optimized flow incident angle which is close to the blade geometrical angle. However, a decrease of the specific energy resulting in an increase of n_{ED} induces a decrease of the incident angle at the runner inlet as illustrated by dashed blue line in Figure 3. In contrast, an increase of the specific energy causes an increase of the flow incident angle (see dashed gray line in Figure 3). The change of the flow incident angle at the runner inlet by a variation of the specific energy particularly affects the flow structure inside the blade channel, causing various cavitation developments such as inlet cavitation.

0.4 State of the art

Francis turbines under off-design operations are subject to various types of cavitation flow depending on the discharge and head conditions [7, 21]. This cavitation flow may occasionally provoke undesirable system instabilities and prevent the stable operations of the generating unit. The problem of system instabilities in hydraulic units was firstly reported by Rheingans [72], describing the amplification of pressure fluctuations and power swings under certain operating conditions.

At full load operating condition, an axisymmetric cavitation vortex rope develops in the draft tube at the runner outlet (see Figure 5a). In 1990s, Jacob *et al.* [36] primarily performed the principal experimental investigation of the pressure surge. Koutnik and Pulpitel [43] applied the transfer matrix method to the full load instabilities for the purpose of stabilization analyses. They characterized the full load cavitation surge using the parameters to determine the cavitation dynamics called the cavitation compliance and the mass flow gain factor. These two parameters were initially introduced by Brennen and Acosta [10] and Ng and Brennen [62] to characterize the dynamics of the cavitation in an inducer. The parametric study was further extended to describe the destabilizing effect of the conical shape of the diffuser by Alligné *et al.* [5] and Chen *et al.* [13]. Recently, Müller *et al.* [58] conducted a local flow and discharge analysis based on PIV measurements for understanding the physical mechanisms of the self-excited cavitation surge. Furthermore, Müller *et al.* [59] investigated the correlation of the oscillation of the cavitation volume evaluated by binary image processing with the discharge fluctuations employing the pressure difference method used by several authors (the reader may refer to Gibson [28], Kashima *et al.* [42], and Yamamoto *et al.* [90]).

Under part load operating conditions, a helical cavitation vortex rope is observed in the draft tube (see Figure 5b). The fundamental studies about the vortex rope were firstly addressed by Nishi *et al.* [64]. They reported the occurrence of a resonance induced by the coincidence of the frequency of the vortex rope precession with the natural frequency of the system, by decomposition of the fluctuating pressure into the synchronous and convective components. Dörfler [15] assumed that the synchronous pressure component is caused by the excitation source and the hydro-acoustic response of the system. In the framework of the FLINDT project [6], 2-D PIV measurements in the presence of the cavitation vortex rope were performed in the draft tube, and the vortex behavior during one cycle of the vortex precession was investigated by Iliescu *et al.* [35]. The investigation of the vortex rope in the draft tube using PIV measurements was further extended to correlate the vortex trajectory with several discharge conditions by Favrel *et al.* [24]. The same authors also investigated the instantaneous velocity fluctuations in the draft tube in and out of resonance condition by LDV measurements [25]. The stability of the vortex rope at part load condition has been also discussed analytically by several authors[51, 68, 84].

Recently, it has become a more and more crucial issue to safely extend the operating range of hydraulic machines into deep part load conditions. Under such an extremely low discharge operating condition, the flow features further complex flow structures, especially inside the blade channel. For the case of pump-turbines, Senoo and Yamaguchi [74] conducted experimental measurements of the velocity inside the runner at no-discharge condition, and they reported complicated flow structures and the development of a vortex inside the blade channel. Staubli *et al.* [79] revealed the development of a recirculating region at the runner inlet during the start-up of the pump-turbine. The development of a backflow region near the runner inlet

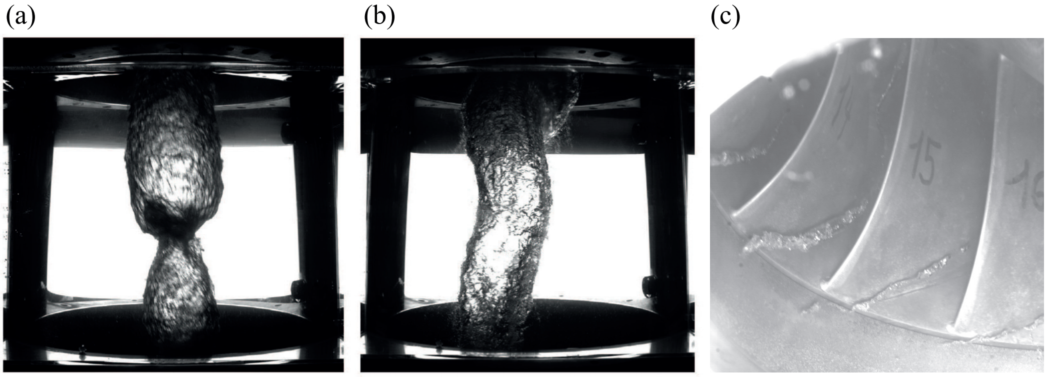

Figure 5 – Axisymmetric cavitation vortex rope at full load operating conditions (a) [57], helical cavitation vortex rope at part load operating conditions (b) [23], and inter-blade cavitation vortices at deep part load operating conditions (c) [91]

was also confirmed recently by the numerical simulation by Jacquet *et al.* [37]. Furthermore, they reported that the backflow development triggers the rotating stall inside the guide vane channels. Hasmatuchi *et al.* [33] experimentally demonstrated the occurrence of the rotating stall under extremely low discharge conditions in the generating mode of a pump-turbine, due to the misaligned flow incident angle at the runner inlet.

For the case of Francis turbine operation at deep part load condition, the development of cavitation vortices inside the runner blade channel called the inter-blade cavitation vortex is observed [7] (see Figure 5c), even though their characteristics are not well documented yet. Experiments including deep part load operations were performed by Farhat *et al.* [22] and Lowys *et al.* [47]. The experiments with on-board instrumentation on the runner blade showed a notable pressure fluctuation under deep part load conditions. In addition to the experiments, Wack *et al.* [87] and Magnoli *et al.* [49] reported numerical computations at deep part load condition and successfully simulated inter-blade vortices.

0.5 Research objective

The primary aim of this research project is to ascertain the flow structures at deep part load operation of Francis turbines, especially focusing on the development of inter-blade cavitation vortices. It is achieved by classic flow survey methods conducted on a physical reduced scale model of a Francis turbine, such as PIV measurements, as well as by a novel visualization technique for the blade channel flow and on-board pressure measurements on the runner blade together with appropriate post-processing tools. The experiments are performed with different operating parameters under deep part load conditions to investigate the flow characteristics in the draft tube as well as the influence of flow conditions on the development of inter-blade cavitation vortices and its dependency on the operating parameters.

Furthermore, an accurate evaluation of the flow structure inside the blade channel is of key importance to understanding the physical mechanisms responsible for the development of the inter-blade vortices. For this purpose, numerical simulations with unsteady RANS equations are performed for the different operating conditions at deep part load operation. The simulated flow structures inside the blade channel are then compared with visualizations and investigated to reveal the underlying mechanisms for inter-blade vortex development.

Finally, all the sets of generated data form an extensive database for further analyses of flow at deep part load operation and analytical flow models in the framework of the HYPERBOLE research project (ERC/FP7-ENERGY-2013-1-Grant 608532).

0.6 Document structure

Chapter 1 gives an overview of the experimental facility, including an illustration of the physical reduced scaled model of a Francis turbine installed on test rig PF3 in the Laboratory for Hydraulic Machines of EPFL. The operating parameters for the targeted deep part load operating condition for investigations of inter-blade vortices are explained together with the theoretical velocity triangles at these operating conditions.

Chapter 2 explains the experimental investigation of the draft tube flow under deep part load operating conditions. The chapter includes the experimental setups for the velocity survey by Particle Image Velocimetry (PIV) as well as flow visualizations of the cavitation vortex rope in the draft tube cone. The flow structures as well as the characteristics of the vortex rope observed at deep part load condition are investigated by analyzing the velocity fields acquired from PIV and pressure measurements in the draft tube together with high-speed visualizations.

Chapter 3 focuses on the visualization of the inter-blade cavitation vortex. The inter-blade cavitation vortex is first characterized by visualizations from the runner downstream through a transparent draft tube cone. For further investigations of the development of inter-blade vortices, a novel technique of visualization through an instrumented guide vane is introduced, and inter-blade cavitation vortices are, for the first time, visualized from the runner upstream. The development of inter-blade cavitation vortices is furthermore analyzed by binary image processing to estimate the vortex line as well as the location of the vortex inception.

Chapter 4 details the on-board pressure measurements on the runner blade. The impact of the inter-blade vortex on the pressure field inside the blade channel is investigated with respect to systematically varied operating parameters. The wall pressure difference between the blade pressure and suction sides is also examined for the estimation of the flow characteristics inside the blade channel under deep part load conditions.

Chapter 5 introduces the setup and the governing equations for the performed unsteady RANS simulations. The convergence of the conducted simulations as well as the preliminary results of characteristics such as specific energy and torque are compared to the experimental results.

Chapter 6 focuses on analyses of the simulated flow in the draft tube based on the comparison with PIV measurements. The characteristics of the flow in the draft tube as well as the vortex rope structure are investigated. Investigations of the pressure recovery as well as specific energy losses through the draft tube are also presented.

Chapter 7 finally investigates the simulated flow structure inside the blade channel. By comparison with visualization results, the development of the inter-blade vortices is highlighted. The flow inside the blade channel relating to the inter-blade vortex development is characterized by velocity surveys. Analysis of skin-friction lines is conducted to identify the flow separation on the hub, which is correlated with the backflow near the hub, a phenomenon closely linked with the development of inter-blade vortices. Furthermore, specific energy losses through the blade channel are calculated using the specific rothalpy, and the specific energy dissipation due to the presence of inter-blade vortices is investigated.

1 General experimental setup

1.1 Physical reduced scale model

Experiments are carried out on a 1:16 reduced scale physical model of a Francis turbine with a specific speed $\nu = 0.27$ at the Best Efficiency Point (BEP). The machine features 20 stay vanes, 20 guide vanes and 16 runner blades. The prototype generating unit is installed in a hydraulic power plant located in western Canada and has a rated output power of 444 MW. The model with the reference diameter $D_{ref} = 0.35$ m is installed in a closed-loop test rig at the EPFL Laboratory for Hydraulic Machines as shown in Figure 1.1. All model tests performed at this laboratory respect the IEC standards [1] for the accurate assessment of prototype characteristics. The torque acting on the shaft, the mean discharge, the turbine rotational frequency, and the turbine specific energy are measured to precisely monitor the operating conditions of the machine. The mean discharge is adjusted by the guide vane opening angle, which is controlled by a servo motor and monitored by an incremental encoder. The turbine specific energy is controlled by the speed of two axial double-volute pumps. The pressure level in the draft tube is set by a vacuum pump connected to the downstream reservoir. Experiments are carried out with degassed water.

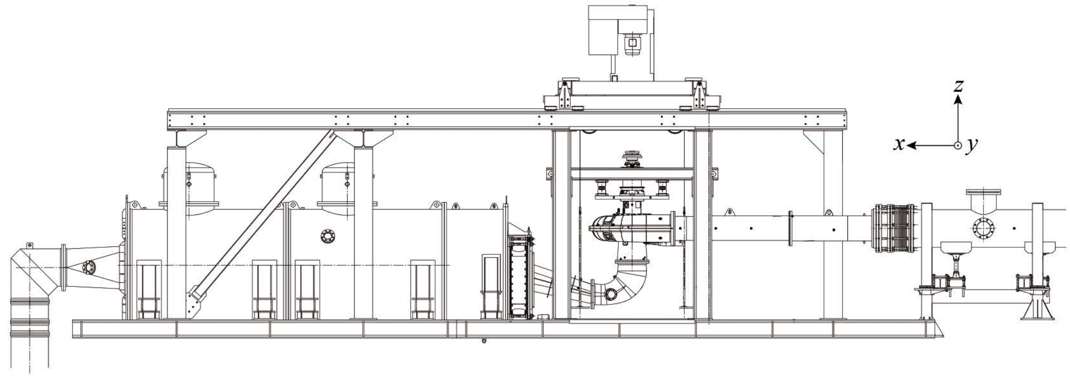

Figure 1.1 – Schematics of the physical reduced scale model of the studied Francis turbine installed on EPFL test rig PF3 [23, 57]

1.2 Pressure sensors on the model and test rig

Flush-mounted pressure transducers are installed on the model to monitor wall pressure distributions as well as pressure fluctuations induced by various flow instabilities. The adopted type of transducer is a piezo-resistive absolute pressure sensor with a range of 5 bar and a maximum measurement uncertainty of 0.07 %. In the draft tube cone, 8 pressure transducers are installed to accurately evaluate the behavior of the cavitation vortex rope in the draft tube as shown in Figure 1.2. Two different horizontal sections are selected, and four pressure transducers are installed at 90 degree intervals in each section as illustrated in Figure 1.2b. The coordinate system is defined as shown in Figure 1.2, and the reference level ($z = 0$ m) and the coordinate origin are set at the center of the runner (see red point in Figure 1.2a). The defined coordinate system is applied to all the experimental results as well as the domain of the numerical simulation (see Section 5.3). The two horizontal sections, referred to as

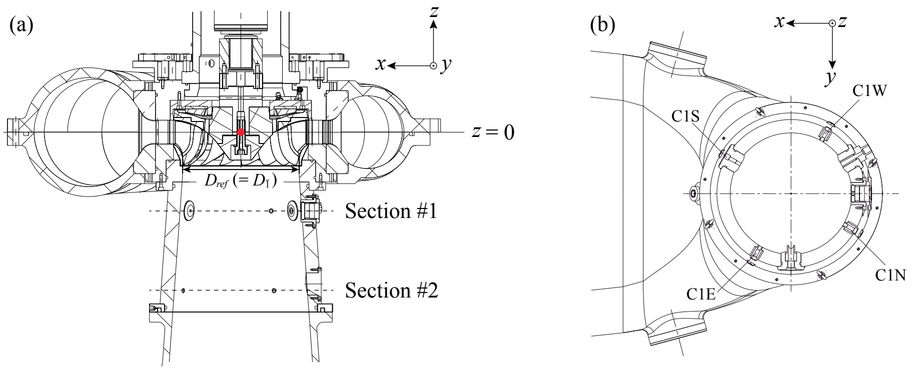

Figure 1.2 – View of the spiral case, runner, and draft tube cone with the sections for the pressure measurement in the draft tube (a) and the locations of the pressure transducers at section #1 (b) [23]

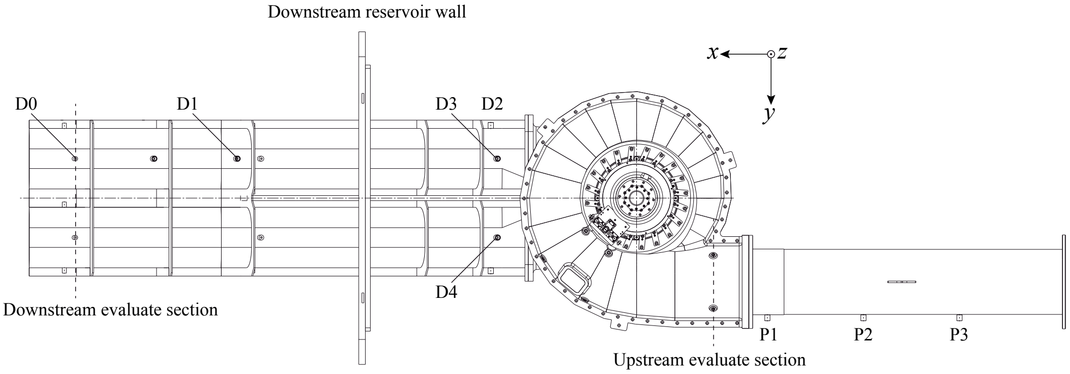
Downstream reservoir wall
x
z
y
D0
D1
D3
D2
D4
Downstream evaluate section
P1
P2
P3
Upstream evaluate section

Figure 1.3 – Top view of the physical reduced scale model with the locations of pressure transducers installed in the straight draft tube and upstream feeding pipe together with upstream and downstream evaluate sections [57]

Section #1 and Section#2 respectively, are situated at $z = -0.237$ m ($-0.68 \times D_{ref}$) and $z = -0.437$ m ($-1.25 \times D_{ref}$). Another draft tube cone, used for high-speed visualization and PIV measurements (see Section 2.2), is equipped with a flat rectangular water-box and four pressure transducers (2 sensors at each section), of which locations correspond to C1N, C1S, C2N, and C2S, respectively. Pressure transducers are also installed in the straight diffuser after the elbow as well as the upstream inlet pipe. These transducers are used to characterize the pressure propagation through the test rig and to identify the eigenmode shape [44]. The specific energy E is evaluated between the upstream and downstream evaluate sections shown in Figure 1.3.

1.3 Targeted operating conditions at deep part load operation

1.3.1 Operating parameters for targeted operating points

In the presented research, several operating points under deep part load conditions are highlighted, especially for the visualizations and the numerical simulations. The visualizations at deep part load [91] revealed that the development of inter-blade vortices is greatly affected by the different n_{ED} conditions. Thus, three different n_{ED} values within the operating range of the prototype at a constant guide vane opening $GVO = 5$ °, referred to as OP#1, OP#2, and OP#3 in the following sections, are selected particularly for the investigation of inter-blade vortex development. It should be noted that the distinctive development of inter-blade cavitation vortices is observed at OP#1, as reported in [91]. The operating parameters at the selected points are summarized in Table 1.1.

In addition to the non-dimensional parameters defined in Equation 0.3, the cavitation number σ plays an essential role for characterizing cavitation phenomena. The Thoma number (cavitation number) σ is defined by the specific energy E and the *Net Positive Suction Energy* ($NPSE$) indicating the absolute pressure level of the turbine on the suction side, such as:

$$\sigma = \frac{NPSE}{E} \tag{1.1}$$

$NPSE$ is defined as the difference of the specific energy at the the suction side $gH_{\bar{I}}$ relative to the reference level of the turbine and the vapor pressure p_v as follows:

Table 1.1 – Operating parameters for the targeted operating points at the deep part load condition

OP	Q_{ED} (-)	n_{ED} (-)	GVO (°)	E (J kg^{-1})	n (Hz)
#1	0.0524	0.317	5	263	14.67
#2	0.0540	0.288	5	263	13.33
#3	0.0554	0.268	5	263	12.40

$$NPSE = gH_{\bar{I}} - gZ_{ref} - \frac{p_v}{\rho} = \frac{p_{atm}}{\rho} - \frac{p_v}{\rho} - g(Z_{\bar{B}} - Z_{ref}) + \frac{C_{\bar{I}}^2}{2} \tag{1.2}$$

where p_{atm} is the atmospheric pressure, $Z_{\bar{B}}$ the water level in the downstream reservoir and $C_{\bar{I}}$ the flow velocity at the draft tube outlet. At a given specific energy, turbine operations with a low pressure cavitation number have a higher risk of cavitation occurrence due to a lower $NPSE$. The values of the cavitation number at the prototype σ_{plant} for OP#1, #2, and #3 correspond to 0.133, 0.110, and 0.095, respectively.

Taking into account scale effects between prototype and reduced scale model, Reynolds number Re and Froude number Fr are also of key importance. These parameters are respectively defined as:

$$Re = \frac{U_{ref} \cdot D_{ref}}{\nu} \qquad Fr = \sqrt{\frac{E}{gD_{ref}}} \tag{1.3}$$

In the present study, Reynolds number is $Re = 5.19 \times 10^6$ at OP#1, 4.90×10^6 at OP#2, and 4.35×10^6 at OP#3. Froude number Fr is kept constant at $Fr = 8.74$ for OP#1, #2, and #3.

1.3.2 Velocity triangles at the selected points

As indicated in Section 0.3, a variation of the n_{ED} value principally modifies the velocity triangle at the runner inlet, resulting in a change of the flow incident angle. At deep part load operation, the flow incident angle is not optimized even at the rated n_{ED} condition. The theoretical velocity triangles at the runner inlet calculated from the discharge velocity $C_Q = Q/A$, with the area A at the runner inlet, guide vane opening GVO and the runner rotational velocity U_1 at OP#1, #2, and #3 are presented in Figure 1.4. It is shown that the flow at deep part load condition features a considerably high negative flow incidence at the runner inlet, especially at OP#1. These negative flow incidences at the inlet may cause singular flow conditions inside the blade channel, which will be further discussed in the following sections.

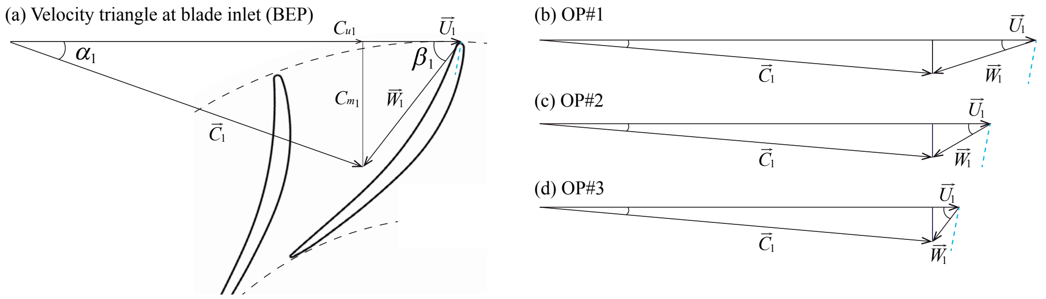

Figure 1.4 – Theoretical velocity triangles at the runner inlet for the BEP (a), OP#1 (b), OP#2 (c), and OP#3 (d). The dashed blue line indicates the geometrical blade angle at the inlet.

2 Flow investigation in draft tube

2.1 Introduction

For Francis turbines, flow conditions in the draft tube play a significant role in machine efficiency by recovering the kinetic energy of the flow into static pressure. However, flow in the draft tube is accompanied by a strong swirling component under off-design conditions, which can provoke undesirable flow instabilities preventing an effective pressure recovery. At part load operating condition, the development of the cavitation vortex rope in the draft tube cone significantly influences the stable operation of the hydraulic unit. As a result, this phenomena is a topic of a number of studies performed over the past years. In the first place, Nishi *et al.* [64] revealed that there are several different flow regimes existing at part load operation and the dynamics of the cavitation vortex rope is changed with respect to the varied discharge conditions. Moreover, there are two pressure oscillation modes decomposed into convective and synchronous components respectively, and the risk of the resonance phenomena was reported. They furthermore mentioned that the behavior and the appearance of the cavitation vortex rope are quite unstable around deep part load operation due to the considerably high swirling component in the flow. Recently, Favrel *et al.* conducted velocity surveys in the draft tube cone by using PIV measurements, and the behavior of the vortex is investigated with respect to varied discharge conditions [24]. Furthermore, the instantaneous velocity fluctuations in the draft tube cone are also investigated by LDV measurements in and out of the resonance condition [25].

In this chapter, it is intended to experimentally investigate flow structures in the draft tube under deep part load operations. First of all, the vortex rope is characterized by frequency analyses of the pressure oscillations measured on the draft tube wall, which is applied to a broad discharge range at the rated n_{ED} condition. In addition, the behavior of the cavitation vortex rope at deep part load condition is investigated by high-speed visualizations through a transparent draft tube cone together with the fluctuating pressure signal related to the vortex precession in the draft tube. The flow investigation is furthermore extended to the mean velocity survey by PIV measurements, which are performed at one vertical section for the axial velocity and two horizontal sections for the circumferential velocity in the draft tube cone. The PIV measurements are systematically conducted for different discharge conditions at rated n_{ED}, and the influences of the discharge value on the mean distributions of the axial and circumferential velocity components are then investigated. Moreover, the backflow development as well as the swirl number based on the velocity profiles acquired from the PIV measurements are calculated, and the flow structure in the draft tube under deep part load operations is discussed.

2.2 Experimental setup

2.2.1 Visualization of the cavitation vortex rope

For high-speed visualizations of the cavitation vortex rope in the draft tube, a transparent draft tube cone equipped with a flat rectangular window is used as shown in Figure 2.1a. The window is filled with water to minimize optical deformations, and a LED screen is used for a backlight source to obtain a better contrast between the water and cavitation regions. The entire experimental setup is presented in Figure 2.1. The endorsed high-speed camera (FastCam SA 1.1) features 675′000 fps at a maximum. For the presented visualization of the cavitation vortex rope, 1′000 fps with a maximum resolution of 1′024 × 1′024 pixels is adopted.

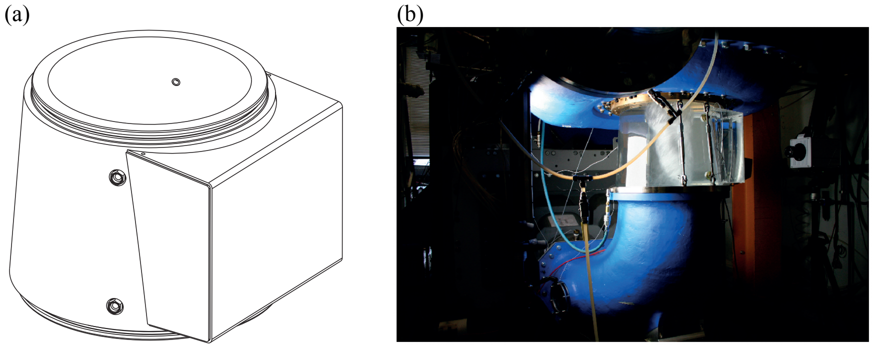

Figure 2.1 – Flat rectangular window for visualizations of the cavitation vortex rope and PIV measurements in the draft tube cone (a) and the experimental setup of high-speed visualizations with the LED screen (b)

2.2.2 Particle Image Velocimetry (PIV)

PIV measurements are conducted to investigate velocity fields in the draft tube cone. PIV measurements enable the acquisition of 2-D velocity fields by illuminated particles using a double pulsed Laser sheet. The general measurement principle is explained in [71]. The measurements are applied to one vertical section and two horizontal sections to investigate both axial and circumferential velocity components. The selected Nd:YAG Laser generates a roughly 2 mm-thick double-pulsed laser sheet with its wavelength of 532 nm and a maximum

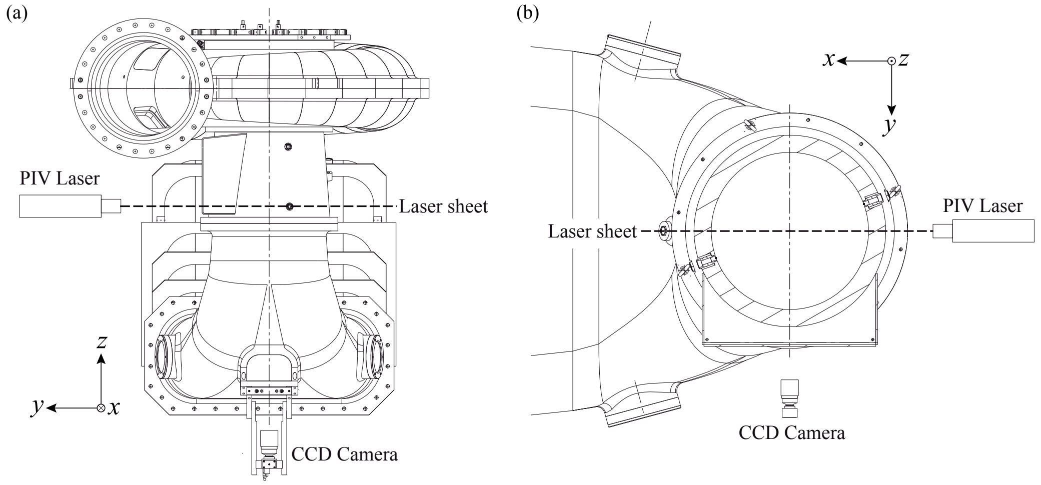

Figure 2.2 – Experimental setups of PIV measurements respectively for the circumferential velocity component C_u (a) and the axial velocity component C_m (b)

emission frequency of 10 Hz. Images with illuminated particles are recorded by a CCD camera with a resolution of $2'048 \times 2'048$ pixels, which is installed perpendicularly to the laser sheet. As seeding particles, 20 μm standard Polyamide particles are adopted. For the measurement of the velocity fields, the frequency of the laser emission is set to be 10 Hz, and acquired images are processed by the algorithm using a cross-correlation method to obtain an instantaneous velocity. A total of $1'200$ instantaneous velocity fields are acquired continuously and averaged to calculate a mean velocity field at each section. All of the PIV measurements are performed under atmospheric pressure condition. The measurement setups for both axial and circumferential velocity components are presented in Figure 2.2, respectively. Further details of the PIV measurements performed in the presented reduced scale model including calibration and image post-processing are described in [23].

2.3 Characteristics of the vortex rope at deep part load

2.3.1 Frequency analysis of the vortex rope

First, the cavitation vortex rope is investigated by frequency analyses with varied Q_{ED} values at rated n_{ED}. In Figure 2.3, the waterfall diagram of the auto-spectral density function G_{xx} [8] for pressure fluctuations measured at section #1 (C1N) at the cavitation number in the prototype ($\sigma = \sigma_{plant} = 0.11$) is presented. Distinct frequency peaks are observed around $f_{rope} = 0.3 \times n$ especially at part load conditions between 50 % and 80 % of Q_{BEP}, which are caused by the precession of the cavitation vortex rope in the draft tube cone (see Figure 2.4) [23]. Dominant frequency peaks also appear at full load condition due to the self-excited oscillation of the cavitation volume in the draft tube [5, 13, 57]. At part load condition, the strength of the frequency peak caused by the vortex rope precession is gradually reduced as discharge decreases, and the dominant frequency peaks are not clearly identified at deep part load condition in Figure 2.3a. However, the diagram of the frequency peaks focused on deep part load condition (see Figure 2.3b) indicates that there are several wide-band peaks between $f = 0.5 \times n$ and $3 \times n$ at deep part load condition, even though the amplitude is considerably small compared to the dominant frequency peak of the vortex rope precession at part load condition. These frequencies are higher than the expected frequency of the vortex precession which is generally estimated between $f_{rope} = 0.3 \times n$ and $0.6 \times n$ [63]. In the previous studies, several authors reported that the development of the multiple vortex ropes within instead of the single-helix vortex rope in the draft tube at the low discharge condition [16, 64, 88]. Assuming that multiple numbers of vortex ropes are developed in the draft tube cone at deep part load condition, the estimated frequency of the pressure oscillation due to the multiple vortex ropes is expressed as follows:

$$f_{ke} = k \times f_{rope},\ k \in \mathbf{N}\ \ (k : \text{number of vortex ropes}) \tag{2.1}$$

The values of the frequency peaks observed at deep part load condition almost correspond to f_{2e}, f_{3e} and f_{4e} as shown in Figure 2.3b. This suggests that a single-helix vortex may be replaced by a double-helix or higher number of vortex structures in the draft tube cone at deep part load operation. In Figure 2.4a, the influence of varied discharge on the precession frequency of the vortex rope f_{rope} is presented. Although the increase of frequency is slightly unstable at the transition from part load to deep part load, the frequency of the vortex precession

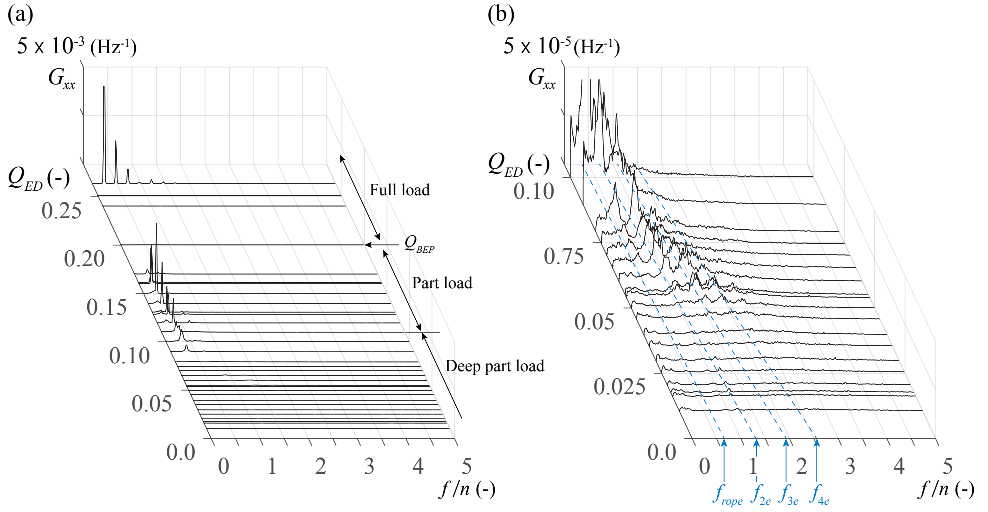

Figure 2.3 – Influence of Q_{ED} on the spectral peaks of the pressure fluctuations measured at C1N for broad discharge range (a) and focused range at deep part load (b) at rated n_{ED} and $\sigma = \sigma_{plant} = 0.11$, together with the linear estimation of the vortex precession frequency f_{rope} and the estimated frequencies of the multiple vortex ropes f_{ke} (dashed blue lines)

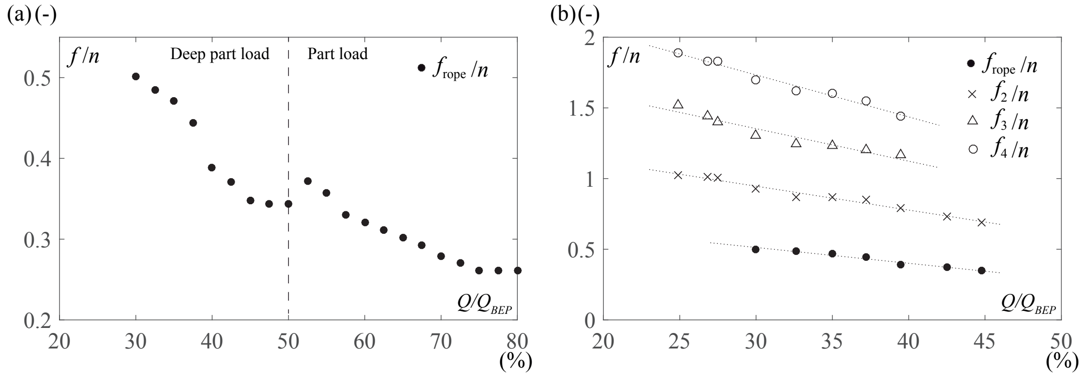

Figure 2.4 – Influence of Q_{ED} on the vortex rope precession frequency for broad discharge range (a) and the evolution of the multiple frequencies detected at deep part load operation (b) at rated n_{ED} and $\sigma = 0.11$

increases almost linearly with respect to the decrease of discharge. However, the frequency f_{rope} becomes less distinct for Q_{ED} values lower than 0.070 (35 % of Q_{BEP}). In contrast, the frequencies of the oscillation caused by the multiple vortex structures become more pronounced as shown in Figure 2.3b. The influence of varied discharge on the measured frequencies f_2, f_3, and f_4 at deep part load condition is also shown in Figure 2.4b. The value of these frequencies is identified by the frequency at which the amplitude of the spectral peak becomes locally maximum at each wide-band frequency peak. The values of these frequencies approximately correspond to the multiples of the vortex precession frequency f_{2e}, f_{3e} and f_{4e}, which evidently confirms that the single-helix vortex structure starts to be replaced by multiple vortex ropes in the draft tube cone at deep part load condition. These frequencies caused by the several vortex ropes start to appear especially at $Q_{ED} = 0.090$ corresponding to 45 % of Q_{BEP}, and they increase almost linearly when discharge decreases. For discharge values lower than $Q_{ED} = 0.054$, the frequency peak of the vortex rope precession f_{rope} is hardly detected, whereas the dominant frequency peaks shift to higher orders of multiple frequencies such as f_3 and f_4, suggesting that the development of multiple vortex ropes becomes more dominant. The spectral peaks of these frequencies are weakened and hardly observed at discharge lower than $Q_{ED} = 0.050$ (25 % of Q_{BEP}).

2.3.2 High-speed visualizations of the vortex rope

The existence of multiple vortex ropes in the draft tube cone is also confirmed by high-speed visualizations. The visualized structure of the cavitation vortex rope at several discharge conditions at rated n_{ED} and $\sigma = 0.11$ together with the centered pressure signal measured at C1N and its frequency analysis results are presented in Figure 2.5. At $Q_{ED} = 0.090$, the flow occasionally features twin vortex structures as shown in Figure 2.5a. Therefore the frequency peak f_2 starts to appear in the frequency domain. However, the appearance of this twin vortex structure is stochastic and the single-helix vortex structure is more dominant, hence, the pressure fluctuation signal shows rather clear fluctuations with the vortex precession at about $0.4 \times n$. Thus, the first peak f_{rope} is still predominant in the frequency domain. At lower discharge such as $Q_{ED} = 0.070$, the volume of cavitation is notably reduced. However, the development of twin vortex structures in the draft tube cone is still confirmed. It appears that the development of the twin vortex structures is more dominant and stable at this condition. Therefore, the pressure is fluctuated at higher frequency as confirmed in the pressure signal in Figure 2.5b. The frequency of the pressure oscillation is estimated to be approximately $f = 0.9 \times n$, which is the frequency caused by the twin vortex ropes f_2. In the frequency domain, the most obvious frequency is f_2, and other multiple frequencies such as f_3 and f_4 start to appear whereas the precession frequency f_{rope} becomes less significant compared to the higher discharge condition. At $Q_{ED} = 0.054$ corresponding to OP#2, the cavitation structure is hardly detected in the draft tube cone. However, the pressure signal still presents periodic oscillations as illustrated in Figure 2.5c. This suggests that the vortex precession may still occur in the draft tube cone. The result of the frequency analysis points out the several frequency peaks corresponding to f_2, f_3, f_4 and f_5, and these multiple frequency peaks become more obvious compared to other higher discharge conditions. This confirms that the several vortex ropes still exist in the draft tube cone, even though cavitation is not developed at the vortex core. The discharge condition of $Q_{ED} = 0.054$ is almost the limit where these frequency peaks are detected, and the frequency peaks become less significant as presented in Figure 2.4.

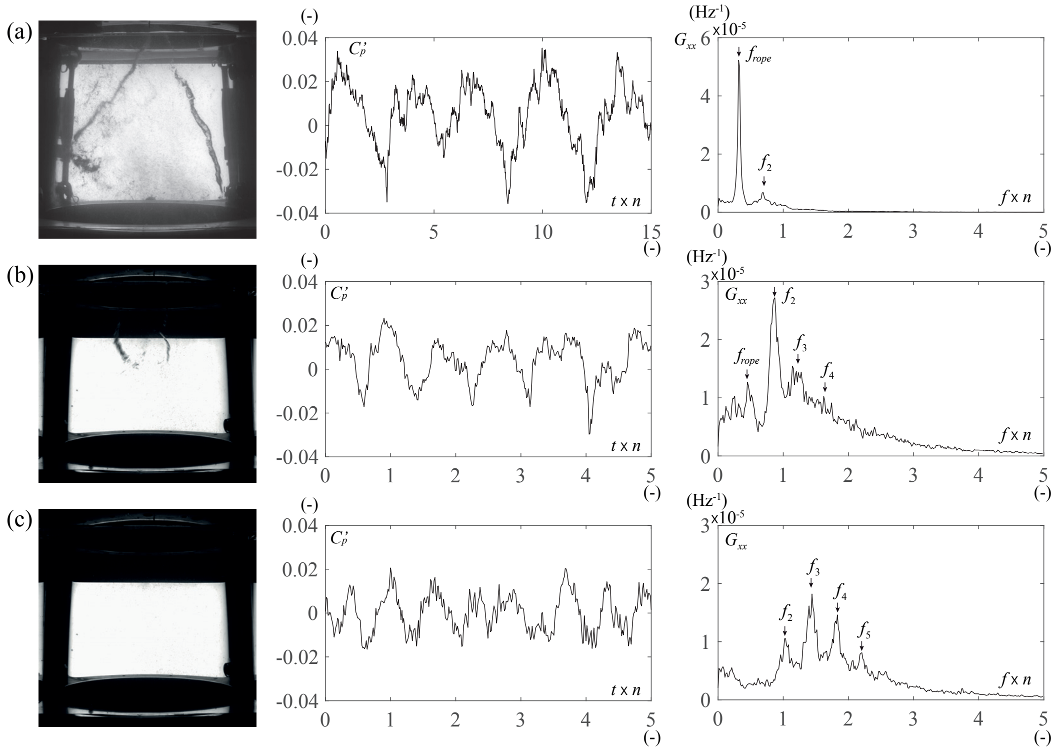

Figure 2.5 – High speed visualizations of the cavitation vortex rope under deep part load operations together with fluctuating pressure signals at C1N and spectral analysis results at $Q_{ED} = 0.090$ (a), 0.070 (b) and 0.054 (OP#2) (c) at rated n_{ED} and $\sigma = 0.11$

2.4 Flow analysis by PIV measurements

2.4.1 Axial velocity distribution

At part load condition, the flow in the draft tube cone is generally accompanied by a backflow region developing at the center of the draft tube and an intense swirl velocity in the surrounding region, which gives rise to the formation of a precessing vortex structure wrapping around the backflow region [23, 63]. This backflow region is closely relevant to discharge values, hence, it is expected that the development of the backflow region is furthermore enhanced at deep part load condition. For the purpose of characterizing the flow in the draft tube at deep part load condition, an axial velocity field is first investigated by PIV measurements. In Figure 2.6, the distributions of the averaged non-dimensional axial velocity C_m^* are shown for different discharge conditions at rated n_{ED} together with the threshold of the backflow inception (see black line in Figure 2.6). The axial velocity is made non-dimensional by the discharge velocity $C_Q = Q/A$ at each horizontal section. For all the presented conditions, it is clearly demonstrated that the significant backflow region is developed at the center of the draft tube cone. Furthermore, the velocity is distributed almost symmetrically, although the velocity is slightly lower near the wall at section #1 ($x = 0.20$ m), which it is assumed is caused by the laser light reflection from the pressure transducer installed on the cone. As the discharge value decreases, the intensity of the backflow region is increased, especially at the lower section. In addition, the location of backflow inception is shifted close to the

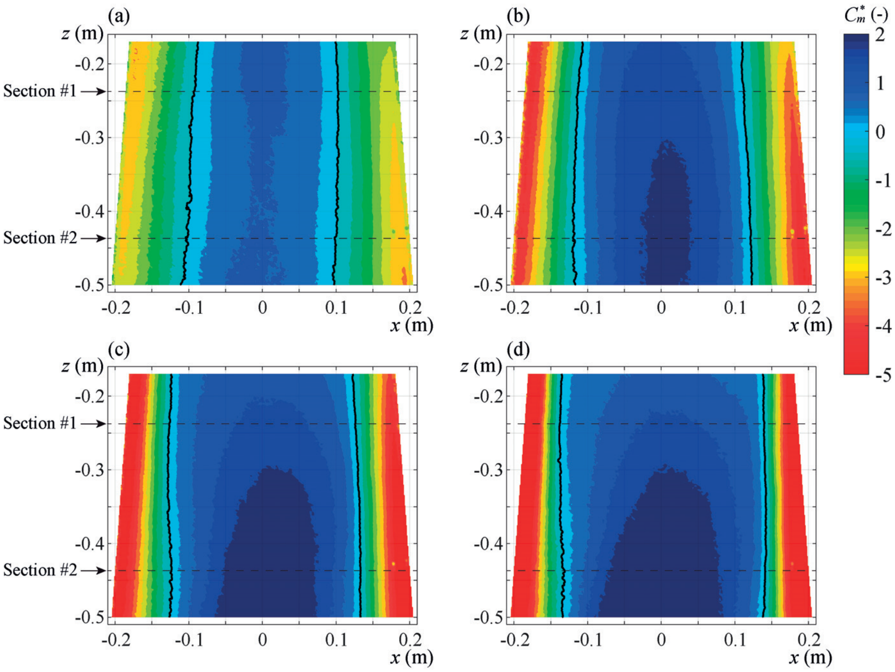

Figure 2.6 – Distribution of the non-dimensional axial velocity C_m^* for $Q_{ED} = 0.100$ (a), 0.070 (b), 0.053 (OP#2) (c), and 0.040 (d) at atmospheric pressure condition and rated n_{ED}. The locations of backflow inception ($C_m^* = 0$) are highlighted by solid black lines.

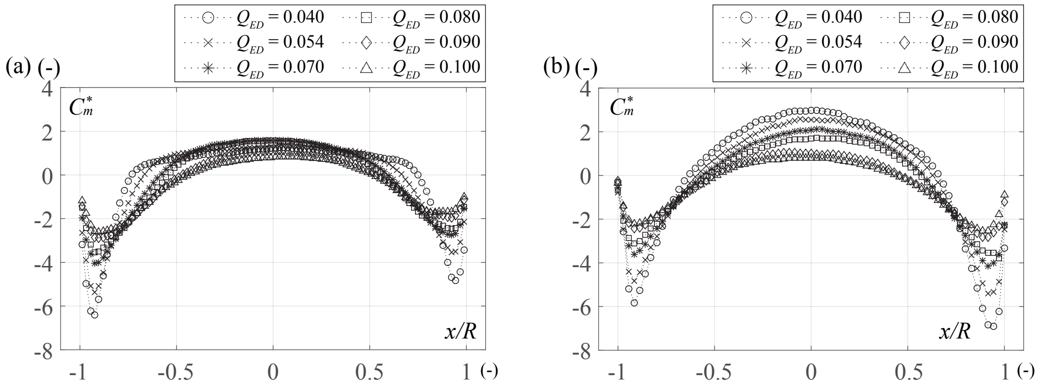

Figure 2.7 – Velocity profiles of the non-dimensional axial velocity C_m^* along the x-axis at section #1 (a) and section #2 (b)

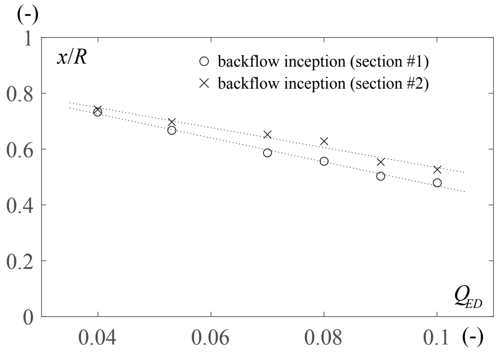

Figure 2.8 – Influence of Q_{ED} on backflow inception point in the draft tube at section #1 and section #2

wall with respect to the reduction of the discharge, correspondingly the velocity near the wall becomes considerably high at the lower discharge condition. At Q_{ED} = 0.040, the backflow intensity becomes significantly high at the center of the draft tube, resulting in considerably high velocity flow in the vicinity of the wall.

In Figure 2.7, the velocity profiles of the axial velocity component C_m^* at both sections #1 and #2 for the different operating conditions are presented. As shown in Figure 2.6, it is confirmed that the flow is dominated by the strong backflow region at the center of the draft tube cone, whereas the velocity becomes remarkably high near the wall. Moreover, the inception of the backflow is gradually shifted close to the wall as discharge decreases, resulting in a highly concentrated velocity near the wall at low discharge. The velocity profiles at section #2 have a similar distribution to section #1. However, the magnitude of the backflow intensity is slightly higher especially at lower discharge values, which leads to a further enhanced axial velocity near the wall to compensate for the backflow discharge. At this section, also the inception of the backflow zone is slightly shifted near the wall compared to section #1 due to the extended backflow development.

The comparison of the backflow onset at both sections #1 and #2 for the different discharge conditions is presented in Figure 2.8. The location of the backflow inception decreases almost linearly with respect to the increase of discharge, and approximately half of the area at section #1 is dominated by the backflow region at $Q_{ED} = 0.054$ (OP#2). The onset of the backflow at section #2 is slightly shifted closer to the wall for all the conditions as confirmed in Figure 2.7.

2.4.2 Circumferential velocity distribution

In Figures 2.9 and 2.10, the distributions of the averaged non-dimensional circumferential velocity component C_u^* at section #1 and section #2 for the different discharge conditions are presented, respectively. The velocity is made non-dimensional by using the runner rotational velocity $U_{ref} = 1/2 D_{ref}\omega$. It is shown that the flow is dominated by a low circumferential velocity region at the center of the draft tube, whereas the circumferential velocity becomes considerably high in the vicinity of the wall. At higher discharge, such as $Q_{ED} = 0.090$, the circumferential velocity seems rather uniformly increased from the center of the draft tube to the wall. However, a low circumferential velocity region at the center of the draft tube is gradually enlarged as discharge decreases, which results in a highly concentrated circumferential velocity near the wall at the lower discharge condition. A similar distribution of the circumferential velocity is observed at section #2, although the magnitude of the circumferential velocity slightly decreases as the area increases.

In Figure 2.11, the velocity profiles of C_y^* along the x-axis at both sections #1 and #2 are presented. It is confirmed that the velocity distribution at higher discharge, such as $Q_{ED} = 0.100$ and 0.090, nearly features the velocity profile of a rigid-body rotation where the circumferential velocity is increased in proportion to a rotating radius. When the discharge value decreases, this velocity profile is changed to the particular velocity profile such that the circumferential velocity lies at zero at the center of the draft tube whereas the velocity is notably amplified near the wall. Such velocity distribution becomes more significant as discharge decreases. The location where the circumferential velocity starts to be amplified is approximately equal to the backflow onset shown in Figure 2.8, suggesting that the development of the stalled region with low kinetic energy at the center of the draft tube is more significant at lower discharge.

2.4.3 Swirl number calculation

For a quantitative evaluation of a swirl flow intensity, the swirl number S is often referred to. The swirl number is defined as the ratio of the axial flux of angular momentum to the axial flux of axial momentum of the flow [31], such as:

$$S = \frac{\int_A C_u C_m r dA}{R\int_A C_m^2 dA} = \frac{\int_0^R C_u C_m r^2 dr}{R\int_0^R C_m^2 r dr} \tag{2.2}$$

The swirl number is initially applied to the draft tube flow by Nishi *et al.* [63], and they

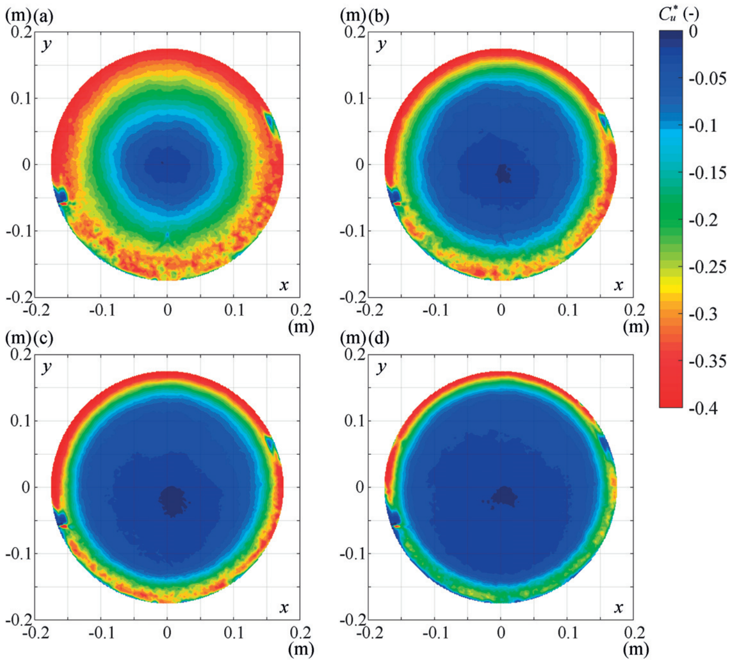

Figure 2.9 – Distribution of the non-dimensional circumferential velocity C_u^* for $Q_{ED} = 0.100$ (a), 0.070 (b), 0.054 (OP#2) (c), and 0.040 (d) at atmospheric pressure condition and rated n_{ED} at section #1

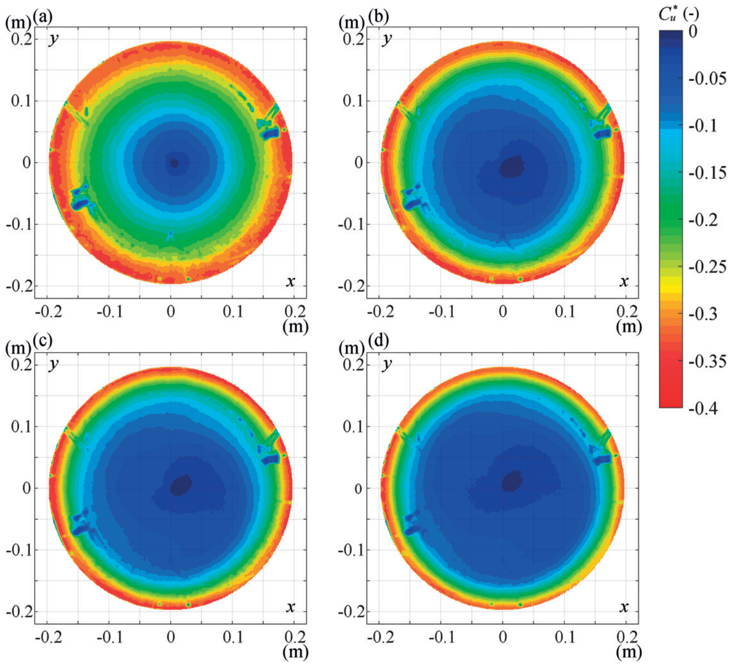

Figure 2.10 – Distribution of the non-dimensional circumferential velocity C_u^* for $Q_{ED} = 0.100$ (a), 0.070 (b), 0.054 (OP#2) (c), and 0.040 (d) at atmospheric pressure condition and rated n_{ED} at section #2

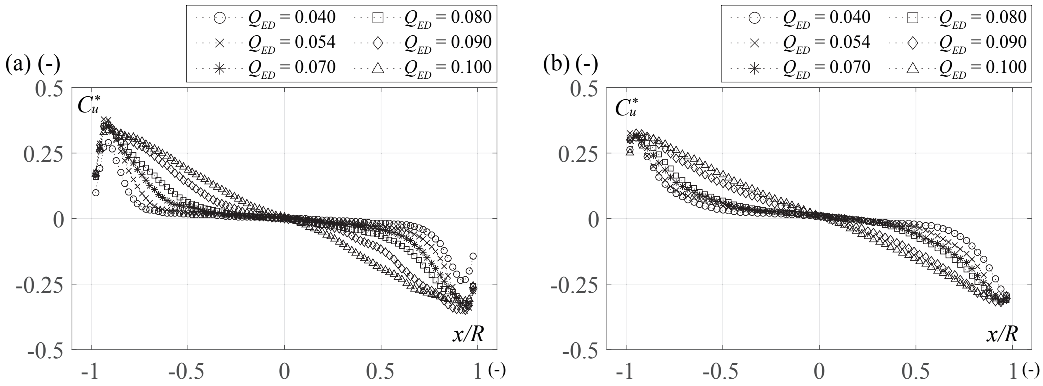

Figure 2.11 – Velocity profiles of the non-dimensional circumferential velocity C_u^* along the x-axis at section #1 (a) and section #2 (b)

characterized the vortex rope behavior by the swirl number of the flow in the draft tube. Later, Favrel [23] calculated the swirl number by the velocity profiles acquired from PIV measurements at part load condition, revealing that the swirl number is linearly increased as discharge decreases at upper part load, whereas the swirl number is kept almost constant at lower part load operation. In Figure 2.12, the influence of varied Q_{ED} on the swirl number S calculated at both sections #1 and #2 is presented. The swirl number S is calculated by the velocity profiles of axial and circumferential velocity components shown in Figures 2.7 and 2.11. The swirl number S at both sections for all investigated discharge conditions lies nearly at $S = 1.0$, which is considered to be an intense swirling flow, although S at section #1 at the lowest discharge is slightly lower. Furthermore, the swirl number S at the both sections becomes maximum at $Q_{ED} = 0.090$, which corresponds to the discharge value where the single-helix cavitation vortex rope starts to be replaced by the double-helix or higher number of vortex ropes in the draft tube cone as shown in 2.3.1. This may indicate that the modification of the swirl intensity occurs at the discharge range where the characteristics of the vortex rope in the draft tube are changed, as Favrel pointed out [23]. At discharge values lower than $Q_{ED} = 0.090$, the swirl number S is decreased and its behavior is slightly stochastic. In theory, the swirl number S is increased when discharge decreases. The slight error of the swirl number calculation may be caused since velocity distributions of axial and circumferential components are not acquired simultaneously. However, the previous study showed that the swirl number S can be deflated or inflated depending on the velocity distribution [86]. This suggests that the particular velocity profile with the highly increased axial velocity near the wall caused by the significant development of the backflow region may affect the variation of the swirl number S. This requires however further investigations to correlate the stochastic behavior of the vortex rope at deep part load with the characteristics of the swirl number S.

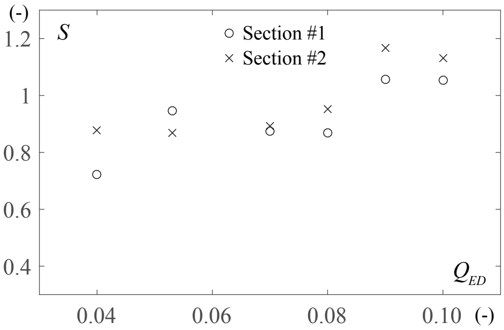

Figure 2.12 – Influence of Q_{ED} on the swirl number S calculated by the velocity profiles acquired from PIV measurements at section #1 and section #2

2.5 Summary

In this chapter, the characteristics of the flow in the draft tube at deep part load condition are investigated by means of pressure measurements together with high-speed visualizations. Furthermore, the velocity field in the draft tube is characterized by PIV measurements. By pressure measurements, it is shown that the intensity of the cavitation vortex rope is drastically reduced at deep part load condition, even though the cavitation vortex structures are still stochastically observed in the draft tube. In particular, the high-speed visualizations reveal that multiple vortex structures may exist at about 40 % of the BEP, and several frequency peaks appear in the frequency domain in accordance. These frequencies almost correspond to multiples of the vortex rope precession frequency, which confirms that multiple vortex ropes develop in the draft tube cone. Furthermore, these frequencies almost linearly increase as discharge decreases.

In addition, the mean velocity distributions of the axial and circumferential components in the draft tube are investigated by PIV measurements. It is demonstrated that the flow is dominated by a large backflow region at the center of the draft tube, which results in a concentrated main flow stream near the draft tube wall. The diameter of the backflow region is almost linearly increased as discharge decreases. The circumferential velocity distribution is also affected by the decrease of discharge, and a concentrated circumferential velocity near the wall is observed at lower discharge.

Finally, based on the velocity profiles acquired by PIV measurements, the swirl number is calculated. It is shown that the swirl number of the flow in the draft tube is consistently high under deep part load operations. Furthermore, it is pointed out that modification of the swirl number may occur at the discharge range where the behavior of the vortex rope in the draft tube is changed, such that a single-helix vortex is replaced by multiple vortex ropes. However, stochastic behaviors of the vortex rope at deep part load condition need to be further investigated for the correlation with the dynamic characteristics of the swirl number.

3 Investigation of inter-blade vortices by visualization

3.1 Introduction

The previous chapter focuses on the investigations of the cavitation vortex rope in the draft tube at deep part load conditions. Although the development of multiple vortex ropes in the draft tube is confirmed, its influence on hydraulic units is assumed to be relatively minor. Instead, Francis turbine operations at deep part load condition may be subject to another cavitation vortex development inside the blade channel called inter-blade cavitation vortices [7]. Thus, this chapter is aimed at revealing the characteristics and the development of inter-blade cavitation vortices by a visualization approach.

For a better understanding of cavitation phenomena, visualizations have played an important role in revealing their dynamic characteristics. Moreover, appropriate image processing enables extensive analyses to characterize cavitation behavior, such as an estimation of the cavity volume oscillation [59]. As a first step in the analysis of inter-blade cavitation vortices, adapted visualization techniques to properly visualize the inter-blade cavitation vortices through a transparent draft tube cone from the downstream of the runner are introduced [91]. Visualizations from downstream are made at several discharge conditions to characterize inter-blade cavitation vortices as well as the cavitation vortex rope in the draft tube. In further effort to visualize the development and onset of inter-blade cavitation vortices in the vicinity of the hub, the present chapter additionally introduces a sophisticated visualization technique enabling an optical access to the blade channel through an instrumented guide vane. This visualization technique is applied for the first time to visualize inter-blade cavitation vortices from the upstream side of the runner, providing an unprecedented image of the inter-blade cavitation vortex development as well as its onset.

Furthermore, binary image processing is employed to evaluate cavitation regions inside the blade channel, and the probability for the development of an inter-blade cavitation vortex inside a blade channel is evaluated for different n_{ED} conditions. In addition, vortex inception point on the hub as well as an averaged vortex line are estimated based on the detected cavitation edge from the binarized cavitation image. The calculated vortex line is mapped on a three dimensional domain by using the simulation domain for further use in the validation of the simulation results.

3.2 Experimental setup for visualization

3.2.1 Setup for visualization from downstream

For the visualization from the low pressure side of the runner, an inclined window is installed on the transparent draft tube cone enabling an optical access to a blade channel from downstream. The schematics of the inclined window as well as the experimental setup with a high-speed camera are presented in Figure 3.1. The attached window to the draft tube cone is filled with water to minimize optical deformations. To illuminate the blade channel, a stroboscopic light and an intensity xenon flash light are adopted for periodic image acquisition and high-speed visualization, respectively. The latter xenon light generates a 11 ms-long high intensity flash light, permitting clear high-speed visualizations for blade channels from downstream of the runner. The xenon flash light and its characteristics of the light emission are presented in Figure 3.2.

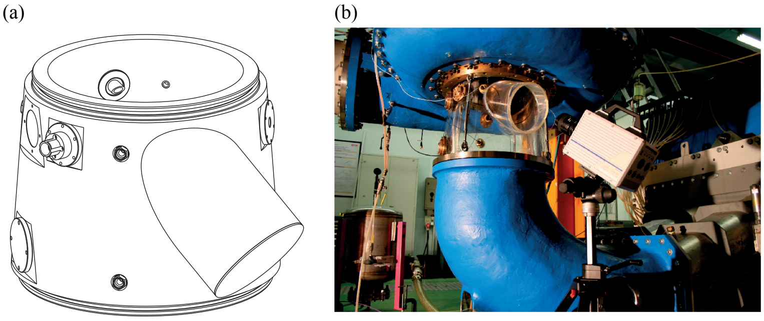

Figure 3.1 – The inclined window installed on the transparent draft tube cone (a) and the setup of visualizations of inter-blade cavitation vortices from the runner downstream (b)

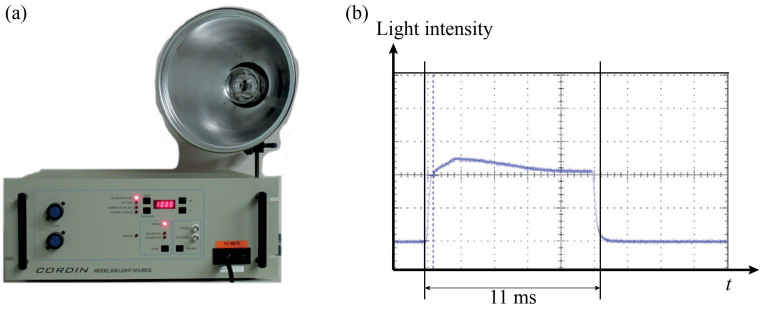

Figure 3.2 – Xenon flash light (a) and its characteristics of light emission intensity (b)

3.2.2 Setup for visualization from upstream

Instrumented guide vane

The presented study highlights a novel visualization technique using an instrumented guide vane equipped with a transparent window made of Polymethyl Methacrylate (PMMA). The instrumented guide vane provides an optical access to a blade channel from the upstream of the runner. Its schematics are illustrated in Figure 3.3 [92]. The geometry of the instrumented guide vane is identical to the original guide vane. The hollow space inside the guide vane is machined to accommodate a visualization device inside, and the transparent window is attached in the middle of the guide vane wall. The surface of the window has the same profile as the guide vane, and it is sufficiently polished to mitigate perturbations of the flow entering the runner.

Borescope

To obtain an optical access to the blade channel via an instrumented guide vane, a borescope is adopted. The general structure of the borescope is presented in Figure 3.4. The borescope enables visualizations in a limited space by a reflecting prism installed inside. However, the coverage of the optical field is dependent on the prism's capability. The selected model for the present application features a swivel deflecting prism (see Figure 3.4), which can vertically change the optical direction covering various visual fields from the shroud to the hub of the blade. The swivel prism is especially helpful for monitoring the onset of inter-blade cavitation vortices. The height and the diameter of the selected borescope (250 mm working length and $\phi = 10$ mm) fit perfectly into the hollow manufactured in the instrumented guide vane, leaving a slight clearance (0.2 mm) between the borescope and the hollow. This clearance allows the rotation of the borescope in the horizontal direction in order to change the optical direction to visualize different parts of the blade, from the pressure side to the suction side of the blade.

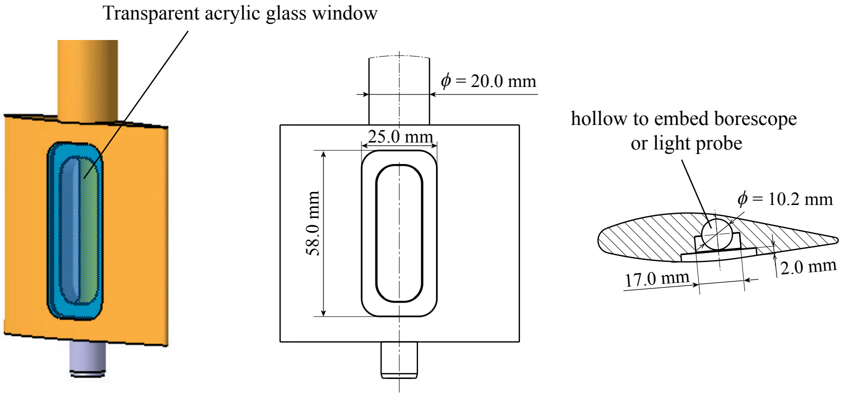

Figure 3.3 – Sketch of the instrumented guide vane with a transparent acrylic window and the hollow space manufactured inside the guide vane

Compact LED

For visualizations in such a limited space, a sufficient light source is a key to appropriate image acquisitions. For the present application, a compact power LED with a basic surface of 3.45 mm × 3.45 mm as shown in Figure 3.5 is adopted as the light source. The endorsed compact LED notably features a luminous flux 1′150 lm at the maximum current 3 A. Its detailed electric characteristics are summarized in Table 3.1. To minimize the loss of light in water, the wavelength of the emitted light from the LED is also taken into account. The selected LED contains more light at short wave lengths such as 660 nm, which has a higher transmittance in water.

Although the compact power LEDs generate highly luminous light, they simultaneously radiate a strong heat which may cause severe damage to the acrylic window as well as the instrumented guide vane itself. Therefore, the installation of an effective heat radiation device is crucial. Hence, the LEDs are attached to an aluminium heat sink to improve their radiation performance and reduce the risk of damage to the acrylic glass (see Figure 3.5b). A set of 5 LEDs is installed on a special probe with the same diameter and length as the borescope. The probe can also be rotated inside the hollow of the instrumented guide vane to optimize the illumination inside the blade channel.

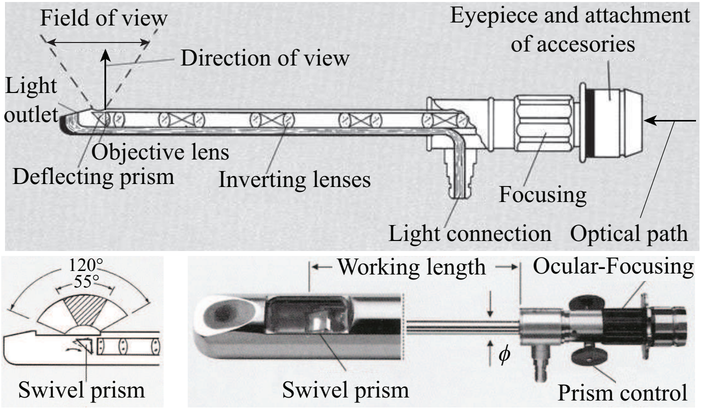
Field of view
Direction of view
Eyepiece and attachment of accesories
Light outlet
Objective lens
Deflecting prism
Inverting lenses
Focusing
Light connection
Optical path
120°
55°
Swivel prism
Working length
Ocular-Focusing
ϕ
Swivel prism
Prism control

Figure 3.4 – Schematics of the general structure of the borescope and the adopted borescope with a swivel deflecting prism

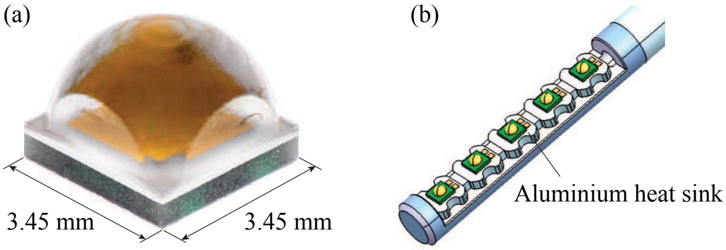
(a)
(b)
3.45 mm
3.45 mm
Aluminium heat sink

Figure 3.5 – Compact LED (a) and light probe with aluminium heat sink (b)

Table 3.1 – Specifications of the compact LED light used for the visualization from the runner upstream

Compact LED	
Manufacturer	CREE
Model	XP-L V5
Size	3.45 x 3.45 (mm)
Power	10.0 (W)
Current	3.0 (A)
Forward voltage	3.3 (V)
Light output	1′150 (lm)

Overview of installation and image acquisition system

In total, three instrumented guide vanes are installed in the model: one is used for the image acquisition with the borescope and two for the light sources. The installation of the instrumented guide vanes as well as the visualization devices are presented in Figure 3.6. A total of 10 LED lights with two probes are prepared, and the borescope is installed between the two light probes (see Figure 3.6) to illuminate the blade channels properly. The LED light emission is controlled by a LED controller generating a pulsed electric current. The pulse width of the current is set to 0.2 ms to obtain an appropriate sharpness of the image. Finally, the image is recorded by a CCD camera connected to the borescope. The endorsed camera features a medium frame rate such as 30 fps at maximum with a resolution of 1′280 × 960 pixels. The image acquisition as well as the LED light emission through the LED controller are synchronized with the turbine rotational frequency, enabling an image acquisition at the same location and angle of the blade every single runner rotation. The image acquisition system is presented in Figure 3.7. This acquisition system is also applicable for the high-speed camera. For high-speed visualizations, the xenon flash is also used to increase the brightness.

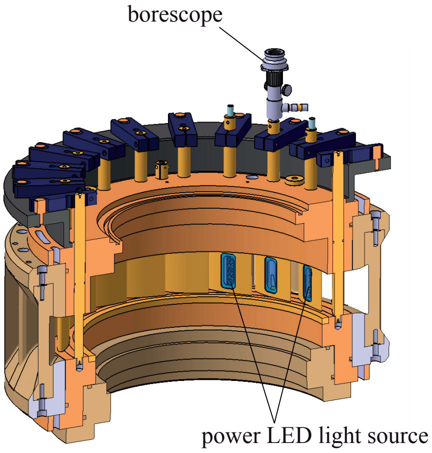

Figure 3.6 – Installation of the instrumented guide vanes and visualization devices

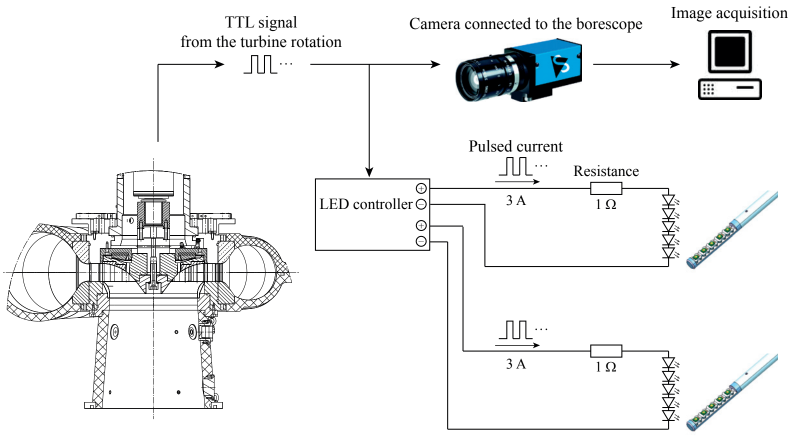
TTL signal
from the turbine rotation
Camera connected to the borescope
Image acquisition
Pulsed current
Resistance
LED controller
3 A
1 Ω
3 A
1 Ω

Figure 3.7 – Acquisition system for guide vane visualization

3.2.3 Operating conditions for visualizations

First of all, visualizations from downstream of the runner are applied to a broad range of discharge at rated n_{ED} and at several points with different n_{ED} conditions including OP#1, #2 and #3 to characterize the development of inter-blade cavitation vortices. Visualizations from upstream of the runner are then conducted especially focusing on OP#1,#2 and #3 to further investigate the development and onset of inter-blade cavitation vortices. The operating parameters for the visualizations are summarized in Table 3.2. The cavitation number σ is focused on $\sigma = \sigma_{plant}$ at OP#2 ($\sigma = 0.11$).

Table 3.2 – Operating conditions for the presented visualizations from downstream and upstream of the runner

Visualization from runner downstream					
Q_{ED} (-)	n_{ED} (-)	GVO (°)	E (J kg^{-1})	n (Hz)	σ (-)
0.010	0.288	0.5	263	13.33	0.11
0.018	0.288	1.3 (SNL)	263	13.33	0.11
0.054	0.288	5 (OP#2)	263	13.33	0.11
0.070	0.288	7	263	13.33	0.11
0.080	0.288	8	263	13.33	0.11
0.100	0.288	10	263	13.33	0.11
0.052	0.317	5 (OP#1)	263	14.67	0.11
0.055	0.268	5 (OP#3)	263	12.40	0.11
Visualization from runner upstream					
0.052	0.317	5 (OP#1)	263	14.67	0.11
0.054	0.288	5 (OP#2)	263	13.33	0.11
0.055	0.268	5 (OP#3)	263	12.40	0.11

3.3 Visualization results

3.3.1 Visualizations from downstream of the runner

In Figure 3.8, the visualized blade channel from the runner downstream with respect to varied Q_{ED} at rated n_{ED} is presented. At the lowest discharge, cavitation appears around the trailing edge near the hub. It is assumed that this cavitation is caused by a shear layer generated by the stagnated flows between the rotating and stationary frames. This cavitation is observed as well at Speed-No-Load (SNL) condition ($Q_{ED} = 0.018$). At $Q_{ED} = 0.054$ corresponding to OP#2, the cavitation structure around the trailing edge near the hub is diminished and almost no cavitation structure is observed in the presented visualization. It should be noted that there is a slight development of inter-blade cavitation vortices which are barely observed at this condition. However, its appearance is considerably infrequent. As discharge increases, a cavitation vortex rope starts to develop. The structure of the cavitation vortex rope appears near the runner crown at $Q_{ED} = 0.070$, and the volume of cavitation is increased when discharge increases. At the discharge range between $Q_{ED} = 0.070$ and 0.090, the performed visualization confirms that the development of multiple vortex structures is occasionally observed near the runner crown, as described in Section 2.3.

In Figure 3.9, the visualization results for varied n_{ED} values at the constant guide vane opening $GVO = 5\,°$ and $\sigma = 0.11$ are presented. Although inter-blade cavitation vortices are not clearly observed at rated n_{ED} (OP#2) and lower n_{ED} (OP#3), the notable development of the inter-blade cavitation vortices is confirmed at the higher n_{ED} condition (OP#1). It should be stressed

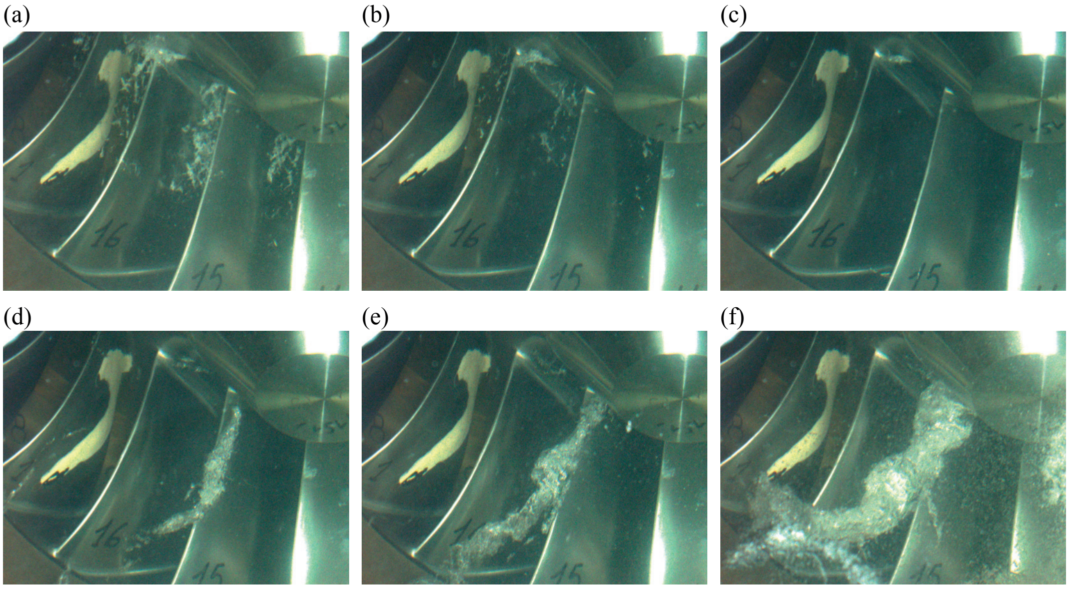

Figure 3.8 – Visualizations from the runner downstream for different Q_{ED} conditions at rated n_{ED} and $\sigma = 0.11$. The discharge values correspond to $Q_{ED} = 0.010$ (a), 0.018 (speed-no-load condition) (b), 0.054 (OP#2) (c), 0.070 (d), 0.080 (e), and 0.090 (f).

that the development of the inter-blade cavitation vortices is not clearly confirmed at any discharge and cavitation number at rated and lower n_{ED} conditions. This suggests that the inter-blade vortex structure is not sufficiently developed at rated and lower n_{ED} conditions. Hence, it is assumed that the modification of the velocity triangle at the blade inlet resulting from the changed n_{ED} condition plays a significant role in the development of inter-blade cavitation vortices, in addition to the discharge condition.

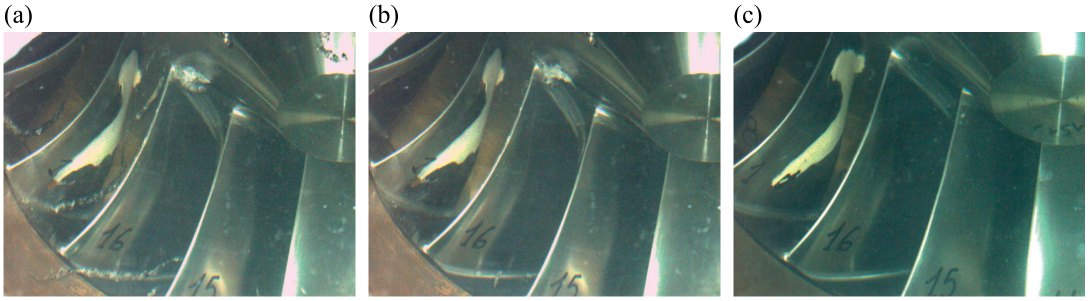

Figure 3.9 – Visualization from the runner downstream for different n_{ED} conditions at constant guide vane opening $GVO = 5\,^\circ$ and $\sigma = 0.11$. The n_{ED} values correspond to $n_{ED} = 0.317$ (OP#1) (a), 0.288 (OP#2) (b), and 0.268 (OP#3) (c).

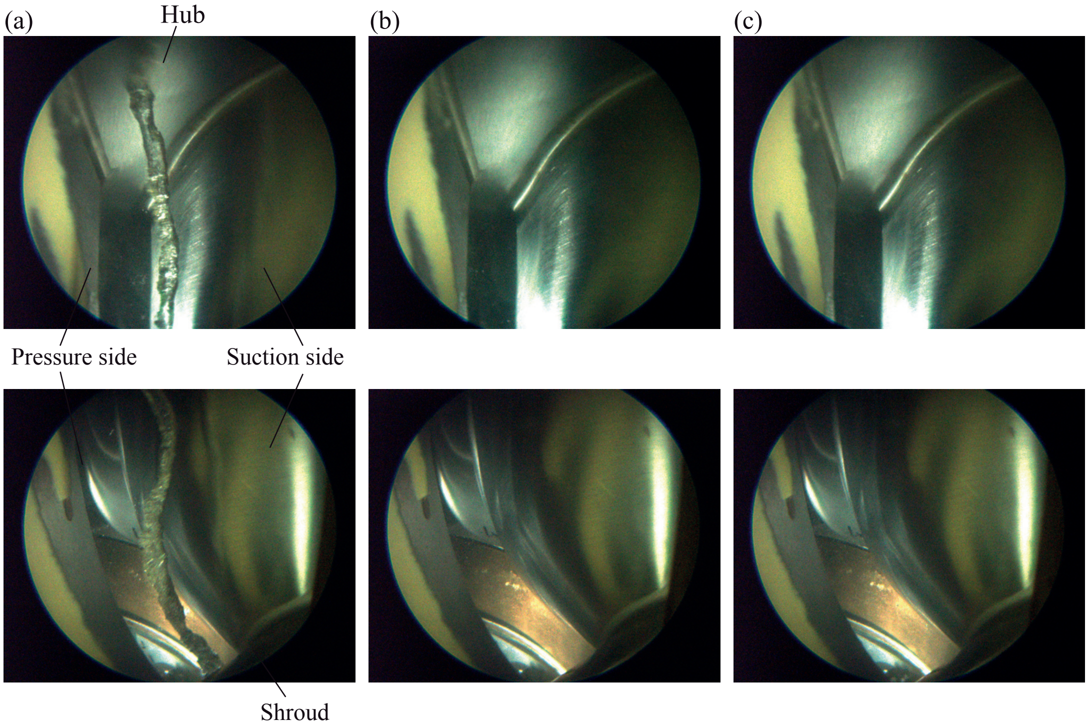

Figure 3.10 – Instantaneous views of the inter-blade cavitation vortex using the instrumented guide vane at OP#1 (a), OP#2 (b), and OP#3 (c) at $\sigma = 0.11$ with different swivel prism angles looking at the hub (upper side) and the shroud (lower side), respectively

3.3.2 Visualization from upstream of the runner

As revealed in Section 3.3.1, the development of inter-blade cavitation vortices is more dependent on the n_{ED} condition. Thus, the visualization from the runner upstream using the instrumented guide vane is carried out focusing on the targeted operating conditions OP#1, #2, and #3 to further investigate the characteristics and the development of the inter-blade cavitation vortex. In Figure 3.10, instantaneous views of the blade channel at $\sigma = 0.11$ obtained by visualizations with the instrumented guide vane are presented. The two different angles of the swivel prism of the borescope are applied to look at the different parts of the blade channels near the hub (upper side in Figure 3.10) and the shroud (lower side in Figure 3.10). The clear development of the inter-blade cavitation vortex at OP#1 is successfully captured, whereas there is no cavitation developing inside the blade channel at OP#2 and OP#3, which is also confirmed by the visualization from downstream (see Figure 3.8). Furthermore, the visualization results at OP#1 evidently show that the cavitation structure is attached to the hub. It also reveals that the vortex develops nearly straight in the vicinity of the hub, even though the vortex line is slightly twisted helically in the middle of the blade channel. The image of the inter-blade cavitation vortex successfully acquired by the visualization from upstream is further investigated by appropriate image processing to characterize its development in the following sections. The results of high-speed visualizations from both upstream and downstream sides of the runner are presented in Appendix B.

3.4 Characterization of the inter-blade cavitation vortex by image processing

3.4.1 Evaluation of the inter-blade cavitation vortex region

It should be stressed that even though the inter-blade cavitation vortex shown in Figure 3.10 is clearly developed at OP#1, a number of images demonstrate that its appearance is slightly unstable due to the stochastic nature of the flow at deep part load condition. Hence, the region of the inter-blade cavitation vortex is evaluated by means of a binary image processing using 500 images of the same visual field in the blade channel obtained by the synchronized image acquisition system mentioned in Section 3.2.2. After adjusting the contrast and brightness of the images, the reference image taken in cavitation free conditions is subtracted from the targeted image in order to isolate the cavitation region. Then, each pixel of the frame is classified into either cavitation region or non-cavitation region by transforming an RGB image into a binary image. In short, the binarized value k at each pixel (i, j) of the image frame is expressed as follows.

$$k(i,j) = \begin{cases} 1 & \text{(Cavitation region)} \\ 0 & \text{(Cavitation free region)} \end{cases} \tag{3.1}$$

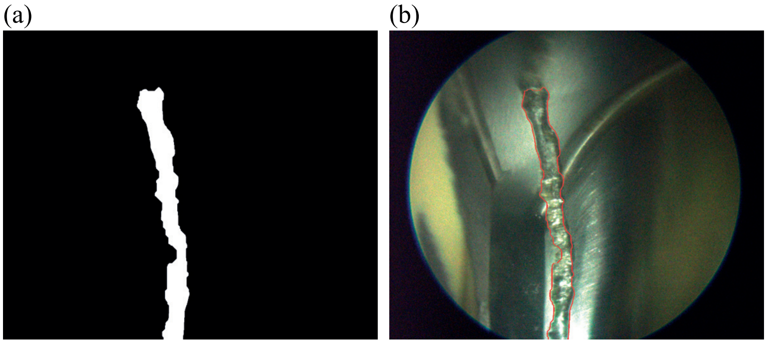

Figure 3.11 – An example of a binarized image of the inter-blade cavitation vortex (a) and the threshold of cavitation based on the edge detection (b)

An example of a binarized image and the threshold for the cavitation detection is shown in Figure 3.11. It can be confirmed that the region occupied by the inter-blade cavitation vortex is accurately evaluated by the described method, and the edge of the cavitation is also successfully detected. The evaluation of the inter-blade cavitation region for 500 images makes it possible to calculate the probability of cavitation presence P at each pixel (i, j), expressed as:

$$P(i,j) = \frac{1}{N}\sum_{n=1}^{N} k_n(i,j) = \frac{1}{500}\sum_{n=1}^{500} k_n(i,j) \tag{3.2}$$

High values of the probability P indicate high prospects of cavitation presence. The contours of the calculated probability P for OP#1, OP#2, and OP#3 at $\sigma = 0.11$ are illustrated on the respective reference image in Figure 3.12. As expected, it is clearly observed that the inter-blade cavitation regions are significantly large at OP#1, while the cavitation regions and the probability are drastically decreased and only observed partially around the runner hub at OP#2, and it disappears completely at OP#3. More interestingly, the high probability value at OP#1 intensifies in the vicinity of the hub, despite the relatively high dispersion of the cavitation region in the middle of the blade channel. This can be also confirmed by the histogram of the probability P shown in Figure 3.13, of which the value is extracted along the line on the hub (see dashed line in Figure 3.12) from the pressure side to the suction side. The value of the probability P is clearly amplified at the middle of the hub at OP#1, whereas the probability becomes considerably low at OP#2 and completely disappears at OP#3. Furthermore, by checking each individual image at OP#1, it is also confirmed that the occurrence of the inter-blade cavitation is considerably high around the hub. This high probability value around the hub may suggest that an intense inter-blade vortex is generated near the hub and the risk of cavitation development is potentially increased.

Furthermore, the location of the inter-blade vortex center as well as the vortex inception points are calculated from the detected cavitation edge. The vortex center line is evaluated by calculating the center of the binarized cavitation vortex at each pixel row, of which an example is presented in Figure 3.14a. Then, the first point of the vortex center line is taken as the

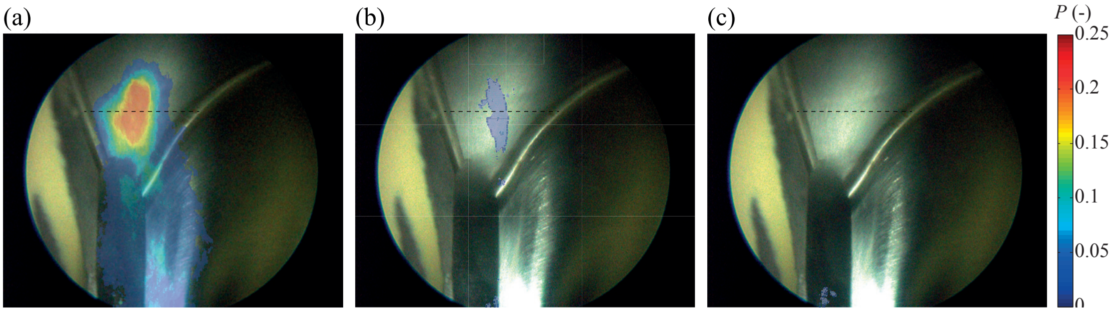

Figure 3.12 – Contour of the calculated probability P overlaid on the each reference image for the targeted operating conditions OP#1 (a), OP#2 (b), and OP#3 (c)

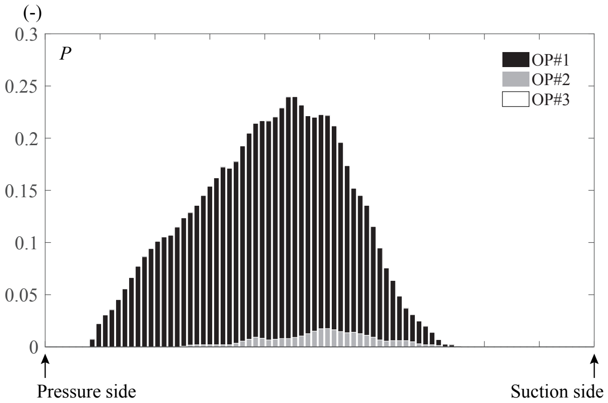

Figure 3.13 – Histogram of the probability P along the horizontal line on the hub

instantaneous vortex inception point on the hub, as shown in Figure 3.14a. The detection of the instantaneous vortex inception point is applied to the acquired images of the inter-blade cavitation vortex, and the mean vortex inception point is then calculated. It should be noted that the images with remarkably small cavitation volume are eliminated to reduce the error of the vortex evaluation. The instantaneous vortex inception points shown in Figure 3.14b are clearly concentrated at the center of the hub, and the averaged location of the vortex inception point is located nearly at the center between the pressure side and the suction side on the hub. This location almost corresponds to the point where the probability becomes maximum.

In the same way, the averaged location of the inter-blade vortex center line is calculated. The calculated mean vortex line starting from the averaged vortex inception point (see Figure 3.14b) as well as its standard deviation are presented in Figure 3.15. The mean vortex line is also calculated for the visualization of the shroud side by the same procedure as the binary image processing. The averaged vortex line on the hub side is nearly straight shape even though it is slightly twisted in the middle, and the standard deviation of the vortex line gradually increases with respect to the distance from the hub wall. The averaged vortex on the shroud side is also nearly straight in shape in the upper part, however the vortex shape becomes slightly unstable around the middle span region corresponding to the non-dimensional span-wise location s^*

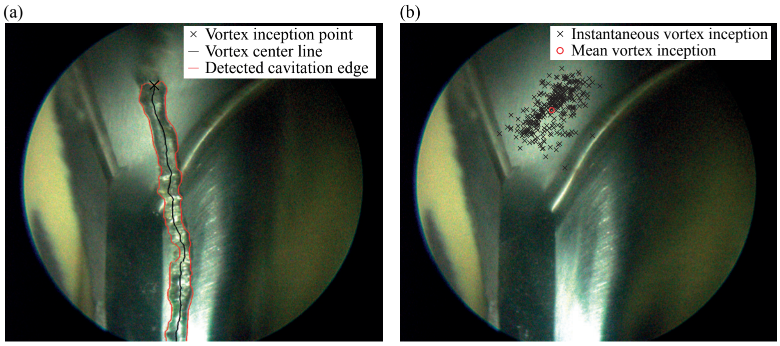
(a)
× Vortex inception point
— Vortex center line
— Detected cavitation edge
(b)
× Instantaneous vortex inception
○ Mean vortex inception

Figure 3.14 – An example of the detected cavitation edge with the vortex center line (a) and the instantaneous vortex inception points together with the averaged location of the vortex inception point on the reference image (b)

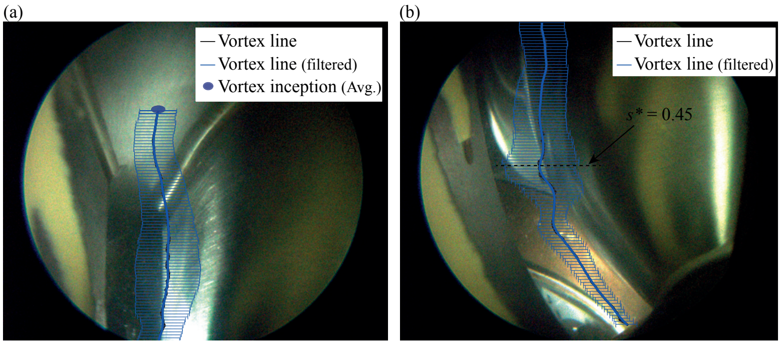
(a)
— Vortex line
— Vortex line (filtered)
● Vortex inception (Avg.)
(b)
— Vortex line
— Vortex line (filtered)
s^* = 0.45

Figure 3.15 – Averaged vortex center lines with the corresponding standard deviation as well as the location of the vortex inception at OP#1 illustrated on the reference image

= 0.45 (see Figure 3.15b). Correspondingly, the standard deviation is also magnified at this location, suggesting a high dispersion of the vortex location around the middle span region. It appears that the shape of the vortex line is also modified at this span-wise location ($s^* = 0.45$), and starts approaching the shroud and the suction side of the blade as shown in Figure 3.15b. The standard deviation also decreases again when the vortex approaches the exit of the blade channel.

3.4.2 Estimation of the vortex region in a three-dimensional domain

In this section, the vortex line obtained from the visualization results is mapped into a three dimensional domain. For the purpose of an accurate estimation of the vortex location, the identical image from the same view point as the visualization is prepared using the three dimensional simulation domain of ANSYS CFX 17.1 (details of simulations will be explained later in Section 5.3). In this reference image, the mesh lines of constant radius, theta, and span-wise location are drawn as mesh indicators (see Figure 3.16a). Then, these lines are overlaid on the real image of the visualization, which fits on the visualized blade channel as confirmed in Figure 3.16b.

To begin with, it should be mentioned that the several assumptions are made in order to map the calculated vortex lines in the two dimensional image on the three dimensional domain.

- The vortex line starts from the average location of the vortex inception point on the runner hub wall. The streamwise location as well as the angular position of the vortex inception point can be calculated by the intersection between the averaged vortex inception point (see Figure 3.15) and the mapped lines of constant streamwise location and angular position on the hub (see Figure 3.16).
- The vortex center location is evaluated at each constant span-wise location s^* every $s^* = 0.05$ from the hub ($s^* = 1.00$) to $s^* = 0.20$ where the inter-blade cavitation vortex disappears near the exit of the blade.
- It is assumed that the vortex is developed in a constant streamwise location plane from the hub ($s^* = 1.00$) to $s^* = 0.45$. The value of this constant streamwise location is equal to the streamwise location of the vortex inception on the hub from the first assumption. This simplified assumption is based on the visual observation that the inter-blade vortex is developed nearly straight close to the hub.
- From $s^* = 0.45$ to 0.20, the location of the vortex center is plotted in different streamwise location planes which are gradually increased from $s^* = 0.45$ to 0.20, in order to satisfy the location where the inter-blade cavitation vortex disappears near the blade channel outlet, which is estimated by the visualization through the inclined window from downstream of the runner.

By using the assumptions above, the location of the vortex center at each constant span-wise location s^* can be given as an intersection of the constant span-wise line on the constant

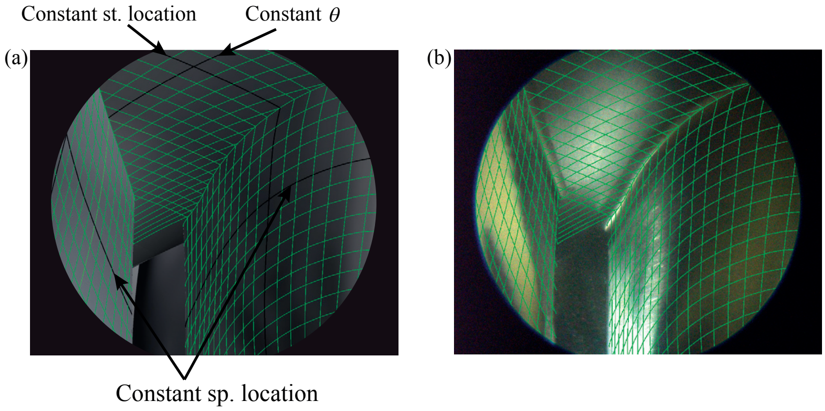

Figure 3.16 – Lines of constant streamwise (st.) location, θ, and span-wise (sp.) location on the same view of the visualization from the CFD domain (a) and the overlaid mesh lines on the visualized blade channel (b)

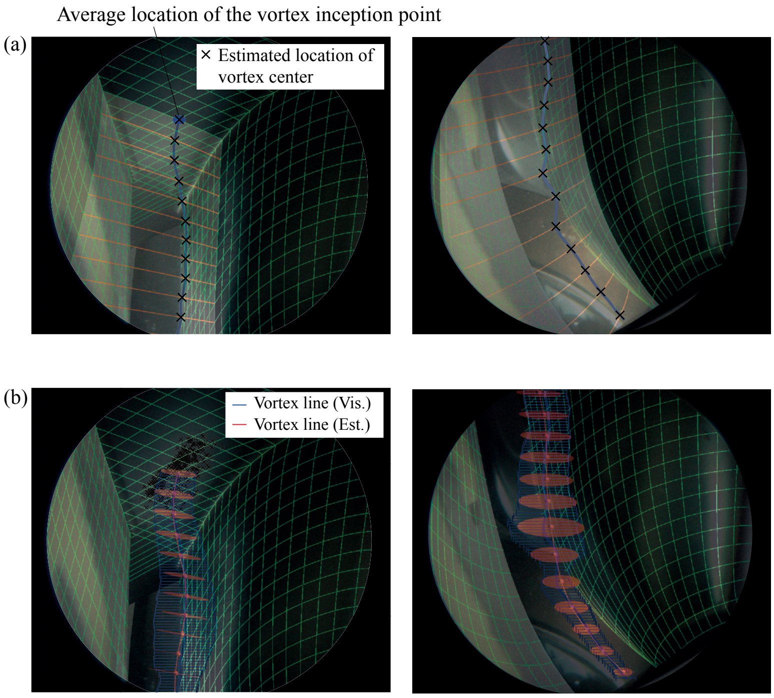
Average location of the vortex inception point
(a)
× Estimated location of vortex center
(b)
— Vortex line (Vis.)
— Vortex line (Est.)

Figure 3.17 – The estimated inter-blade vortex center locations given by intersections with constant span-wise lines at a constant streamwise location (a) and comparison of the calculated vortex line with the estimated location of the vortex center with the standard deviation in the 3-D domain (b)

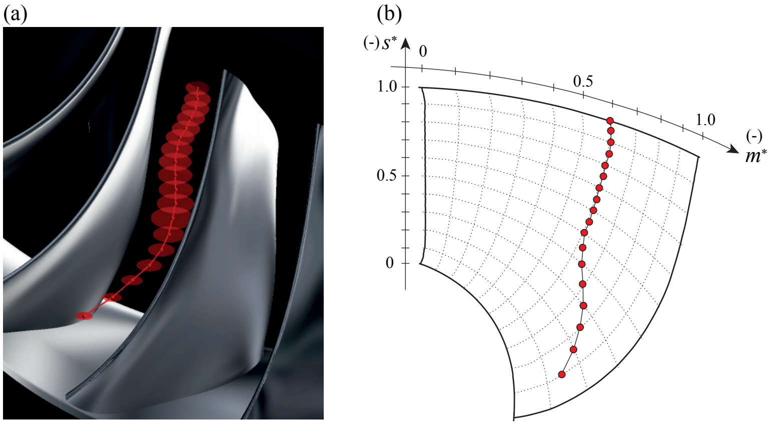

Figure 3.18 – View of the mapped vortex line from downstream of the runner (a) and the projected vortex line on the meridional plane (b)

streamwise location plane (see orange line in Figure 3.17) with the calculated vortex line as shown in Figure 3.17. After plotting the predicted location of the vortex center, if necessary, the vortex location on each constant span-wise location is slightly adjusted to achieve the smooth connection of the vortex line. As a result, the location of the vortex can be mapped in a three dimensional domain as shown in Figure 3.17. The standard deviation of the vortex location in Figure 3.15 is also estimated by using the span-wise line on the constant streamwise location plane, and plotted as a circle in the three dimensional domain. It can be confirmed that the estimated vortex lines as well as the standard deviation are in good agreement by comparison with the vortex line calculated by the visualization results. Moreover, the estimated vortex line is also in a good agreement with the visualized inter-blade vortex from downstream of the runner (see Figure 3.9). The projected vortex location on the meridional plane illustrated in Figure 3.18b also reveals the inter-blade vortex onset on the hub at the streamwise location $m^* = 0.60$. It should be emphasized as well that this estimated vortex line is compared to the simulated inter-blade vortex by the authors [93] and shows very good agreement. The comparison of the vortex line mapped on the three dimensional domain with the simulated inter-blade vortex is explained in Section 7.2 in more detail.

3.5 Summary

This chapter focuses on the visualization of inter-blade cavitation vortices. Firstly, the visualization from the downstream side of the runner using the inclined window is systematically applied to several operating conditions to characterize the development of the inter-blade cavitation vortex at deep part load conditions. As a result, the formation of inter-blade cavitation vortices is not clearly observed at the rated and lower n_{ED} conditions even at the lowest cavitation number, whereas the clear development of inter-blade cavitation vortices is confirmed at the higher n_{ED} condition. This suggests that the occurrence of inter-blade cavitation vortices may be affected by the velocity triangle at the runner inlet caused by varying the n_{ED} conditions, in addition to the discharge conditions.

For further investigations of the inter-blade cavitation vortex characteristics, visualizations using an instrumented guide vane is conducted focusing on three targeted operating conditions at the constant guide vane opening of $GVO = 5$ °. The proposed visualization successfully captures the development of an inter-blade cavitation vortex inside a blade channel, which reveals the onset of the cavitation vortex on the surface of the hub. The acquired images of the inter-blade cavitation vortex are then classified into cavitation and non-cavitation regions by binary image processing. The probability of inter-blade cavitation formation is calculated. Consequently, high probability is concentrated near the hub, suggesting that the flow in the vicinity of the hub plays an important role on the development of a strong inter-blade cavitation vortex. In addition, the mean vortex inception point on the hub as well as the vortex line are estimated based on the threshold of the cavitation detected by the binary image processing. It has been shown that the averaged vortex inception point is located almost at the center of the hub at the streamwise location $m^* = 0.60$. The mean vortex line together with the standard deviation are nearly straight shape around the hub, whereas there is a high dispersion in the middle-span region. Furthermore, the estimated vortex line is extended into a three dimensional domain using a duplicated angle of the visualization made by the simulation domain. The comparison with the visualization from the downstream confirms the successfully mapped vortex location in the three dimensional domain. This vortex line is used for the validation of the simulation results, of which details are presented in Section 7.2.

4 Investigation of inter-blade vortex by on-board pressure measurement

4.1 Introduction

In the previous chapter, the development of inter-blade cavitation vortices is characterized by the flow visualizations from upstream and downstream sides of the runner, revealing the notable influence of the speed factor n_{ED} on the development of inter-blade vortices. The present chapter attempts to further investigate the characteristics of an inter-blade vortex and its influence on the pressure field in the blade channel using on-board pressure measurements on the runner blade. In the framework of the HYPERBOLE research project, an instrumented runner equipped with pressure sensors and strain gauges on runner blades is prepared to study an impact of flow instabilities on the pressure field through the blade channel as well as the mechanical behavior of the runner. For the acquisition system, a wireless transmission assembly called telemetry measurement system is adopted, which is mounted on a specially instrumented runner shaft.

The on-board pressure measurements on the blade of a Francis turbine under deep part load operations have been performed and reported previously by Farhat *et al.* [22] and Lowys *et al.* [47]. These measurements were performed over a broad range of the discharge values in order to characterize cavitation and flow behaviors under off-design operations. They reported that pressure fluctuations are observed at deep part load operations. However, the specific source of the pressure oscillations is not clearly identified. The influence of the cavitation vortex rope at part load condition on the pressure field as well as the stress fluctuations inside the runner using the presented on-board instrumentation has been successfully conducted and reported by several authors [18, 23].

For the purpose of revealing the impact of the inter-blade vortex on the pressure field on the blade, on-board pressure measurements are systematically applied by changing the operating parameters of the runner, especially the discharge factor Q_{ED} and the speed factor n_{ED}. The influence of inter-blade cavitation vortices as well as their dependency on the operating parameters are then characterized in the frequency domain as well as by studying amplitude evaluations. Furthermore, the mean pressure distribution on the blade wall is inspected with respect to the different operating parameters, and the flow structure inside the blade channel related to inter-blade vortex development is estimated base on the wall pressure difference between pressure and suction sides of the blade.

4.2 Experimental setup for on-board measurement

4.2.1 Instrumented runner

For the on-board pressure measurements on the runner blade, an instrumented runner is prepared. The instrumented runner is a mono-block runner equipped with 4 pressure sensors on a single blade, and the runner features the exact same geometry as the original runner (see Figure 4.1a). For the installation of the pressure sensors, two locations on one blade are selected, and two pressure sensors are installed at each location on both the suction side and the pressure side of the blade. The selected locations of the pressure sensors are close to the trailing edge of the blade to accurately characterize the effect of the inter-blade cavitation vortex. The sensor locations are summarized in Table 4.1. Bridge-based piezometric pressure transducers with a range of 1 MPa are adopted. The pressure transducers are then connected to the transmission system by wires installed through grooves sealed by a special putty.

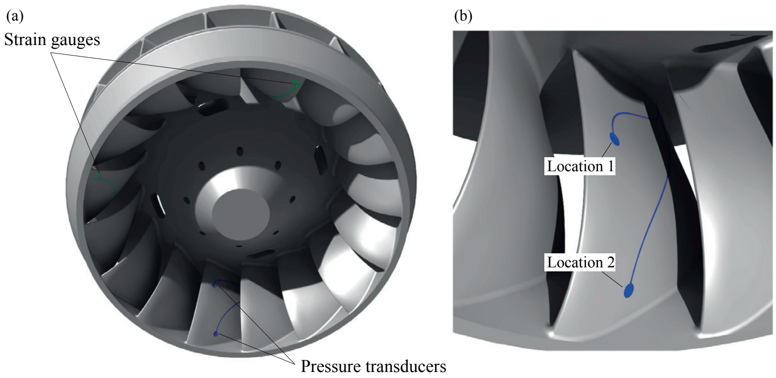

Figure 4.1 – Schematics of the instrumented runner (a) and the locations of the installed pressure transducers on the runner blade (b)

Table 4.1 – Summary of the normalized span-wise and streamwise locations of the pressure sensors installed on the runner blade

Sensor name	Span-wise location s^*	Streamwise location m^*	Blade side
# 1 *Suc*	0.62 (-)	0.92 (-)	Suction
# 1 *Prs*	0.62 (-)	0.92 (-)	Pressure
# 2 *Suc*	0.12 (-)	0.90 (-)	Suction
# 2 *Prs*	0.12 (-)	0.90 (-)	Pressure

4.2.2 Telemetry acquisition system

For the acquisition of on-board pressure measurements on the runner blade, the measured data need to be transmitted accurately from the rotating frame to the stationary frame without a time delay. The most common tool for data acquisition on a rotating frame is a slip ring, which allows the transmission of signals through an electrical connection between the rotating and stationary assemblies using metal rings and brushes. However, it is not sufficiently suitable for harsh operating conditions and long-term use due to fatigues at the contact of the rotating component with the stationary part, which may adversely affect substantial and reliable measurements. Hence, for this series of on-board pressure measurements, a wireless transmission unit for electrical signals is installed on the instrumented shaft as shown in Figure 4.2. The signal from the sensor is first amplified and then transmitted from the rotating frame to the stationary frame through the rotor and stator antennas. These antennas transfer the electrical signals as well as power through an electromagnetic field induced by the coil wirelessly, providing more robust and reliable data acquisition.

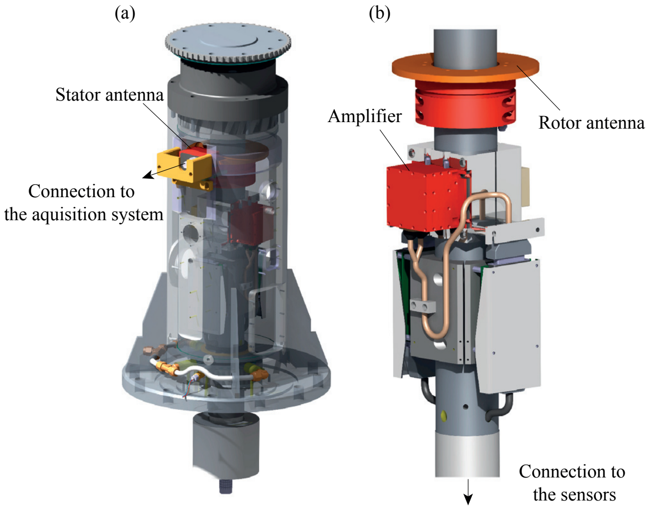

Figure 4.2 – Instrumented shaft used for on-board pressure measurements (a) and the wireless transmission system installed inside the shaft (b)

4.2.3 Operating conditions for on-board pressure measurement

First of all, the raw pressure signals acquired from all the pressure sensors on the runner blade at the operating conditions OP#1, #2, and #3 are compared to check the impact of the inter-blade cavitation vortex. Then, its influence on the pressure field is investigated in detail, by varying operating parameters such as Q_{ED}, n_{ED}, and the cavitation number σ. The operating parameters for the points where the on-board pressure measurements are conducted are summarized in Table 4.2. Pressure measurements are performed with a sampling frequency of $1'000$ Hz and total measurement time of 120 s.

Table 4.2 – Operating conditions of the on-board pressure measurements on the runner blade

Q_{ED} (-)	n_{ED} (-)	GVO (°)	E (J kg^{-1})	n (Hz)	σ (-)
Q_{ED} influence					
0.005 - 0.200	0.317	0.5 - 20	263	14.67	σ_{plant} and σ_{atm}
0.005 - 0.200	0.288	0.5 - 20	263	13.33	σ_{plant} and σ_{atm}
0.005 - 0.200	0.268	0.5 - 20	263	12.40	σ_{plant} and σ_{atm}
n_{ED} influence					
0.051 - 0.056	0.245 - 0.360	5	263	-	0.11
σ influence					
0.052	0.317	5 (OP#1)	263	14.67	0.07 - σ_{atm}
0.054	0.288	5 (OP#2)	263	13.33	0.07 - σ_{atm}

4.3 Pressure measurement results

4.3.1 Comparison of the raw pressure signals measured on the blade

The time history of the centered non-dimensional pressure signals measured at the four pressure sensors on the blade at operating conditions OP#1, #2, and #3 are shown in Figure 4.3. The cavitation number σ is set to be the prototype value σ_{plant}. Raw and filtered signals by means of a moving average method are simultaneously shown in Figure 4.3. By comparing the measured pressure signals at each location, it appears that the pressure fluctuation on the pressure side of the blade is relatively small, although the amplitude location #2 is slightly higher, and there is no significant difference in the presented conditions. On the suction side, the amplitude of the pressure fluctuation is also approximately equal at location #1 for the different n_{ED} conditions. However, at location #2, negative pressure peaks appear in the signal at OP#1, whereas these pressure peaks are not observed at OP#2 and OP#3. As confirmed in Figure 3.9, the pressure sensor located at #2 Suc is close to the region where the inter-blade cavitation vortex is developed. Thus, it is assumed that this pressure oscillation is caused by the presence of the inter-blade cavitation vortex. Furthermore, the observed pressure appears to be stochastically oscillated due to the stochastic nature of the inter-blade vortex.

4.3.2 Frequency analysis

In Figure 4.4, the frequency analysis results of the measured signal at location #2 Suc over the non-dimensional frequency is presented. The analyzed pressure signal corresponds to the signal shown in Figure 4.3d. Even though several peaks appear in the low frequency range, a

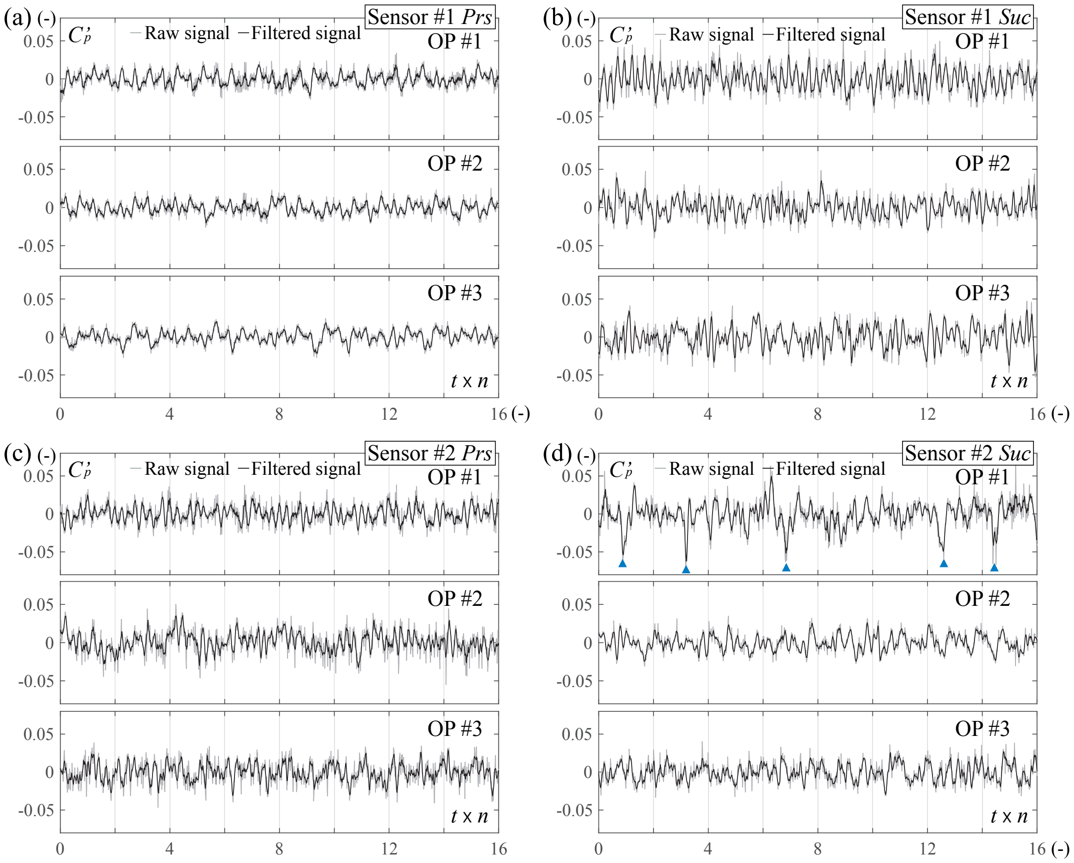

Figure 4.3 – Comparison of the measured pressure signals over 16 runner revolutions at #1 Prs (a), #1 Suc (b), #2 Prs (c), and #2 Suc (d) for OP#1, #2 and #3 at $\sigma = \sigma_{plant}$

dominant peak in the high frequency range is only confirmed at the blade passage frequency from the rotating domain corresponding to the number of the guide vanes ($20 \times n$) at OP#1. In the low frequency range (see Figure 4.4b), several peaks appear at an almost constant interval of the frequency, especially at OP#1 and OP#2.

Based on the pressure measurement results in the draft tube presented in Section 2.3, it is confirmed that multiple vortex structures may develop in the draft tube cone at deep part load condition. Thus, the dominant peaks shown in Figure 4.4 are expected to be caused by the precession of these multiple vortex ropes developing in the draft tube. Taking into account the rotating frequency of the runner n, the frequency of the vortex precession in the stationary domain is transformed to $f' = f - n$ in the rotating domain. Therefore, the estimated oscillation frequencies caused by multiple vortex structures expressed in Equation 2.1 are then written in the rotating frame as follows:

$$f'_{ke} = k \times (n - f_{rope}) \quad k \in \mathbf{N} \tag{4.1}$$

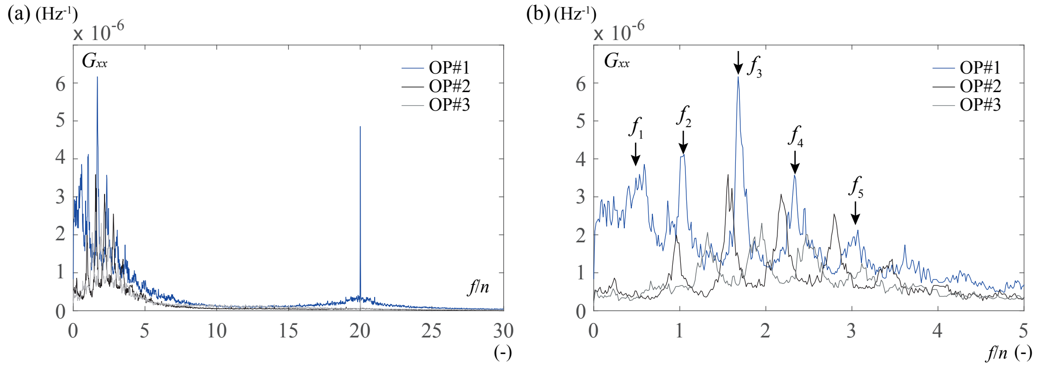

Figure 4.4 – Comparison of the frequency spectrum of the pressure signals measured at #2 Suc over a wide range of frequencies (a) and in the low frequency range (b) for OP#1, #2 and #3 at $\sigma = \sigma_{plant}$

According to the frequency analysis at the section #1 in the draft tube cone, the confirmed frequencies of the vortex precession at OP#1 are mainly $f_2 = 0.95 \times n$, $f_3 = 1.32 \times n$, and $f_4 = 1.73 \times n$. The estimated frequencies in the rotating domain f'_{ke} calculated by Equation 4.1 are summarized in Table 4.3. By comparison with measured frequencies f'_k, the estimated frequencies are in good agreement with the measured frequencies, which confirms that the observed frequency peaks at #2 Suc result from the oscillations caused by multiple vortex ropes developing in the draft tube cone. These frequencies from multiple vortex ropes are particularly observed at location #2 Suc since vortex structures at the presented operating condition are assumed to develop considerably close to the draft tube wall, due to the development of a large backflow region at the center of the draft tube.

Even though the spectral peaks resulting from the precession of the vortex rope in the draft tube cone are observed at #2 Suc, the frequency peaks caused by the inter-blade cavitation vortex are not distinctly identified in the frequency analysis. However, by comparison of the frequency analyses at OP#1 and OP#2, the amplitude of the wide-band noise in the low frequency range is clearly magnified at OP#1 (see Figure 4.4b). It is assumed that the elevation of the wide-band noise amplitude in the low frequency range is caused by the stochastic pressure oscillation induced by the presence of the inter-blade vortex (see Figure 4.3d).

Influence of the non-dimensional discharge factor Q_{ED}

In Figure 4.5, the influence of varied Q_{ED} on the spectral peaks of the pressure signals measured at #2 Suc for OP#1, #2, and #3 is presented. For the spectral peaks within the low frequency range, the linear estimation of the multiple vortex rope precession frequencies $f'_k e$ is presented for $k = 1:5$ (see dashed blue line in Figure 4.5b). In the high frequency range presented in Figure 4.5a, no dominant peaks are observed except for the blade passing frequency (20 ×n). In the low frequency range (see Figure 4.5b), the dominant frequency peak,

Table 4.3 – Detected frequencies f_k of the pressure oscillations caused by the multiple vortex ropes measured at C1N, estimated frequencies f'_{ke} from Equation 4.1 and the measured frequency f'_k on the blade at location #2 *Suc* from $k = 1$ (f_{rope}) to 5

k	f_k	f'_{ke}	f'_k
1 (f_{rope})	$0.45 \times n$ (Hz)	$0.55 \times n$ (Hz)	$0.51 \times n$ (Hz)
2	$0.95 \times n$ (Hz)	$1.05 \times n$ (Hz)	$1.02 \times n$ (Hz)
3	$1.33 \times n$ (Hz)	$1.67 \times n$ (Hz)	$1.69 \times n$ (Hz)
4	$1.73 \times n$ (Hz)	$2.27 \times n$ (Hz)	$2.35 \times n$ (Hz)
5	$2.25 \times n$ (Hz)	$2.75 \times n$ (Hz)	$3.01 \times n$ (Hz)

with a remarkably high amplitude, is caused by the precession of the cavitation vortex rope and is observed around $Q_{ED} = 0.100$ [23]. For discharge values lower than $Q_{ED} = 0.080$ (40 % of Q_{BEP}), multiple frequencies, such as f'_2, f'_3, and f'_4, start to appear especially at rated n_{ED} ($n_{ED} = 0.288$). This is also observed in the frequency analysis of pressure signals measured

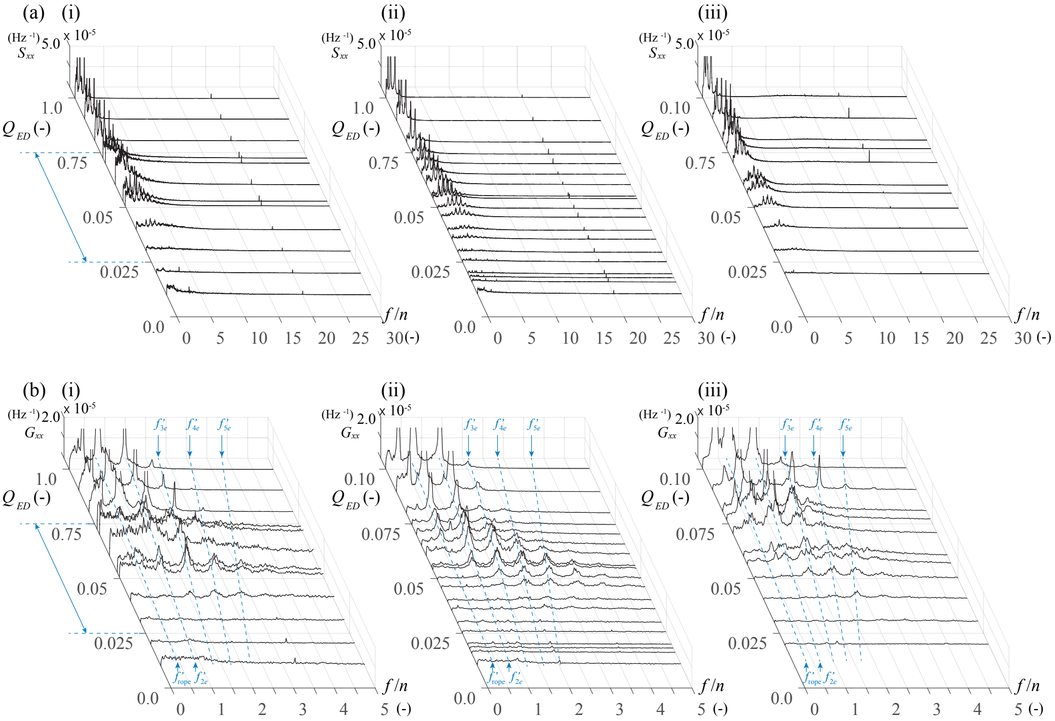

Figure 4.5 – Influence of Q_{ED} at deep part load condition on the spectral peaks of the pressure fluctuations measured at location #2 *Suc* for the different n_{ED} conditions $n_{ED} = 0.317$ (i), 0.288 (ii), and 0.268 (iii) over a wide range of the frequencies (a) and in the low frequency range (b) at $\sigma = \sigma_{plant}$. The blue arrow in (i) indicates the discharge range of the inter-blade cavitation vortex development.

at the draft tube cone (see Section 2.3.1). The frequencies f'_k decrease almost linearly with respect to the decrease of discharge as confirmed by the straight estimation line, and the same evolution of frequencies is observed for all n_{ED} conditions. By comparing the different n_{ED} conditions, the amplitude of the wide-band noise observed in the low frequency range at $n_{ED} = 0.317$ becomes magnified within the discharge range where inter-blade vortices develop (see blue arrows in Figure 4.5b (i)), which results from the stochastic pressure oscillations caused by the inter-blade vortex. However, all the detected spectral peaks are related to the vortex precession frequency, suggesting that the inter-blade vortex induces only stochastic pressure oscillations.

Influence of the non-dimensional speed factor n_{ED}

To identify the influence of the speed factor n_{ED} on pressure fluctuations induced by the inter-blade cavitation vortex, the value of n_{ED} is changed from 0.245 to 0.360 at the constant guide vane opening of $GVO = 5\,°$ including OP#1, #2, and #3. The cavitation number σ is kept constant at $\sigma = 0.11$. First of all, the appearance of inter-blade cavitation vortices at different n_{ED} conditions visualized from downstream of the runner is presented in Figure 4.6. Although the shape of the inter-blade cavitation vortices is not significantly changed even at high n_{ED} conditions, it seems that the cavitation volume is increased and the location of inter-blade vortex development is slightly shifted to the runner outlet when the n_{ED} value is increased. At lower n_{ED} conditions, such as $n_{ED} = 0.245$, inter-blade cavitation vortices are completely diminished, and instead the structure of the cavitation vortex rope appears again near the runner crown as shown in Figure 4.6f.

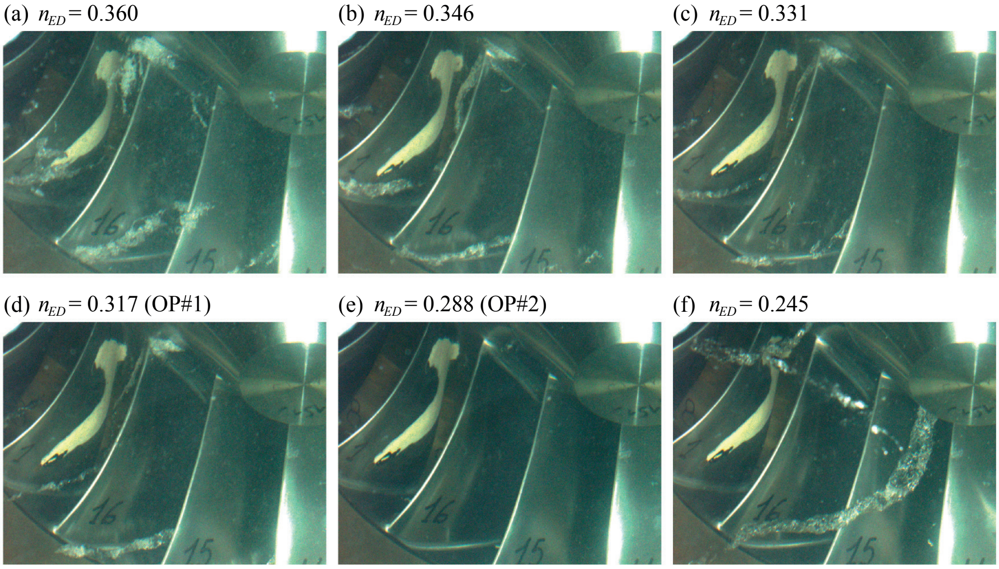

Figure 4.6 – Appearance of inter-blade cavitation vortices for different n_{ED} conditions at constant guide vane opening $GVO = 5\,°$ and $\sigma = 0.11$

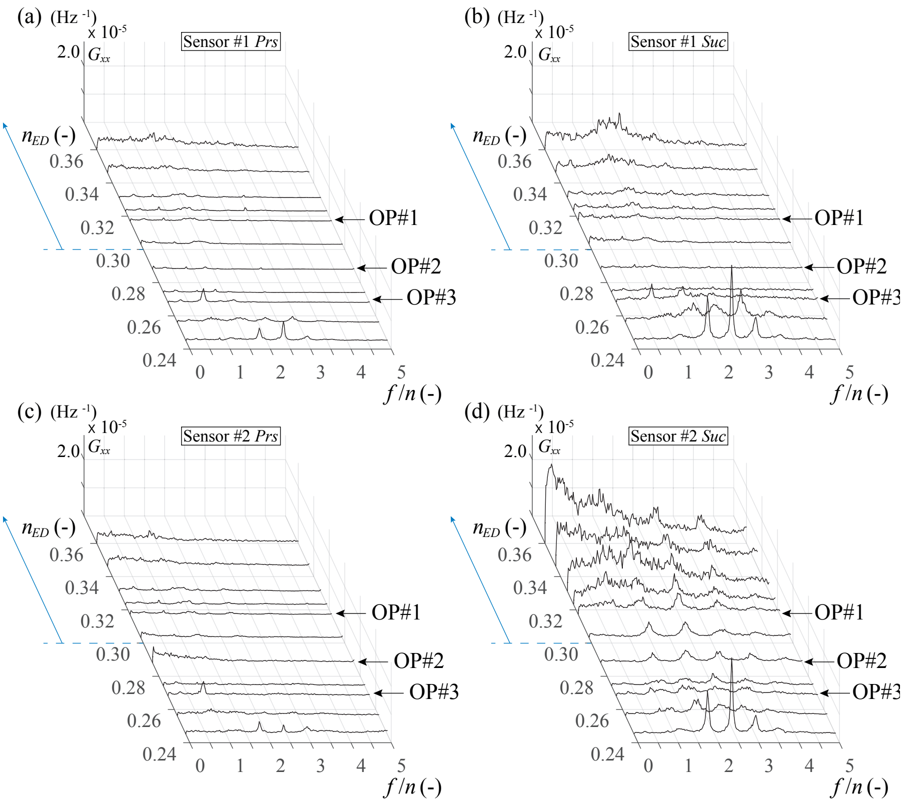

Figure 4.7 – Influence of n_{ED} on the spectral peaks of the pressure fluctuations measured at all sensors on the runner blade #1 Prs (a), #1 Suc (b), #2 Prs (c), and #2 Suc (d) at constant guide vane opening $GVO = 5\,°$ and $\sigma = 0.11$. The blue arrow indicates the range of inter-blade cavitation vortex development.

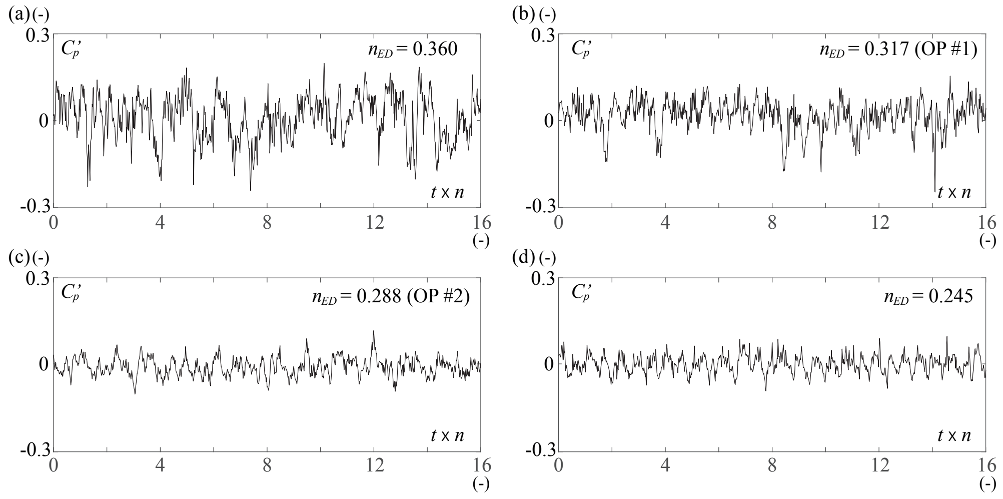

Figure 4.8 – Comparison of fluctuating pressure signals measured at #2 Suc for the different n_{ED} conditions, $n_{ED} = 0.360$ (a), 0.317 (OP#1) (b), 0.288 (OP#2) (c), and 0.245 (d) at $\sigma = 0.11$

In Figure 4.7, the influence of varied n_{ED} on the spectral peaks of pressure measured from the pressure sensors on the runner blade at $\sigma = 0.11$ is presented. At lower n_{ED} conditions, such as $n_{ED} = 0.245$, since the multiple cavitation vortex ropes are developed as shown in Figure 4.6f, several distinct peaks related to the vortex precession are confirmed, especially on the suction side of the blade. When n_{ED} is increased, the peaks of the vortex rope precession becomes less significant, and it only appears in #2 Suc since the location of the vortex is gradually shifted close to the wall according to the increase of the circumferential velocity in the draft tube cone. On the pressure side of the blade, it appears that the frequency peaks are less obvious than on the suction side, and there is no remarkable difference between the two locations of the sensors on the blade.

Over the limit of inter-blade vortex development (see blue arrow in Figure 4.7), the influence on the pressure side is not clearly confirmed. However, the wide-band noise in the low frequency range starts to appear especially at #2 Suc as shown in Figure 4.7d, which is caused by the stochastic pressure oscillation induced by the inter-blade vortex. The amplitude of the wide-band noise in the low frequency range at #2 Suc is significantly amplified as n_{ED} increases, and the slight amplification of the wide-band noise amplitude is also confirmed at #1 Suc at the highest n_{ED} condition $n_{ED} = 0.360$. Based on the visualization presented in Figure 4.6, the structure of the inter-blade cavitation vortex becomes more obvious with respect to the increase of n_{ED}, hence, it is assumed that the stochastic oscillation caused by the inter-blade vortex is intensified accordingly. It is also considered that the slight shift of the vortex location to the blade channel outlet with respect to the increase of n_{ED} may also cause the amplification of the wide-band noise at #1 Suc.

In Figure 4.8, the raw fluctuating pressure signals acquired at #2 Suc for $n_{ED} = 0.360$, 0.317 (OP#1), 0.288 (OP#2), and 0.245 at $\sigma = 0.11$ are presented. As confirmed in Figure 4.6, remarkable stochastic pressure oscillations are observed at the highest n_{ED} condition and OP#1. This stochastic pressure oscillations are gradually reduced when n_{ED} is decreased. In contrast, the periodic pressure oscillation caused by the precession of the cavitation vortex rope (see Figure 4.6f) becomes more obvious in the pressure signal at the lowest n_{ED} condition, $n_{ED} = 0.245$.

Influence of the cavitation number σ

In Figure 4.9, the influence of the cavitation number σ on the frequency analysis results at #2 Suc is presented. The value of σ is changed from the lowest value $\sigma = 0.07$ to the value corresponding to atmospheric pressure condition σ_{atm}. It is confirmed that the frequency of the vortex precession and its amplitude shown in Figure 4.9 are kept almost constant over the varied σ, including at atmospheric pressure condition. Therefore the influence of σ at both conditions OP#1 and #2 is assumed to be relatively minor. Moreover, the amplitude of the wide-band noise in the low frequency range caused by the stochastic pressure oscillation induced by the inter-blade cavitation vortex at OP#1 is regularly higher than OP#2 for all σ conditions. Furthermore, its amplitude is not drastically changed with respect to the variation of σ. This may allow the conclusion that the stochastic pressure oscillation induced by the

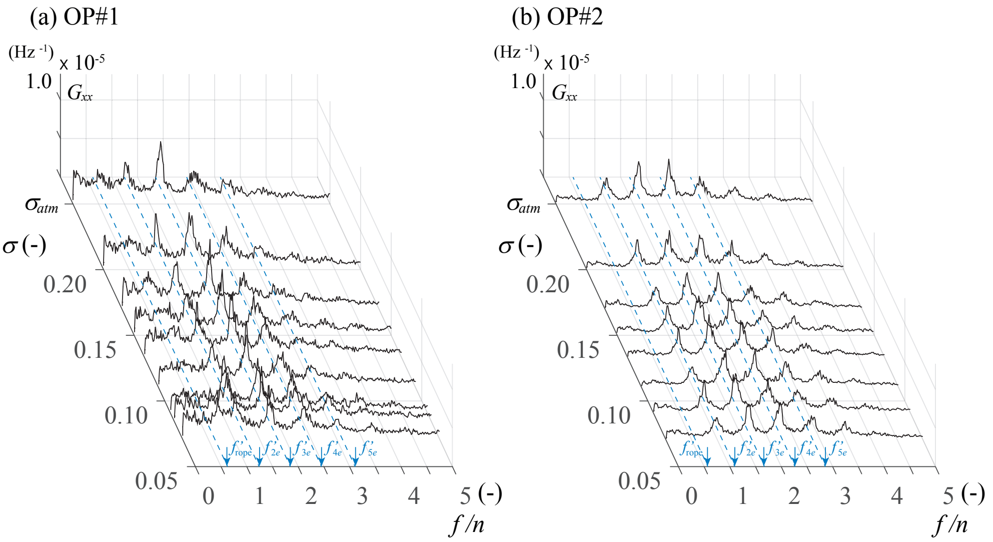

Figure 4.9 – Influence of the cavitation number σ on the spectral peaks of the pressure fluctuations measured at #2 Suc at OP#1 (a) and OP#2 (b). The value of σ is changed from the lowest value $\sigma = 0.07$ to the value corresponding to atmospheric pressure condition σ_{atm}

inter-blade vortex is not severely affected by variations of σ, and the significant amplification of the pressure fluctuation, such as a resonance phenomenon often observed at part load operation, is not observed at the investigated deep part load operating condition.

4.3.3 Evaluation of the pressure amplitude

As shown in the frequency analysis results in Section 4.3.2, the influence of the inter-blade cavitation vortex is not distinctly observed in the frequency domain, even though it appears as a wide-band noise in the low frequency range caused by the stochastic pressure oscillation from the inter-blade vortex. Hence, this section intends to evaluate the amplitude of the pressure fluctuations caused by the inter-blade vortex more precisely by introducing the peak-to-peak value and the standard deviation of the measured pressure signals on the blade. The peak-to-peak value $|C_p|_{P-P}$ is calculated as the difference between the maximum and minimum values of each pressure signal, ignoring the highest/lowest 3 % of the total samples. The standard deviation $|C_p|_{STD}$ is calculated as:

$$|C_p|_{STD} = \frac{1}{\rho E}\sqrt{\frac{1}{N}\sum_{n=1}^{N}(p_n - \bar{p})^2} \tag{4.2}$$

where $\bar{p}$ represents the mean value of each pressure signal and p_n is the pressure value of each sample. Taking into account the stochasticity of the pressure oscillation, these amplitude

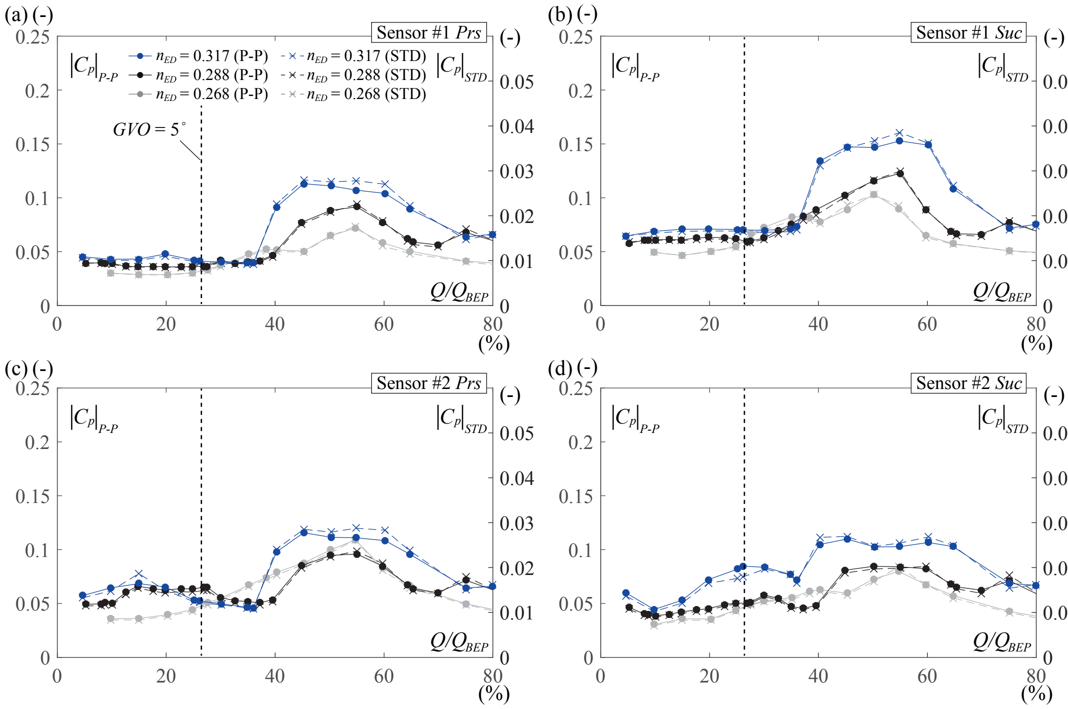

Figure 4.10 – Influence of Q_{ED} on the pressure amplitude measured at the pressure sensors on the blade, #1 Prs (a), #1 Suc (b), #2 Prs (c), #2 Suc (d) for three different n_{ED} conditions at $\sigma = \sigma_{plant}$

values are computed in several windows split from one measured pressure signal, and then the value is averaged. In the present case, a 5 second time window is selected for the calculation of both peak-to-peak values and standard deviations.

Influence of the non-dimensional discharge factor Q_{ED}

In Figure 4.10, the influence of varied Q_{ED} on both peak-to-peak values and standard deviations from all pressure sensors at the three different n_{ED} conditions at the prototype cavitation number σ_{plant} are presented. It is pointed out that the amplitude for all the sensors on the blade are remarkably high between 40 % and 60 % of Q_{BEP}, which is caused by the precession of the cavitation vortex rope in the draft tube. Below 40 % of Q_{BEP}, the amplitude values are kept low throughout the deep part load operations for the case of $n_{ED} = 0.288$ and 0.268. On the contrary, for $n_{ED} = 0.317$, both the peak-to-peak value and the standard deviation at #2 Suc is again increased at the discharge region where the inter-blade vortex develops (see Figure 4.10d), especially the peak-to-peak value, which reaches its maximum value at $GVO = 5\,°$ below 40 % of Q_{BEP}. It is assumed that this amplitude elevation is caused by the stochastic pressure oscillation induced by the inter-blade cavitation vortex. As shown in Figure 4.3, the influence of this stochastic pressure oscillation is most significant at #2 Suc and it is not distinctly observed at the other pressure transducers. Therefore the increase of the

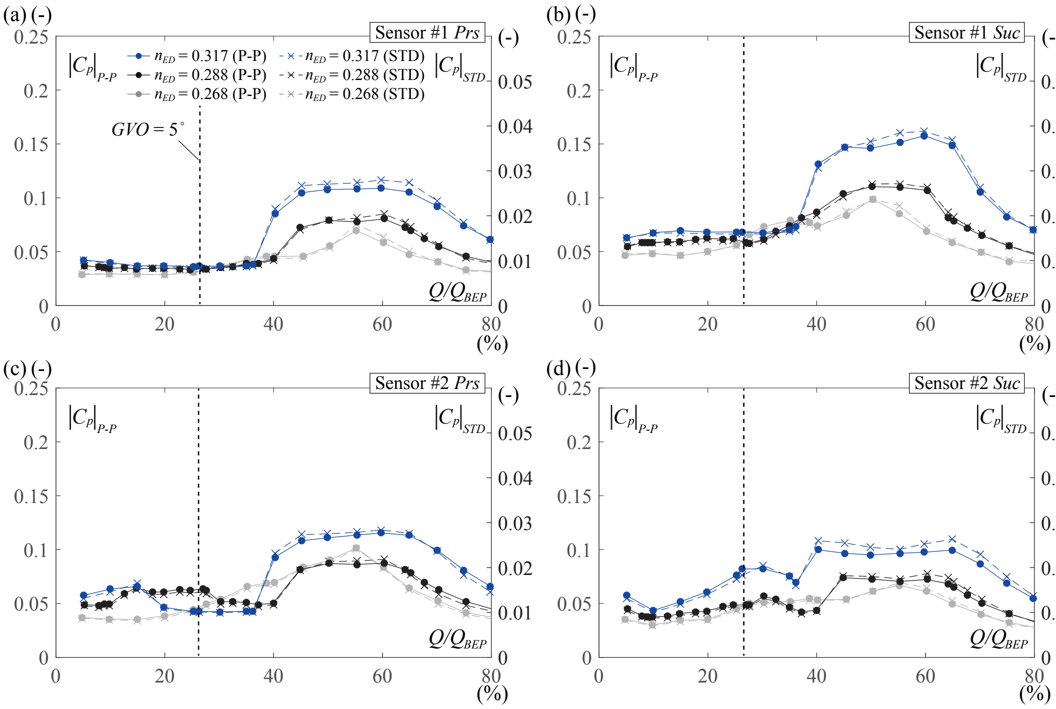

Figure 4.11 – Influence of Q_{ED} on the pressure amplitude measured at the pressure sensors on the blade, #1 Prs (a), #1 Suc (b), #2 Prs (c), #2 Suc (d) for three different n_{ED} conditions at atmospheric pressure condition σ_{atm}

pressure amplitude at $GVO = 5\,°$ is only confirmed at #2 Suc. It is considered that the impact of the inter-blade cavitation vortex on the pressure is relatively local. Nonetheless, it evidently confirms that the presence of the inter-blade cavitation vortex induces an amplification of the pressure fluctuation especially on the suction side, which adversely affects stabilized operations of the machine as well as the fatigue life of the runner blade.

In Figure 4.11, the influence of varied Q_{ED} on the pressure amplitude at atmospheric pressure condition σ_{atm} is presented. As confirmed by comparison with Figure 4.10, both the peak-to-peak amplitude and the standard deviation have almost the same values as at σ_{plant} condition. This confirms that the influence of the cavitation number is relatively minor, which has been also shown by the frequency analysis result with varied σ (see Section 4.3.2). The influence of the inter-blade vortex at location #2 Suc is also confirmed by increase of the amplitude at $GVO = 5\,°$ for OP#1.

Influence of the non-dimensional speed factor n_{ED}

As shown in Section 4.3.2, the speed factor n_{ED} is found to play a significant role on the development of the inter-blade vortex as well as the induced pressure oscillations inside the blade channel. The influence of varied n_{ED} on the amplitude of the pressure oscillation at

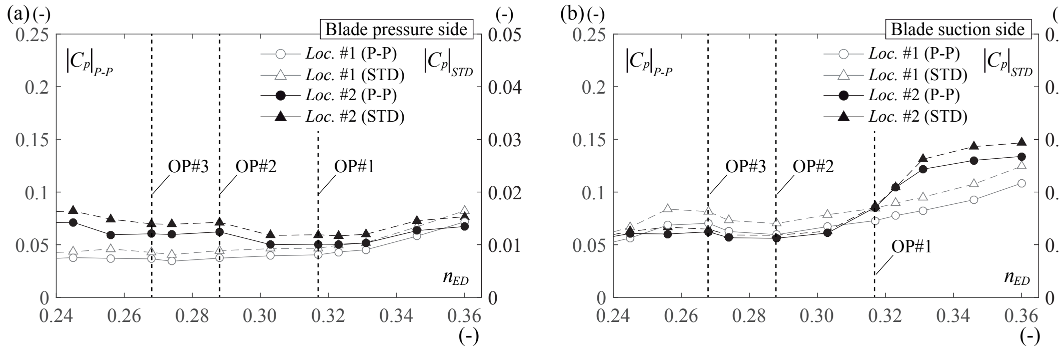

Figure 4.12 – Influence of n_{ED} on the amplitude of the pressure measured on the pressure side of the blade (a) and the suction side of the blade (b) at both the locations #1 and #2 at $GVO = 5\,°$ and $\sigma = 0.11$

the constant guide vane opening of $GVO = 5\,°$ is presented in Figure 4.12. It is shown that the amplitude on the pressure side is not largely affected by the variation of n_{ED} and is kept approximately constant. At the highest n_{ED} condition, the amplitude is slightly increased since the location of inter-blade cavitation vortex development is shifted close to the exit (see Figure 4.6). In contrast, both the peak-to-peak amplitude and the standard deviation on the blade suction side are significantly amplified especially at location #2, which has been also confirmed in the frequency analysis result (see Figure 4.7). The increase of the amplitude starts from $n_{ED} = 0.300$ which almost corresponds to the visual limit of inter-blade cavitation vortex development at $GVO = 5\,°$ (see Appendix A). At the highest n_{ED} condition, both the amplitude values at #2 Suc are roughly 2 to 2.5 times higher than the values at the low n_{ED} condition, and the amplitude at #1 Suc is also slightly amplified. This suggests that the strength of the inter-blade vortex as well as the induced stochastic pressure oscillation are intensified as n_{ED} increases, which results in the enhanced unsteadiness of the flow inside the blade channel.

Influence of the cavitation number σ

The frequency analysis with respect to the varied cavitation number σ in Section 4.3.2 reveals that the influence of σ on pressure oscillations induced by inter-blade cavitation vortices is relatively minor. In the same way, the impact of σ on the amplitudes of the pressure oscillations for the two operating conditions OP#1 and OP#2 is investigated. The influence of varied σ on both peak-to-peak amplitudes and standard deviations at #1 and #2 is presented in Figure 4.13. It demonstrates that even though the amplitude values are slightly magnified at the lowest σ condition, the values are kept approximately constant, including at atmospheric pressure condition σ_{atm}. Moreover, the amplitudes at OP#1 are regularly higher, especially at #2 Suc, due to the development of the inter-blade vortices. However, its difference is not significantly changed with respect to σ. Consequently, it can be concluded that the cavitation number σ does not have a notable influence on the amplitude of the pressure oscillation caused by the

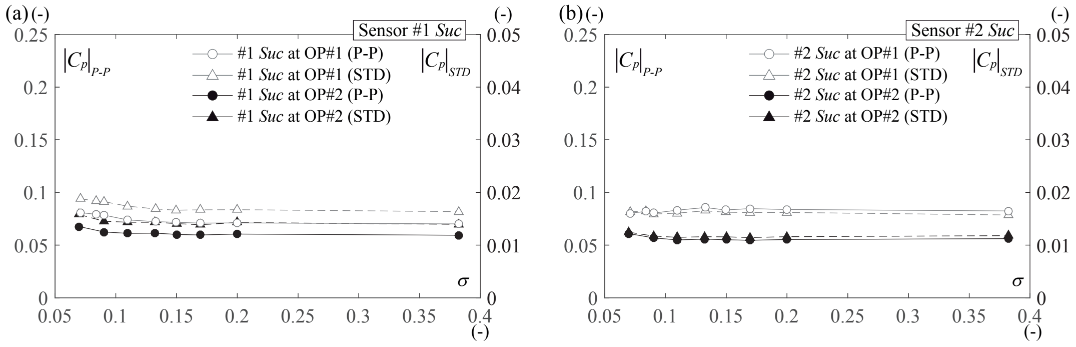

Figure 4.13 – Influence of σ on the pressure amplitude measured at location #1 (a) and location #2 (b) on the suction side of the blade at a constant guide vane opening $GVO = 5$ °

inter-blade cavitation vortex, suggesting that the flow structure and the unsteadiness of the flow inside the blade channel are not greatly affected by different σ conditions.

4.3.4 Pressure difference on the blade

As mentioned above, the speed factor n_{ED} is of key importance for the development of inter-blade vortices. In this section, the pressure distribution on the runner blade is examined at different n_{ED} conditions. It is then intended to evaluate the characteristics of the flow structure inside the blade channel. The influence of Q_{ED} on the mean pressure factor C_p with the reference pressure $p_{ref} = 0$ Pa on the blade wall at locations #1 and #2 for different n_{ED} conditions is presented in Figure 4.14. At location #1, the pressure on the blade pressure side is almost linearly decreased with respect to the decrease of discharge, whereas the pressure on the blade suction side is increased. At part load condition between 40 % and 70 % of Q_{BEP}, the pressure on the blade suction side is kept constant. However, the pressure on the blade pressure side continues to decrease. At deep part load conditions, the pressure on the blade suction side starts to increase again, while the decrease of the pressure on the blade pressure side is slightly accelerated. As a consequence, the pressure on the blade pressure side finally becomes lower than the pressure on the suction side, which causes a negative blade loading. At location #2, the evolution of the pressure on the blade suction side is similar to that of location #1, and the pressure does not change significantly for the three different n_{ED} conditions. In contrast, the pressure on the blade pressure side is different according to the different n_{ED} conditions, especially at deep part load conditions. Moreover, the pressure on the pressure side is higher than the pressure on the suction side for all of the discharge conditions.

In Figure 4.15, the wall pressure difference on the blade $\Delta C_p = \Delta\bar{p}/\rho E$ between the pressure side and the suction side of the blade at atmospheric pressure condition as well as at σ_{plant} is presented. The pressure difference ΔC_p for both the locations at the BEP are approximately equal, suggesting that the wall pressure difference is equally distributed near the blade channel

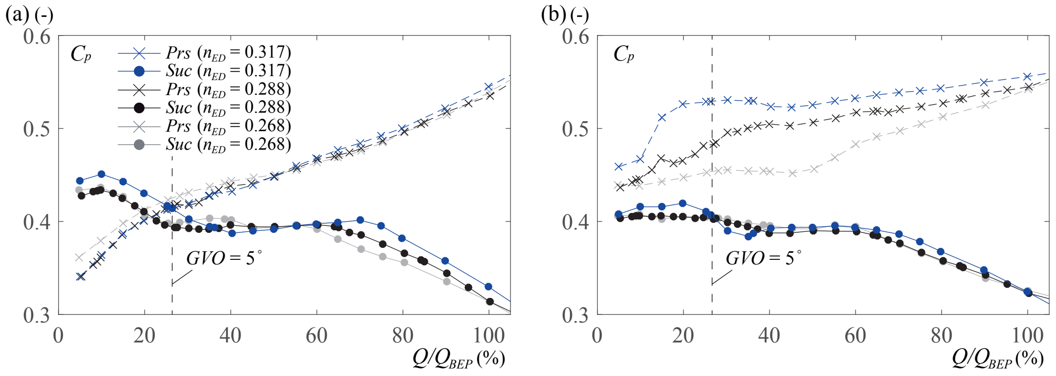

Figure 4.14 – Influence of Q_{ED} on the mean pressure factor C_p on the blade wall at location #1 (a) and location #2 (b) at atmospheric pressure condition σ_{atm}

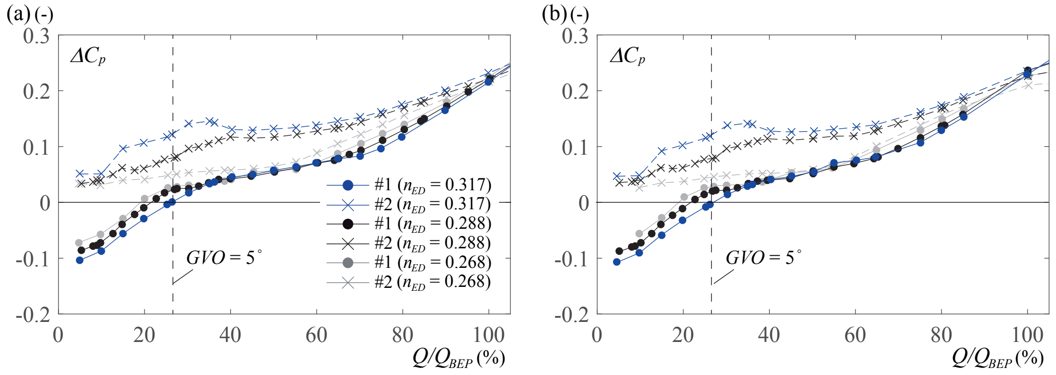

Figure 4.15 – Influence of Q_{ED} on the non-dimensional pressure difference ΔC_p between pressure and suction sides of the blade at atmospheric pressure condition σ_{atm} (a) and $\sigma = \sigma_{plant}$ (b)

outlet at the BEP. This evidently demonstrates that the flow is uniformly distributed at Q_{BEP}, resulting in an equally allocated blade loading near the blade trailing edge. ΔC_p is then gradually reduced with respect to the decrease of discharge, and the decrease of ΔC_p at location #1 is more significant. This suggests that the flow near the blade channel outlet starts to be distributed non-uniformly, leading to low blade loading near the hub and high blade loading concentrated on the shroud side. The difference of ΔC_p between two locations #1 and #2 is highest at $n_{ED} = 0.317$, which implies that the non-uniform distribution of the flow is most significant at $n_{ED} = 0.317$. At 35 % of Q_{BEP}, the decrease of ΔC_p at location #1 is further accelerated and finally becomes negative as shown in Figure 4.15 at OP#1. This discharge region corresponds to the discharge range where inter-blade cavitation vortices develop. The significant difference of ΔC_p between two locations particularly seen at $n_{ED} = 0.317$ potentially shows that the flow distribution becomes strongly non-uniform between the hub and shroud sides inside the blade channel. Furthermore, the negative blade loading observed near the hub may indicate the development of a singular flow condition close to the hub such as the formation of a backflow region, which is assumed closely relevant to the development of the inter-blade vortex. The comparison of ΔC_p between σ_{plant} and the atmospheric condition confirms that there is no significant difference between the two conditions, which suggests that the σ value does not have major effect on the flow structure though the blade channel nor the development of the inter-blade vortex structure at deep part load conditions.

In Figure 4.16, the influence of varied n_{ED} on the mean pressure factor C_p at $GVO = 5\,°$ is presented. The cavitation number σ is kept constant at $\sigma = 0.11$. At low n_{ED} conditions, the pressure on the blade pressure side at location #1 is higher than the pressure on the blade suction side. However, the pressure on the pressure side is reduced while the pressure on the suction side is slightly increased as n_{ED} increases. Then, the pressure on the pressure side becomes lower than the suction side at $n_{ED} = 0.317$ corresponding to OP#1 as shown in Figure 4.17. On the contrary, the pressure on the blade pressure side at location #2 is increased and the pressure on the blade suction side is kept almost constant when n_{ED} is increased, which results in a constantly positive wall pressure difference at location #2.

In Figure 4.17, the wall pressure difference ΔC_p between the pressure and suction sides of the

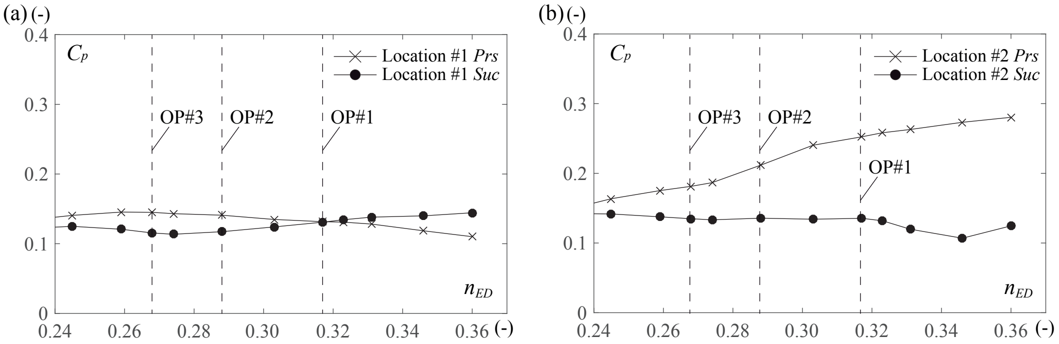

Figure 4.16 – Influence of n_{ED} on the mean pressure factor C_p on the blade wall at location #1 (a) and location #2 (b) at constant guide vane opening $GVO = 5\,°$ and $\sigma = 0.11$

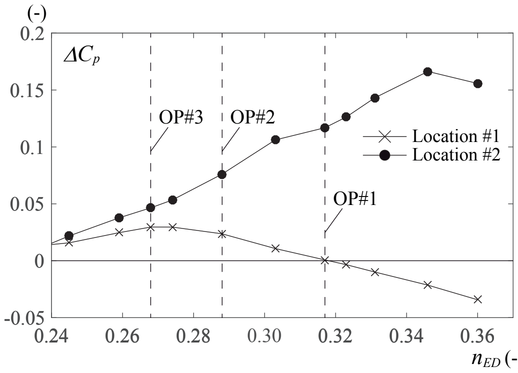

Figure 4.17 – Influence of n_{ED} on the non-dimensional pressure difference ΔC_p between pressure and suction sides of the blade at constant guide vane opening $GVO = 5\,°$ and $\sigma = 0.11$

blade is presented. It demonstrates that ΔC_p at location #2 reaches its maximum at OP#3, and it starts decreasing as the n_{ED} value is increased. The value becomes negative at OP#1 producing a negative blade load near the hub, and continues to decrease almost linearly as n_{ED} increases. In contrast, ΔC_p at location #1 gradually increases with respect to the increase of n_{ED}, resulting in the enlarged discrepancy between the two locations #1 and #2. This suggests that the flow near the hub does not contribute to the energy transfer due to the development of singular flow conditions, whereas the main flow producing a positive blade loading is concentrated near the shroud side. Furthermore, this non-uniform flow distribution from the hub to the shroud is enhanced as n_{ED} increases.

4.4 Flow structure inside the blade channel

As shown in Section 4.3.4, the wall pressure difference between the blade pressure and suction sides indicates the significant difference between the two measurement locations at deep part load condition. In particular, ΔC_p close to the hub indicates a negative blade loading when discharge is decreased down into deep part load condition.

Inside the blade channel, generally a pressure gradient between the suction side and the pressure side of the blade is created due to the flow streamline curvature and the Coriolis force. Hence, the pressure on the pressure side of the blade becomes higher than the pressure on the suction side. However, the wall pressure difference on the blade may change depending on the characteristics of the flow inside the channel [29, 60]. For instance, the inverse pressure difference between the pressure side and the suction side is observed near the blade channel inlet for the case of pump-turbines in generating mode for particular flow conditions featuring a recirculating flow region near the blade channel inlet [37]. This suggests that the negative pressure difference observed at location #1 at deep part load condition may indicate the development of singular flow conditions, such as a backflow region formed by the separated flow. The formation of the backflow region close to the trailing edge near the hub is also detected by the numerical simulation performed in [93], revealing that this back flow region is of key importance for the development of the inter-blade vortex.

Furthermore, the discharge value for which the pressure difference becomes zero at location #1 is shifted to the higher discharge value when the n_{ED} value is increased as confirmed in Figures 4.15 and 4.17. It suggests that the inception of the backflow region occurs at higher discharge for higher n_{ED} conditions. As presented in Section 1.3.2, variation in n_{ED} modifies the flow incident angle at the runner inlet. At higher n_{ED} conditions, the flow features a higher negative incident angle at the blade channel inlet as shown in Figure 1.4, generating a complex flow structure inside the blade channel. It is assumed that the misaligned flow condition at the blade channel inlet causes the development of a backflow region near the hub close to the blade channel outlet as illustrated in Figure 4.18. The formation of this backflow region may be generated by a flow separation on the hub, which can be of key importance for the development of a strong inter-blade vortex. The detailed investigations about the flow

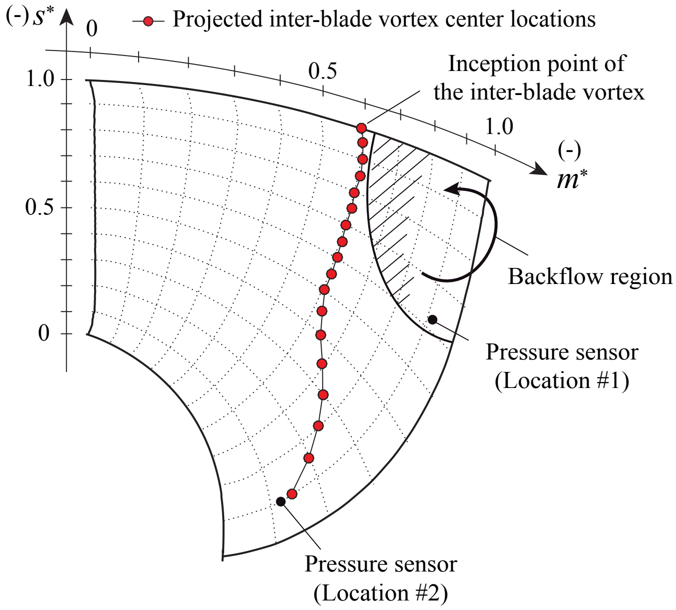
(-) s^*
0
0.5
1.0
0
0.5
1.0
(-) m^*
Projected inter-blade vortex center locations
Inception point of the inter-blade vortex
Backflow region
Pressure sensor (Location #1)
Pressure sensor (Location #2)

Figure 4.18 – Meridional view of the estimated flow structure in the blade channel and inter-blade vortex development at deep part load condition

structure inside the blade channel and the analyses of the flow separation on the hub are furthermore investigated by performing unsteady RANS simulations in Chapter 7.

4.5 Summary

To investigate the influence of the inter-blade vortex on the pressure field, on-board pressure measurements on the runner blade are conducted. By comparison of the raw pressure signals measured on the blade for OP#1, #2, and #3, it is confirmed that a stochastic pressure oscillation is induced by the presence of an inter-blade cavitation vortex especially on the suction side of the blade near the shroud. The impact of the inter-blade vortex and its dependency on operating parameters are furthermore examined with varied parameters such as Q_{ED}, n_{ED}, and σ, by means of frequency analyses and the amplitudes of the measured pressure signals.

The frequency analyses demonstrate that the spectral peaks observed in the frequency domain are mainly caused by the precession of multiple vortex ropes developing in the draft tube cone. Even though distinct frequency peaks related to the inter-blade cavitation vortex are hardly detected, the influence of the inter-blade vortex appears as a wide-band noise in the low frequency range due to the stochastic nature of its fluctuation. The intensity of the stochastic pressure oscillation induced by the inter-blade vortex is significantly affected by varied n_{ED} values. This suggests that the strength of the inter-blade vortex is intensified by the variation of the n_{ED} value, or in other words by change of the velocity triangle at the runner inlet. The amplitudes of the pressure fluctuations evaluated by peak-to-peak values and standard deviations reveal an increase of the pressure fluctuation amplitude in the range of discharge values for which inter-blade cavitation vortices develop. It is also confirmed that the amplitude of the pressure fluctuation is significantly affected by the n_{ED} value whereas it is kept almost constant with respect to varied σ. This shows that the n_{ED} value plays a decisive role on the development of the inter-blade vortex structure as well as the pressure oscillations induced by the inter-blade vortex.

In addition, the mean pressure on the blade wall as well as the wall pressure difference between the blade pressure and suction sides are investigated with respect to different operating parameters. The wall pressure difference on the blade indicates a decrease in blade loading when discharge is decreased from the BEP. Furthermore, a decrease in blade loading is more significant on the hub side than on the shroud side. This potentially shows that the flow starts to be distributed non-uniformly inside the blade channel as discharge decreases. The discrepancy of the pressure difference between the hub and the shroud is then further enhanced at deep part load operation, and the wall pressure difference near the hub becomes negative especially in the range of discharge where the inter-blade vortex develops. This negative blade loading suggests that the singular flow condition such as a backflow region may develop near the hub, which it is assumed is closely related to inter-blade vortex development. The detailed flow structure inside the blade channel at deep part load condition is further investigated in the following chapters by using numerical simulations.

5 Numerical setup

5.1 Introduction

In recent years, numerical flow simulations have been extensively used for various purpose from fundamental research of fluid dynamics to various engineering applications thanks to the notable progress of simulation softwares and hardware developments. On one hand, the appropriate use of the numerical flow simulation is quite powerful as it can provide various detailed data of the flow. On the other hand, one must know that the flow simulation faces inherent limitations depending on its computational method to solve the Navier-Stokes equations. In particular, the simulation of turbulent flows containing various scales of eddies requires massive computations to resolve the smallest scale eddies to large scale ones. This is achieved by direct numerical simulation (DNS) [56, 65]. However, the computational cost is typically too high for engineering applications.

Large Eddy Simulations (LES) is one of the computational ways to characterize turbulent flows, firstly proposed by Smagorinsky [77] to reduce the high computational cost of DNS, enabling studies for variable engineering applications. LES explicitly solves for large scale motions of the flow and eddies, whereas small scale eddies are filtered and modeled by subgrid-scale (SGS) modeling [27, 70]. The LES filtering is based on a computational grid size, hence, the simulation with finer mesh grids provides more physically accurate results. However, it still requires excessive amounts of computational power, even though a constant increase of computational resources in recent years makes the use of LES for industrial applications more and more feasible. For applications in hydraulic turbines, recently the rotating stall under part load conditions of a pump-turbine in pump mode was successfully simulated by LES [67].

The most popular computational methods for engineering applications are Reynolds Averaged Navier-Stokes (RANS) and unsteady RANS (URANS) simulations, which decompose pressure and velocity into mean and fluctuating quantities and applies the Reynolds averaging. In the RANS approach, all the turbulence regarding the fluctuating quantity is modeled by the so-called turbulence model [78]. Therefore, the computational cost is drastically reduced compared to DNS and LES, which allows the application of flow simulations to complicated geometries including pumps and turbines. However, the accuracy of simulated flow physics is strongly dependent on the adopted turbulence model. Hence, the model must be appropriately selected taking into account the advantages of each turbulence model. Recently, hybrid models between LES and RANS such as DES (Detached Eddy Simulation) and SRS (Scale Resolving Simulation) were proposed [19, 20, 55, 75] especially for a better estimation in unsteady flow regimes. These models were successfully applied to simulate flow instabilities observed in hydraulic machines [37, 49, 93, 87].

This chapter aims to introduce the governing equations for the performed unsteady RANS simulations in the present research as well as the fundamentals of the implemented models for the simulation. The adopted calculation domain and the specification of the computational grid are also presented. Finally, the computational convergence as well as the preliminary simulation results are discussed.

5.2 Governing equation

5.2.1 Conservation equations

Stationary frame

The dynamics of the flow are governed by the conservation of mass and momentum. By assuming incompressible flow, which is generally applicable for most of the cases in hydraulic machines, the conservation equations are expressed as follows.

$$\nabla \cdot \vec{C} = 0 \tag{5.1}$$

$$\frac{\partial \vec{C}}{\partial t} + (\vec{C} \cdot \nabla)\vec{C} = -\frac{1}{\rho}\nabla p + \nu \nabla^2 \vec{C} \tag{5.2}$$

where ρ is the density and ν the kinematic viscosity. For multiphase flows including cavitation flows, the concept of a homogeneous flow model is often adopted. In this model, it is assumed that the relative motion between phases can be neglected and the fluids in all of the phases share the same velocity and pressure to simplify the governing equations. Thus, the homogeneous model treats the multiphase flow as a single phase flow featuring average fluid properties. For a homogeneous flow including water and vapor, the mixture density ρ_m becomes a function of the liquid and vapor volume fractions, such as:

$$\rho_m = \rho_l \gamma_l + \rho_v \gamma_v = \rho_l (1 - \gamma_v) + \rho_v \gamma_v \tag{5.3}$$

where ρ_l represents the water density, γ_l the water volume fraction, ρ_v the vapor density, and

γ_v the vapor volume fraction. The mass and momentum conservations of a homogeneous mixture fluid is then rewritten from Equations 5.1, 5.2, and 5.3 by changing all of the quantities into mixture quantities as follows:

$$\frac{\partial C_i}{\partial x_i} = 0 \tag{5.4}$$

$$\frac{\partial C_i}{\partial t} + C_j \frac{\partial C_i}{\partial x_j} = -\frac{1}{\rho}\frac{\partial p}{\partial x_i} + \frac{1}{\rho}\frac{\partial \tau_{ij}}{\partial x_j} \tag{5.5}$$

The shear stress tensor τ_{ij} is expressed by the Newton Stokes model, such as

$$\tau_{ij} = 2\mu S_{ij} \tag{5.6}$$

where μ is the viscosity and S_{ij} is the rate-of-strain tensor, which is expressed by the symmetric part of the velocity gradient tensor:

$$S_{ij} = \frac{1}{2}\left(\frac{\partial C_i}{\partial x_j} + \frac{\partial C_j}{\partial x_i}\right) \tag{5.7}$$

Combining Equations 5.5 and 5.6, the momentum equation for the homogeneous fluid is then expressed as follows:

$$\frac{\partial C_i}{\partial t} + C_j \frac{\partial C_i}{\partial x_j} = -\frac{1}{\rho}\frac{\partial p}{\partial x_i} + 2\frac{\mu}{\rho}\frac{\partial S_{ij}}{\partial x_j} = -\frac{1}{\rho}\frac{\partial p}{\partial x_i} + 2\nu\frac{\partial S_{ij}}{\partial x_j} \tag{5.8}$$

Rotational frame of reference

When the concerned calculation domains include rotating machines, it is more convenient for simulations to use a reference frame rotating together with the machine. When this rotating coordinate is considered, the mass conservation and the Navier-Stokes equations are then expressed by the relative velocity $\vec{W}$ instead of the absolute velocity $\vec{C}$. Under constant rotating frequency of the machine, the Lagrangian derivative of the absolute velocity is expressed by the angular velocity vector $\vec{\omega}$ and the position vector $\vec{r}$, such as:

$$\rho\frac{D\vec{C}}{Dt} = \rho\frac{D\vec{W}}{Dt} + \rho\vec{\omega}\times(\vec{\omega}\times\vec{r}) + 2\rho\vec{\omega}\times\vec{W} \tag{5.9}$$

The additional terms appear in the right-hand side of the equation, which represent the contributions of the centrifugal force and the Coriolis force, respectively. The Navier-Stokes equations in the rotating frame of reference are then transformed by using the relative velocity:

$$\frac{\partial W_i}{\partial t}+W_j\frac{\partial W_i}{\partial x_j}=-\frac{1}{\rho}\frac{\partial p}{\partial x_i}+2\nu\frac{\partial S_{ij}}{\partial x_j}+f_r \tag{5.10}$$

Thus, the Navier-Stokes equations in the rotating frame are essentially same as the equation in the stationary frame except that the additional term f_r concerning the centrifugal force and the Coriolis force appears.

5.2.2 Reynolds Averaged Navier-Stokes Equations

By a Reynolds averaging approach which decomposes a quantity q into a mean part $\bar{q}$ and a fluctuating part q' such as $q=\bar{q}+q'$, the conservation equations in Equations 5.4 and 5.5 are then transformed into the following equations:

$$\frac{\partial \bar{C}_i}{\partial x_i}=0 \tag{5.11}$$

$$\frac{\partial \bar{C}_i}{\partial t}+\bar{C}_j\frac{\partial \bar{C}_i}{\partial x_j}=-\frac{1}{\rho}\frac{\partial \bar{p}}{\partial x_i}+2\bar{\nu}\frac{\partial \bar{S}_{ij}}{\partial x_j}+\frac{1}{\rho}\frac{\partial}{\partial x_j}(-\rho\overline{C_i'C_j'}) \tag{5.12}$$

Equation 5.12 is called the incompressible Reynolds Averaged Navier-Stokes (RANS) equations, and is extensively used for simulations for many industrial applications. However, the RANS equation generates the additional term $-\rho\overline{C_i'C_j'}$ from the non-linear term of the Navier-Stokes equations. The term $-\rho\overline{C_i'C_j'}$ is called Reynolds stress (or turbulent stress $\tau_t=-\rho\overline{C_i'C_j'}$). It causes a closure problem where the system is not directly closed by equations for the Reynolds stress because of the unknown correlations of velocity perturbations. Hence, the Reynolds stress needs to be modeled at a certain stage to close the equation system, which is called turbulence modeling.

5.2.3 Eddy viscosity turbulence model

To model the Reynolds stress, an eddy viscosity turbulence model is adopted for the present study. The model is based on the Boussinesq's hypothesis, assuming the same dependence of the Reynolds stress on the rate-of-strain tensor as for the viscous stresses of a Newtonian fluid, such that

$$-\rho\overline{C_i'C_j'}=\mu_t\left(\frac{\partial \bar{C}_i}{\partial x_j}+\frac{\partial \bar{C}_j}{\partial x_i}\right)-\frac{2}{3}\rho\delta_{ij}k=2\mu_t\bar{S}_{ij}-\frac{2}{3}\rho\delta_{ij}k \tag{5.13}$$

where μ_t is the eddy viscosity (turbulent viscosity) and k the specific turbulence kinetic energy.

The specific turbulence kinetic energy is defined as:

$$k = \frac{\overline{C_i' C_i'}}{2} \tag{5.14}$$

Based on the Prandtl-Kolmogoro analogy, the eddy viscosity μ_t can be expressed by the characteristic velocity $\sqrt{k}$ and the turbulence length scale l both of which characterize the turbulent flow motion, such that

$$\mu_t = C_\mu \rho \sqrt{k} l \tag{5.15}$$

where C_μ is a model constant. The two-equation eddy viscosity models for the turbulence model [40, 52], which are adopted for a wide range of engineering applications, provide independent transport equations for the turbulence length scale l (or parameters related to l) and the specific turbulence kinetic energy k. The most popularly used two-equation models are the $k-\epsilon$ model and the $k-\omega$ model. The former model, which was firstly proposed by Jones *et al.* [40], introduces the dissipation rate ϵ at which the kinetic energy of the smallest turbulent eddies is transferred to thermal energy at the molecular level. In contrast, $k-\omega$ model [89] solves for only the rate at which the dissipation occurs called the turbulent eddy frequency ω. Several comparative studies [12, 54] have proven that the $k-\epsilon$ model provides the most reliable result for modeling the flow far from solid walls, whereas the $k-\omega$ model accurately predicts boundary layer flows. In order to combine their advantages, Menter [53] proposed the blended model termed Shear Stress Transport (SST) model, which switches $k-\omega$ for the boundary layer flow and $k-\epsilon$ for the free shear layer flow far from the wall. The extensive applications of the SST model to various flow conditions have concluded that the model is the most suitable for predicting flow separations with an adverse pressure gradient.

For a better prediction of unsteady flow regimes, Egorov *et al.* [19] proposed the SST-SAS turbulence model, which enables the unsteady SST turbulence model to operate in SRS (Scale Resolving Simulation) mode. This is achieved by introducing the SAS source term including the turbulent length scale l and the von Karman length scale, which describes the second derivative of the velocity field, into the transport equation for the turbulence eddy frequency ω. This additional source term allows the model to dynamically adjust to resolved structures in URANS simulations. The SAS-SST model provides results similar to LES particularly in the unsteady flow region, and this model was used for various industrial applications with satisfactory results in recent years [20, 55]. Several authors have applied the SST-SAS model to the simulation of inter-blade vortices at deep part load operation, reporting successfully captured inter-blade vortex structures [49, 93]. In particular, Wack *et al.* [87] conducted the comparative simulations of the inter-blade cavitation vortices with SST and SST-SAS models, and they concluded that SST-SAS is superior in terms of the cavitation structure as well as the stochastic oscillation, particularly observed at deep part load operation of Francis turbines.

5.2.4 Cavitation model

When taking into account cavitation, the liquid-vapor mass transfer is governed by the vapor transport equation as follows.

$$\frac{\partial \rho_v}{\partial t} + C_j \frac{\partial (\rho_v \gamma_v)}{\partial x_j} = S_{vc} \tag{5.16}$$

where S_{vc} represents the mass transfer source term expressing the dynamics of the vapor bubbles, which can be decomposed into source terms for the growth (vaporization process, S_{vp}) and collapse (condensation process, S_{cn}) of the bubble, respectively:

$$S_{vc} = S_{vp} + S_{cn} \tag{5.17}$$

These terms are derived from the simplified Rayleigh-Plesset equation describing the dynamics of the gas bubble in a liquid.

$$S_{vp} = F_{vp} \frac{3\gamma_{nuc}(1-\gamma_v)\rho_v}{R_B} \sqrt{\frac{2}{3}\frac{p_v - p}{\rho_l}}, \text{ if } p < p_v \tag{5.18}$$

$$S_{vp} = F_{cn} \frac{3\gamma_{nuc}\gamma_v\rho_v}{R_B} \sqrt{\frac{2}{3}\frac{p - p_v}{\rho_l}}, \text{ if } p > p_v \tag{5.19}$$

where γ_{nuc} and R_B are the volume fraction of the nucleation sites and the radius of a bubble, respectively. F_{vp} and F_{cn}, are empirical factors taking into account the fact that the vaporization and condensation processes have different time scales. In this study, the following default values are used [95].

$$\gamma_{nuc} = 5 \times 10^{-4},\ R_B = 10^{-6}(\text{m}),\ F_{vp} = 50, \text{ and } F_{cn} = 0.01 \tag{5.20}$$

5.2.5 Discretization

To predict flow, the derivative terms regarding space and time in the governing equations are discretized by differential equations. Amongst the discretization methods for fluid dynamics applications, the finite volume (FV) method is the most used for engineering problems. In this method, the investigated volume is represented by a mesh made of volume elements defined by their vertex nodes, which divide the simulation domain into a large number of control volumes. The conservation laws for mass and momentum are established for each control volume, and each term of the governing equations is converted to mesh element volume integrals and element surface integrals. The advection term on the model equations is discretized based on the upwind difference scheme using the value at the upwind node. The time-dependent term is expressed using first order or second order implicit Euler scheme involving the values at the current and previous time steps.

Boundary conditions

In the finite volume method, the assembly of the equation systems is based on the fluxes determined from solution field and their gradients. This requires appropriate boundary conditions to specify the fluxes of the quantities such as mass, momentum and energy, on all sides of the computational domain and all surfaces lying within the domain. For computations of hydraulic turbines, it is straightforward to prescribe the conditions of the mass flow rate at the domain inlet, the static pressure at the outlet, and non-slip condition where the velocity on the surface is zero at wall boundaries.

5.3 Calculation domain

5.3.1 Calculation setup

For the present research, numerical simulations are conducted by using the commercial flow solver ANSYS CFX 17.1. The calculation domain includes a spiral case, stay vanes, guide vanes, runner, and draft tube as shown in Figure 5.1 with a total number of nodes of roughly 16 million nodes. The simulation is targeted at the operating conditions OP#1, #2 and #3 at the guide vane opening of $GVO = 5\,°$. For the boundary conditions, a constant mass flow rate at the inlet and average static pressure at the outlet which are extracted from the experimental

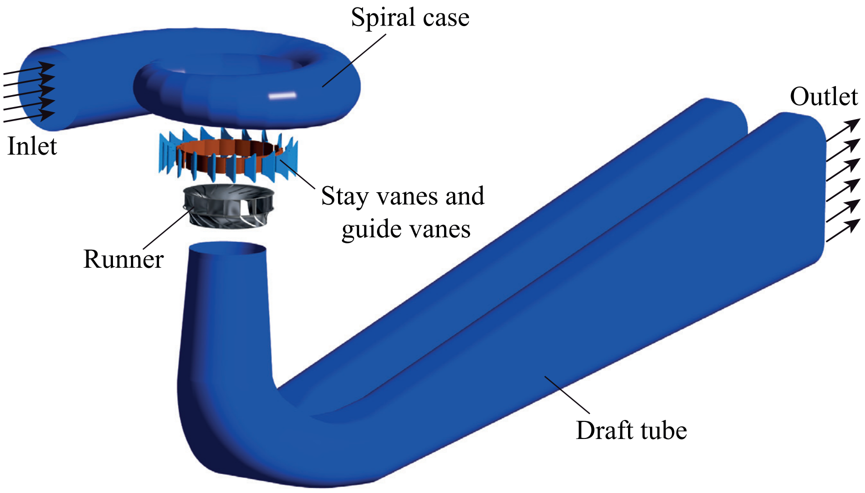

Figure 5.1 – Calculation domain for numerical simulations

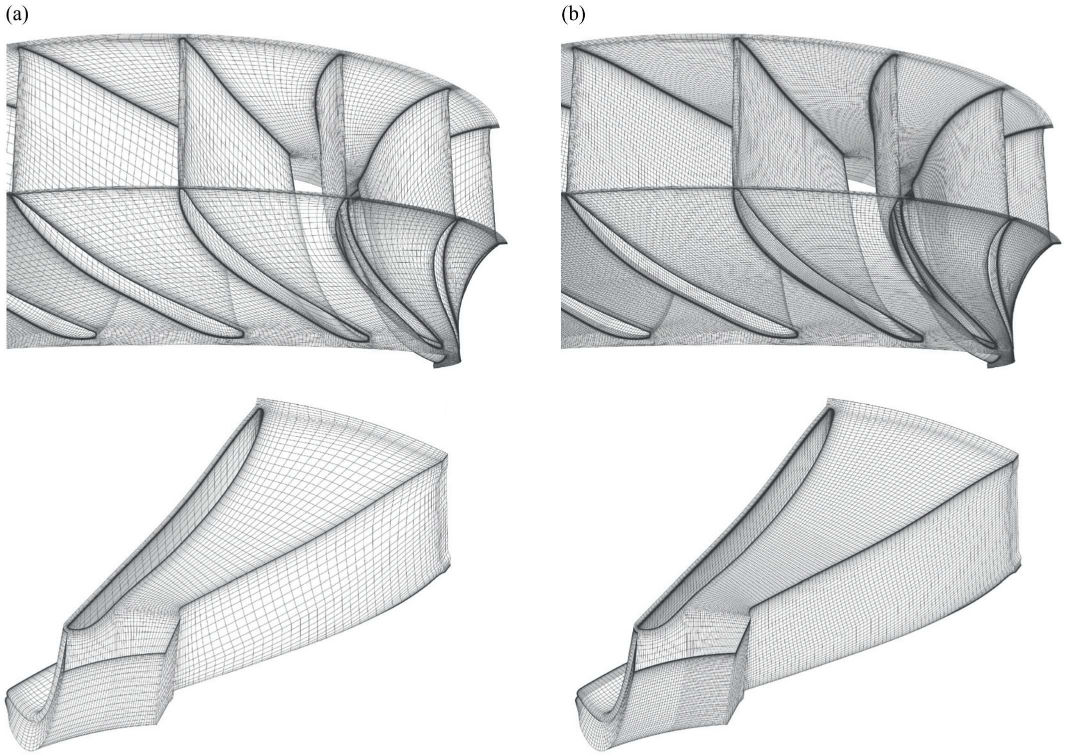

Figure 5.2 – Two runner calculation grids: coarse grid (a) and refined grid (b)

results are imposed respectively, and non-slip wall is used for the wall boundaries. For the interface between rotating and stationary frames, the transient rotor-stator which can predict transient interactions of the flow between rotating and stationary parts is adopted. Fluids (water and vapor) are treated as isothermal and homogeneous fluid. The cavitation number σ is targeted at $\sigma = 0.11$. The time step is set 0.0001 s (about 0.5 ° of the runner rotation) for OP#1 and 0.0002 s for OP#2 and OP#3. As a turbulence model, SAS-SST and k-ω SST are used for URANS and RANS simulations, respectively. For discretization of the governing equations, the high-resolution scheme and the second-order implicit scheme are applied to advection and transient terms, respectively.

5.3.2 Computational grid

Accuracy as well as reliability of numerical simulations are extremely dependent on the quality of the computational grids. In the present simulation, the grids are generated by ICEM CFD 17.1, and all the domains are composed of a hexahedral mesh. To evaluate the generated mesh quality, ICEM CFD offers a number of evaluation criteria. Amongst these criteria, equiangular skew, volume change, and aspect ratio are generally referred to for assessing the mesh quality [2, 66]. The equiangular skewness is the parameter indicating the mesh distortion between 0 and 1, which requires ideally a higher value than 0.50. The volume change shows the ratio between the volumes of one element and neighboring elements. The aspect ratio measures the elongation of an element. The values of these parameters as well as the number of nodes for each computational domain are summarized in Table 5.1. It can be confirmed that all the criteria are within the satisfactory range, even though the maximum aspect ratio shows a high value. This high aspect ratio only appears in the boundary layer mesh, which requires sufficiently small height in the direction normal to the wall. Nevertheless, the evaluation criteria confirm that the generated mesh is of sufficient quality.

For the present simulation, the flow structure inside the runner blade channel, especially the development of the inter-blade vortex is of primary focus. Therefore, the grid quality as well as the evaluation of the mesh dependency of the result in the runner domain are crucial. Thus, a refined runner domain with a higher grid density is prepared and the results are briefly compared by steady state simulation to check the mesh dependency of the result, especially inter-blade vortex development. The comparison of both computational grids in the runner are shown in Figure 5.2.

Table 5.1 – Number of nods for each calculation domain and the evaluation criteria of equiangular skew (Eq. skew), volume change (Vol. change), and aspect ratio (Asp. ratio)

Domain name	Spiral case	SV. and GV.	Runner	Runner (refined)	Draft tube
Mesh size	830’460	3’127’980	2’632’752	8’191’872	4’293’853
Eq. Skew (Min.)	0.351	0.327	0.301	0.301	0.311
Eq. Skew (Avg.)	0.846	0.728	0.709	0.715	0.824
Vol. change (Max.)	4.95	2.99	2.58	3.38	7.91
Vol. change (Avg.)	1.21	1.38	1.37	1.25	1.15
Asp. ratio (Max.)	969	654	634	612	981
Asp. ratio (Avg.)	39.9	26.5	31.3	37.3	35.9

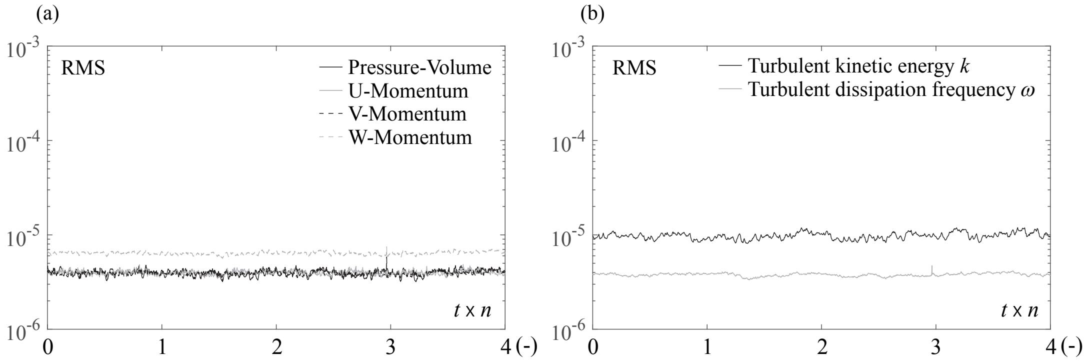

Figure 5.3 – Computational convergence of the unsteady RANS simulation at OP#1 during four runner revolutions

5.3.3 Computational convergence

For numerical simulations, the computational convergence is one criterion to evaluate the reliability of simulation results. In Figure 5.3, the computational convergence (RMS) of the performed unsteady RANS simulation at OP#1 with the refined runner grid during four runner revolutions is presented. Before these four runner revolutions, the runner is rotated for three rotations as a start-up. It can be confirmed that all the residual values lie within a sufficiently low range, suggesting the satisfactory quality of the performed simulation. It should be emphasized that the convergence of the simulations at OP#2 and OP#3 is almost same as the value at OP#1.

5.3.4 Preliminary computation result

Dimensionless wall distance y^+ for each domain

As an indicator of the mesh fineness, the dimensionless wall distance y^+ calculated based on the distance from the wall to the first node and the wall shear stress [3] is often referred to. For resolving boundary layer flow, the value of y^+ with the turbulence model SST and SAS-SST should be sufficiently low such as $y^+ \approx 1$. However, it is a demanding task to achieve such a low value especially when computational domains feature complicated geometry such as the case with pumps and turbines. In such cases, y^+ value is higher and the boundary layer is modeled by using the wall function [3]. In Table 5.2, the resulting values of y^+ of each domain is presented. It can be confirmed that the values for all the domains lie within the acceptable range.

Table 5.2 – Averaged and maximum y^+ values for each computational domain for the steady state calculation at OP#1

Domain name	Spiral case	SV. and GV.	Runner	Runner (refined)	Draft tube
y^+ (Avg.)	3.0	9.6	5.9	5.3	5.0
y^+ (Max.)	19.1	22.0	24.3	21.0	33.2

Specific energy and torque

Since the mass flow rate and the static pressure are given at the domain inlet and outlet as boundary conditions respectively, the specific energy E is a resulting parameter of the simulation. In Figure 5.4, the computed specific energy E as well as the torque T for the performed simulations at OP#1, #2, and #3 are presented. The specific energy is evaluated in the same evaluation planes as the experiment. For the unsteady simulations, the values are averaged for four runner revolutions. It is shown that both the specific energy E and the torque T are underestimated for all the operating conditions, and the discrepancy is approximately 12% to 13%. Furthermore, the discrepancy is not affected by the mesh refinement of the runner. This difference is also examined by different boundary conditions as well as further mesh refinements by Wack *et al.* [87], and it is confirmed that their influence is minor. It is assumed that the discrepancy comes from geometrical reasons such as a simplified runner geometry without runner crown bores and side gaps. Even though further investigations about these discrepancies are necessary, they are accepted in the present study since the inter-blade vortex structure as well as the velocity characteristics in the draft tube are in good agreement with the experimental results, which will be described in the following chapters.

Mesh dependency of the inter-blade vortex

Although the discrepancies of the specific energy and the torque are not greatly affected by the grid refinement of the runner, Wack *et al.* [87] mentioned that the inter-blade cavitation volume is considerably influenced by the grid density inside the runner blade channel. In Figure 5.5, the flow structures highlighted by the flow streamline on the hub (skin-friction line) and the pressure distribution by the steady state simulation at OP#1 performed using two runner grids are compared, together with the calculation grids on the hub. It is confirmed that the flow structures are similar and both the results show the vortex structure in the blade channel. However, the pressure at the vortex core with the coarse grid is not sufficiently decreased due to the relatively coarse grids inside the vortex. This may lead to the underestimation of the cavitation volume, as reported by Wack *et al.* [87]. Hence, all the unsteady RANS simulations presented in the following chapters are performed by using the refined runner grid to obtain a better estimation of the inter-blade cavitation vortex.

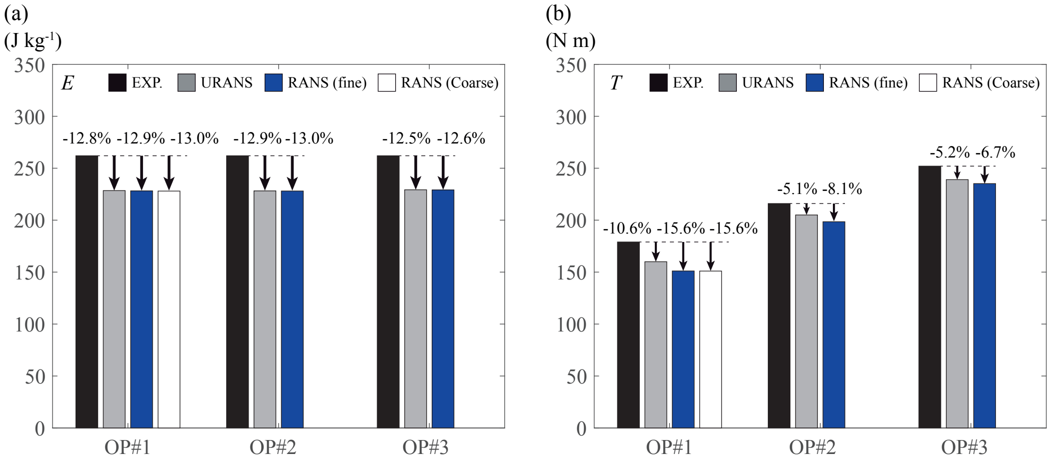

Figure 5.4 – Comparison of the simulated specific energy E (a) and torque T (b) with the experimental results

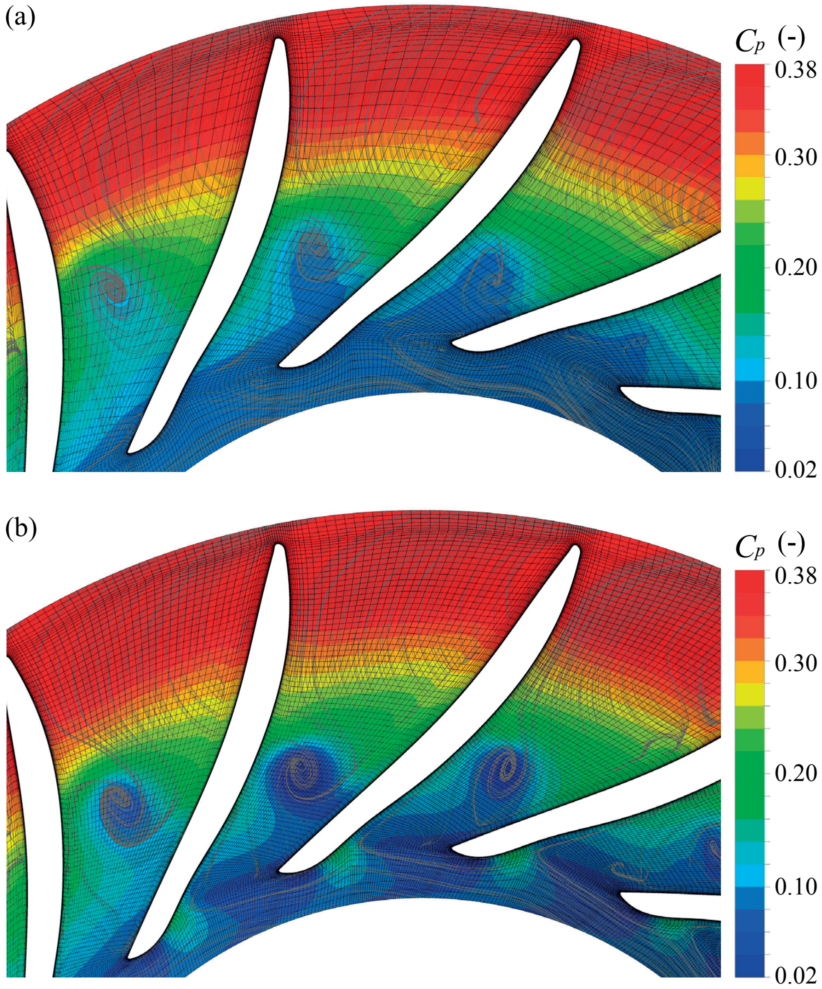

Figure 5.5 – The flow structure highlighted by the streamline (skin-friction line) and the distribution of the pressure coefficient C_p on the hub with the coarse runner grid (a) and the refined runner grid (b) by steady state calculation

6 Flow simulations in draft tube

6.1 Introduction

Francis turbine operation at part load condition experiences the development of a cavitation vortex rope in the draft tube, which acts as an excitation source for hydraulic systems [23, 44]. This induces pressure fluctuations in hydraulic units and endangers their stable operations. For the better understanding of the dynamical characteristics and the development of the cavitation vortex rope, different studies of the draft tube flow, from simulations of simplified components to entire hydraulic machines, have been conducted and reported in the past decades [61, 68, 73, 83, 94].

The draft tube plays a significant role in a pressure recovery to minimize a kinetic energy loss. However, a smooth pressure recovery is occasionally prevented by the occurrence of a vortex rope as well as the development of the stalled region accompanied by the flow separation. Therefore, comprehensive studies of flow characteristics in the draft tube are a crucial issue for hydraulic machines to understand adverse influence of singular flows in the draft tube and improve efficiency. Recent efforts include the estimation in the flow separation at part load operation in the draft tube using RANS simulations, revealing that the draft tube efficiency is significantly affected by the occurrence of the flow separation in the draft tube [51, 80].

At deep part load operation, although notable system instabilities such as resonances induced by the precessing cavitation vortex rope at part load condition are not observed in the experimental investigations, the periodic pressure fluctuations caused by multiple vortex ropes in the draft tube are still detected. Furthermore, velocity surveys by PIV measurements show that the flow in the draft tube features a strong swirling flow combined with the development of a significant backflow region at the center of the draft tube, which may cause a substantial reduction of the effective pressure recovery in the draft tube. Thus, this chapter intends to reveal fundamental flow characteristics in the draft tube at deep part load condition, including the comparison with PIV measurement data, by using simulation results. Furthermore, the characteristics of the pressure recovery as well as the specific energy loss through the draft tube are investigated and discussed.

6.2 Flow analysis in the draft tube

6.2.1 Mean flow characteristics

Simulated flow characteristics in the draft tube cone

As observed in the experimental velocity survey using PIV measurements in Section 2.4, the flow in the draft tube at deep part load operation features the development of a significant backflow region at the center of the draft tube cone. In Figure 6.1, the averaged flow structure for four runner revolutions at OP#1 in the draft tube highlighted by velocity vectors and flow streamlines is presented. The velocity vectors on the cross-section at $y = 0$ in the draft tube (see Figure 6.1a) show a strong recirculating region developed at the center of the draft tube, which causes the concentrated main flow stream close to the wall. The 3-D flow streamlines colored by the specific kinetic energy of the flow also indicate the high kinetic energy in the vicinity of the wall. On the contrary, the flow at the center of the draft tube is stagnated and dominated by the low kinetic energy flow, which is expected from the velocity survey by PIV measurements.

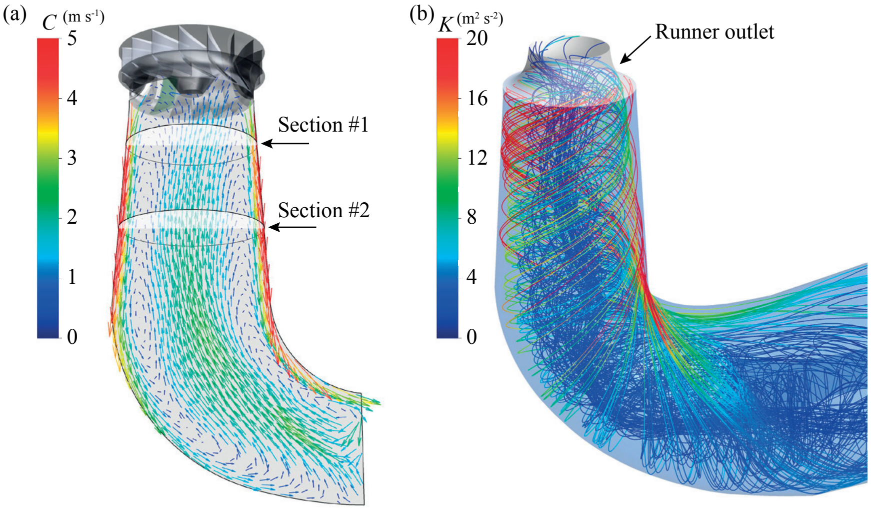

Figure 6.1 – Velocity vector plot at $y = 0$ cross-section in the draft tube (a) and flow streamlines colored by specific kinetic energy of the flow (b) at OP#1. Both the velocity vector and the flow streamlines are drawn by the averaged velocity over four runner revolutions.

Axial velocity distribution

In Figure 6.2, the mean and instantaneous distributions of the non-dimensional axial velocity C_m^* at $y = 0$ are presented together with the velocity field acquired by the PIV measurement. The threshold of a backflow region ($C_m^* = 0$) is also illustrated by the solid black line. Both instantaneous and averaged velocity distributions highlight the remarkable development of a backflow region at the center of the draft tube cone, resulting in high velocity flow concentrated near the wall. In the averaged velocity field, the velocity distribution is in very good agreement with the PIV measurement results. Furthermore, the onset of the backflow region is well estimated when compared with the PIV results. The velocity shows a slightly axisymetric distribution expecialy near the runner outlet, which it is assumed is caused by the draft tube elbow. It appears that the instantaneous velocity field shows the slightly unstable distribution near the wall at $x = -R$. However, the development of the backflow region at the center of the draft tube is quite stable. The backflow region becomes intensified in the downstream of the draft tube, which is also confirmed by the experimental investigation.

The averaged velocity profile of C_m^* along the x-axis at sections #1 and #2 together with the velocity profile acquired by PIV measurements is shown in Figure 6.3. The standard deviation of the simulated axial velocity $C_{m\_STD}^*$ is also plotted together. At section #1, the backflow velocity at the center of the cone is well estimated and both experimental and simulation results indicate the backflow onset at about 0.7 × R. In the vicinity of the wall, the simulated axial velocity is in good agreement with the experiment at $x = -R$. However, the amplitude of the simulated velocity is higher than the experiment at $x = R$, which is caused by the error in

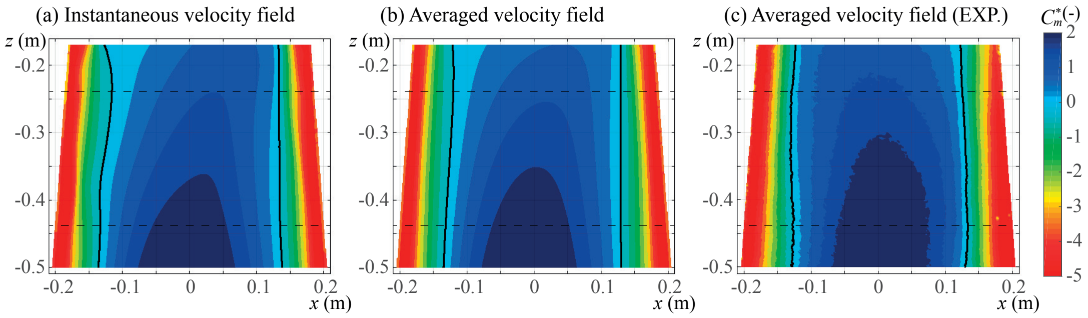

Figure 6.2 – Instantaneous (a) and averaged (b) distributions of the non-dimensional axial velocity C_m^* at $y = 0$ and the PIV measurement result (c) at OP#1. The averaged velocity of the simulation is calculated over four runner revolutions. Threshold of the backflow region is highlighted by a solid black line. Both sections #1 and #2 are indicated as dashed black lines.

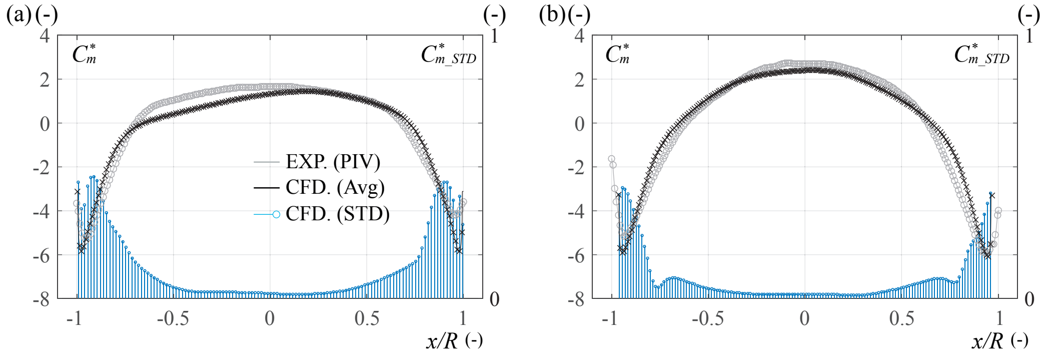

Figure 6.3 – Velocity profile of C_m at $y = 0$ together with the standard deviation at section #1 (a) and section #2 (b)

the experimental measurement due to the reflection of the laser light off the pressure sensor. As this measurement error is reduced at section #2, it can be confirmed that the simulated velocity profile is in very good agreement with the experimental result as presented in Figure 6.3b.

Circumferential velocity distribution

In Figures 6.4 and 6.5, the distributions of the non-dimensional circumferential velocity C_u^* at both sections #1 and #2 are presented, respectively. As observed in the PIV measurement result, a low circumferential velocity region is developed at the center of the draft tube cone, whereas the velocity becomes significantly amplified near the wall. The averaged circumferential velocity is symmetrically distributed at both sections #1 and #2. However, the instantaneous circumferential velocity is a bit higher near the wall and it slightly deviates from the symmetric

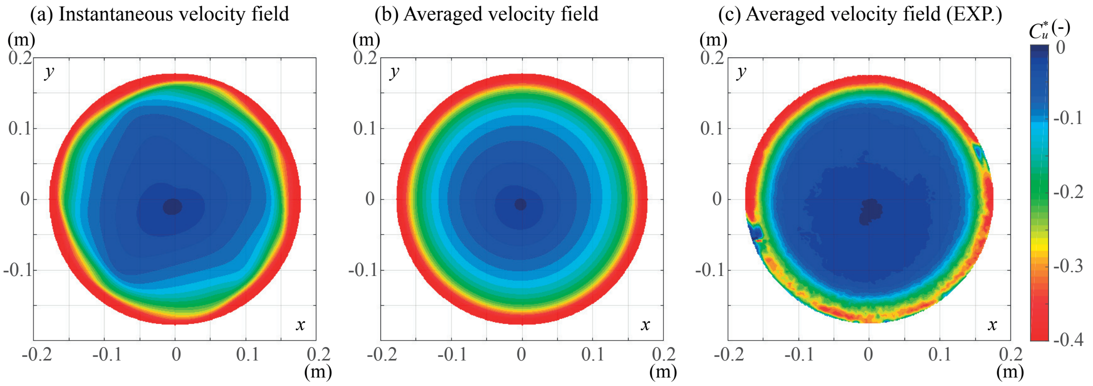

Figure 6.4 – Instantaneous (a) and averaged (b) distributions of the non-dimensional circumferential velocity C_u^* at section #1 and the PIV measurement results (c) at OP#1. The averaged velocity of the simulation is calculated over four runner revolutions.

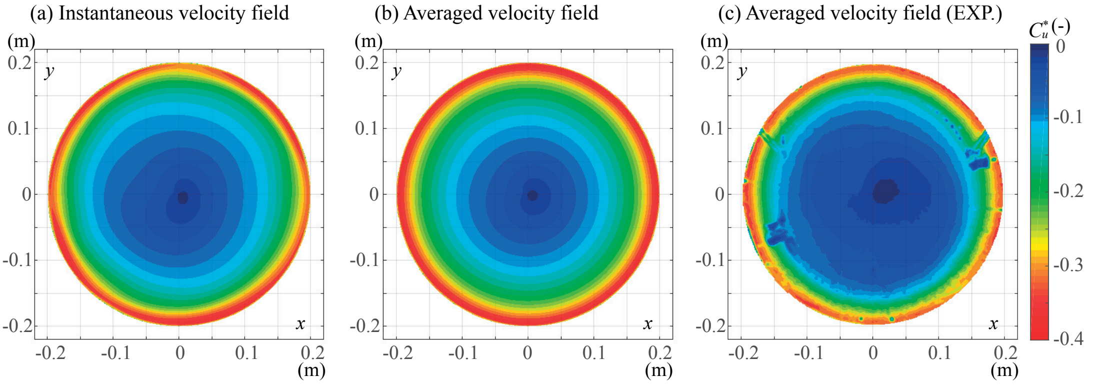

Figure 6.5 – Instantaneous (a) and averaged (b) distributions of the non-dimensional circumferential velocity C_u^* at section #2 and the PIV measurement result (c) at OP#1. The averaged velocity of the simulation is calculated over four runner revolutions.

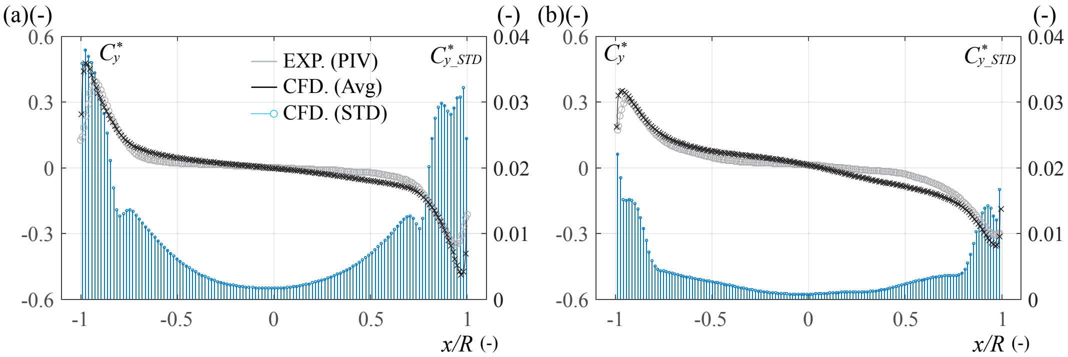

Figure 6.6 – Velocity profile of C_y^* at $y = 0$ together with the standard deviation at section #1 (a) and section #2 (b)

distribution, especially at section #1. This may suggest that the unsteadiness of the flow is relatively high at section #1.

The simulated velocity profiles of C_y along the x-axis at both sections #1 and #2 together with the standard deviation as well as the experimental results are shown in Figure 6.6. Since it is considered that the measurement error of the velocity amplitude is relatively high at section #1 due to the reflection of the laser light, the amplitude of the simulated velocity close to the wall is slightly overestimated at section #1 especially near the wall at $x = R$. However, as the experimental error decreases at section #2, the simulated circumferential velocity profile shows very good agreement with the experimental result, even though the velocity near the center is slightly overestimated. The profiles at both sections #1 and #2 demonstrate that the significant increase of the circumferential velocity starts at about $0.7 \times R$, which almost corresponds to the backflow inception observed in Figure 6.3. The standard deviation is also increased after the backflow inception, and its value is especially high at section #1. Based on the experimental investigations, multiple vortex structures may still exist in the draft tube cone and it is assumed that the existence of these multiple vortex structures causes the velocity perturbations at section #1.

6.2.2 Transient characteristics of the simulated flow in the draft tube

As shown in the experimental investigations (see Section 2.3.2), it is considered that multiple structures of the vortex rope still exist in the draft tube cone under deep part load operations, which induce periodic pressure fluctuations. In the performed simulation, even though the cavitation structure in the draft tube is not detected same as observed in the experiment, the development of low pressure region related to the multiple vortex cores appear in the draft tube as shown in Figure 6.7. In the experiment, the cavitation vortex rope is not visible at OP#1 at the σ_{plant} condition. However, small cavitation structures in the draft tube occasionally appear when σ is set to be the lowest value $\sigma = 0.07$ (see Figure 6.7b). This suggests that the low pressure cores related to the multiple vortex structures are still developed in the draft tube cone at OP#1. As shown in Figure 6.7a, four low pressure cores are developed near section #1, which are also detected in the instantaneous distribution of the pressure at section #1 in Figure 6.8a. In Figure 6.8b, instantaneous flow streamlines at section #1 is presented. In such a strong swirling flow, however, a swirl velocity is so high that small vortex structures existing in the flow are not visualized properly. Hence, the velocity is decomposed into the mean component and the fluctuating part for extracting small vortex structures in a swirling flow, such that

$$C_x = \bar{C}_x + \tilde{C}_x \qquad\qquad C_y = \bar{C}_y + \tilde{C}_y \tag{6.1}$$

Tangential flow streamlines are then rewritten by using the fluctuating components $\tilde{C}_x$ and $\tilde{C}_y$ to highlight small vortex structures existing in a strong swirling flow. As shown in Figure 6.8c, the vortex structures are successfully visualized by streamlines of the fluctuating velocity components. Furthermore, their locations correspond to the region of the high vorticity calculated by the fluctuating velocity component and the low pressure zone shown in Figure 6.8a.

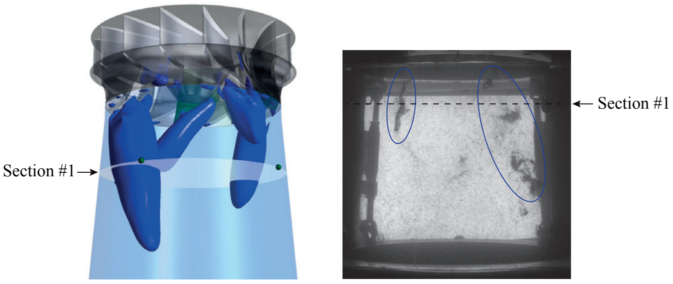

Figure 6.7 – Comparison of the low pressure structure at OP#1 in the simulation with the visualized cavitation vortex rope at the lowest cavitation number $\sigma = 0.07$. The simulated low pressure core is highlighted by the iso-surface of $C_p = 0.08$

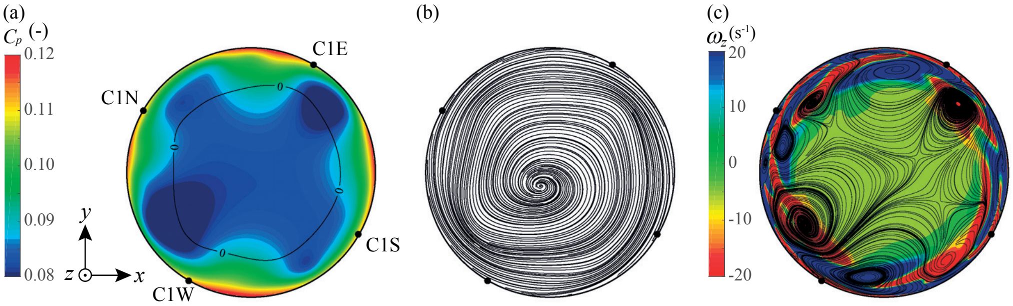

Figure 6.8 – Contour of the instantaneous pressure factor distribution (a) and the tangential streamlines drawn by the instantaneous velocity (b) and fluctuating velocity together with the vorticity ω_z (c)

The vortex structures are developed along the backflow inception line (see black line in Figure 6.8a), suggesting that these small vortex structures are generated by a shear layer between the high circumferential velocity near the wall and the stalled region at the center of the draft tube. There are several small vortex structures close to the wall. However, the main vortices generating the low pressure core are four, which are located at almost 90 degree intervals. In Figure 6.9, the time history of the low pressure core locations over two runner revolutions as well as the time history of the centered pressure signals at section #1 (C1N, C1E, C1S and C1W) over 5 runner revolutions are presented. The images of the low pressure cores in the draft tube are captured every 90 degrees of the runner revolution, and the corresponding points are indicated in the time history of the pressure oscillations. It is confirmed that the low pressure cores related to the multiple vortex structures in the draft tube are rotated in the same direction as the runner rotation. This precession of the low pressure cores causes periodic pressure oscillations with a period of approximately $2 \times n$. Since the four major cores are developed in 90 degree shifted locations, the pressure fluctuations in the four measurement locations at section #1 have almost the same phase. In Figure 6.10, the instantaneous distribution of the pressure factor C_p as well as tangential flow streamlines written by the fluctuating component

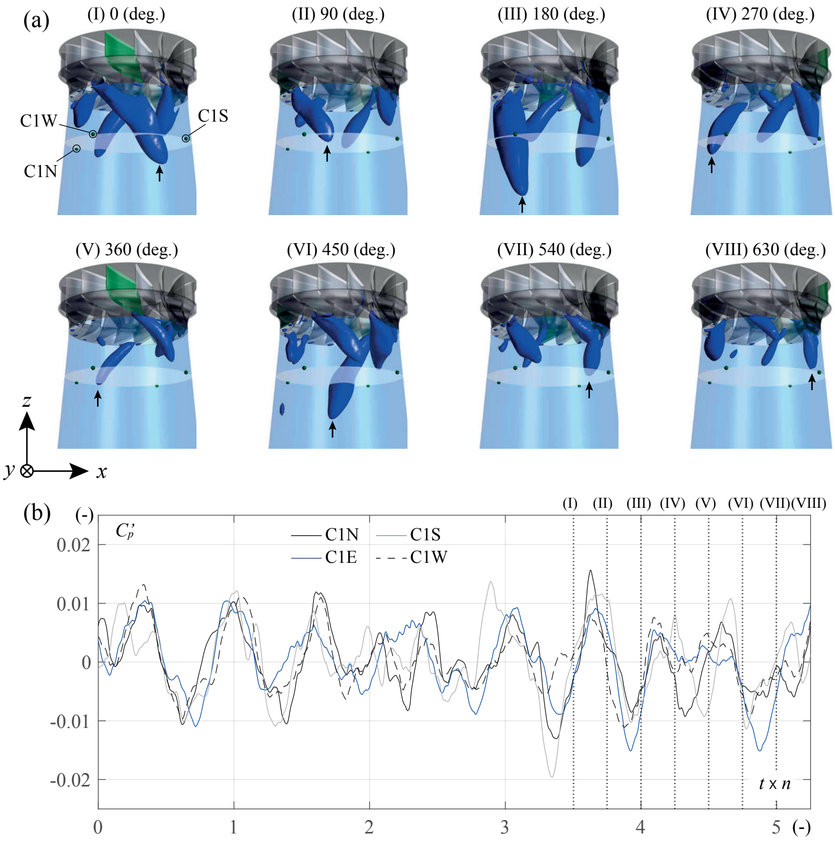

Figure 6.9 – Time history of the rotating low pressure cores caused by the multiple vortex ropes in the draft tube cone (a) and the pressure signals at section #1 over 5 runner revolutions (b). The roman numbers shown in (b) correspond to the points in (a).

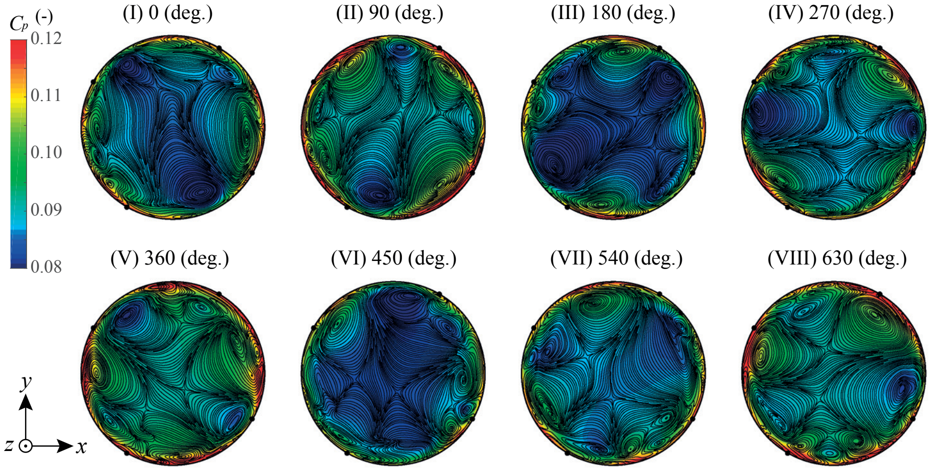

Figure 6.10 – Time history of instantaneous distributions of the pressure factor C_p together with the tangential flow streamline drawn by the fluctuating velocity components

in Equation 6.1 are presented. The roman numbers correspond to the points shown in Figure 6.9a. It can be confirmed that multiple vortex structures leading to low pressure cores rotate at a frequency approximately equal to half of the runner rotational frequency as confirmed in Figure 6.9. Moreover, the passage of these low pressure zones corresponds to the pressure oscillation observed at section #1 illustrated in Figure 6.9b.

In Figure 6.11, the comparison of the centered pressure signal acquired from C1N at section #1 in the simulation with the experimental pressure signal at C1N is presented. It can be confirmed that the simulated pressure fluctuation due to the passage of multiple vortex structures is well captured by comparison with the experimental results, even though the fluctuating amplitude is slightly underestimated. For the simulation, there are principally four low pressure zones related to the vortex cores in the draft tube cone, which rotate with a period of approximately 0.5 × n. Thus, the frequency of the pressure oscillation almost corresponds

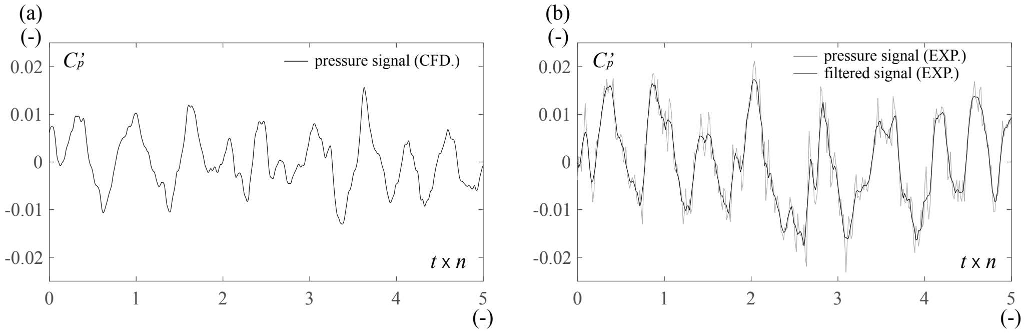

Figure 6.11 – Comparison of the centered pressure signals at C1N of the simulation (a) and the experiment (b) for five runner revolutions.

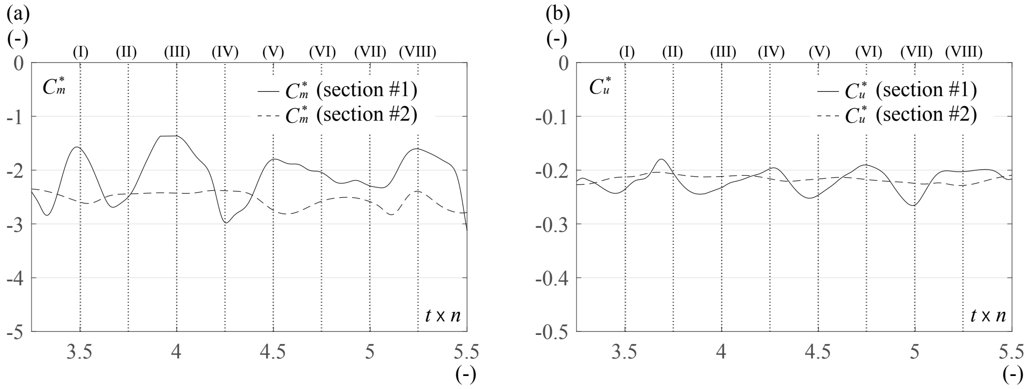

Figure 6.12 – Time history of the non-dimensional axial velocity C_m^* (a) and the non-dimensional circumferential velocity C_u^* (b) at both sections #1 and #2. The roman numbers correspond to the points shown in Figure 6.9a

to $f_4 = 2 \times n$. In the experimental result, the frequency of $k = 4$ based on the spectral analysis of the fluctuating pressure signal from C1N at OP#1 is $f_4 = 1.92$ (see Equation 2.1), which is in good agreement with the simulation result.

It is assumed that the precession of multiple vortex ropes in the draft tube causes velocity fluctuations, which results in a high standard deviation values for the velocity near the wall as shown in Figures 6.3 and 6.6. In Figure 6.12, the time history of the axial and circumferential velocities at section #1 and section #2 over two runner revolutions is presented. The roman numbers correspond to the points in Figure 6.9a. The velocity is acquired at $0.75 \times R$ inside each section ($0.25 \times R$ from C1N and C2N). It is shown that the axial velocity at section #1 is fluctuated due to the precession of the multiple vortex ropes, whereas the fluctuations are not clearly observed at section #2 since the vortex intensity is reduced at this section. The circumferential velocity is also fluctuated more periodically by the vortex passage at section #1. However the oscillation is not clearly detected at section #2. These velocity fluctuation may lead to the variations of the pressure recovery and the specific energy loss through the draft tube.

6.2.3 Pressure recovery and loss coefficient in the draft tube

In the previous section, the simulated flow at deep part load operation is characterized by the significant development of a backflow region as well as multiple vortex ropes in the draft tube. The role of the draft tube is to recover the kinetic energy into static pressure. However, it has been shown that the effective pressure recovery is prevented depending on flow conditions in the draft tube [51, 68, 80]. The efficiency of the draft tube can be quantitatively evaluated by the pressure recovery factor χ and the loss coefficient ζ through the draft tube [50]. Taking into account the balance of the specific energy and the mass continuity, the pressure recovery through the draft tube without the specific energy loss can be expressed as follows:

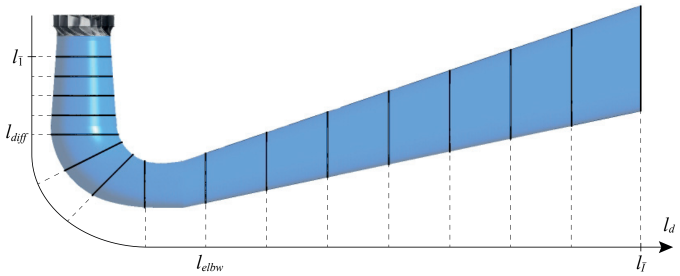

Figure 6.13 – Evaluation planes of the pressure recovery factor χ and the loss coefficient ζ in the draft tube

$$p_{\bar{I}} - p_{\bar{1}'} = \frac{1}{2}\rho C_{\bar{1}'}^2 - \frac{1}{2}\rho C_{\bar{I}}^2 = \frac{1}{2}\rho C_{\bar{1}'}^2\left[1 - \left(\frac{A_{\bar{1}'}}{A_{\bar{I}}}\right)^2\right] \tag{6.2}$$

The indices $\bar{1}'$ and $\bar{I}$ represent the draft tube inlet and outlet, respectively. In the real flow, however, the pressure recovery becomes less than Equation 6.3 due to the existence of the specific energy losses through the draft tube E_r, such that

$$p_{\bar{I}} - p_{\bar{1}'} = \frac{1}{2}\rho C_{\bar{1}'}^2\left[1 - \left(\frac{A_{\bar{1}'}}{A_{\bar{I}}}\right)^2\right] - E_r \tag{6.3}$$

For the case of a flow in a diffuser, the specific energy loss between two cross-sections can be written as follows taking into consideration the conservation of the momentum:

$$E_r = \frac{1}{\rho Q}\left(\left.\int_A gH\rho\vec{C}\cdot\vec{n}dA\right|_{\bar{1}'} - \left.\int_A gH\rho\vec{C}\cdot\vec{n}dA\right|_{\bar{I}}\right) \tag{6.4}$$

Based on the expression above, the pressure recovery factor and specific energy loss coefficient are then expressed as follows:

$$\chi = \frac{p_{\bar{I}} - p_{\bar{1}'}}{\frac{1}{2}\rho C_{\bar{1}'}^2} \tag{6.5}$$

$$\zeta = \frac{\frac{1}{\rho Q}\left(\int_A gH\rho\vec{C}\cdot\vec{n}dA|_{\bar{1}'} - \int_A gH\rho\vec{C}\cdot\vec{n}dA|_{\bar{I}}\right)}{\frac{1}{2}\rho C_{\bar{1}'}^2} \tag{6.6}$$

For the evaluation of the pressure recovery, the draft tube is split into several parts as shown in Figure 6.13. The pressure recovery factor χ and the loss coefficient ζ are then evaluated from the inlet of the draft tube ($l_d = l_{\bar{1}}$) which is set at section #1 to a given cross-section. Hence, the recovery factor and the loss coefficient at $l_d = l_{\bar{I}}$ correspond to the values throughout the draft tube from the inlet to the outlet. The ideal pressure recovery factor for the studied draft tube calculated by Equation 6.3 is equal to 0.948. The evaluated pressure recovery factor χ and the loss coefficient ζ at OP#1 over the non-dimensional draft tube length l_d^* ($l_d^* = 0$ at the inlet $\bar{\mathrm{I}}$ and $l_d^* = 1$ at the outlet $\bar{I}$) are shown in Figure 6.14. Generally, the largest pressure recovery occurs in the draft tube cone (straight diffuser) at the outlet of the runner, however the pressure recovery factor χ in the diffuser is considerably low in the presented case. It is assumed that the significant development of a backflow region preventing the main flow in draft tube cone causes considerably high specific energy losses. Furthermore, the flow may encounter high friction losses on the wall due to the concentrated high velocity flow near the wall. Correspondingly, the slope of the loss coefficient ζ in the draft tube cone is remarkably high (see Figure 6.14a), suggesting that the specific energy loss is particularly high in the straight diffuser. The pressure recovery factor χ then starts increasing in the middle of the elbow. Correspondingly, the slope of the loss coefficient is reduced around this region. In the straight diffuser after the elbow, the pressure recovery factor is smoothly increased, and loss coefficient is almost kept constant, suggesting that the specific energy loss is small.

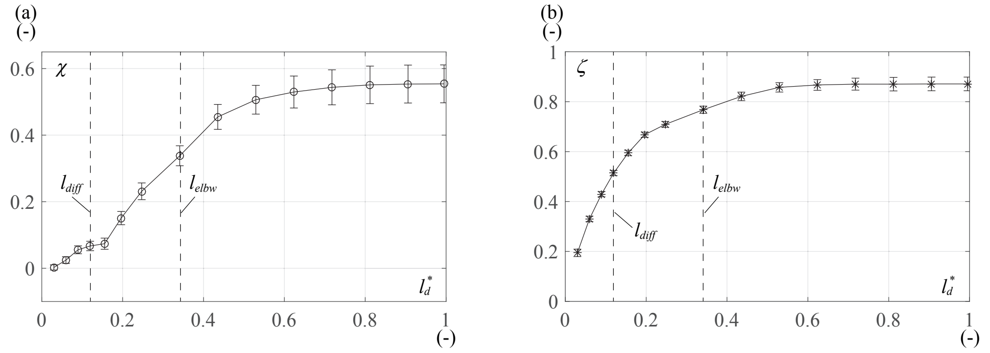

Figure 6.14 – Calculated mean recovery factor χ (a) and loss coefficient ζ (b) together with the standard deviations in the draft tube

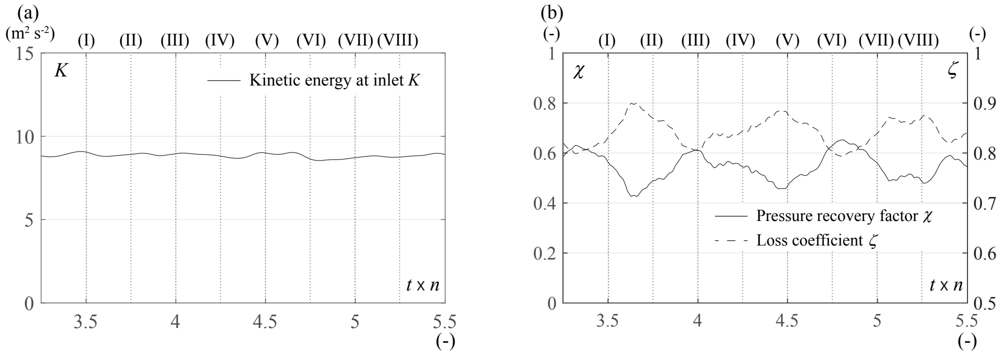

Figure 6.15 – Time history of the specific kinetic energy K at the draft tube inlet (a) and the pressure recovery factor χ as well as the loss coefficient ζ through the draft tube (b) over two runner revolutions. The roman numbers correspond to the points shown in Figure 6.9a

In Figure 6.15, the time history of the averaged specific kinetic energy K of the flow at the draft tube inlet plane (section #1), the pressure recovery factor χ and the loss coefficient ζ through the draft tube over two runner revolutions are presented. The corresponding points shown in Figure 6.9a are also presented together. It demonstrates that the specific kinetic energy at the draft tube inlet is almost kept constant, whereas the pressure recovery factor is fluctuated with the close frequency to the precession of multiple vortex ropes observed at section #1. The variation of the pressure recovery due to the part load vortex rope was also pointed out in [50]. The presented results suggest that the rotating vortex structure at deep part load also induces the periodic fluctuation of the pressure recovery, even if the vortex intensity is not as high as the intensity of the part load vortex rope. Since the specific kinetic energy at the draft tube inlet is not oscillated but kept almost constant as shown in Figure 6.15a, the fluctuation of the pressure recovery is caused by the fluctuating specific energy loss E_r through the draft tube, which can be confirmed by the time history of the loss coefficient ζ (see Figure 6.15b). The loss coefficient is oscillated in the opposite phase as the pressure recovery factor. This confirms that the precessing motion of multiple vortex ropes induces the periodic variation of the specific energy loss, resulting in the fluctuation of the pressure recovery in the draft tube.

6.3 Summary

The presented chapter focuses on flow analyses in the draft tube by numerical simulations. As expected from the velocity survey performed by PIV measurements, the flow in the draft tube at presented deep part load condition features the development of a significant backflow region, resulting in the concentrated main flow stream near the wall. Moreover, the simulated flow structure in the draft tube is validated by comparison with the velocity field acquired by PIV measurements. The performed simulation successfully captures the development of the multiple vortex ropes resulting in low pressure cores in the draft tube cone, which induces periodic pressure fluctuations. The precession of these multiple vortex ropes is found to cause velocity perturbations in both axial and circumferential velocity components at section #1.

In addition, the influence of the flow structure at the simulated condition on the draft tube efficiency is investigated by the pressure recovery factor and the loss coefficient through the draft tube. As a result, it is shown that the pressure recovery is considerably low in the draft tube cone. It is assumed that the effective pressure recovery is prevented by the development of a backflow region and a high velocity flow near the wall, which cause the high specific energy loss in the draft tube cone. Correspondingly, the notable increase of the loss coefficient is detected in the draft tube cone. Instantaneous variations of the pressure recovery factor and the loss coefficient reveal that they are dynamically changed with the close frequency to the precession of the multiple vortex ropes in the draft tube. This suggests that the precession of multiple vortex ropes in the draft tube cone causes the periodic variation of the specific energy loss through the draft tube, which requires further investigations to correlate behaviors of the loss coefficient with transient flow characteristics in the draft tube.

7 Simulated flow investigations in blade channels

7.1 Introduction

At deep part load operation of Francis turbines, the flow inside the blade channel is subject to the development of inter-blade cavitation vortices, as confirmed by visualizations in Section 3.3. Using on-board pressure measurements on the runner blade shown in Section 4.3.1, it is revealed that inter-blade vortices induce stochastic pressure fluctuations, especially on the suction side of the blade. Furthermore, the wall pressure difference between the blade pressure and suction sides near the hub becomes negative at deep part load condition, suggesting that a backflow region develops in the vicinity of the hub. This singular flow condition may be caused by the flow separation on the hub. It is assumed that the flow separation on the hub is induced by the misaligned flow inside the blade channel caused by the high incident angle at the blade inlet under deep part load operations. However, detailed investigations of the flow inside the runner to specify underlying mechanisms of inter-blade vortex development has not yet been achieved and behaviors of inter-blade vortices are still unknown.

To obtain a better understanding of flow characteristics related to inter-blade vortices, several authors have performed and reported the numerical simulations of inter-blade vortices at deep part load condition [49, 87]. In particular, Yamamoto *et al.* [93] revealed the development of a backflow region inside the blade channel near the hub, which is closely linked to the development of inter-blade vortices. This chapter is aimed at further investigating the characteristics of the flow inside the blade channel and ascertain the physical mechanisms responsible for the development of inter-blade vortices by the numerical simulation. The simulated inter-blade cavitation vortices are first compared and validated by the visualized inter-blade cavitation vortices from the experiment. The flow structures are then characterized by velocity surveys inside the blade channel, including the flow incident angle at the blade channel inlet and the relative flow angle at the outlet. The inter-blade vortex intensity defined by the circulation as well as the pressure distribution related to inter-blade vortex development are also investigated. The study is further extended to the skin-friction analysis to identify the flow separation on the hub, and the mechanism underlying the development of inter-blade vortices is clarified. Finally, the specific energy loss through the blade channel is quantitatively evaluated by the specific rothalpy, and the influence of the inter-blade vortex on the energy dissipation through the blade channel is discussed.

7.2 Inter-blade cavitation vortex structure

7.2.1 Comparison of simulated and visualized inter-blade cavitation vortices

Instantaneous inter-blade vortex structure

First of all, the simulated structure of inter-blade cavitation vortices at OP#1 is compared with the visualization results. In Figure 7.1, the instantaneous view of the inter-blade cavitation

(a) Cavitation surface defined by vapor volume fraction $\gamma_v = 0.1$ (CFD.)

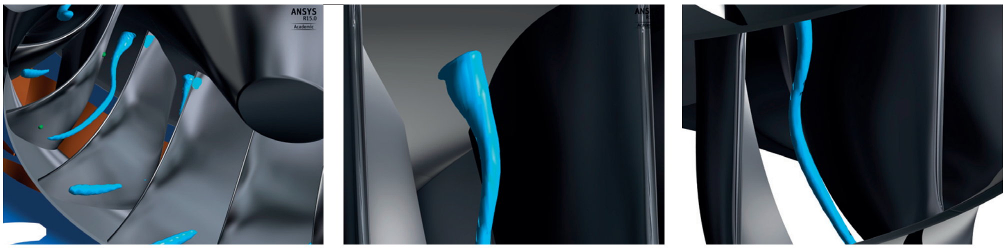

(b) Visualization result (EXP.)

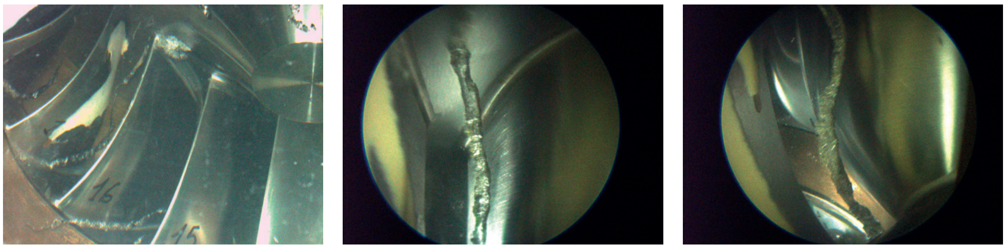

Figure 7.1 – Instantaneous view of the cavitation structure of inter-blade cavitation vortices (a) and the visualized inter-blade cavitation vortices in the experiment (b) for OP#1 at $\sigma = 0.11$. The cavitation surface is determined by the iso-surface of the vapor volume fraction $\gamma_v = 0.1$

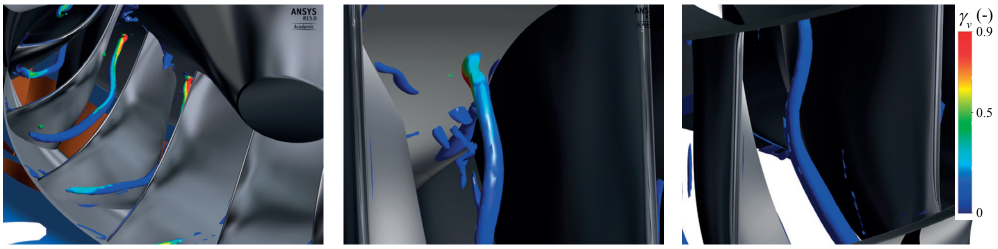

Figure 7.2 – Instantaneous view of the inter-blade vortex structure highlighted by non-dimensional Q-criterion $Q^* = 3.0 \times 10^4$. The vortex structure is colored by the level of the vapor volume fraction γ_v.

structure at OP#1, of which the surface is defined by the vapor volume fraction $\gamma_v = 0.1$, is presented together with the visualized inter-blade cavitation vortex. It can be confirmed that inter-blade cavitation vortices are successfully captured by the performed simulation and in very good agreement with the visualized inter-blade cavitation vortex. Furthermore, the simulated cavitation structure is also attached to the hub, and it features helical in shape at the middle of the channel. In Figure 7.2, the instantaneous view of the inter-blade vortex structure highlighted by the non-dimensional Q-criterion $Q^* = 3.0 \times 10^4$ (for further detail of the vortex identification, the reader may refer to Appendix D) is presented. The vortex structure is also colored by the level of the vapor volume fraction γ_v. By comparison with visualized inter-blade cavitation vortices shown in Figure 7.1b, instantaneous vortex structures are also in good agreement with the experimental result. Furthermore, the high void fraction level appears especially in the vicinity of the hub. This suggests that a strong inter-blade vortex structure may be generated due to the development of a singular flow region near the hub and the risk of cavitation development is potentially high. This is also confirmed by the calculation of probability P based on the visualization results in Section 3.4.1. The comparison of the simulation result with high-speed visualizations is presented in Appendix B.

Averaged inter-blade vortex structure

In Figure 7.3, the comparison of the mean vortex line and inter-blade vortex structure highlighted by the averaged non-dimensional Q-criterion $Q^* = 3.0 \times 10^4$ with the experimental inter-blade vortex line estimated by the visualization in Section 3.4.2 are presented. The averaged Q^* is calculated over four runner revolutions. The vortex line in the simulation is drawn by connecting the locations of the inter-blade vortex center at each span-wise location every $s^* = 0.05$, which is identified by the point at which the value of Q^* reaches its maxi-

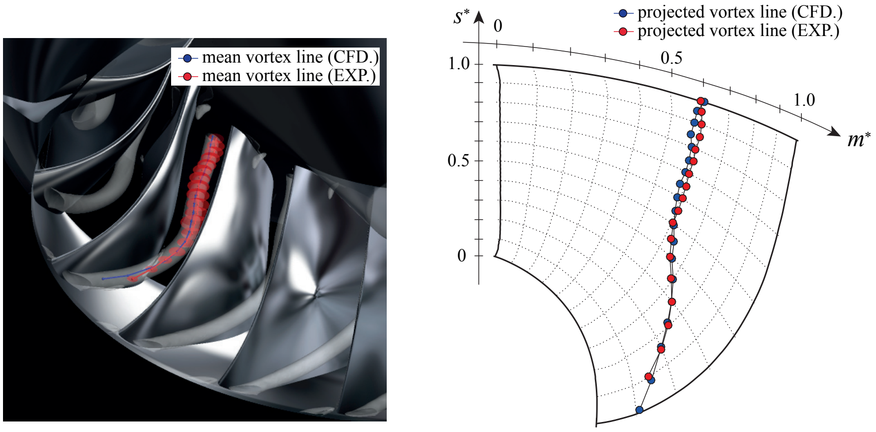

Figure 7.3 – Comparison of the averaged inter-blade vortex structure and vortex center locations of the simulation with the vortex line evaluated based on the visualization (a) and the projected vortex line on the meridional plane (b). The mean vortex structure is highlighted by $Q^* = 3.0 \times 10^4$, which is averaged over four runner revolutions.

mum in the inter-blade vortex region. The comparison shows that the simulated inter-blade vortex is in very good agreement with the experimental result, which is also confirmed by the plot of the projected vortex locations on the meridional plane (see Figure 7.3 b). Especially, both simulation and the experimental result indicate the vortex onset on the hub at the non-dimensional streamwise location $m^* = 0.60$. Furthermore, it appears that the simulated vortex line develops at almost constant streamwise location between $s^* = 1.0$ and 0.50, which validates the assumption used for the estimation of the inter-blade vortex locations from the visualization results in Section 3.4.2.

7.2.2 Comparison of vortex structures for different operating points

In the experiment, the development of the inter-blade cavitation vortex is notably affected when the operating condition is changed among OP#1, #2 and #3. The comparison of the averaged structures of the cavitation and the inter-blade vortices in the simulation at OP#1, #2, and #3 for $\sigma = 0.11$ is presented in Figure 7.4a. It is shown that the highlighted vortex structure is most significantly developed inside the blade channel at OP#1 as observed in the experiment, and the averaged cavitation structure is also developed especially near the hub and the runner outlet. Although the inter-blade vortex structure still exists in the blade channel at OP#2, the cavitation structure is already diminished, suggesting that the intensity

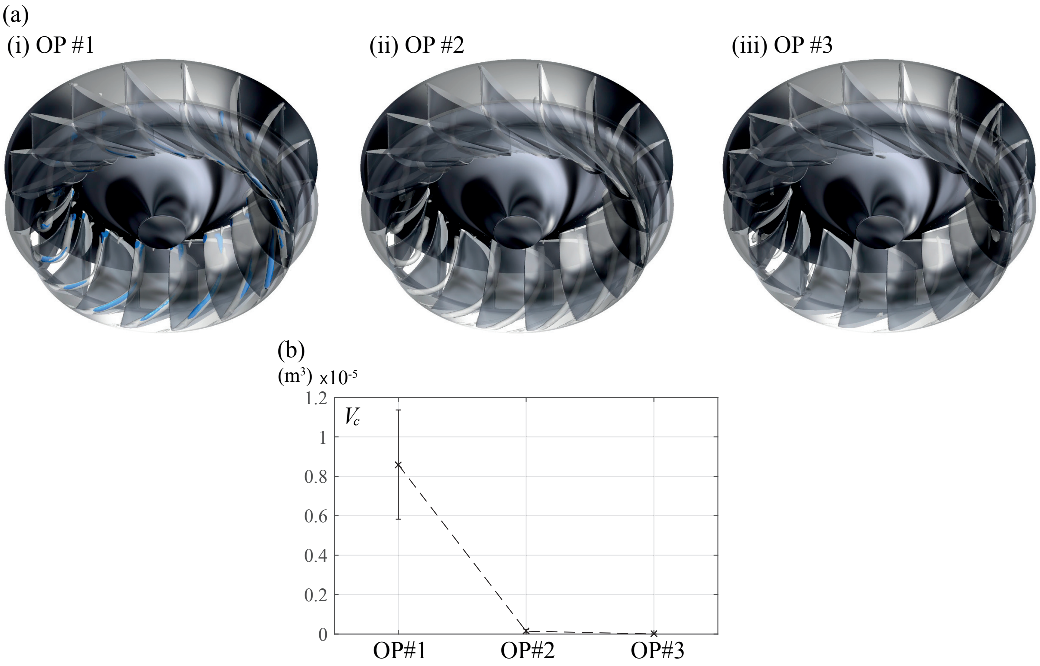

Figure 7.4 – Comparison of the averaged inter-blade vortex structure (white surface, $Q^* = 3.0 \times 10^4$) and cavitation structure (blue surface, $\gamma_v = 0.1$) at the targeted operating conditions OP#1, #2, and #3 (a) and the averaged cavitation volume in the runner domain together with the standard deviation (b). The quantities are averaged over four runner revolutions.

of inter-blade vortices is decreased compared to that of OP#1. At OP#3, the volume of the highlighted inter-blade vortex region is clearly reduced. In Figure 7.4b, the comparison of the inter-blade cavitation volume V_c averaged over four runner revolutions is shown together with the standard deviation. The volume of the inter-blade cavitation vortex is given by the volume integration of the vapor volume fraction γ_v in the runner domain. Both the mean value and the standard deviation are clearly high at OP#1, whereas they are drastically decreased at OP#2 and OP#3, which is also observed in the experimental investigations.

7.3 Velocity investigation inside the blade channel

7.3.1 Velocity distribution

In this section, the flow structures relating to the development of inter-blade vortices are characterized by the velocity field inside the blade channel (refer to Appendix C for definition of the coordinate and calculation of the velocity components inside the blade channel). Three non-dimensional span-wise locations $s^* = 0.99$, 0.50, and 0.10 are selected to investigate velocity characteristics (see Figure 7.5). All the velocities shown in this section is averaged over four runner revolutions. The mean velocity vectors together with the tangential flow streamlines and the mean distributions of the non-dimensional meridional velocity C_m^* and relative circumferential velocity W_u^* at $s^* = 0.99$, 0.50, and 0.10 for OP#1, #2, and #3 over the non-dimensional streamwise location m^* are presented in Figures 7.6, 7.7 and 7.8, respectively. At $s^* = 0.99$, the flow has a high negative incident angle at the inlet of the blade channel especially for OP#1 as described in Section 1.3.2. In particular, a high negative incidence of the flow at the inlet generates a stalled velocity region on the blade pressure side near the leading edge at OP#1. The development of the inter-blade vortex structure is clearly detected in the vector plot at the middle of the channel at OP#1 and OP#2, which creates a partially high circumferential velocity region. Furthermore, the distribution of the non-dimensional

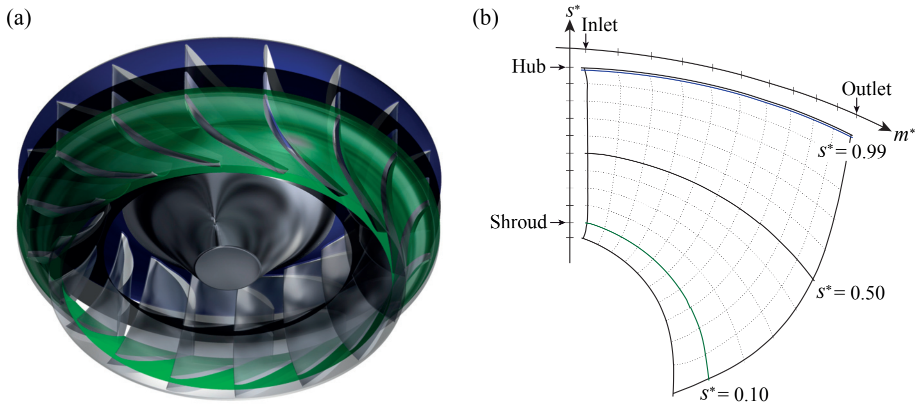

Figure 7.5 – Investigated non-dimensional span-wise location $s^* = 0.99$ (blue), 0.50 (black), 0.10 (green) in the runner domain (a) and on the meridional plane (b)

(a) OP#1

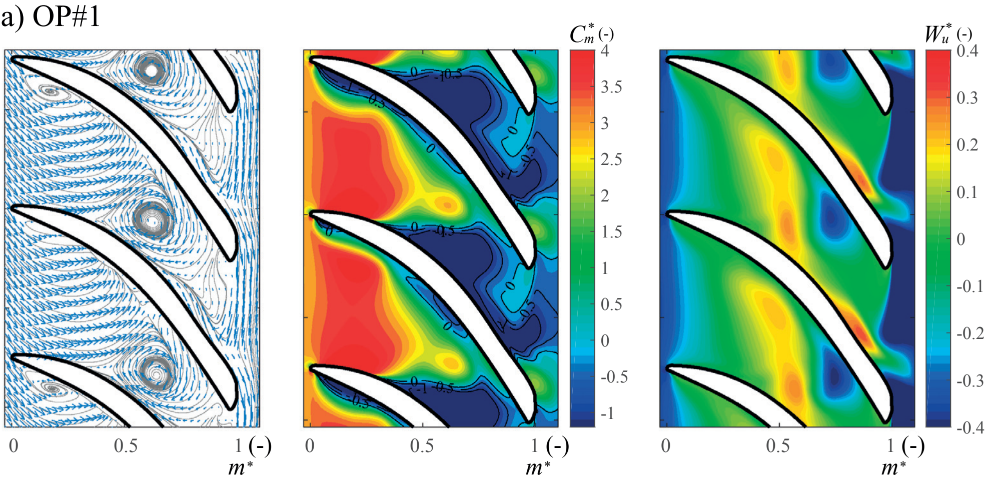

(b) OP#2

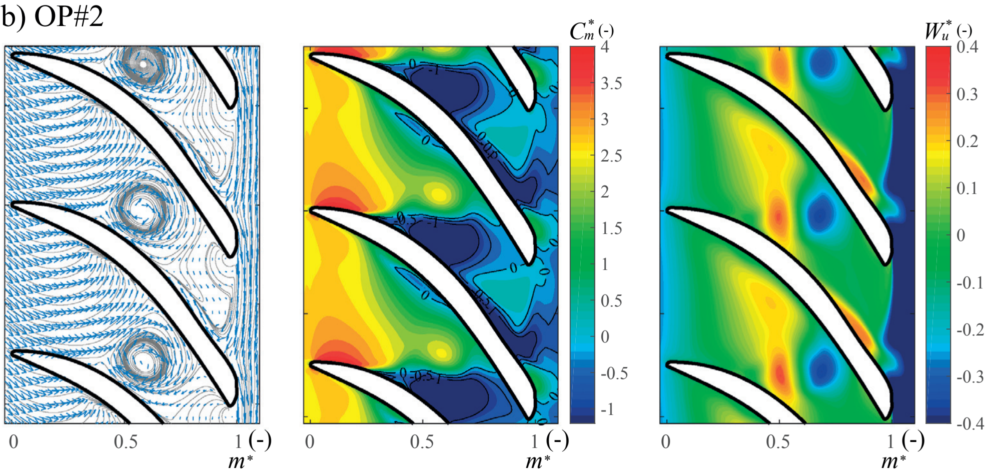

(c) OP#3

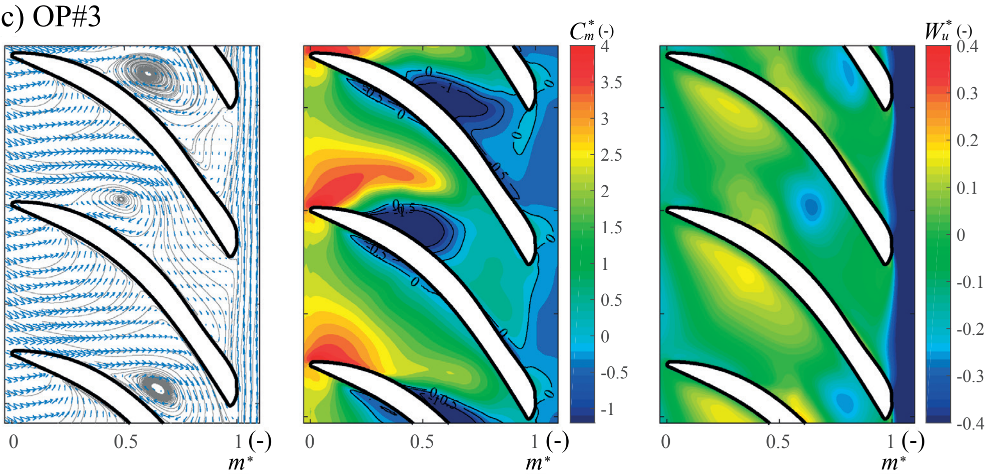

Figure 7.6 – Velocity vectors together with the tangential flow streamlines and the distributions of the non-dimensional meridional velocity C_m^* and the non-dimensional relative circumferential velocity W_u^* at constant span-wise location of $s^* = 0.99$ for OP#1 (a), #2 (b), and #3 (c). All velocities are averaged over four runner revolutions

(a) OP#1

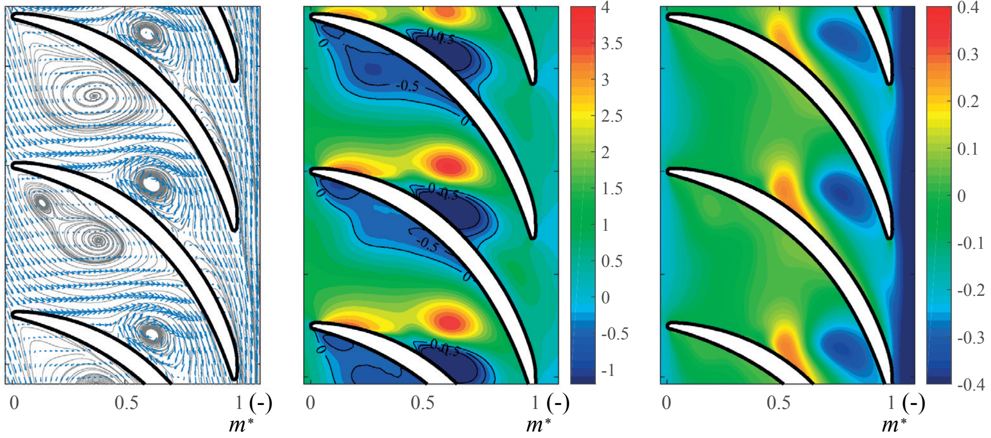

(b) OP#2

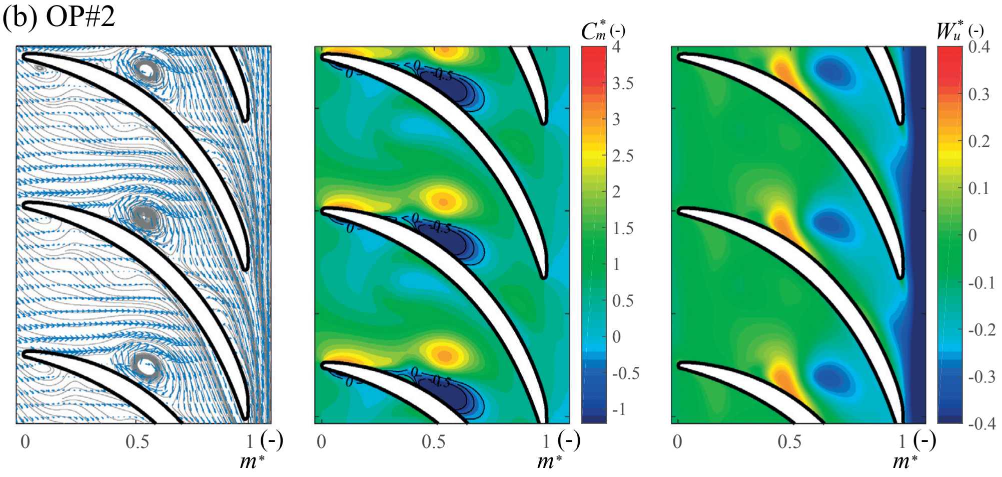

(c) OP#3

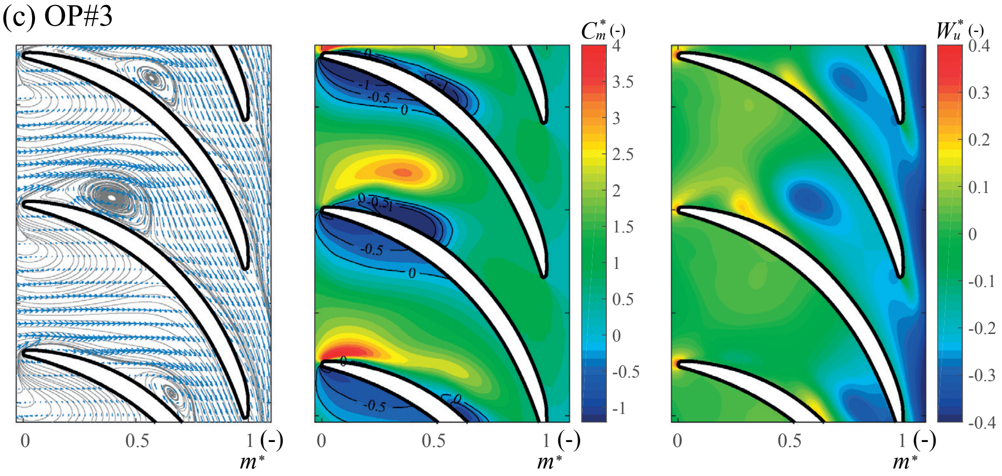

Figure 7.7 – Velocity vectors together with the tangential flow streamlines and the distributions of the non-dimensional meridional velocity C_m^* and the non-dimensional relative circumferential velocity W_u^* at constant span-wise location of $s^* = 0.50$ for OP#1 (a), #2 (b), and #3 (c). All velocities are averaged over four runner revolutions

(a) OP#1

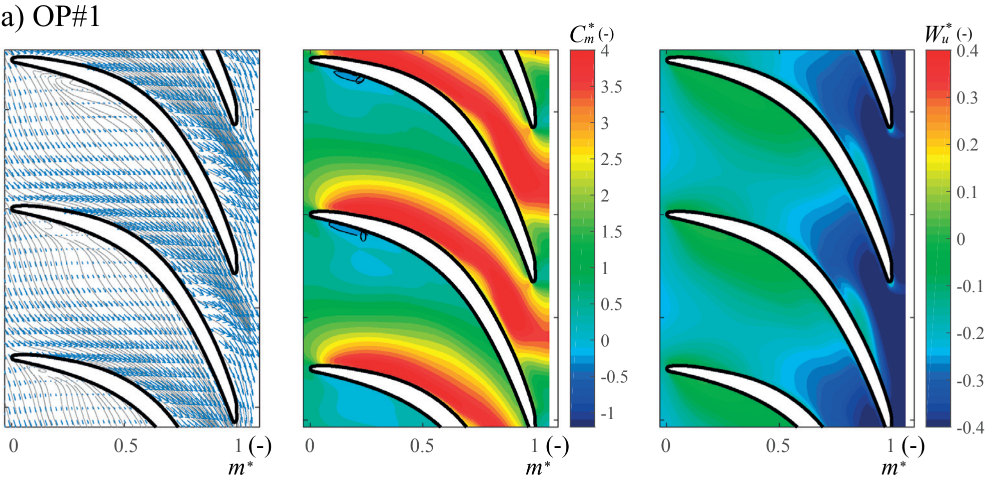

(b) OP#2

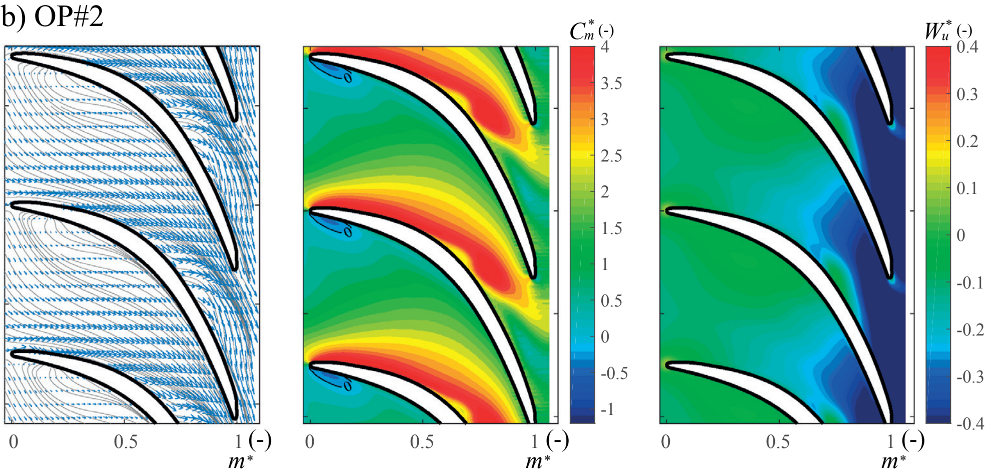

(c) OP#3

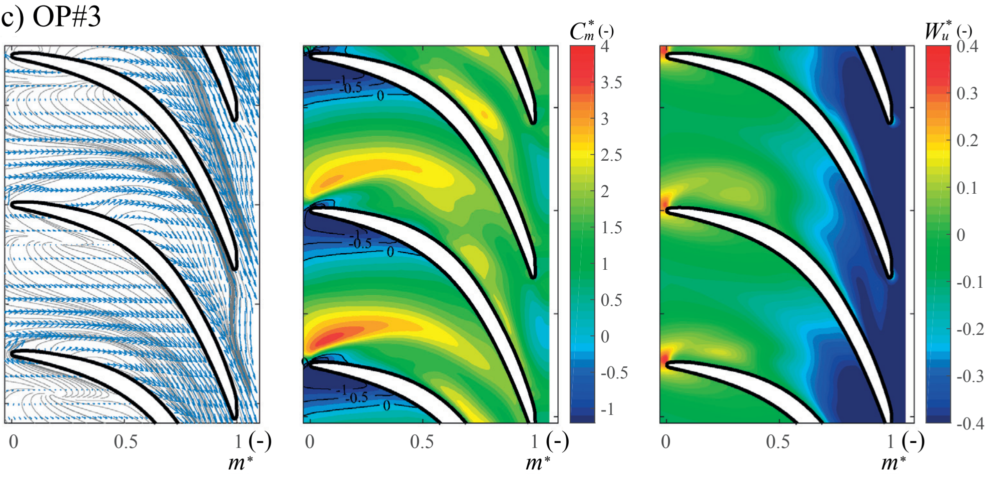

Figure 7.8 – Velocity vectors together with the tangential flow streamlines and the distributions of the non-dimensional meridional velocity C_m^* and the non-dimensional relative circumferential velocity W_u^* at constant span-wise location of $s^* = 0.10$ for OP#1 (a), #2 (b), and #3 (c). All velocities are averaged over four runner revolutions

meridional velocity reveals the development of a backflow region dominating the flow near the blade channel outlet especially at OP#1, which is also suggested by the wall pressure difference of the blade estimated in Section 4.4. On the contrary, the flow at the inlet has a relatively high meridional velocity, resulting in a significantly non-uniform distribution of the velocity inside the blade channel near the hub. It is assumed that this backflow region is generated by the flow separation on the hub, which is caused by a misaligned flow condition inside the blade channel induced by a high negative incident angle. The intensity of the backflow region near the blade channel outlet is reduced at OP#2, although the vortex structure is still detected at the middle of the channel. Since the negative flow incident angle is reduced when the operating conditions are changed, the location of the inter-blade vortex is slightly shifted upstream in the blade channel compared to OP#1. At OP#3, the backflow region at the blade outlet is considerably decreased. Correspondingly, the inter-blade vortex structure is also reduced as the flow incident angle increases.

At the middle span-wise location ($s^* = 0.50$), the development of the stalled region at the outlet of the blade channel is no longer observed, and the non-uniform distribution of the velocity is clearly decreased compared to the flow near the hub. At OP#1, the velocity vector and the tangential flow streamline indicate the clear development of the inter-blade vortex structure at $m^* = 0.60$. A stalled region also appears on the blade pressure side near the leading edge due to the negative flow incidence at the inlet of the blade channel, therefore the low meridional velocity region can be confirmed in the distribution of C_m^*. At OP#2, this low velocity region on the blade pressure side near the inlet is considerably decreased and shifted to the upstream with respect to the increase of the flow incident angle. Hence, the location of the inter-blade vortex is also slightly shifted to the upstream. The meridional velocity and the circumferential velocity are partially intensified due to the the inter-blade vortex structure. However, its magnitude is lower than the velocity at OP#1, suggesting that the strength of inter-blade vortices is decreased. At OP#3, the low velocity zone is furthermore shifted to the upstream and it starts preventing the incoming flow at the leading edge, therefore the velocity distribution near the inlet shows slightly unstable pattern. The flow especially on the blade pressure side near the leading edge is blocked by the low velocity region, which results in a partially positive flow incidence on the suction side. It appears that the inter-blade vortex structure is considerably reduced due to the increase of the flow incident angle.

At $s^* = 0.10$, the velocity is more uniformly distributed than the velocity near the hub and the middle-span plane. Since the inter-blade vortex structure flows to the outlet of the blade channel at this span-wise location, the velocity vector and the tangential flow streamline show no vortex structures inside the blade channel. Even though the meridional velocity becomes partially low near the leading edge on the blade pressure side at OP#1 and OP#2, the distribution of the meridional and circumferential velocities are uniformly distributed. Furthermore, the amplitude of the meridional velocity is obviously higher than the ones at the other planes, suggesting that the main flow stream is concentrated on the shroud side. At OP#3, the meridional velocity near the leading edge on the pressure side of the blade has a negative meridional velocity and block the flow. As a consequence, the flow near the leading

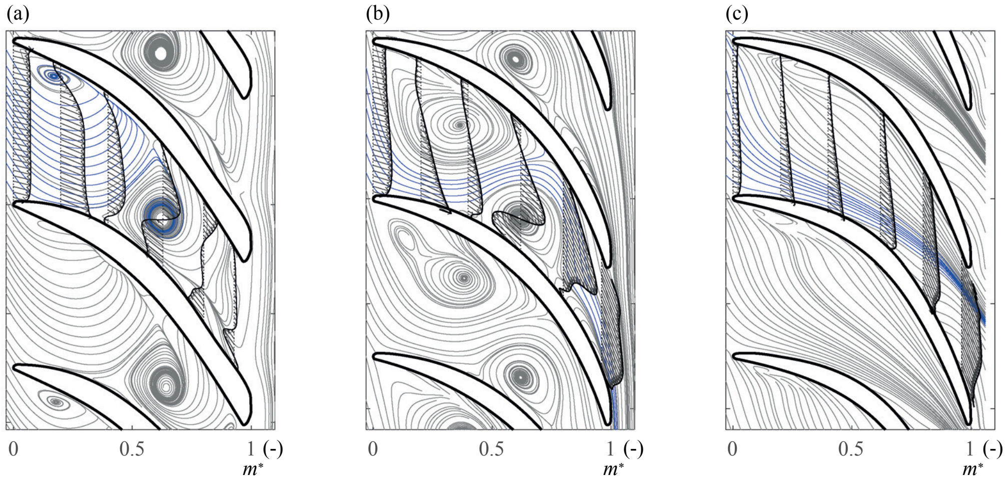

Figure 7.9 – Distribution of the velocity along the blade together with the tangential flow streamlines at the span-wise location $s^* = 0.99$ (a), 0.50 (b). and 0.10 (c) for OP#1. The flow streamlines starting from the blade channel inlet are highlighted in blue. All velocities are averaged over four runner revolutions.

edge on the suction side is throttled and it induces a partially positive flow incidence at the blade leading edge.

In Figure 7.9, the distributions of the velocity along the blade chamber line C_b (see Appendix C for further details) at several streamwise locations for three span-wise planes at OP#1 are presented. The tangential flow streamline at OP#1 is shown together, and the streamlines starting from the inlet of the blade channel are highlighted by the blue lines. It is found that the velocity at the inlet is uniformly distributed, whereas the velocity starts to be non-uniformly distributed in the blade channel at about $m^* = 0.40$ due to the high negative flow incidence. Furthermore, the velocity distribution along the inter-blade vortex structure shows a typical velocity pattern which is characterized by a forced vortex inside the vortex core and a free vortex outside. More interestingly, the flow streamlines from the inlet near the hub (see the blue line in Figure 7.9a) converge on the inter-blade vortex structure and no streamlines from the inlet reach the outlet, which implies that the flow is separated from the hub. On the contrary, the flow near the shroud has an uniform flow distribution and the streamlines from the inlet smoothly flows toward the blade channel outlet. This strongly suggests that the flow structure near the hub is of key importance to the development of inter-blade vortices.

7.3.2 Meridional velocity distribution

As confirmed by the velocity survey at different span-wise locations, the flow velocity inside the blade channel features a highly non-uniform distribution especially near the hub. Furthermore, the development of the backflow region near the hub close to the outlet is observed especially at OP#1 as expected from the on-board pressure measurement in Section 4.3.4.

In Figure 7.10, the averaged distribution of the meridional velocity C_m^* on the meridional plane is presented. The velocity is circumferentially averaged from the suction side to the pressure side at each streamwise and span-wise location in a single blade channel. At OP#1, the locations of the simulated inter-blade vortex as well as the vortex locations estimated by the visualization are shown together. It reveals that the flow having a high meridional velocity is clearly concentrated on the shroud side for all the operating conditions, whereas the flow close to the hub is dominated by a low velocity flow especially near the outlet of the blade channel. At OP#1, the development of the backflow region is detected near the hub close to the outlet, yielding distorted velocity distribution at the blade channel outlet. The backflow region is clearly reduced when the operating condition is changed, and it almost disappears at OP#3. Furthermore, the inception point of the backflow region at OP#1 corresponds to the onset of the inter-blade vortex on the hub, suggesting that the development of the backflow region near the hub is closely related to the inter-blade vortex formation.

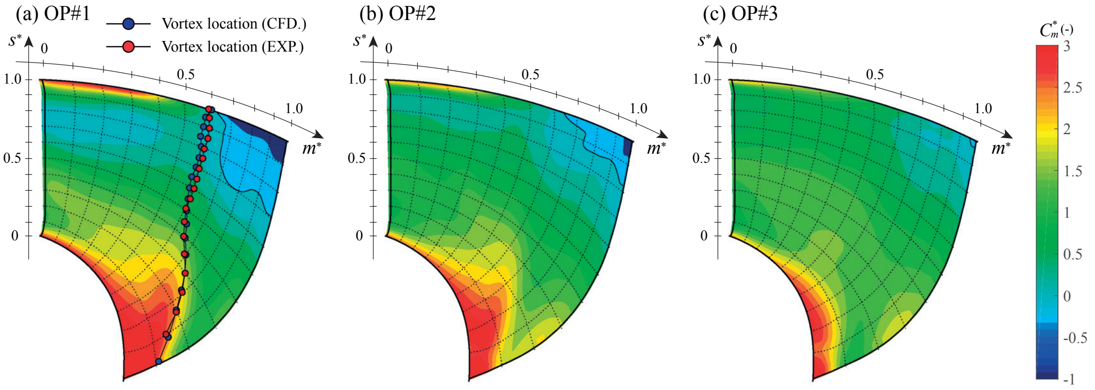

Figure 7.10 – Meridional distribution of the meridional velocity C_m^* averaged in one blade channel at OP#1, #2, and #3. At OP#1, the simulated vortex locations as well as the vortex center locations estimated by the visualization are shown together. The threshold of a backflow region is highlighted by a solid black line.

7.3.3 Flow incident angle

As shown in Section 1.3.2, the main difference of the targeted operating conditions is the variation of the velocity triangle at the runner inlet. In addition, the velocity surveys reveal that the non-uniform flow distribution induced by the incident angle at the blade inlet is strongly linked to inter-blade vortex development. In this section, the flow incident angle at the blade channel inlet β'_1 and the relative flow angle at the blade channel outlet $\beta'_{\bar{1}}$ are calculated by the trigonometric relationship of the relative circumferential velocity and the meridional velocity, as follows.

$$\begin{aligned}\beta'_1 &= \tan^{-1}\left(\frac{W_{u1}}{C_{m1}}\right) = \tan^{-1}\left(\frac{U_1 - C_{u1}}{C_{m1}}\right) = 90 - \beta_1 \\ \beta'_{\bar{1}} &= \tan^{-1}\left(\frac{W_{u\bar{1}}}{C_{m\bar{1}}}\right) = \tan^{-1}\left(\frac{U_{\bar{1}} - C_{u\bar{1}}}{C_{m\bar{1}}}\right) = 90 - \beta_{\bar{1}}\end{aligned} \tag{7.1}$$

The coordinate is settled as shown in Figure 7.11, and the sign of the angle is defined according to the settled coordinate. The geometric blade angles at the inlet β'_{1b} and the outlet $\beta'_{\bar{1}b}$ at investigated span-wise locations are summarized in Table 7.1.

The variation of the flow incident angle at the inlet β'_1 and the relative angle at the outlet $\beta'_{\bar{1}}$ from the blade suction side to the pressure side at three span-wise locations for OP#1, #2, and #3 is shown in Figure 7.12. At the inlet, the circumferential variation of the flow incident angle β'_1 is not remarkably high except for OP#3. At OP#1 and OP#2, the incident angle constantly has a negative incident angle which is lower than the blade geometrical angle β'_{1b} from the

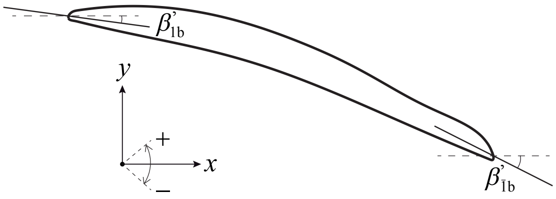

Figure 7.11 – Definition of the incident angle at the inlet of the blade channel and relative flow angle at the outlet of the blade channel

Table 7.1 – Blade geometric angle at given span-wise locations

span-wise location s^* (-)	β'_{1b} (°)	$\beta'_{\bar{1}b}$ (°)
0.99	-14.2	-47.1
0.50	-11.9	-61.2
0.10	-11.6	-68.0

blade suction side to the pressure side. β'_1 becomes slightly higher at $s^* = 0.01$ due to the high meridional velocity. At OP#3, the variation of the flow incident angle is obviously high at the middle span-wise location ($s^* = 0.50$) and $s^* = 0.90$, which is caused by the low velocity region developed at the leading edge on the pressure side. At $s^* = 0.50$, the incident angle is partially positive near the blade suction side and pressure side due to the stalled velocity region at the leading edge on the pressure side (see Figure 7.7). At $s^* = 0.10$, β'_1 at OP#3 becomes lower than -90 ° near the pressure side due to the development of the backflow region at the leading edge.

At the outlet of the blade channel, since the relative flow angle $\beta'_{\bar{1}}$ near the hub $s^* = 0.99$ is mostly lower than -90 ° or higher than 90 ° due to the stalled velocity region near the hub, the data are not shown in Figure 7.12b. At $s^* = 0.50$, $\beta'_{\bar{1}}$ is kept almost constant from the suction side to the pressure side, and its value almost corresponds to the geometric angle $\beta'_{\bar{1}b}$. The relative flow angle $\beta'_{\bar{1}}$ at $s^* = 0.10$ also has a value close to the geometric angle $\beta'_{\bar{1}b}$, even though a slight variation is observed in the middle of the blade channel due to the inter-blade vortex structure near the outlet at this span-wise location.

In Figure 7.13, the averaged flow incident angle β'_1 and relative flow angle $\beta'_{\bar{1}}$ in one single blade channel are presented over the non-dimensional span-wise location s^*. The geometrical angles of the blade at the inlet β'_{1b} and the outlet $\beta'_{\bar{1}b}$ are also shown together. At the inlet, OP#1 and OP#2 feature a similar variation from the hub to the shroud. Furthermore, the calculated flow incident angles at OP#1 and OP#2 are close to the estimated flow incident angle from the velocity triangle in Section 1.3.2 (see dashed blue line in Figure 7.13a), even though β'_1 becomes slightly higher near the hub and the shroud due to a high meridional velocity. As explained in Section 1.3.2, the flow incident angle at OP#1 has a considerably high negative incidence at the inlet compared to the blade geometrical angle β'_{1b}. At OP#3,

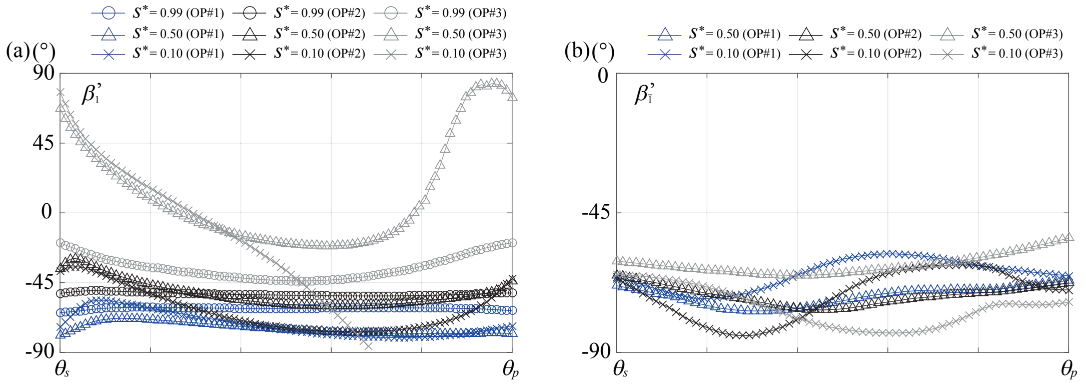

Figure 7.12 – Variations of the flow incident angle at the blade channel inlet β'_1 (a) and the relative flow angle at the blade channel outlet $\beta'_{\bar{1}}$ (b) from the blade suction side to the pressure side for OP#1, #2, and #3. The angles are calculated from the averaged velocity over four runner revolutions

β'_1 is higher than the blade geometrical angle β'_{1b}. This is caused by the development of the recirculating region on the blade pressure side near the leading edge resulting in the positive flow incident angle on the suction side of the blade.

At the outlet, the difference of the relative flow angles $\beta'_{\bar{1}}$ at three different conditions is not as obvious as the flow incident angle β'_1. In the vicinity of the hub, the relative flow angle $\beta'_{\bar{1}}$ is lower than -90 °, which is caused by the negative meridional velocity in the stalled region especially at OP#1. The relative flow angle $\beta'_{\bar{1}}$ is gradually increased as reduction of the backflow velocity region with regard to the span-wise location. At the middle span-wise location, $\beta'_{\bar{1}}$ almost corresponds to the geometrical blade angle $\beta'_{\bar{1}b}$, and it is nearly aligned to $\beta'_{\bar{1}b}$ between $s^* = 0.50$ and the shroud for all the operating conditions. Near the shroud side around $s^* = 0.90$, a deviation from the geometrical angle is observed especially at OP#1 due to the inter-blade vortex structure on one hand, and not at OP#2 and OP#3 on the other hand. The presented comparison suggests that the flow characteristics at the blade channel outlet according to the relative flow angle $\beta'_{\bar{1}}$ are similar for the presented operating at conditions, except for the development of the backflow region near the hub. In contrast, the flow incident angle β'_1 has a distinct variation for the different operating conditions, which plays a decisive role for inter-blade vortex development.

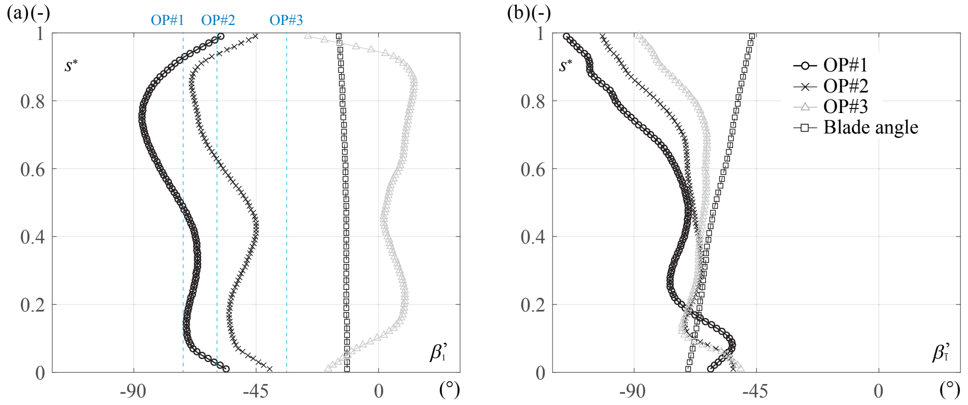

Figure 7.13 – Variations of the flow incident angle at the blade channel inlet β'_1 (a) and the relative flow angle at the blade channel outlet $\beta'_{\bar{1}}$ (b) over the non-dimensional span-wise location s^*. The angles are averaged in one blade channel and calculated from the averaged velocity over four runner revolutions

7.4 Inter-blade vortex intensity

7.4.1 Vorticity distribution inside blade channel

To characterize the intensity of the inter-blade vortex for the different operating conditions, the distributions of the vorticity ω_z at the constant span-wise locations $s^* = 0.99$, 0.50, and 0.10 for OP#1, #2, and #3 are presented in Figure 7.14. At OP#1, a strong clockwise-rotating vorticity appears in the middle of the channel due to the inter-blade vortex structure. The strong vorticity is generated by the shear layer created between the flow with a high velocity from the inlet of the blade channel and the stalled region developing near the outlet of the blade channel. Due to the interaction of the stalled velocity region near the outlet of the blade channel with the stalled region in the draft tube cone after the blade ($m^* > 1$), a strong shear layer leading to a high vorticity ω_z is created at the outlet of the blade channel at $m^* = 1$. At the middle of the plane ($s^* = 0.50$), the high vorticity region due to the inter-blade vortex region is still clearly developed in the middle of the channel. The backflow region near the outlet of the runner is diminished at this span-wise location and therefore the strong vorticity at the runner outlet is no longer observed. At $s^* = 0.10$, the inter-blade vortex structure is developed near the outlet of the runner and the velocity distribution is relatively uniform. Therefore, the vorticity only appears near the outlet of the blade channel and no remarkable vorticity is detected inside the blade channel. At OP#2, the distributions of the vorticity at the three span-wise locations are similar to OP#1. However the strength of the vorticity is reduced especially at $s^* = 0.99$ and 0.50, suggesting that the intensity of the inter-blade vortex is decreased at OP#2.

At OP#3, the appearance of the vorticity distribution is dramatically changed. In the vicinity of the hub, the strength of the vorticity is significantly reduced compared to OP#1 and OP#2 and the locations of inter-blade vortices appear to be quite unstable. Since the partially positive flow incident angle appears at the inlet, the positive vorticity region appears at the leading edge on the suction side at $s^* = 0.50$ and $s^* = 0.10$.

7.4.2 Vortex circulation

For a quantitative evaluation of inter-blade vortex intensity, the vortex circulation $\mathit{\Gamma}$ is calculated and compared for OP#1, #2 and #3. The circulation is given by the contour integral of the velocity on the vortex threshold, which is transformed into the surface integral of the vorticity by Stokes' theorem, such that

$$\mathit{\Gamma} = \oint_{\mathscr{C}} C \cdot d\vec{l} = \int_S \vec{\mathit{\Omega}} \cdot \vec{n} dS \qquad (7.2)$$

where $\mathscr{C}$ and S represent the contour and the surface of the vortex region, respectively. For an accurate evaluation of the circulation, it is necessary to correctly determine the vortex

(a) OP#1

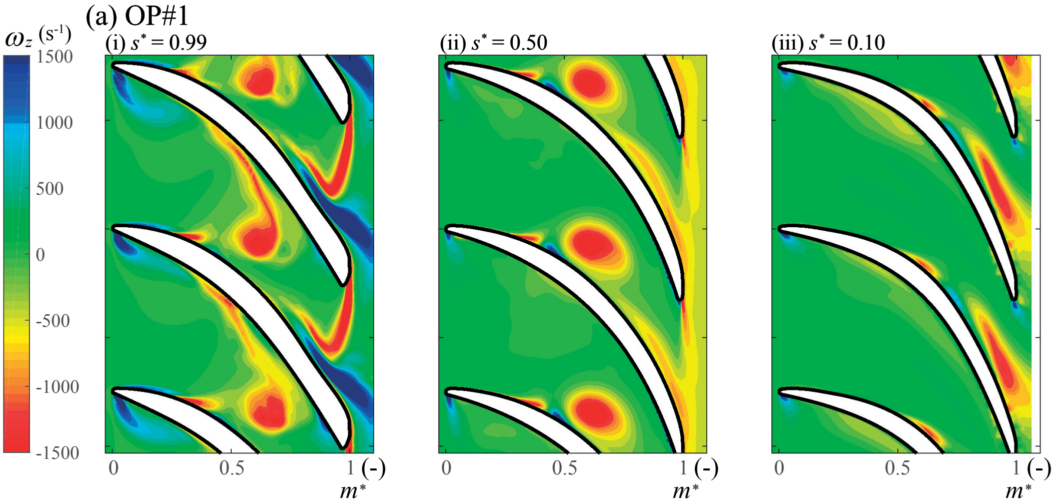

(b) OP#2

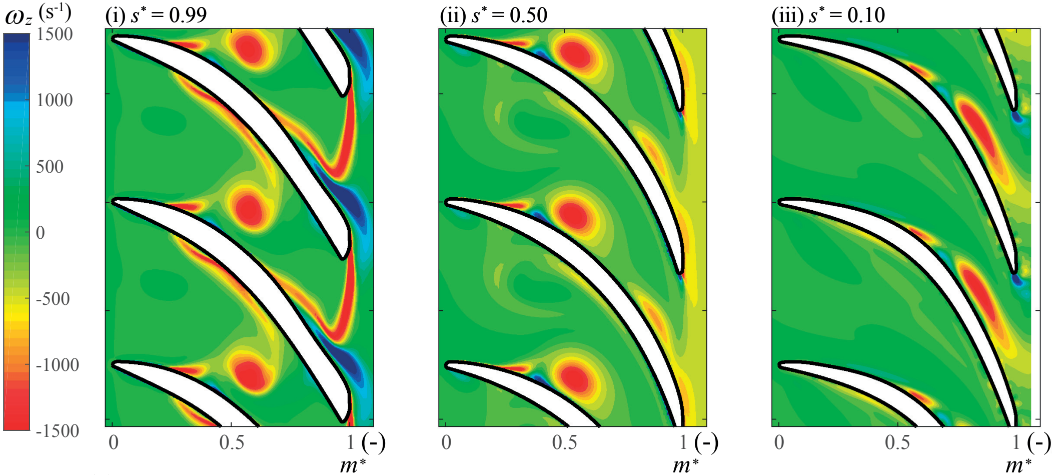

(c) OP#3

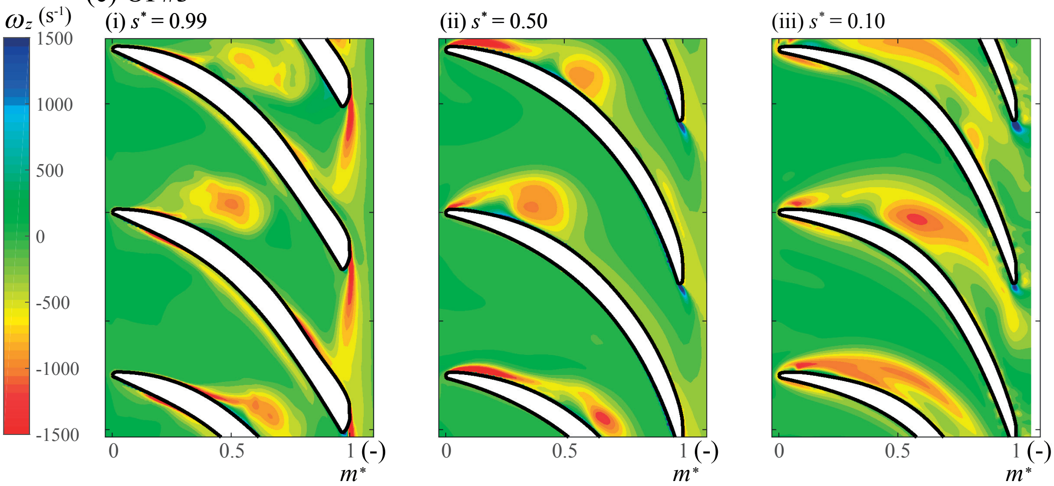

Figure 7.14 – Distribution of the vorticity ω_z at constant span-wise locations $s^* = 0.99$, 0.50, and 0.10 for OP#1 (a), #2 (b), and #3 (c)

threshold. In the presented case, the inter-blade vortex threshold is identified by $Q^* = 0$ (for further details, the reader may refer to Appendix D). In Figure 7.15, the circulation Γ evaluated at constant span-wise locations s^* in one blade channel is presented. The circulation is calculated every $s^* = 0.05$ based on the averaged vorticity over four runner revolutions. It should be noted the appearance of inter-blade vortices at OP#3 is unstable and its threshold is not accurately detected, which increases the calculation error at OP#3. Nonetheless, it demonstrates that the circulation Γ at OP#1 is higher than the other operating conditions, which confirms that the inter-blade vortex is most intensely developed at OP#1. Furthermore, the high value of the circulation Γ as well as the high standard deviation appear especially in the vicinity of the hub, which evidently shows that the strong inter-blade vortex structure is generated near the hub. Then, the strength of inter-blade vortices is gradually decayed from the hub to the shroud side due to the viscous effect. As emphasized in Section 7.3, inter-blade vortex development near the hub is heavily related to the backflow formation on the hub, which may be caused by the flow separation. Further analyses to correlate the flow near the hub with inter-blade vortex development is given by study of the skin-friction in Section 7.6.

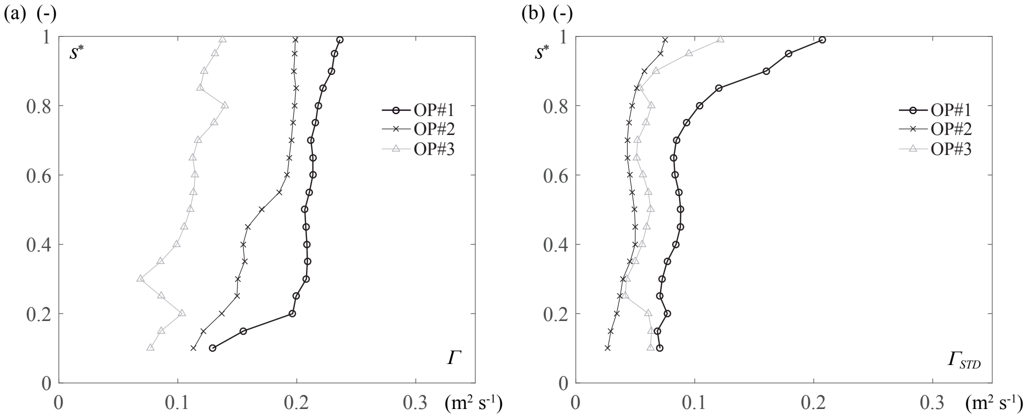

Figure 7.15 – Comparison of the calculated circulation Γ (a) and corresponding standard deviation (b) at OP#1, #2, and #3. The circulation Γ is evaluated at each constant span-wise location using the inter-blade vortex threshold identified by $Q^* = 0$

7.5 Pressure distribution

7.5.1 Pressure distribution in the blade channel

Vortex development is accompanied by a low pressure zone at the vortex core, which may cause the development of cavitation. As shown in Figure 7.4, the cavitation volume of the inter-blade cavitation vortex is remarkably high at OP#1, suggesting that a low pressure region is generated by the strong inter-blade vortex structure. In Figure 7.16, the distribution of the averaged pressure factor C_p at the middle span-wise location $s^* = 0.50$ for three operating conditions are presented. At OP#1, the notable development of a low pressure region at the vortex core appears due to the strong inter-blade vortex formation. When the operating conditions are changed, the low pressure zone is clearly reduced with respect to the decrease of the inter-blade vortex intensity. Even though the low pressure core is still observed at OP#2, it becomes considerably small and is not evident in every bade channel at OP#3.

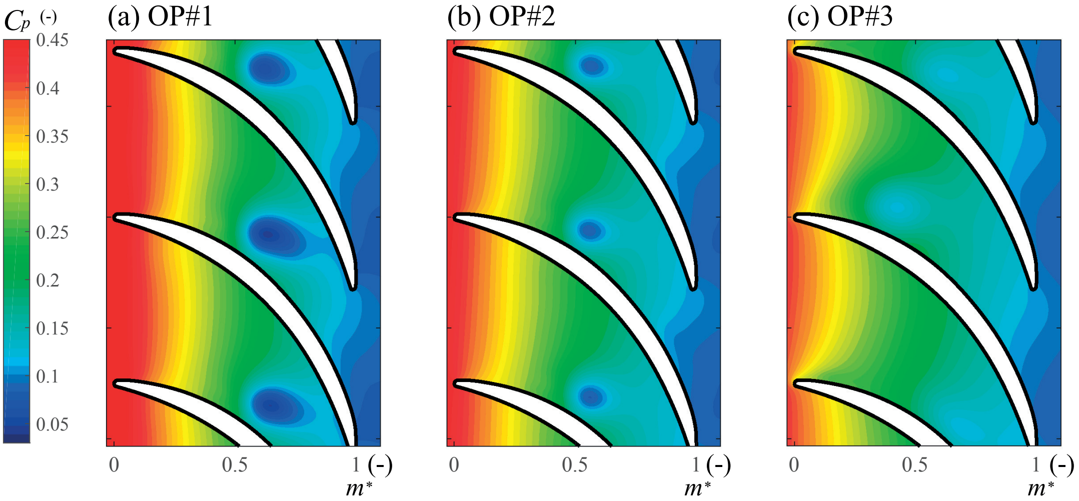

Figure 7.16 – Distribution of the pressure factor C_p at the middle span-wise location $s^* = 0.50$ for OP#1, #2, and #3. The pressure is averaged over four runner revolutions.

7.5.2 Blade loading

Using on-board pressure measurements, the wall pressure difference between the pressure and suction sides of the blade shows a negative blade loading especially near the hub at deep part load operation (see Section 4.3.4). In Figure 7.17, the comparisons of the averaged distribution of the static pressure coefficient on the blade wall as well as the wall pressure difference between the pressure side and suction side along the non-dimensional streamwise location m^* at three different span-wise locations are presented. The static pressure coefficient Ψ_b is calculated by the reference rotational velocity of the runner $U_{ref} = 1/2\omega D_{ref}$ and the mean static pressure at the inlet of the blade channel as follows:

$$\Psi_b = \frac{p - p_1}{1/2\rho U_{ref}^2} \tag{7.3}$$

In the vicinity of the hub ($s^* = 0.99$), there is a peak in the static pressure coefficient on the suction side of the blade observed at the blade leading edge especially for OP#1, caused by the negative flow incident angle resulting in a high pressure on the suction side of the blade and low pressure on the pressure side of the blade. Thus, the pressure difference indicates an intense negative peak near the leading edge especially at OP#1. The peak of the static pressure coefficient at the leading edge is decreased as reduction of the negative flow incident angle from OP#1 to OP#3, which is also confirmed by the wall pressure difference. The static pressure coefficient on the blade pressure side becomes higher than the value on the suction side in the middle of the blade resulting in a positive blade loading, and the different operating conditions have similar distributions. However, downstream of the inter-blade vortex region at about $m^* = 0.60$, the static pressure coefficient at OP#1 on the suction side starts to increase. The pressure on the suction side eventually becomes higher than the value on the pressure side at around $m^* = 0.70$, leading to a negative blade loading near the blade outlet. It is considered that this negative wall pressure difference between blade pressure and suction sides is caused by the development of the backflow region close to the blade outlet (see Figure 7.6). The pressure difference reaches a minimum near $m^* = 0.95$, then it becomes zero at the trailing edge of the blade. By comparison of the three different operating conditions, it is confirmed that the intensity of the negative wall pressure difference is clearly reduced as a backflow region dissipates.

In the middle span-wise location ($s^* = 0.50$), the static pressure coefficient on the pressure side is almost linearly decreased, whereas the influence of the inter-blade vortex on the suction side of the blade is clearly observed. Furthermore, the location of the static pressure drop is moved to upstream from OP#1 to OP#3 according to the shift of the inter-blade vortex location. Due to the decrease of static pressure on the blade suction side, the blade loading is partially increased in the middle of the blade channel. Downstream of the inter-blade vortex region, the wall pressure difference is kept almost constant, and the negative blade loading observed in the vicinity of the hub near the blade outlet is no longer observed at this span-wise location.

In the vicinity of the shroud ($s^* = 0.10$), the distribution of the static pressure coefficient on both the pressure and suction sides of the blade becomes much more uniform compared to the ones at the other planes shown above. The wall pressure difference between the pressure and suction sides is entirely increased, and the blade loading remains positive over all the streamwise location, except for the instant pressure drop at the trailing edge. Since the inter-blade vortex structure is only observed near the outlet of the blade channel, its influence is lightly detected on the blade suction side near the blade outlet at OP#1 and OP#2. The uniform distribution of the static pressure coefficient and the high blade loading along the entire blade wall results from the main flow stream consolidated on the shroud side.

(a) $s^* = 0.99$

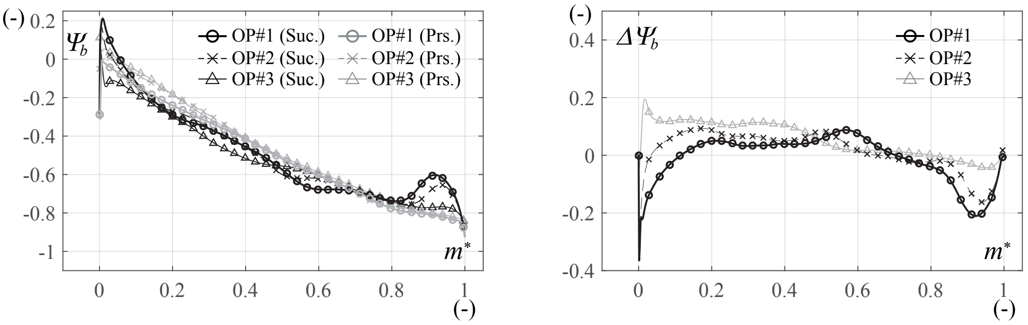

(b) $s^* = 0.50$

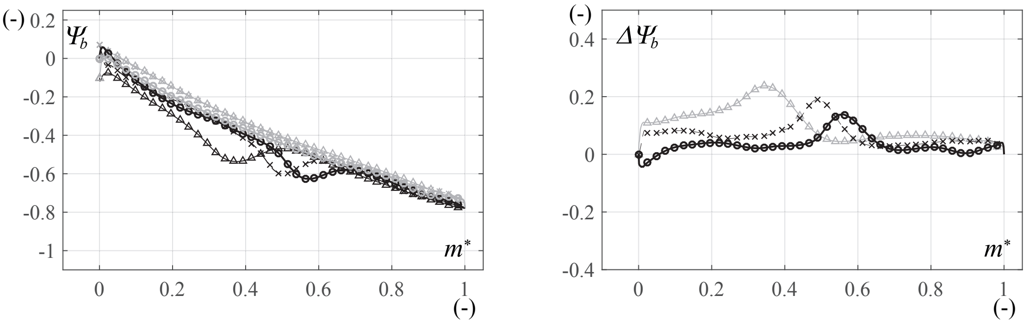

(c) $s^* = 0.10$

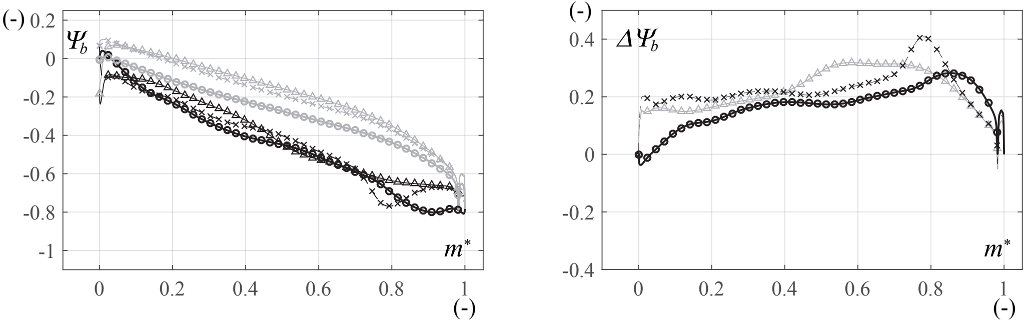

Figure 7.17 – Comparison of the static pressure coefficient Ψ_b along the non-dimensional streamwise location m^* on both the suction and pressure side of the blade (left side) and the difference of the static pressure coefficient $\Delta\Psi_b$ (right side) at three span-wise locations $s^* = 0.99$ (a), 0.50 (b), and 0.10 (c) for OP#1, #2, and #3

Table 7.2 – Comparison of the simulated non-dimensional pressure difference $\Delta\Psi_b$ with the experimental results at both locations #1 and #2 for on-board pressure measurements

	OP#1		OP#2		OP#3	
	EXP.	CFD.	EXP.	CFD.	EXP.	CFD.
Location #1	1.41×10^{-3}	1.31×10^{-4}	0.057	0.051	0.083	0.073
Location #2	0.235	0.243	0.185	0.181	0.131	0.173

Using on-board pressure measurements on the runner blade, same wall pressure differences highlighting a low blade loading near the hub and a high blade loading on the shroud side near the blade trailing edge are observed. In Table 7.2, the comparison of the static pressure difference $\Delta\Psi_b$ at both locations #1 and #2 in the simulation with the on-board pressure measurement results (see Table 4.1 for the precise location) is presented. It can be confirmed that the pressure difference at both the locations are accurately estimated by the performed simulation, although slight discrepancy at location #2 for OP#3 is observed.

7.5.3 Pressure fluctuation on the blade

In the experimental investigation by on-board pressure measurements in Section 4.3, it is shown that the presence of an inter-blade vortex induces a stochastic pressure fluctuation especially on the blade suction side. In the performed simulation, the stochastic pressure fluctuation induced by the inter-blade vortex is also observed. In Figure 7.18, the centered pressure signals of the simulation acquired from the same locations as the pressure transducers on the blade are presented. As shown in the experimental investigations in Section 4.3, the influence of the inter-blade vortex on the blade pressure side is relatively minor in both the locations. The main fluctuations observed in the simulated pressure signals are the fluctuations caused by the blade passing, even though the pressure at OP#1 is slightly oscillated stochastically. On the contrary, pressure fluctuations on the blade suction side are remarkable. Especially at location #2, the amplitude of the pressure fluctuation at OP#1 is considerably intensified, although the fluctuation is stochastic, which is also observed in the measured pressure signal by on-board measurements (see Section 4.3).

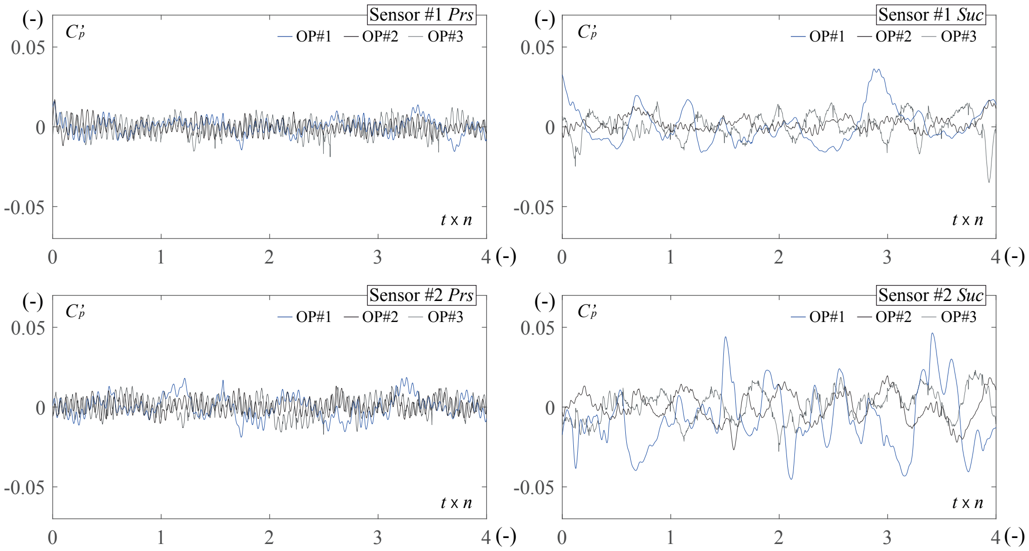

Figure 7.18 – Comparison of the simulated pressure fluctuations at the same locations as on-board pressure measurements on the runner blade (#1 Prs, #1 Suc, #2 Prs and #2 Suc) for OP#1, #2, and #3 over four runner revolutions

(a) Blade pressure side

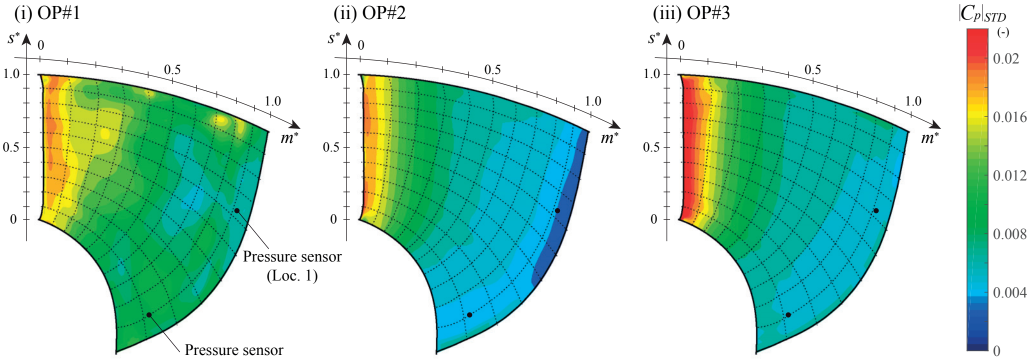

(b) Blade suction side

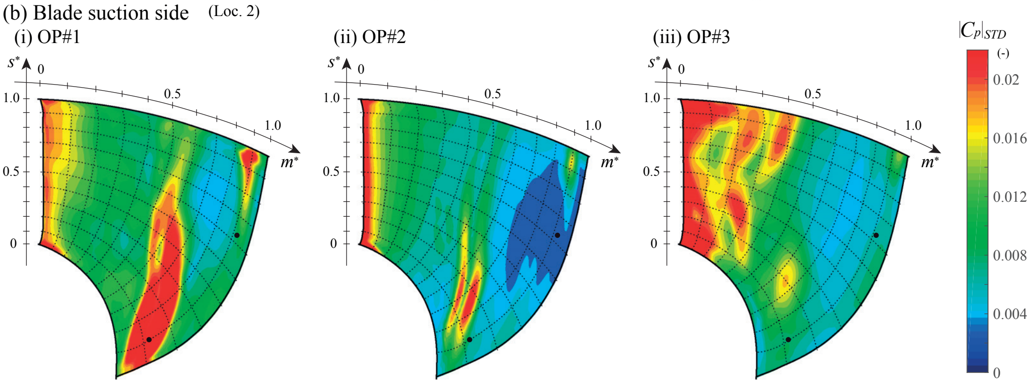

Figure 7.19 – Comparison of the standard deviation of pressure oscillations on the blade pressure side (a) and the blade suction side (b) for OP#1, #2, and #3

In Figure 7.19, the standard deviation of the static pressure on the blade suction and pressure sides for the three operating conditions is presented. On the blade pressure side, the influence of the inter-blade vortex is not clearly confirmed. A high standard deviation only appears at the leading edge, due to the pressure oscillation caused by the rotor-stator interaction. In contrast, the region of high standard deviation appears on the suction side. Especially at OP#1, the high standard deviation is obviously caused by the inter-blade vortex region where location #2 is included, suggesting that the stochastic pressure oscillation observed in Figure 7.18 is induced by the presence of the inter-blade vortex. When the operating conditions are changed, the high standard deviation in the inter-blade vortex region is reduced with respect to the decrease of the inter-blade vortex intensity. The influence of the rotor-stator interaction is strongly observed at OP#3. It is assumed that a small vortex structure near the leading edge on the suction side caused by a partially positive flow incident angle at OP#3 generates pressure oscillations, leading to a high standard deviation near the leading edge. The presented results confirm intensified pressure oscillations on the suction side of the blade caused by inter-blade vortices and it is assumed that pressure fluctuations are caused by the stochastic behaviors of inter-blade vortices. Further investigations are needed to correlate these characteristics with transient flow structures inside the blade channel to better understand a stochastic nature of inter-blade vortices.

7.6 Flow topology

7.6.1 Skin-friction pattern on the hub

As shown in the velocity survey in Section 7.3, the development of the inter-blade vortex is assumed to be closely related to the misaligned flow condition inside the blade channel caused by the high negative flow incident angle. Furthermore, the backflow development on the hub near the runner outlet is also found to be a key component to the underlying mechanisms of inter-blade vortex development. A backflow region is often caused by flow separation, and an adverse pressure gradient along flow streams generally plays a decisive role for its occurrence [76, 81]. Therefore, the flow inside hydraulic pumps has higher risk for the occurrence of flow separations, which trigger various types of flow instabilities. On the contrary, the flow inside hydraulic turbines is usually prone to suppress flow separations since the pressure gradient is normally negative along flow streamlines. However, at extremely low discharge conditions of pump-turbines in generating mode, it was reported that the flow may locally experience an adverse pressure gradient, and flow instabilities related to flow separations, such as a rotating stall, have been observed [33, 37].

Although the pressure gradient is of key importance, an identification of flow separations in three dimensional domains is still an arguable issue. In the previous works, a hypothesis based on the streamlines of the wall shear stress on a body surface called skin-friction line or limiting streamline is proposed to characterize flow separation and attachment [45, 46]. It suggests that the wall shear stress vector vanishes and forms singular points situated in the flow field, which correspond to three dimensional flow separation/attachment depending on the pattern formed. The analyses of the flow separation based on the skin-friction line have been applied to a wide range of engineering applications in the past [14, 69, 82, 85]. Particularly for the case of hydraulic turbines, skin-friction analyses were applied to the flow in the draft tube at part load condition by Mauri *et al.* [51], and they successfully correlated the efficiency drop at part load condition with the flow separation evaluated by the skin-friction pattern on the draft tube wall.

The wall shear stress τ_w is given by the derivative of the velocity in the direction normal to the wall surface. In the presented case, the wall shear stress on the hub according to the settled coordinate definition (see Appendix C) is given by the derivative of the relative velocity by the dimensional span-wise location s, such that

$$\tau_w(m) = \mu \frac{\partial W_m}{\partial s} = \mu \frac{\partial C_m}{\partial s} \qquad \tau_w(\theta) = \mu \frac{\partial W_u}{\partial s} \tag{7.4}$$

where m is the dimensional streamwise location. At a singular point where the direction of the shear-stress vector cannot be defined, the skin friction lines provide a particular pattern. The type of skin-friction pattern is classified by the sign of the eigenvalues of its Jacobian matrix, which can be calculated as follows in the presented case.

$$J = \begin{bmatrix} \frac{\partial \tau_w(m)}{\partial m} & \frac{\partial \tau_w(m)}{r\partial \theta} \\ \frac{\partial \tau_w(\theta)}{\partial m} & \frac{\partial \tau_w(\theta)}{r\partial \theta} \end{bmatrix} = \begin{bmatrix} \frac{\partial^2 C_m}{\partial m \partial s} & \frac{\partial^2 C_m}{r\partial \theta \partial s} \\ \frac{\partial^2 W_u}{\partial m \partial s} & \frac{\partial^2 W_u}{r\partial \theta \partial s} \end{bmatrix} \tag{7.5}$$

The two eigenvalues of the Jacobian matrix λ_{J1} and λ_{J2} are then calculated from the characteristic equation of Equation 7.5.

$$\begin{aligned} \lambda_{J1}, \lambda_{J2} = & \frac{1}{2}\left(\frac{\partial^2 C_m}{\partial m \partial s} + \frac{\partial^2 W_u}{r\partial \theta\, \partial s}\right) \\ & \pm \frac{1}{2}\sqrt{\left(\frac{\partial^2 C_m}{\partial m \partial s} + \frac{\partial^2 W_u}{r\partial \theta\, \partial s}\right)^2 - 4\left(\frac{\partial^2 C_m}{\partial m \partial s}\frac{\partial^2 W_u}{r\partial \theta\, \partial s} - \frac{\partial^2 C_m}{r\partial \theta \partial s}\frac{\partial^2 W_u}{\partial m \partial s}\right)} \end{aligned} \tag{7.6}$$

The singular points are then mathematically identified by the combination of the eigenvalues, as described in [41] (see Figure 7.20). The vortex formation corresponds to the focus pattern, and it is normally accompanied by a separation line.

In Figure 7.21, the comparison of the averaged skin-friction lines on the hub together with the region of focus identified by Equation 7.6 at OP#1, #2, and #3 is presented. All the skin-friction patterns show the focus pattern appears in the middle of the channel corresponding to the inter-blade vortex onset, although the focus pattern at OP#3 is slightly unstable. At OP#1, the saddle point appears near the pressure side of the blade, which creates the separation line where the skin-friction lines from the inlet of the blade channel converge. This indicates that the flow may start separating from the hub at this location. This separation line emanates from the focus near the leading edge on the blade pressure side and ends at the focus caused by the inter-blade vortex, suggesting that the development of the inter-blade vortex is generated by the separated flow from the hub. The flow separation as well as the strong development of the inter-blade vortex causes the blockage of the flow, and the flow does not reattach to the hub. This leads to the significant development of a stalled velocity region near the blade outlet, as

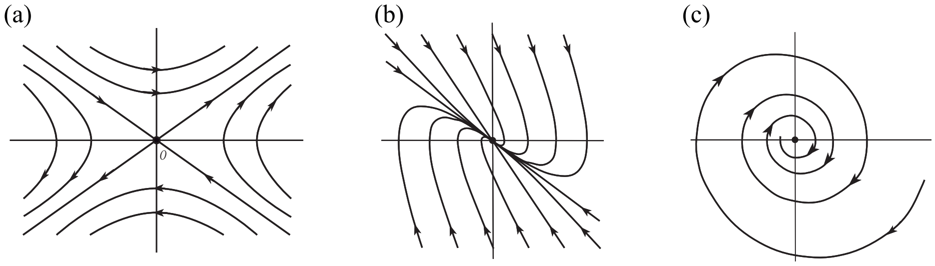

Figure 7.20 – Examples of the singular points identified by the combination of the eigenvalues, saddle (a), node (b), and focus (c) [41]

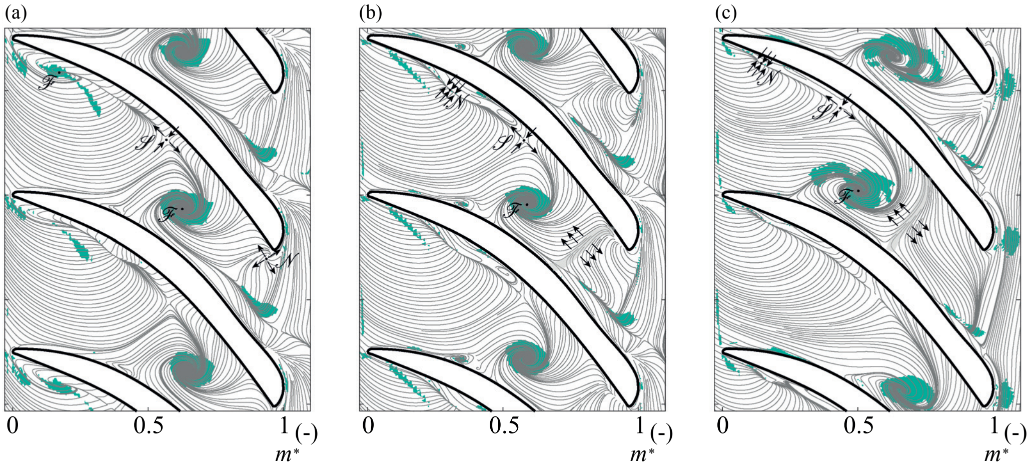

Figure 7.21 – Skin-friction pattern on the hub together with the region of focus identified by Equation 7.6 at OP#1 (a), #2 (b) and #3 (c) ($\mathscr{F}$: Focus, $\mathscr{N}$: Node, $\mathscr{S}$: Saddle). The skin-friction lines are written by the averaged wall shear stress over four runner revolutions.

confirmed in Section 7.3. At OP#2, the skin-friction structures are similar to OP#1. However the focus pattern observed at the leading edge is transformed to a node with respect to the increase of the flow incident angle at the inlet. Near the blade outlet, the attachment line (see light gray line in Figure 7.21b) appears instead of the node observed at OP#1. This implies that the flow starts to reattach near the outlet of the blade channel, which reduces the backflow region at the outlet. At OP#3, the skin friction structure shows more unstable patterns, even though the vortex structure still exists as a focus in the middle of the channel. However, the attachment line near the blade channel outlet observed at OP#2 becomes clearer and moved to the upstream, suppressing the backflow region developing near the outlet.

7.6.2 Pressure gradient along the flow streamline

For the occurrence of the flow separation, the positive pressure gradient along the flow stream plays a decisive role. For Francis turbines, in addition to the main pressure gradient from the blade channel inlet to outlet, a positive pressure gradient is created from the blade suction side to the pressure side due to the curvature of flow streamlines and the Coriolis force inside the blade channel. In the simulated conditions, the flow has a considerably high negative flow incident angle at the inlet especially at OP#1. The flow with the high negative incident angle at the inlet causes the flow directed from the suction side to the pressure side in the middle of the blade channel. Since the pressure is higher on the blade pressure side than on the suction side, such flow from the suction side to the pressure side may be partially subject to an adverse pressure gradient along the flow streamline. In Figure 7.22a, the variation of the pressure factor C_p along one selected flow streamline starting from the inlet (see solid black line in Figure 7.22b) as well as the pressure gradient along the streamline $\partial C_p / \partial l_{str}$ are presented. The pressure first decreases along the streamline leading to a negative value of the derivative

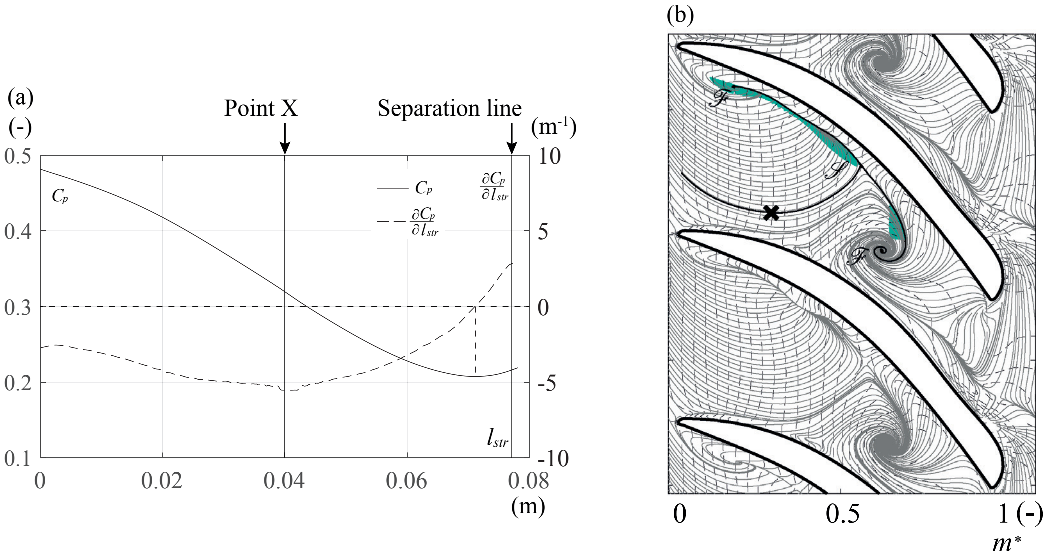

Figure 7.22 – Variation of the pressure factor C_p and the pressure gradient $\partial C_p / \partial l_{str}$ along one flow streamline starting from the blade channel inlet (a) and the region of the adverse pressure gradient along streamline (light blue zone) created near the separation line (b). The selected flow streamline in (a) is highlighted by solid black line in (b)

$\partial C_p / \partial l_{str}$ near the inlet. However, the slope of the decrease of $p/\rho E$ is remarkably reduced at the point where the flow direction is modified (see Point X in Figure 7.22b), accordingly the derivative $\partial C_p / \partial l_{str}$ starts increasing. Finally, the derivative $\partial C_p / \partial l_{str}$ becomes positive at the location corresponding to the separation line. In Figure 7.22b, the region where the pressure gradient along the flow streamlines starting from the inlet becomes positive is highlighted on the skin-friction plot. The region of the adverse pressure gradient appears near the separation line, suggesting that the adverse pressure gradient induced by the misaligned flow plays a significant role for the occurrence of the flow separation on the hub.

7.6.3 Three dimensional flow pattern near the hub

In Figure 7.23, the averaged 3-D flow streamline starting from the inlet of the blade channel near the hub from $s^* = 0.95$ to 1.00 as well as the tangential streamline on the span-wise plane at $s^* = 1.00$ corresponding to the skin-friction line on the hub, 0.75, 0.50, 0.25 and 0.10 are presented. As presented in Section 7.6.1, the flow streamline starting near the hub at OP#1 shows the separated flow from the hub near the pressure side of the blade, of which location corresponds to the separation line shown in Figure 7.21. The stalled region near the outlet of the blade channel is rolled up by the separated flow, yielding the strong inter-blade vortex structure observed in the middle of the channel. Since the flow separation at OP#1 is most intensely developed among the presented cases and the separated flow is not reattached on the hub, no streamlines pass through the blade channel outlet near the hub and they are concentrated on the shroud side. At OP#2, although the general characteristics of the flow stream is found to be similar to OP#1 and the flow seems separated from the hub near the pressure side, some of the streamlines remain near the hub, resulting in the more distributed flow at the outlet of the blade channel. At OP#3, the flow streamlines close to the pressure side near the blade channel inlet create the backflow region and re-enter the next blade channel as shown in Figure 7.7 , hence the flow streamlines show a slightly irregular pattern. Although the separation line near the pressure side and the vortical structure are formed, the strength of the flow separation is less intense and the re-attachment of the flow occurs downstream of the vortex region. Therefore, the back-flow region observed at OP#1 and #2 is suppressed and streamlines passing through the outlet of the blade channel near the hub appear at OP#3.

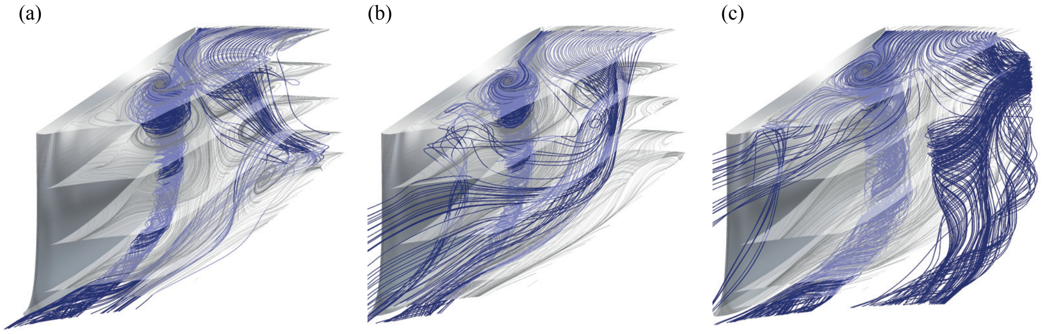

Figure 7.23 – 3-D flow streamlines starting from the inlet of blade channel inlet from $s^* = 0.95$ to 1.00 at OP#1 (a), #2 (b), and #3 (c). The streamlines are written by the averaged velocity over four runner revolutions.

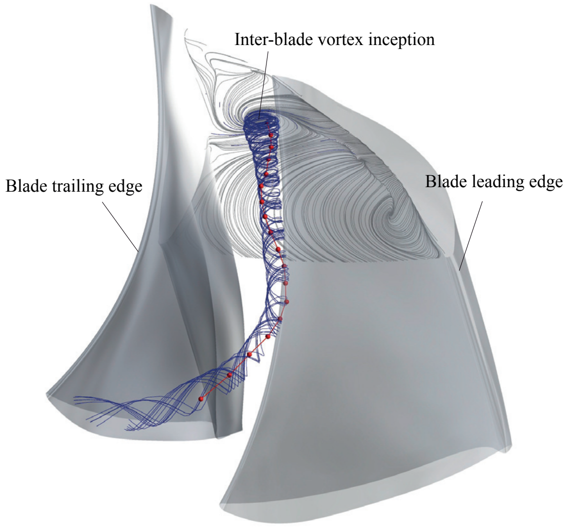

Figure 7.24 – Comparison of the inter-blade vortex structure highlighted by the flow streamlines starting from the hub with the locations of the inter-blade vortex estimated by the visualization results (red line) together with the skin-friction lines on the hub

The presented flow streamlines evidently confirm that the flow separation on the hub yielding the formation of the backflow region plays a significant role for the development of the strong inter-blade vortex.

In Figure 7.24, a downstream view of the vortex structure highlighted by the averaged flow streamline starting from the hub together with the skin-friction line on the hub at OP#1 is presented. The estimated inter-blade vortex location based on the visualization is also shown together. It clearly shows that the inter-blade vortex structure emanates from the focus of the skin-friction line on the hub. Furthermore, the vortex location estimated from the visualization as well as its inception are in very good agreement with the simulated results, suggesting that the location of the flow separation on the hub is accurately evaluated by the performed simulation.

7.7 Influence of inter-blade vortices on the specific energy loss

7.7.1 Specific energy distribution

In the hydraulic machines, the backflow formation associated with the flow separation induces the adverse influence on the efficiency of the machine. In this section, the influence of inter-blade vortex development on the dissipation of the specific energy is characterized by the variation of the specific energy as well as the specific rothalpy through the blade channel. The comparison of the mean distribution of the dimensionless specific energy gH/E_b for OP#1, #2 and #3 averaged in one blade channel is presented in Figure 7.25. E_b represents the specific energy of one single blade channel. The meridional contour demonstrates that the decrease of the specific energy at the middle of the channel around $m^* = 0.60$ is rather significant at OP#1 due to the strong inter-blade vortex structure, whereas the specific energy is more uniformly decreased at OP#3. To evaluate the quantitative specific energy evolution through the blade channel, it is necessary to consider the specific energy balance in an appropriately settled control volume. The variation of the specific energy flux through a control volume rotating with the runner is given by the following equation.

$$\Delta F_E = \int_{\partial V} \left(\frac{p}{\rho} + \frac{1}{2}\vec{C}^2 + gz \right) \rho \vec{W} \cdot \vec{n} dA \equiv \int_{\partial V} gH \vec{W} \cdot \vec{n} dA \tag{7.7}$$

By setting the boundary of the control volume on a given streamwise location, the outlet of the channel, and wall boundaries of the channel such as the hub, shroud, and blade surfaces, Equation 7.7 is transformed into surface integrations and the specific energy $E_{m^* \div \bar{1}}$ between a given streamwise location m^* and the blade channel outlet is then calculated as:

$$E_{m^* \div \bar{1}} = \frac{1}{\rho Q} \left(\int_A gH \rho \vec{W} \cdot \vec{n} dA \bigg|_{m^*} - \int_A gH \rho \vec{W} \cdot \vec{n} dA \bigg|_{m^*=1} \right) \tag{7.8}$$

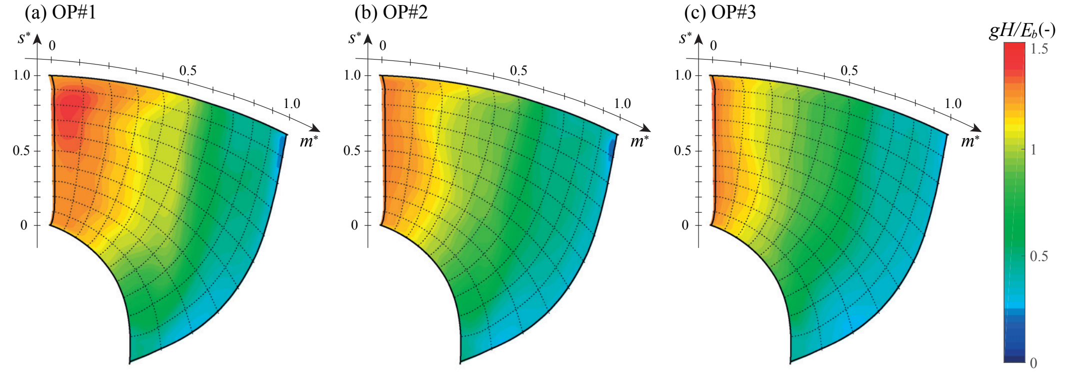
(a) OP#1 (b) OP#2 (c) OP#3

Figure 7.25 – Meridional distribution of the specific energy gH/E_b averaged in one blade channel at each streamwise and span-wise location for OP#1 (a), #2 (b), #3 (c). The quantity is averaged over four runner revolutions.

The integration divided by ρQ in the right-hand side of Equation 7.8 potentially indicates the mass flow weighted average of the quantity at a given streamwise surface. Taking into account the geometrical relation of the span-wise location with the z-axis, Equation 7.8 is then calculated as follows:

$$E_{m^*\div\bar{1}} = \frac{1}{\rho Q}\left(\int_{z_{sh}}^{z_{hb}}\int_{\theta_s}^{\theta_p}\rho\, C_m\, gH\, r\sin\gamma\, d\theta dz\bigg|_{m^*} - \int_{z_{sh}}^{z_{hb}}\int_{\theta_s}^{\theta_p}\rho C_m\, gH\, r\sin\gamma\, d\theta dz\bigg|_{m^*=1}\right) \tag{7.9}$$

where z_{hb} and z_{sh} are the axial position of the hub and shroud at a given streamwise location, and γ the deflection angle between the span-wise plane and z-axis (see Appendix C). In the presented way, the calculation of Equation 7.9 at $m^* = 0$ corresponds to the specific energy of the evaluated blade channel E_b. The specific energy at a given non-dimensional streamwise location m^* is made non-dimensional by the specific energy of the blade E_b as follows:

$$E^*(m^*) = \frac{E_{m^*\div\bar{1}}}{E_b} \tag{7.10}$$

Then, the values of non-dimensional specific energy $E^*(m^*)$ correspond to 1 at the blade channel inlet ($m^* = 0$) and 0 at the outlet ($m^* = 1$). In Figure 7.26, the comparison of $E^*(m^*)$ over the non-dimensional streamwise location m^* for OP#1, #2, and #3 is shown. It can be confirmed that the specific energy decrease at OP#1 near the inter-blade vortex region is high as estimated in Figure 7.25, whereas the evolution of E^* becomes more uniform when the operating conditions is changed. This potentially indicates that the presence of the inter-blade vortex may cause a specific energy loss through the blade channel.

7.7.2 Specific energy dissipation evaluated from rothalpy

For the quantitative evaluation of the specific energy loss in the rotational frame, the specific rothalpy (or often called relative total pressure) is adopted. The specific rothalpy I for the isothermal fluid in the rotating frame is expressed as follows:

$$I = \frac{p}{\rho} + \frac{1}{2}\vec{W}^2 - \frac{1}{2}\vec{U}^2 + gz = \frac{p}{\rho} + \frac{1}{2}\vec{W}^2 - \frac{1}{2}(R\omega)^2 + gz \tag{7.11}$$

In Figure 7.27, the meridional distribution of the averaged non-dimensional specific rothalpy $I^* = (I - I_1)/E_b$ is presented. It highlights a significant decrease of the specific rothalpy especially at OP#1 in the region of the inter-blade vortex. Downstream the inter-blade vortex structure especially near the hub, the rothalpy is increased again due to the backflow development. The rothalpy decrease at OP#2 is mitigated according to the reduction of the vortex intensity, and it shows slightly irregular pattern at OP#3 due to the unstable vortex

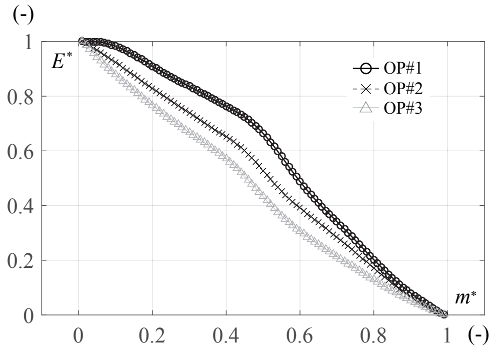

Figure 7.26 – Evolution of the non-dimensional specific energy E^* over the non-dimensional streamwise location m^*

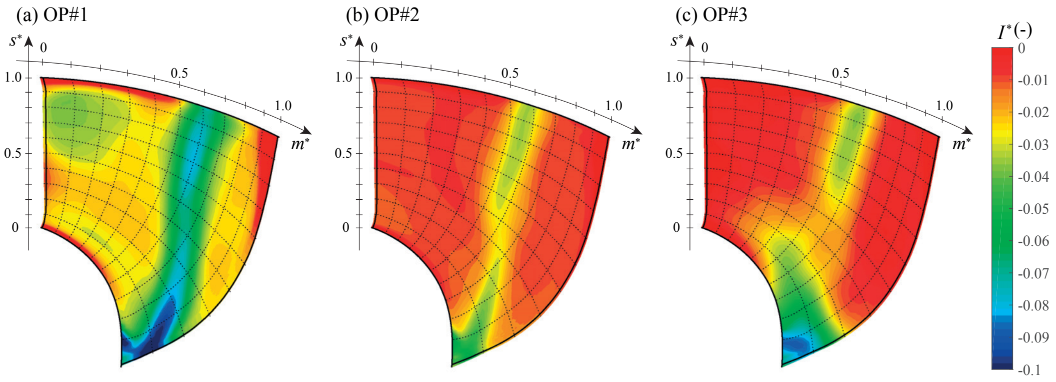

Figure 7.27 – Meridional distribution of the non-dimensional specific rothalpy I^* averaged in one blade channel at each streamwise and span-wise location for OP#1 (a), #2 (b), #3 (c). The quantity is averaged over four runner revolutions.

appearance. Nevertheless, the remarkable decrease of the rothalpy at OP#1 strongly suggests that the inter-blade vortex can be a major source for specific energy to dissipate through the blade channel.

In the same way as Equation 7.7, the variation of the energy flux defined by the specific rothalpy F_I through a control volume rotating with the runner is expressed as follows:

$$\Delta F_I = \int_{\partial V} \left(\frac{p}{\rho} + \frac{1}{2}\vec{W}^2 - \frac{1}{2}(R\omega)^2 + gz \right) \rho \vec{W} \cdot \vec{n} dA \equiv \int_{\partial V} I \vec{W} \cdot \vec{n} dA \tag{7.12}$$

In previous studies, it was proven that the energy flux ΔF_I is conserved under certain conditions in turbomachineries [9, 48]. However, they reported that ΔF_I is dissipated due to the effects of the viscosity, singular and regular energy losses, and the flow unsteadiness. By setting the boundaries of the control volume in a way similar to Equation 7.8, the specific energy loss E_r given by the principle of the specific rothalpy conservation can be calculated from the blade channel inlet ($m^* = 0$) to a given streamwise location m^*, such as:

$$\begin{aligned} E_{r_{1\div m^*}} &= \frac{1}{\rho Q} \left(\int_A I \rho \vec{W} \cdot \vec{n} dA \bigg|_{m^*=0} - \int_A I \rho \vec{W} \cdot \vec{n} dA \bigg|_{m^*} \right) \\ &= \frac{1}{\rho Q} \left(\int_{z_{sh}}^{z_{hb}} \int_{\theta_s}^{\theta_p} \rho\, C_m\, I\, r \sin\gamma\, d\theta dz \bigg|_{m^*=0} - \int_{z_{sh}}^{z_{hb}} \int_{\theta_s}^{\theta_p} \rho\, C_m\, I\, r \sin\gamma\, d\theta dz \bigg|_{m^*} \right) \end{aligned} \tag{7.13}$$

Then, the non-dimensional energy loss e is introduced using the specific energy loss $E_{r_{1\div m^*}}$, such that

$$e = 1 - \frac{E_{r_{1\div m^*}}}{E_b} \tag{7.14}$$

In such a way, the non-dimensional energy loss e decreases with respect to the increase of m^* due to the dissipated specific rothalpy flux, and e at the blade channel outlet $m^* = 1$ becomes equal to the local energetic efficiency of one single blade channel η_b, as follows:

$$e|_{m^*=1} = 1 - \frac{E_{r_{1\div 1}}}{E_b} \equiv \eta_b \tag{7.15}$$

In Figure 7.28, the evolution of the energy dissipation rate e as well as the derivative of e over the streamwise location m^* at OP#1, #2, and #3 are presented. It demonstrates that the non-dimensional energy loss e is almost constantly decreased near the inlet. However the slope of the decrease at OP#1 is clearly modified from $m^* = 0.55$ to 0.60, which corresponds to the region where the inter-blade vortex is developed. The modification of the slope is also observed at OP#2, however it is much smaller compared to OP#1. The derivative $\partial e / \partial m^*$ indicates a significant decrease starting at about $m^* = 0.50$ and reaches its minimum value at

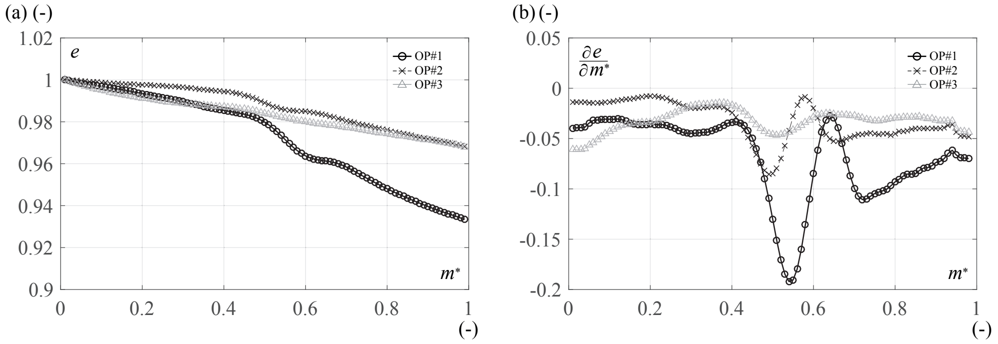

Figure 7.28 – Evolution of the non-dimensional energy loss e (a) and the derivative $\partial e/\partial m^*$ (b) over the non-dimensional streamwise location for OP#1, #2, and #3

about $m^* = 0.55$, whereas this decrease is clearly reduced at OP#2 and OP#3. This evidently shows that the presence of the inter-blade vortex increases the energy dissipation through the blade channel.

When considering the contributions of viscosity and turbulence to the energy dissipation of the flow, the conservation of the specific rothalpy in Equation 7.12 is expressed as follows:

$$\frac{1}{\rho Q}\int_{\partial V}\left(\frac{p}{\rho}+\frac{1}{2}\vec{W}^2-\frac{1}{2}(R\omega)^2+gz\right)\rho\vec{W}\cdot\vec{n}dA=-\frac{1}{\rho Q}\int_V \Phi\rho dV-\frac{1}{\rho Q}\int_V P_k\rho dV \tag{7.16}$$

where Φ and P_k represent the viscous dissipation term and the turbulence production, respectively. These terms are expressed by the the rate-of-strain tensor S and the Reynolds stress τ_t as follows.

$$\Phi = 2\nu\mathbf{S}^2 = 2\frac{\mu}{\rho}\mathbf{S}^2 \tag{7.17}$$

$$P_k = \frac{1}{\rho}\tau_t\mathbf{S} \tag{7.18}$$

Based on the Boussinesq's assumption, the Reynolds stress is linked to the eddy viscosity μ_t expressed by the specific turbulence kinetic energy k. In turbulent flows, the eddy viscosity is considerably larger than the molecular viscosity μ. Hence, the contribution of the eddy viscosity to the energy dissipation of the main flow is more dominant. Thus, it is considered that the viscous dissipation term Φ is negligible compared to the turbulence production term P_k. In the context of model equations, this turbulence kinetic energy is not retrieved to the energy of the mean flow, but only dissipated eventually into thermal energy according to the energy cascade. In other words, the turbulence kinetic energy k produced by the turbulent flow is considered a lost energy from an engineering perspective. In Figures 7.29 and 7.30, the comparisons of the average turbulence kinetic energy k over four runner revolutions as well as its standard deviation k_{STD} at the middle span-wise location $s^* = 0.50$ for OP#1, #2, and #3 are presented, respectively. It is observed that a high turbulence kinetic energy region is generated around the inter-blade vortex structure especially at OP#1, which is caused by a strong turbulence introduced by the inter-blade vortex. Simultaneously, the standard deviation of k becomes remarkably high near the inter-blade vortex region at OP#1. These findings suggest that the kinetic energy of the mean flow is transported to the turbulence kinetic energy of the turbulent flow induced by a strong inter-blade vortex and this yields a high specific energy dissipation through the blade channel.

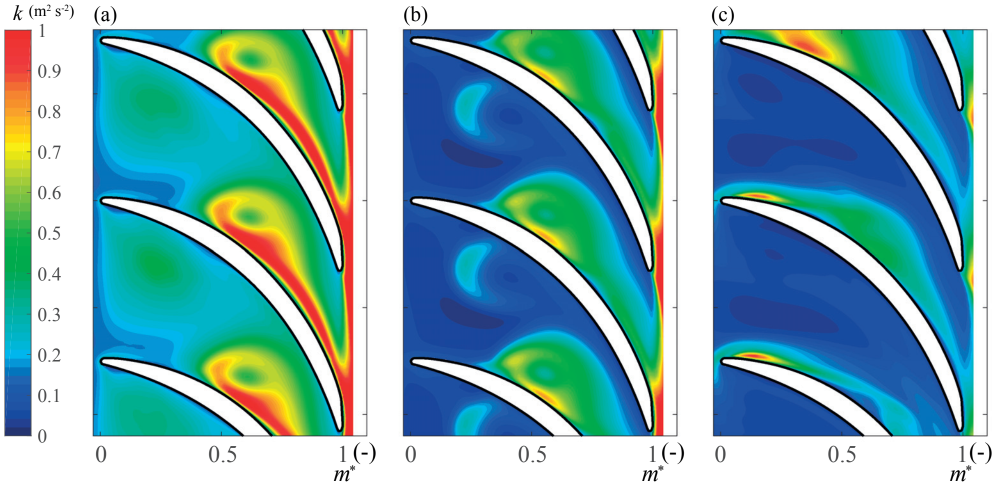

Figure 7.29 – Distribution of the specific turbulence kinetic energy k at the middle span-wise loction $s^* = 0.50$ for OP#1 (a), #2 (b), and #3 (c). The values are averaged over four runner revolutions.

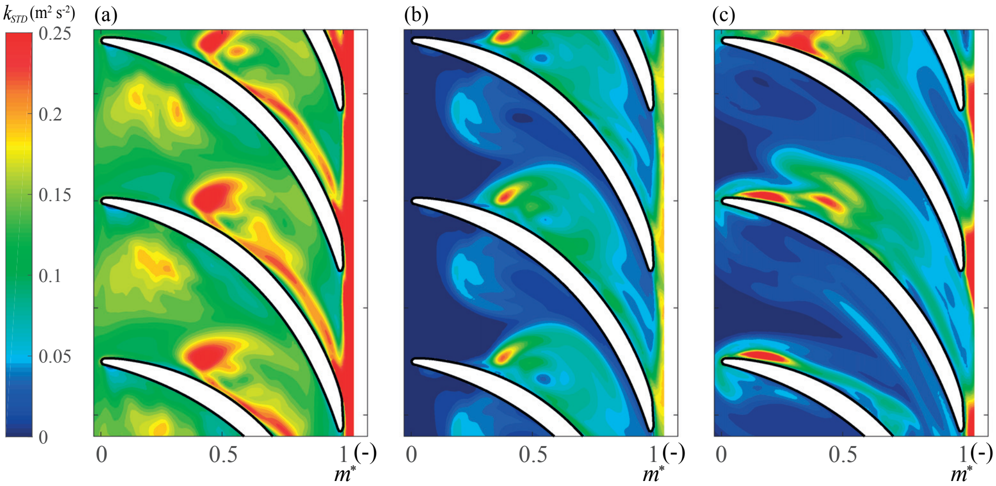

Figure 7.30 – Standard deviation of the specific turbulence kinetic energy k_{STD} calculated over four runner revolutions at the middle span-wise loction $s^* = 0.50$ for OP#1 (a), #2 (b), and #3 (c)

7.8 Summary

In this chapter, the flow structure inside the blade channel as well as the physical mechanisms responsible for inter-blade vortex development are investigated. The performed simulations successfully captures the inter-blade vortex structure, which is validated by the visualization results. Furthermore, the velocity survey inside the blade channel reveals the development of the backflow region on the hub near the outlet of the runner. Moreover, the flow has a considerably non-uniform distribution inside the blade channel caused by the high negative flow incident angle, which seems closely related to inter-blade vortex development. The distribution of the vorticity and the calculated vortex circulation shows the most intense inter-blade vortex structure at OP#1. Furthermore, the strength of inter-blade vortices is intensified especially near the hub. It is confirmed that the presence of a strong inter-blade vortex intensifies stochastic pressure fluctuations especially on the suction side of the blade as confirmed in the on-board pressure measurement. These stochastic nature of inter-blade vortices need to be further investigated to correlate their characteristics with transient flow structures inside the blade channel.

In addition, the flow structure near the hub is studied by application of the skin-friction analysis to identify the flow separation and to describe the mechanisms underlying the development of inter-blade vortices. As a result, it is revealed that the skin-friction lines show a particular pattern that indicates the flow separation on the hub, which induces the backflow region near the runner outlet. The skin-friction lines also show the focus pattern connected to the separation line, which emanates the inter-blade vortex structure. This confirms that the flow separation on the hub is key to the development of inter-blade vortices. Furthermore, the pressure investigation along the flow streamline on the hub reveals that the flow experiences an adverse pressure gradient due to the misaligned flow condition caused by the high negative flow incidence angle at the runner inlet, which plays a decisive role for the flow separation on the hub.

Finally, the specific energy loss due to the presence of an inter-blade vortex is analyzed by introducing the specific rothalpy. The comparison shows that a region of the low specific rothalpy is generated by the inter-blade vortex structure. Furthermore, the quantitatively evaluated specific energy loss by the principle of the specific rothalpy shows that the high energy loss is observed at OP#1, particularly in the region where the inter-blade vortex is significantly developed. This specific energy loss is induced by the high turbulence kinetic energy region, which is caused by the turbulent flow generated from the inter-blade vortex structure. The presented findings confirm that the presence of inter-blade vortices causes the energy dissipation through the blade channel.

Even though the flow structure as well as the development of inter-blade vortices are successfully analyzed by the performed simulation, extensive investigations are required to better understand unsteady characteristics of the inter-blade vortices as well as the stochastic nature of the flow under deep part load operations. These analyses also need to be extended to identify the parameter governing the cavitation dynamics such as cavitation compliance and mass flow gain factor of the inter-blade cavitation vortex. These analyses can enable the development of a one-dimensional model of the flow to investigate the interaction of inter-blade cavitation vortices with hydraulic systems under deep part load operations.

8 Conclusions and perspectives

8.1 Conclusions

At deep part load operating condition, hydraulic machines are subject to particular flow conditions characterized by the significant development of a stalled region in the draft tube. Furthermore, Francis turbines may experience the development of inter-blade cavitation vortices inside the runner at deep part load operation, of which physical properties are insufficiently understood. The present research investigates the flow structures in the draft tube and the fundamental characteristics of inter-blade vortices by experimental and simulation approaches.

The experiments are conducted on a physical reduced scale model of a Francis turbine reproducing actual flow behaviors in prototype machines. Wall pressure measurements as well as high speed visualization are primarily performed to investigate the unsteady characteristics of the flow in the draft tube. The analyses reveal that multiple vortex ropes develop in the draft tube, generating periodic pressure oscillations. In addition, velocity surveys based on Particle Image Velocimetry performed in the draft tube confirm the development of a significant backflow region at the center of the draft tube cone.

To properly capture inter-blade cavitation vortices, the present study introduces a novel visualization technique using instrumented guide vanes, enabling an unprecedented visualization of inter-blade vortex development from the runner inlet. Binary image processing to classify cavitation and non-cavitation regions allows further analyses to evaluate the probability for the development of an inter-blade cavitation vortex and the prediction of the inter-blade vortex locations. The presented results confirm the influence of the speed factor n_{ED} on inter-blade vortex development as well as the higher probability for the formation of cavitation near the hub. This suggests that the intense inter-blade vortex structure is generated especially near the hub. The inter-blade vortex locations are estimated in the 3-D domain by using the simulation domain to validate the simulation results. In addition, the on-board measurement instrumentation installed on the runner blade makes it possible to evaluate the impact of the inter-blade vortex on the pressure field inside the blade channel. On-board pressure measurements with systematically varied operating parameters highlight stochastic pressure oscillations induced by the inter-blade vortex, resulting in the increase of the pressure amplitude especially on the suction side of the blade. Moreover, the wall pressure difference between the pressure and suction sides of the blade demonstrates the occurrence of a negative blade loading near the hub in the discharge range where the inter-blade vortex is observed. This finding suggests the development of a backflow region inside the blade channel near the hub.

In a further effort to understand the flow characteristics in the draft tube and the physical mechanisms responsible for inter-blade vortex development, unsteady RANS simulations are performed. The comparison of the flow structure in the draft tube with the velocity field acquired by PIV as well as the inter-blade vortex structure based on the visualizations show very good agreement, even though the resulting turbine specific energy E and torque T are underestimated. The flow analysis in the draft tube confirms the periodic pressure fluctuation induced by the multiple vortex structures in the draft tube cone as well as the significant backflow development dominating the flow at the center of the diffuser. They prevent an effective pressure recovery and induce a high loss coefficient in the draft tube.

The simulated flow structure inside the runner blade channel is characterized by a considerably non-uniform velocity distribution caused by the high flow incident angle and the development of a backflow region on the hub near the runner outlet. The backflow formation on the hub is found to be closely related to the strong development of the inter-blade vortex, of which strength is evaluated by the vortex circulation Γ. The pressure surveys confirm a negative blade loading near the hub associated with backflow development, and stochastic pressure oscillations induced by the inter-blade vortex. The further study of skin-friction lines enables the identification of the flow separation on the hub. It reveals that the misaligned flow due to the high incident angle causes the flow separation on the hub, inducing the stalled region near the blade channel outlet. Furthermore, the interaction of the separated flow with the stalled region is key to the development of a strong inter-blade vortex structure. The analysis is extended to investigate the influence of the inter-blade vortex on the specific energy loss. The quantitative evaluation of the specific energy loss allowed by the conservation of the specific rothalpy reveals the specific energy dissipation caused by the intensified turbulence due to the inter-blade vortex structure.

It is concluded that flow conditions under deep part load operations are characterized by the development of a significant backflow region. In particular, the development of inter-blade vortices, which is the profound focus of the presented research, is found to be closely relevant to a flow separation on the hub caused by a non-uniform flow distribution as a result of the high incident angle.

8.2 Perspectives

Additional data sets of experimental and computational results obtained during this research project contribute to further studies of the flow under deep part load operations. The primary aims of the presented research, the identification of the fundamental characteristics and the physical mechanisms underlying the inter-blade vortex development, are achieved. However, several different aspects still need to be addressed.

From an experimental perspective, the flow structure related to the inter-blade vortex development needs to be verified by establishment of measurement techniques to clarify the velocity field inside the blade channel. The main obstacles are the runner rotation as well as the complicated runner geometry near the trailing edge of the blade, limiting the access of experimental tools. Such a measurement can be realized by synchronizing velocity measurements by LDV and PIV with the runner rotation. The successful application of the instrumented guide vanes presented in this research may allow for additional measurement applications from the runner inlet. The presented research strongly suggests the stochastic nature of inter-blade vortex appearance and induced pressure oscillations. These stochastic behaviors should be understood additionally, which requires practical synchronization of the on-board pressure measurement (or the velocity survey mentioned above) with continuous visualizations by a more substantial light supply. Furthermore, an interaction of inter-blade vortices with other unsteady flow phenomena such as vortex rope precession in the draft tube and rotor-stator interaction, even though the interaction is not clearly identified in the studied case. In addition, the influences of Reynolds number as well as Froude number need to be addressed for the actual prediction of the inter-blade vortex in the prototype.

From a computational perspective, the flow structures including the development of inter-blade cavitation vortices at the deep part load condition are successfully captured by the performed simulation in the present work. However, the full-domain calculation of the reduced scale model with limited computational resources restricts the mesh numbers distributed to each domain, yielding the discrepancy of the resulting turbine head and torque. Even though the SRS (Scale Resolving Simulation) turbulence model provides satisfactory results in terms of cavitation and vortex development, the stochastic nature of inter-blade vortices may be not fully reproduced. These aspects are achieved by more physically reliable simulations such as LES with more powerful computational resources. Furthermore, the unsteady characteristics and behaviors of inter-blade vortices need to be correlated by transient flow structures inside the blade channel to better understand their stochastic nature.

Finally, the findings of the investigations above, in addition to the present results, lead to the evaluation of the parameters governing the dynamics of cavitation such as the cavitation compliance and the mass flow gain factor. The successful derivation of these parameters enables the development of a one-dimensional model of the flow to further evaluate the interaction of inter-blade cavitation vortices with hydraulic systems.

A Hill-chart of the reduced scale model

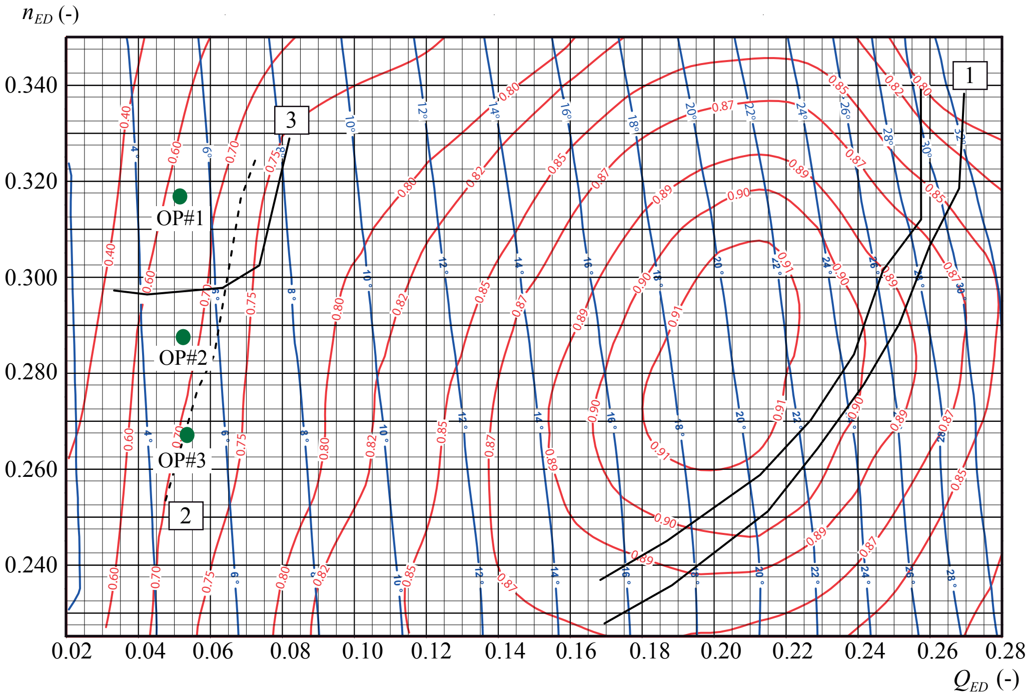

Figure A.1 – Hill-chart of the reduced scale physical model of the tested Francis turbine. (1: Region of no cavitation vortex rope, 2: Visual limit of the cavitation vortex rope, 3: Visual limit of the inter-blade cavitation vortices)

B High-speed visualizations

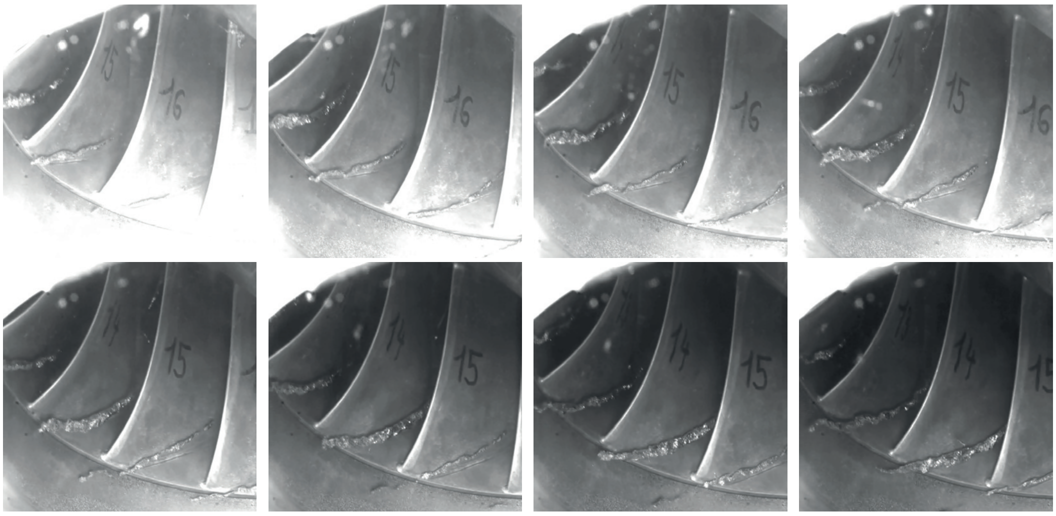

Figure B.1 – High speed visualization of the inter-blade cavitation vortex from the runner downstream using a xenon flash light at OP #1 and $\sigma = 0.11$

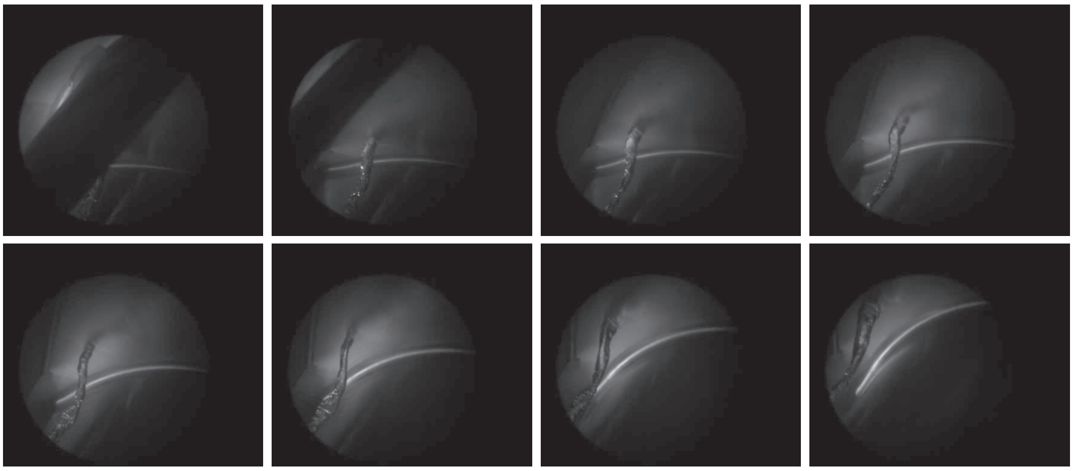

Figure B.2 – High speed visualization of the inter-blade cavitation vortex on the hub side from the runner upstream using the instrumented guide vane at OP #1 and $\sigma = 0.11$

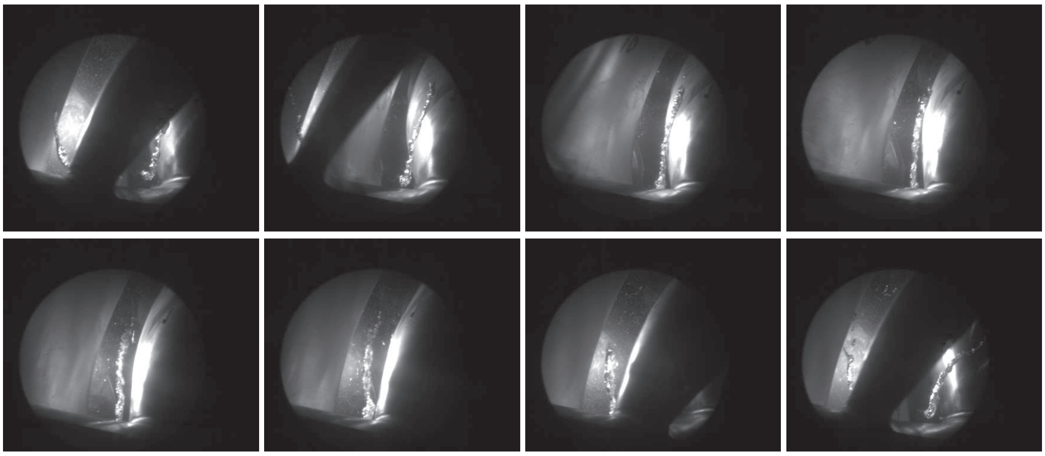

Figure B.3 – High speed visualization of the inter-blade cavitation vortex on the shroud side from the runner upstream using the instrumented guide vane at OP #1 and $\sigma = 0.11$

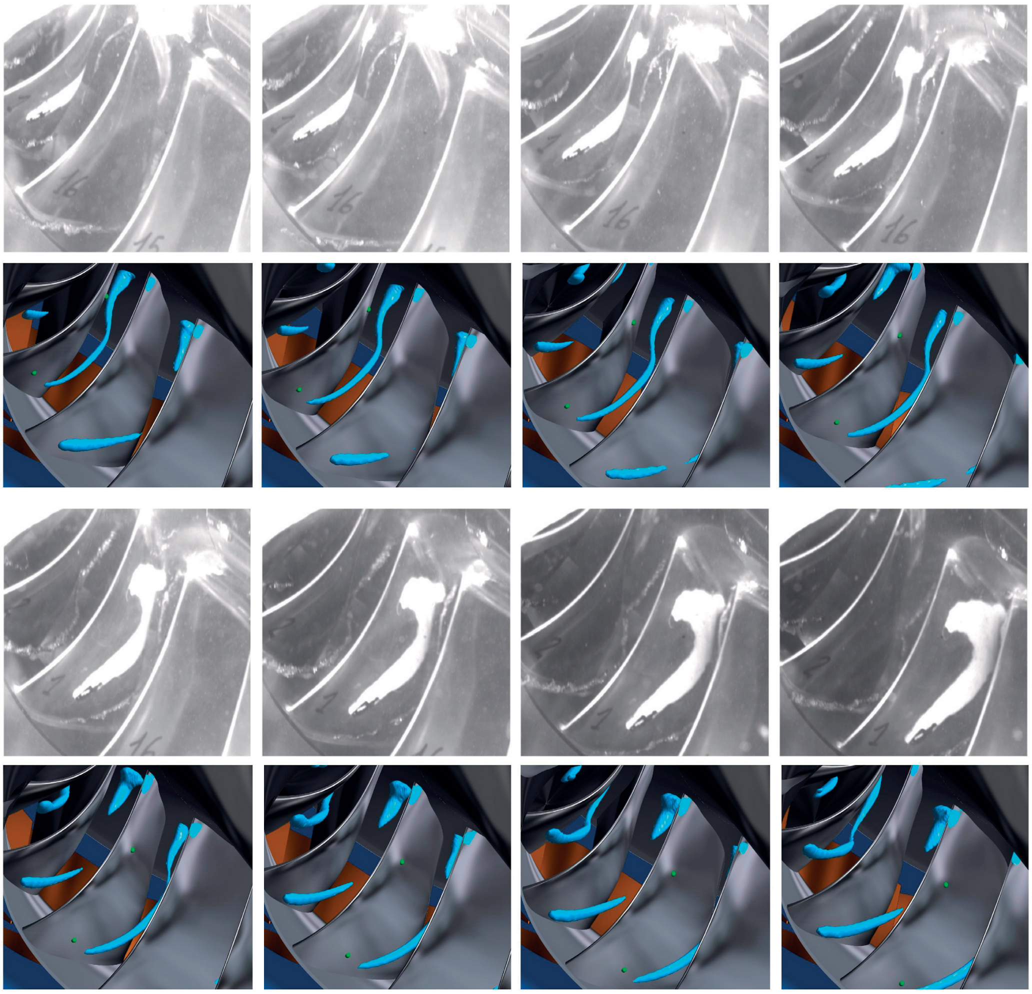

Figure B.4 – Comparison of the high-speed visualization of inter-blade cavitation vortices between the experiment and the simulation at OP #1 and $\sigma = 0.11$

C Calculation of the velocity component

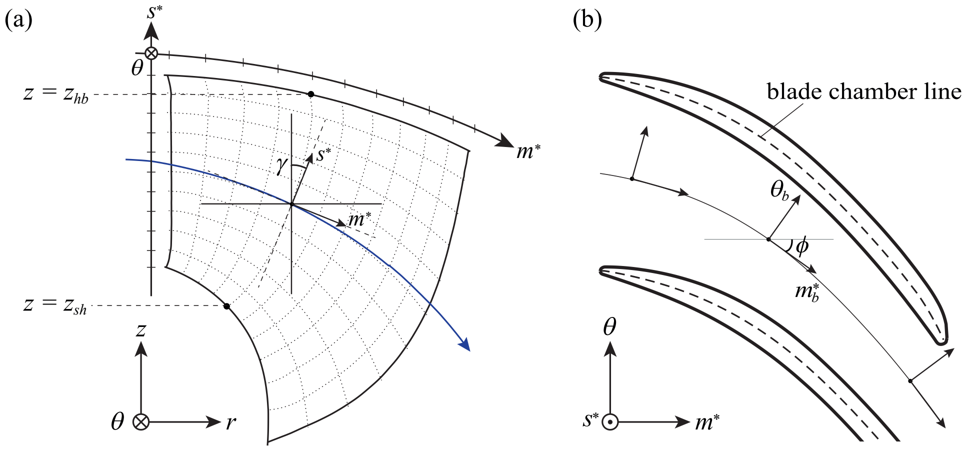

Figure C.1 – Definition of the meridional coordinate (a) and the calculation of the velocity along the blade chamber line (b)

For the investigation of the flow structure inside the blade channel, the meridional coordinate is introduced. The meridional coordinate is defined by three parameters (see Figure C.1a), such as;

$$m : \text{streamwise loctaion} \qquad \theta : \text{theta} \qquad s : \text{span-wise location} \tag{C.1}$$

The streamwise and span-wise locations are made non-dimensional by using the streamwise length and span-wise length respectively, and the non-dimensional streamwise and span-wise locations m^* and s^* correspond to

$$m^* = 0 \,\text{at blade channel inlet,}\ m^* = 1 \,\text{at blade channel outlet for a given span-wise location} \tag{C.2}$$

$$s^* = 0 \text{ at shroud}, \quad s^* = 1 \text{ at hub} \quad \text{for a given streamwise location} \tag{C.3}$$

According to the definition of the coordinate shown in Figure C.1a, the meridional velocity component in the blade channel C_m is given by the radial velocity C_r the axial velocity C_z and the deflection angle γ between the span-wise plane and z-axis as follows.

$$C_m = C_r \cos\gamma + C_z \sin\gamma \tag{C.4}$$

Then, the meridional velocity is made non-dimensional by the discharge velocity $C_Q = Q/A$ at a given streamwise location, as follows.

$$C_m^* = C_m / C_Q \tag{C.5}$$

By using the meridional velocity C_m and the the deflection angle ϕ between the meridional axis and the blade chamber line (see Figure C.1b), the velocity along the chamber line C_b is given by the following equation.

$$C_b = C_m \cos\phi - W_u \sin\phi \tag{C.6}$$

D Inter-blade vortex identification

In order to extract the vortex structure, the accurate definition of the vortex parameter is of key importance. For a vortex detection, there are a number of parameters suggested in the objective of an accurate vortex evaluation [32, 38, 39]. One of the most common parameters is Q-criterion base on the invariant of the velocity gradient tensor $\mathbf{L} = \nabla \mathbf{W}$, which was firstly proposed by Hunt *et al.* [34]. Q-criterion has been conventionally used for many applications to detect and visualize vortex structures, even though a rather simplified method based on the velocity field omitting the calculation of the velocity gradient is proposed [30] and successfully applied [24, 17]. In the present study, Q-criterion is made non-dimensional by the amplitude of relative velocity at the runner inlet and the runner reference diameter, as follows:

$$Q^* = \left(\frac{D_{ref}}{W_1}\right)^2 Q = \frac{1}{2}\left(\frac{D_{ref}}{W_1}\right)^2 [(tr(\mathbf{L}))^2 - tr(\mathbf{L}^2)] = \frac{1}{2}\left(\frac{D_{ref}}{W_1}\right)^2 [||\mathbf{\Omega}||^2 - ||\mathbf{S}||^2] \tag{D.1}$$

where $tr(\mathbf{L})$ represents a first invariant of the velocity gradient tensor, $||\mathbf{\Omega}||$ and $||\mathbf{S}||$ are the Euclidean norm of the vorticity tensor and the rate-of-strain tensor. Thus, Q-criterion potentially indicates the balance of the shear strain rate and the vorticity. Generally, regions of $Q^* > 0$ where the magnitude of the vorticity excesses the one of the rate-of-strain are referred to as a vortex region [32].

Another criterion which is also widely used for the vortex detection is λ_2-criterion. It is calculated based on the helicity of pressure without the unsteady effect and the viscous force of the flow [32]. By decomposing the gradient of the Navier-Stokes equation into the symmetric and antisymetric parts and omitting effects of unsteady shear strain and viscosity, helicity of the pressure is then expressed only by matrices of the rate-of-strain and vorticity, such as:

$$-\frac{1}{\rho} p_{ij} = -(\Omega_{ik}\Omega_{kj} + S_{ik}S_{kj}) \tag{D.2}$$

The λ_2-criterion is defined as the second eigenvalue of the symmetric matrices $\mathbf{\Omega}^2 + \mathbf{S}^2$. The vortex region is considered as regions of $\lambda_2 < 0$, which corresponds to the condition that the local minimum value of the pressure exists [32]. In the present case, the eigenvalue λ_2 is made non-dimensional in the same way as Q-criterion in Equation D.1, such that

$$\lambda_2^* = \left(\frac{D_{ref}}{W_1}\right)^2 \lambda_2 \tag{D.3}$$

As an example of the inter-blade vortex detection, the contours of calculated non-dimensional Q-criterion and non-dimensional λ_2 as well as the plot of velocity vector and tangential streamlines at the middle span plane ($s^* = 0.50$) at OP#1 are presented in Figure D.1. The criteria as well as the vector and streamline plots are based on the averaged velocity field over four runner revolution. The contours of Q^* and λ_2^* show that both values are significantly intensified in the region of the inter-blade vortex, which can be also confirmed in the vector and streamline plot in Figure D.1c. Furthermore, it is confirmed that there is no remarkable difference between distributions of the two criteria. Although proposed criteria sufficiently highlight the inter-blade vortex structure, regions of $Q^* > 0$ or $\lambda_2^* < 0$ tend to cover the most of flow regimes in such a complex flow structure, which prevents an accurate evaluation of the targeted vortex region. In the presented case, positive Q-criterion regions (or negative λ_2^* criterion regions) appear also near the blade leading edge due to a negative incident angle of the flow at the blade channel inlet, even though the magnitude of the criteria is considerably low compared to the inter-blade vortex region. Therefore, the detection of the inter-blade vortex region using $Q^* > 0$ throughout a blade channel at a given span-wise location fails to work properly. Thus, in order to isolate the inter-blade vortex region, the main structure of the

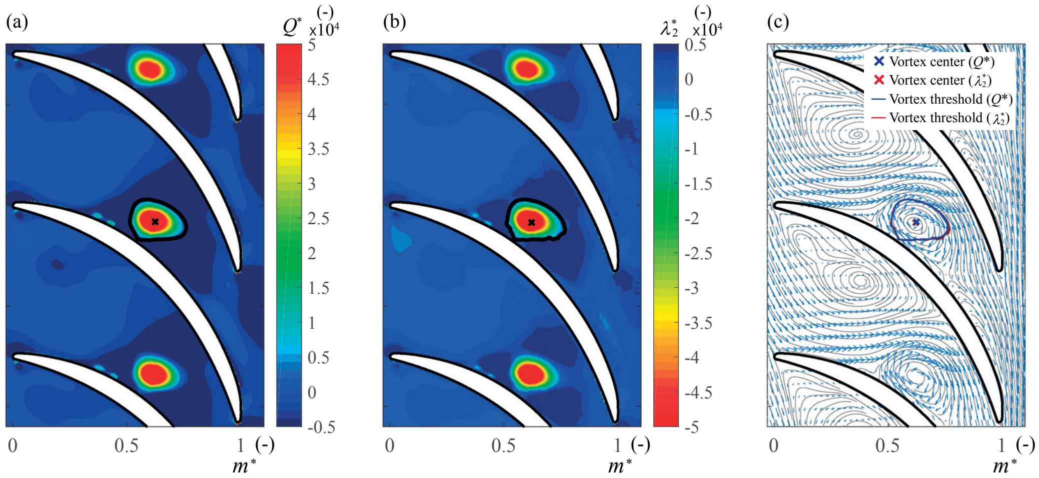

Figure D.1 – Contour of the non-dimensional Q-criterion Q^* (a) and the non-dimensional lambda-2 criterion λ_2^* (b) and the vector and streamline plots (c) at the middle span plane ($s^* = 0.50$) at OP#1, together with the detected center and threshold of the inter-blade vortex region

inter-blade vortex is extracted by increasing a threshold level of the criteria and determine the center of the inter-blade vortex identified by the point of the local maximum/minimum value of the non-dimensional Q-criterion/λ_2 criterion. The inter-blade vortex region is then evaluated by finding the nearest closed curve of $Q^* = 0$ (or $\lambda_2^* = 0$). An example of the vortex center location evaluated by the maximum/minimum value of Q^*/λ_2^* as well as detected inter-blade vortex thresholds are shown in Figure D.1. The thresholds and center of the inter-blade vortex are accurately evaluated. Moreover, both criteria present almost the same locations of the threshold of the inter-blade vortex region and the location of the vortex center. It can be confirmed that the detected vortex center also coincides with the vortex center estimated by the vector and the streamline plots, suggesting that the described methods correctly identify the inter-blade vortex region. Based on the presented results, hence, the non-dimensional Q-criterion Q^* is mainly used for highlighting the vortex structure in the presented research.

Bibliography

[1] *IEC Standards 60193: hydraulic turbines, storage pumps and pump-turbines - model acceptance tests*. International Commision, 2 edition, 1999.

[2] *ANSYS Inc. ANSYS CFX-Solver Modeling Guide*. ANSYS CFX 17.1, 2016.

[3] *ANSYS Inc. ANSYS CFX-Solver Theory Guide*. ANSYS CFX 17.1, 2016.

[4] International Energy Agency. Key world energy statistics 2016. 2016.

[5] S. Alligne, C. Nicolet, Y. Tsujimoto, and F. Avellan. Cavitation surge modelling in francis turbine draft tube. *Journal of Hydraulic Research*, 52(3):399–411, 2014.

[6] F. Avellan. Flow investigation in a francis draft tube: the flindt project. In *Proceedings of the 6th the 20th IAHR Symposium on Hydraulic Machinery and Systems, Charlotte, U.S.A*, 2000.

[7] F. Avellan. Introduction to cavitation in hydraulic machinery. In *Proceedings of the 6th International Conference on Hydraulic Machinery and Hydrodynamics, Timisoara, Romania*, 2004.

[8] J. S. Bendat and A. G. Piersol. *Random Data: Analysis andMeasurement Procedures*. Wiley, fourth edition.

[9] C. Bosman and O.C. Jadayel. A quantified study of rothalpy conservation in turbomachines. *International Journal of Heat and Fluid Flow*, 17(4):410–417, 1996.

[10] C. Brennen and A.J. Acosta. Dynamic transfer function for a cavitating inducer. *Journal of Fluids Engineering, Transactions of the ASME*, 98 Ser 1(2):182–191, 1976.

[11] C. E. Brennen. *Cavitation and Bubble Dynamics*. Oxford University Press.

[12] P. Catalano and M. Amato. An evaluation of rans turbulence modelling for aerodynamic applications. *Aerospace Science and Technology*, 7(7):493–509, 2003.

[13] C. Chen, C. Nicolet, K. Yonezawa, M. Farhat, F. Avellan, and Y. Tsujimoto. One-dimensional analysis of full load draft tube surge. *Journal of Fluids Engineering, Transactions of the ASME*, 130(4):0411061–0411066, 2008.

[14] J.M. Délery. Robert legendre and henri werlé: Toward the elucidation of three-dimensional separation. *Annual Review of Fluid Mechanics*, 33:129–154, 2001.

[15] P. Doerfler. System dynamics of the francis turbine half load surge. In *Proceedings of the 11th IAHR Symposium on Operating problems of pump stations and power plants, Amsterdam, Netherland*, pages 441–453.

[16] P. D orfler, M. Sick, and A. Coutu. *Flow-Induced Pulsation and Vibration in Hydroelectric Machinery*. Springer.

[17] M. Dreyer. Mind the gap: Tip leakage vortex dynamics and cavitation in axial turbines. *PhD thesis, EPFL*, 2015.

[18] F. Duparchy, A. Favrel, P.-Y. Lowys, C. Landry, A. Müller, K. Yamamoto, and F. Avellan. Analysis of the part load helical vortex rope of a francis turbine using on-board sensors. volume 656, 2015.

[19] Y. Egorov and F. Menter. Development and application of sst-sas turbulence model in the desider project. *Notes on Numerical Fluid Mechanics and Multidisciplinary Design*, 97:261–270, 2008.

[20] Y. Egorov, F.R. Menter, R. Lechner, and D. Cokljat. The scale-adaptive simulation method for unsteady turbulent flow predictions. part 2: Application to complex flows. *Flow, Turbulence and Combustion*, 85(1):139–165, 2010.

[21] X. Escaler, E. Egusquiza, M. Farhat, F. Avellan, and M. Coussirat. Detection of cavitation in hydraulic turbines. *Mechanical Systems and Signal Processing*, 20(4):983–1007, 2006.

[22] M. Farhat, S. Natal, F. Avellan, F. Paquet, and M. Couston. Onboard measurements of pressure and strain fluctuations in a model of low head francis turbine - part 1: Instruction. In *Proceedings of the 21th IAHR Symposium on Hydraulic Machinery and Systems, Lausanne, Switzerland*, 2002.

[23] A. Favrel. Dynamics of the cavitation precessing vortex rope for francis turbines at part load operating conditions. *PhD thesis, EPFL*, 2016.

[24] A. Favrel, A. Müller, C. Landry, K. Yamamoto, and F. Avellan. Study of the vortex-induced pressure excitation source in a francis turbine draft tube by particle image velocimetry. *Experiments in Fluids*, 56(12):1–15, 2015.

[25] A. Favrel, A. Müller, C. Landry, K. Yamamoto, and F. Avellan. Ldv survey of cavitation and resonance effect on the precessing vortex rope dynamics in the draft tube of francis turbines. *Experiments in Fluids*, Article in Press.

[26] J-P. Franc, F. Avellan, and B. Belahadji. *La Cavitation*. Presses Universitaires de Grenoble.

[27] M. Germano, U. Piomelli, P. Moin, and W.H. Cabot. A dynamic subgrid-scale eddy viscosity model. *Physics of Fluids A*, 3(7):1760–1765, 1991.

[28] N.R. Gibson. The gibson method and apparatus for measuring the flow of water in closed conduit. *Journal of Hydraulic Research*, 45:343–392, 1923.

[29] A. Goto and M. Zangeneh. Hydrodynamic design of pump diffuser using inverse design method and cfd. *Journal of Fluids Engineering, Transactions of the ASME*, 124(2):319–328, 2002.

[30] L. Graftieaux, M. Michard, and G. Nathalie. Combining piv, pod and vortex identification algorithms for the study of unsteady turbulent swirling flows. *Measurement Science and Technology*, 12(9):1422–1429, 2001.

[31] A.K. Gupta, D. G. Lilley, and N. Syred. *Swirl flows*. Abacus Press, UK, 1984.

[32] G. Haller. An objective definition of a vortex. *Journal of Fluid Mechanics*, 525:1–26, 2005.

[33] V. Hasmatuchi, M. Farhat, S. Roth, F. Botero, and F. Avellan. Experimental evidence of rotating stall in a pump-turbine at off-design conditions in generating mode. *Journal of Fluids Engineering, Transactions of the ASME*, 133(5), 2011.

[34] J. C. R. Hunt, A. Wray, and P. Moin. Eddies, stream, and convergence zones in turbulent flows. *Center for Turbulence Research Report*, CTR-S88, 1988.

[35] M.S. Iliescu, G.D. Ciocan, and F. Avellan. Analysis of the cavitating draft tube vortex in a francis turbine using particle image velocimetry measurements in two-phase flow. *Journal of Fluids Engineering, Transactions of the ASME*, 130(2):0211051–02110510, 2008.

[36] T. Jacob and J. Prénat. Identification of a hydraulic turbomachine's hydro-acoustic transmission parameters. In *Proceedings of the IAHR 5th International Meeting of Work Group on the Behaviour of Hydraulic Machinery under Steady Oscillatory Conditions,, Milano,Italy*, 1991.

[37] C. Jacquet, R. Fortes-Patella, L. Balarac, and J-B. Houdeline. Cfd investigation of complex phenomena in s-shape region of reversible pump-turbine. *IOP Conference Series: Earth and Environmental Science*, 49, 2016.

[38] J. Jeong and F. Hussain. On the identification of a vortex. *Journal of Fluid Mechanics*, 285:69–94, 1995.

[39] J. Jeong, F. Hussain, W. Schoppa, and J. Kim. Coherent structures near the wall in a turbulent channel flow. *Journal of Fluid Mechanics*, 332:185–214, 1997.

[40] W. Jones and B. Launder. The prediction of laminarization with a twoequation model of turbulence. *International Journal of Heat and Mass Transfer*, 15, 1972.

[41] D. W. Jordan and P. Smith. *Nonlinear Ordinary Differential Equations: An Introduction for Scientists and Engineers*. Oxford University Press, New York.

[42] A. Kashima, P.J. Lee, M.S. Ghidaoui, and M. Davidson. Experimental verification of the kinetic differential pressure method for flow measurements. *Journal of Hydraulic Research*, 51(6):634–644, 2013.

[43] J. Koutnik and L. Pulpitel. Modeling of the francis turbine full-load surge. In *Proceedings of the Modeling, Testing and Monitoring for Hydro Power Plants*, volume 3, pages 143–154, 1996.

[44] C. Landry. Hydroacoustic modeling of a cavitation vortex rope for a francis turbine. *PhD thesis, EPFL*, 2015.

[45] R. Legendre. Séparation de l'écoulement laminaire tridimensionnel. *La Rech. Aéronaut*, 54:3–8, 1956.

[46] M.J. Lighthill. Attachment and separation in three-dimensional flows. *Laminar Boundary Layer Theory*, Sect. II 2.6:72–82, 1963.

[47] P. Y. Lowys, F. Paquet, M. Couston, M. Farhat, S. Natal, and F. Avellan. Measurements of pressure and strain fluctuations in a model of low head francis turbine - part 2: Measurements and preliminary analysis results. In *Proceedings of the 21th IAHR Symposium on Hydraulic Machinery and Systems, Lausanne, Switzerland*, 2002.

[48] F.A. Lyman. On the conservation of rothalpy in turbomachines. *Journal of Turbomachinery*, 115(3):520–526, 1993.

[49] M.V. Magnoli and M. Maiwald. Influence of hydraulic design on stability and on pressure pulsations in francis turbines at overload, part load and deep part load based on numerical simulations and experimental model test results. volume 22, 2014.

[50] S. Mauri. Numerical simulation and flow analysis of an elbow diffuser. *PhD thesis, EPFL*, 2002.

[51] S. Mauri, J.L. Kueny, and F. Avellan. Werlé-legendre separation in a hydraulic machine draft tube. *Journal of Fluids Engineering, Transactions of the ASME*, 126(6):976–980, 2004.

[52] F. Menter. Two-equation eddy-viscosity turbulence models for engineering applications. *AIAA Journal*, 32(8):1598–1605, 1994.

[53] F. Menter. A comparison of some recent eddy-viscosity turbulence models. *Journal of Fluids Engineering, Transactions of the ASME*, 118:514–519, 1996.

[54] F. Menter. Eddy viscosity transport equations and their relation to the k-ϵ model. *Journal of Fluids Engineering, Transactions of the ASME*, 119(4):876–884, 1997.

[55] F. Menter and Y. Egorov. The scale-adaptive simulation method for unsteady turbulent flow predictions. part 1: Theory and model description. *Flow, Turbulence and Combustion*, 85(1):113–138, 2010.

[56] P. Moin and K. Mahesh. Direct numerical simulation: A tool in turbulence research. *Annual Review of Fluid Mechanics*, 30:539–578, 1998.

[57] A. Müller. Physical mechanisms governing self-excited pressure oscillations in francis turbines. *PhD thesis, EPFL*, 2014.

[58] A. Müller, M. Dreyer, N. Andreini, and F. Avellan. Draft tube discharge fluctuation during self-sustained pressure surge: Fluorescent particle image velocimetry in two-phase flow. *Experiments in Fluids*, 54(4), 2013.

[59] A. Müller, K. Yamamoto, S. Alligne, K. Yonezawa, Y. Tsujimoto, and F. Avellan. Measurement of the self-oscillating vortex rope dynamics for hydroacoustic stability analysis. *Journal of Fluids Engineering, Transactions of the ASME*, 138(2), 2016.

[60] M. Murakami, K. Kikuyama, and E. Asakura. Velocity and pressure distributions in the impeller passages of centrifugal pumps. *Journal of Fluids Engineering, Transactions of the ASME*, 102(4):420–426, 1980.

[61] T. Nakashima, R. Matsuzaka, K. Miyagawa, K. Yonezawa, and Y. Tsujimoto. Study on flow instability and countermeasure in a draft tube with swirling flow. *International Journal of Fluid Machinery and Systems*, 8(4):230–239, 2015.

[62] S.L. Ng and C. Brennen. Experiments on the dynamic behavior of cavitating pumps. *Journal of Fluids Engineering, Transactions of the ASME*, 100(2):166–176, 1978.

[63] M. Nishi and S. Liu. An outlook on the draft-tube-surge study. *International Journal of Fluid Machinery and Systems*, 6(1):33–48, 2013.

[64] M. Nishi, S. Matsunaga, Y. Senoo, and T. Kubota. Flow regimes in an elbow-type draft tube. In *Proceedings of the 11th IAHR Symposium on Hydraulic Machinery and Systems*, volume 2, pages 38/1–13, 1982.

[65] S.A. Orszag. Analytical theories of turbulence. *Journal of Fluid Mechanics*, 41(2):363–386, 1970.

[66] O. Pacot. Large scale computation of the rotating stall in a pump-turbine using an overset finite element large eddy simulation numerical code. *PhD thesis, EPFL*, 2014.

[67] O. Pacot, C. Kato, Y. Guo, Y. Yamade, and F. Avellan. Large eddy simulation of the rotating stall in a pump-turbine operated in pumping mode at a part-load condition. *Journal of Fluids Engineering, Transactions of the ASME*, 138(11), 2016.

[68] S. Pasche, F. Avellan, and F. Gallaire. Part load vortex rope as a global unstable mode. *Journal of Fluids Engineering, Transactions of the ASME*, Article in Press.

[69] V. C. Patel. Some observations on skin friction and velocity profiles in fully developed pipe and channel flows. *Journal of Fluid Mechanics*, 38(pt 1):181–201, 1969.

[70] U. Piomelli. Large-eddy simulation: achievements and challenges. *Progress in Aerospace Sciences*, 35(4):335–362, 1999.

[71] M. Raffel, C.E.Willert, and J. Kompenhans. *Particle Image Velocimetry: A Practical Guie*. Springer.

[72] W. J. Rheingans. Power swings in hydroelectric power plants, transaction of. *ASME*, 62:171–184, 1940.

[73] P. Rudolf and D. Stefan. Decomposition of the swirling flow field downstream of francis turbine runner. volume 15, 2012.

[74] Y. Senoo and M. Yamaguchi. Study on unstable s-shape characteristic curves of pump turbines at no-flow. *Journal of Turbomachinery*, 109(1):77–82, 1987.

[75] M.L. Shur, P.R. Spalart, M.Kh. Strelets, and A.K. Travin. A hybrid rans-les approach with delayed-des and wall-modelled les capabilities. *International Journal of Heat and Fluid Flow*, 29(6):1638–1649, 2008.

[76] R.L. Simpson. Turbulent boundary layer separation. *Annu Rev Fluid Mech*, 21:205–234, 1989.

[77] J. Smagorinsky. General circulation experiments with the primitive equations. *Monthly Weather Review*, 91:99, 1963.

[78] P.R. Spalart. Strategies for turbulence modelling and simulations. *International Journal of Heat and Fluid Flow*, 21(3):252–263, 2000.

[79] T. Staubli, F. Senn, and M. Sallaberger. Instability of pump-turbines during start-up in the turbine mode. Number 9.6, 2008.

[80] D. Stefan, P. Rudolf, A. Skotak, and L. Motycak. Energy transformation and flow topology in an elbow draft tube. *Applied and Computational Mechanics*, 6:93–106, 2012.

[81] B.S. Stratford. The prediction of separation of the turbulent boundary layer. *Journal of Fluid Mechanics*, 5(1):1–16, 1959.

[82] A. Surana, O. Grunberg, and G. Haller. Exact theory of three-dimensional flow separation. part 1. steady separation. *Journal of Fluid Mechanics*, 564:57–103, 2006.

[83] R. Susan-Resiga, G.D. Ciocan, I. Anton, and F. Avellan. Analysis of the swirling flow downstream a francis turbine runner. *Journal of Fluids Engineering, Transactions of the ASME*, 128(1):177–189, 2006.

[84] R.F. Susan-Resiga, S. Muntean, F. Avellan, and I. Anton. Mathematical modelling of swirling flow in hydraulic turbines for the full operating range. *Applied Mathematical Modelling*, 35(10):4759–4773, 2011.

[85] M. Tobak and D.J. Peake. Topology of three-dimensional separated flows. *Annu. Rev. Fluid Mech*, 14:61–85, 1982.

[86] I.K. Toh, D. Honnery, and J. Soria. Axial plus tangential entry swirling jet. *Experiments in Fluids*, 48(2):309–325, 2010.

[87] J. Wack and S. Riedelbauch. Numerical simulations of the cavitation phenomena in a francis turbine at deep part load conditions. *Journal of Physics: Conference Series*, 656(1), 2015.

[88] T. L. Wahl, M. M. Skinner, and H. T. Falvey. The twin vortex draft tube surge. In *Waterpower'91*, pages 2011–2020.

[89] D. C. Wilcox. Turbulence modeling for cfd. *DCW Industries*, 1998.

[90] K. Yamamoto, A. Müller, T. Ashida, K. Yonezawa, F. Avellan, and Y. Tsujimoto. Experimental method for the evaluation of the dynamic transfer matrix using pressure transducers. *Journal of Hydraulic Research*, 53(4):466–477, 2015.

[91] K. Yamamoto, A. Müller, A. Favrel, C. Landry, and F. Avellan. Pressure measurements and high speed visualizations of the cavitation phenomena at deep part load condition in a francis turbine. *IOP Conference Series: Earth and Environmental Science*, 22, 2013.

[92] K. Yamamoto, A. Müller, A. Favrel, C. Landry, and F. Avellan. Guide vanes embedded visualization technique for investigating francis runner inter-blade vortices at deep part load operation. In *Proceedings of the 6th IAHR International Meeting of the Workgroup on Cavitation and Dynamic Problems in Hydraulic Machinery and Systems, Ljubljana, Slovenia*, 2015.

[93] K. Yamamoto, A. Müller, A. Favrel, C. Landry, and F. Avellan. Numerical and experimental evidence of the inter-blade cavitation vortex development at deep part load operation of a francis turbine. *IOP Conference Series: Earth and Environmental Science*, 49, 2016.

[94] K. Yonezawa, D. Konishi, K. Miyagawa, F. Avellan, P. Doerfler, and Y. Tsujimoto. Cavitation surge in a small model test facility simulating a hydraulic power plant. *International Journal of Fluid Machinery and Systems*, 5(4):152–160, 2012.

[95] P. Zwart, A. G. Gerber, and T. Belamri. A two-phase model for predicting cavitation dynamics. In *Proceedings of the 5th International Conference on Multiphase Flow, Yokohama, Japan*, 2004.

Curriculum Vitae

Keita Yamamoto
Chemin du Stand 19E, 1024
Ecublens, Switzerland

Date of birth : 25.11.1988
Nationality : Japanese
Phone : +41 21 6937382
E-mail : `keita.yamamoto@epfl.ch`

Education

2013–2017	**PhD** École polytechnique fédérale de Lausanne (EPFL), Switzerland
2011–2013	**Master of Science MSc (Engineering)** Graduate School of Engineering Science, Osaka University, Japan
2011 (2 months)	**Internship** National University of Singapore (NUS), Singapore
2007–2011	**Bachelor of Science BSc (Engineering)** School of Engineering Science, Osaka University, Japan

Research projects

2013–2017	**HYPERBOLE - HYdropower plants PERformance and flexiBle Operation towards Lean integration of new renewable Energies** ERC/FP7-ENERGY-2013-1-Grant 608532 Laboratory for Hydraulic Machines (LMH), EPFL Supervisor : Professor François Avellan
2011–2013	**Master thesis (Unsteady behavior of cavitating draft tube flow)** Graduate School of Engineering Science, Osaka University Supervisor : Professor Yoshinobu Tsujimoto
2011 (2 months)	**Internship (Research about Very Large Floating Structures)** National University of Singapore Supervisor : Professor Chien Ming Wang

Activities

- Sports (Especially Football, Karate, and Ski)
- Traveling across Europe and Asia
- Motorcycling and Photography

Skills and Languages

Programming	Matlab, Visual Basic, LabView, C, Fortran, SLURM, Perl
Software	Microsoft Office, LaTeX, Adobe Illustrator, Adobe Photoshop, Canvas, Ansys CFX, AutoCAD
Languages	Japanese — Native proficiency English — Professional working proficiency French — Elementary proficiency

Publications

Papers in international journal

K. Yamamoto, A. Müller, T. Ashida, K. Yonezawa, F. Avellan, Y. Tsujimoto. Experimental method for the evaluation of the dynamic transfer matrix using pressure transducers, in Journal of Hydraulic Research, vol. 53, p. 466 - 477, 2015. doi:10.1080/00221686.2015.1050076

K. Yamamoto, A. Müller, A. Favrel, F. Avellan. Experimental evidence of inter-blade cavitation vortex development in Francis turbines at deep part load condition, submitted to Experiments in Fluids

A. Müller, K. Yamamoto, S. Alligne, K. Yonezawa, Y. Tsujimoto, F. Avellan. Measurement of the Self-Oscillating Vortex Rope Dynamics for Hydroacoustic Stability Analysis, in Journal of Fluids Engineering, vol. 138, 2016. doi:10.1115/1.4031778

A. Favrel, A. Müller, Landry, C. K. Yamamoto, F. Avellan. Study of the vortex-induced pressure excitation source in a Francis turbine draft tube by particle image velocimetry, in Experiments in Fluids, vol. 56, 2015. doi:10.1007/s00348-016-2257-y

A. Favrel, A. Müller, Landry, C. K. Yamamoto, F. Avellan. LDV survey of cavitation and resonance effect on the precessing vortex rope dynamics in the draft tube of Francis turbines, in Experiments in Fluids, vol. 57, 2016. doi:10.1007/s00348-016-2257-y

Papers in conference proceedings

K. Yamamoto, A. Müller, A. Favrel, C. Landry, F. Avellan. Flow characteristics and influence associated with inter-blade cavitation vortices at deep part load operations of a Francis turbine, in Proceedings of the HYPERBOLE conference, Porto, Portugal, 2017

K. Yamamoto, A. Müller, A. Favrel, C. Landry, F. Avellan. Numerical and experimental evidence of the inter-blade cavitation vortex development at deep part load operation of a Francis turbine, in Proceedings of the 28th IAHR Symposium on Hydraulic Machinery and Systems, Grenoble, France, 2016

K. Yamamoto, A. Müller, A. Favrel, C. Landry, F. Avellan. Guide vanes embedded visualization technique for investigating Francis runner inter-blade vortices at deep part load operation, in Proceedings of the 6th IAHR International Meeting of the Workgroup on Cavitation and Dynamic Problems in Hydraulic Machinery and Systems, Ljubljana, Slovenia, 2015

K. Yamamoto, A. Müller, A. Favrel, C. Landry, F. Avellan. Pressure measurements and high speed visualizations of the cavitation phenomena at deep part load condition in a Francis turbine, in Proceedings of the 27th IAHR Symposium on Hydraulic Machinery and Systems, Montreal, Canada, 2014

A. Favrel, C. Landry, A. Müller,K. Yamamoto, F. Avellan. Space and time reconstruction of the precessing vortex core in Francis turbine draft tube by 2D-PIV, in Proceedings of the 28th IAHR Symposium on Hydraulic Machinery and Systems, Grenoble, France, 2016

J. Wack, S. Riedelbauch, K. Yamamoto, F. Avellan. Two-phase flow simulations of the inter-blade vortices in a Francis turbine, in Proceedings of the 9th International Conference on Multiphase Flow, ICMF 2016, Firenze, Italy, 2016

F. Duparchy, A. Favrel, P.-Y. Lowys, C. Landry, A. Müller, K. Yamamoto, F. Avellan. Analysis of the part load helical vortex rope of a Francis turbine using on-board sensors, in Proceedings of the 9th International Symposium on Cavitation, CAV 2015, Lausanne, Switzerland, 2015

A. Müller, A. Favrel, C. Landry, K. Yamamoto, F. Avellan. On the physical mechanisms governing self-excited pressure surge in Francis turbines, in Proceedings of the 27th IAHR Symposium on Hydraulic Machinery and Systems, Montreal, Canada, 2014

A. Favrel, C. Landry, A. Müller,K. Yamamoto, F. Avellan. Hydro-acoustic resonance behavior in presence of a precessing vortex rope: Observation of a lock-in phenomenon at part load Francis turbine operation, in Proceedings of the 27th IAHR Symposium on Hydraulic Machinery and Systems, Montreal, Canada, 2014

C. Landry, A. Favrel, A. Müller, C. Nicolet, K. Yamamoto, F. Avellan. Experimental investigation of the local wave speed in a draft tube with cavitation vortex rope, in Proceedings of the 27th IAHR Symposium on Hydraulic Machinery and Systems, Montreal, Canada, 2014

Teaching

Teaching assistant for courses

- Experiments of mechanical engineering (2012)

  Bachelor course, Osaka University

- Hydropower Plants : Generating And Pumping Units (2013–2017)

  Master course, EPFL

Awards and distinctions

- Fellow award of young researchers from the Japan Society of Mechanical Engineers (2013)

  Presentation title: Dynamic characteristics of cavitating draft tube flow